Stabilization of the Resistive Wall Mode and Error Field Modification by a Rotating Conducting Wall

by

Carlos Alberto Paz-Soldan

A dissertation submitted in partial fulfillment of

the requirements for the degree of

Doctor of Philosophy

(Physics)

at the

University of Wisconsin-Madison

2012

Date of final oral examination: 05/11/12

The dissertation is approved by the following members of the Final Oral Committee:

Cary Forest, Professor, Physics

Paul Terry, Professor, Physics

John Sarff, Professor, Physics

Chris Hegna, Professor, Nuclear Engineering and Engineering Physics

Carl Sovinec, Professor, Nuclear Engineering and Engineering Physics

Stabilization of the Resistive Wall Mode and Error Field Modification by a Rotating Conducting Wall

Carlos Alberto Paz-Soldan

Abstract

The hypothesis that the Resistive Wall Mode (RWM) can be stabilized by high-speed differentially rotating conducting walls is tested in the laboratory. A solid rotating wall capable of routine operation at speeds of 300 km/h, equivalent to a magnetic Reynolds number (R_m) of 5, was designed, assembled, and fielded. Fast wall rotation is found to decrease the RWM growth rate and increase the RWM stable operation window to higher plasma current (I_p), thus demonstrating the stabilizing effect of the wall. The interaction of the rotating wall with non-axisymmetric fields (error fields) is found to lead to asymmetries in wall rotation direction. Analytic theory is used to demonstrate that as wall rotation increases the error field is not necessarily shielded but can instead destabilize the RWM. Error fields are also found to mediate MHD mode-locking bifurcations, which are observed for the first time in a linear plasma column. A torque balance model which includes the effect of the error field, plasma rotation, and wall rotation is developed and applied to the experiment. Asymmetry in wall rotation is also found in the torque balance, with one wall rotation direction eliminating the mode-locking bifurcation. Insertable probes are used to characterize the plasma and show that the column is diamagnetic at low I_p. This diamagnetic equilibrium enables the line-tying boundary condition at the device anode to be verified. At high I_p a persistent helical state is found and reconstructed using correlation techniques. Probes also illustrate that individual flux ropes from the device's discretized plasma gun array merge to form an axisymmetric profile within a short axial distance.

In memory of Roch Kendrick

Acknowledgments

Firstly, I would like to thank my advisor, Cary Forest. Thank you for hiring me to the project, and for giving me the space to make it my own. Thank you for always being eager to discuss physics and for seeing the problem from a new angle. Thank you for challenging me to focus on the essence of the problem, without getting bogged down in details. You have built a very strong and diverse program which I have been honored to be a part of. I wish it well.

Thank you as well to Chris Hegna and John Sarff. I have been very lucky to have such knowledgeable people nearby, and I thank you for always keeping an open door to my queries. Thank you both for showing interest in my work, and for paying attention to the smallest details while also asking the right questions to further my understanding. Special thanks to Abdulgader Almagri. Your expertise in probe making and more was invaluable to this work.

No work is done in isolation, and my studies benefited directly and tremendously from all the work put in by the previous graduate students, David Hannum and Will Bergerson. David and Will built the majority of the hardware used for this work, taking the lab from an empty room to first plasma and beyond. David built the probe rail system which I often used, and helped me understand the experiment during my first years. Will taught me how the bias system and digitization worked, and was always available for further questioning despite having graduated before my arrival. He also challenged me to understand the effects of the bias return leads, which proved to be of critical importance.

Special recognition is necessarily given to Matthew Brookhart. Although he claims I have taught him much, I know that in truth it is I who is deeply indebted to him for all

his efforts on the project, which are too many to list. Good luck doing battle with the experiment to fix the next exploded piece of hardware, fried circuit, or bugged program.

I would also like to acknowledge all the undergraduates with whom I have worked with over the years on the experiment. Andrew Eckhart, especially, put in countless hours to both operate the experiment (at any time of day) and to design various components. Jonathan Jara-Almonte designed and commissioned an optical diagnostic system for the lab, was knowledgeable ahead of his years, and always eager to learn more. Eric Mueller found zen in the lab winding magnetic coils big and small. Adam Clinch and Gabriel Mengin experienced the joy (or terror) of having me as their mentor during their summer projects. I hope they benefited from their work as much as we did, not to mention had a fun summer in Madison.

I also thank the other graduate students and post-docs I shared lab and office space with: Elliot, Cami, Zane, David, Noam, Kian. Thank you for the helping hands whenever necessary, and for putting up with my need for organization and tidiness. I wish everyone great science and speedy finishes.

I have been fortunate to have a great engineering staff to work with. Mike Clark and John Wallace, thank you for all your help in this project, and for being such great people to work with. Good luck on all your projects in the future, both home and work. Bill Zimmerman and Paul Nonn, masters of the dark arts of construction and instrumentation, thank you for all your attention to detail and for freely sharing your wisdom on any topic. I hope to one day know as much as you both do now.

The scientists and faculty of the Plasma Physics group have taught me so much. Gennady, Ellen, Paul, Weixing, Vladimir: thank you for always keeping an open door. I also thank the staff of the Plasma Group for putting up with me for all these years. Russ, Jane, and Dale in the office, and Paul, Andrey and Alex in the Hacquarium. Thank you for all your efforts processing my technical and non-technical requests without complaint.

Dale, all efforts in plasma land benefit immensely from your skillful scouring of federal surplus.

The machinists of the Physics Department Instrument Shop also deserve recognition. Bill, Dave, Doug, Sarah, Mike, Steve, you all did the real work of taking drawings with dimensions to the third decimal place and actually making them real. Keep up the superb work.

My parents, Carlos and Patricia have also continually supported my decision to go to graduate school, and I am proud to be the first in my family to receive a doctoral degree. Thank you for nurturing my curiosity and for giving me the freedom to pursue it.

Finally, and most importantly, thank you to Lana. Thank you for taking the leap with me in this new place. Thank you for your unwavering support, and for all you have given. Our next adventure awaits.

Definitions

Common definitions used throughout this thesis are presented:

MHD	Magneto-hydrodynamics
RWM	The resistive wall mode MHD instability
XK	The external kink MHD instability
the device	The Rotating Wall Machine at the University of Wisconsin-Madison
RFP	The reversed field pinch
RFA/EFA	Resonant/Error field amplification
r_w	The radius of an undefined wall
δ_w	The thickness of an undefined wall
σ_w	The conductivity of an undefined wall
r_p	The plasma radius in the top-hat model
r_a	The radius of the inner stationary wall (vacuum vessel)
r_b	The radius of the outer rotating wall
r_c	The radius of the rotating wall structural support
τ_a	The wall time of the stationary wall
τ_b	The wall time of the rotating wall
τ_c	The wall time of the rotating wall structural support
$q(r_p)$	The safety factor at the plasma edge in the top-hat model
$q(r)$	The safety factor experimentally measured at radius r
q_{crit}	The critical safety factor for instability onset

I_p	The total plasma current driven by electrostatic bias between electrodes
L	The device length
m	The (integer) azimuthal wavenumber of an MHD mode
k_z	The axial wavenumber of an MHD mode
B_z	The axisymmetric guide field applied by external solenoids
B_0	The axisymmetric equilibrium field (B_z and B_θ)
δB_z	The $m = 0$ global perturbation to B_z due to plasma diamagnetism
$\tilde{B}_z$	The $m = 0$ localized perturbation to B_z by localized coils
B_{ext}	The primarily $m = 1$ error field, both intrinsic and actively applied
B_{eq}	The $m = 1$ field produced by the plasma current in response to B_{ext}
B_{mode}	The $m = 1$ field produced by MHD instabilities (XK or RWM)
Ω_ϕ	The plasma toroidal angular velocity in other devices
Ω_w	The angular velocity of the rotating wall
Ω_0	The 'natural' angular velocity of the plasma column
Ω_{ExB}	The ExB angular velocity of the plasma column
ω	The angular velocity of the rotating plasma column
γ	The (complex) growth or decay rate of the MHD mode
$\omega \equiv \Im[\gamma]$	The real frequency of the MHD mode
$\gamma^r \equiv \Re[\gamma]$	The growth or decay rate of the MHD mode
$R_m \equiv \Omega_w \tau_b$	The magnetic Reynolds number of the rotating wall in the lab frame
$R_a \equiv \omega \tau_a$	The magnetic Reynolds number of the static wall in the plasma frame
$R_b \equiv (\omega - \Omega_w)\tau_b$	The magnetic Reynolds number of the rot. wall in the plasma frame

Contents

List of Figures

List of Tables

Chapter 1

Introduction and Motivation

> What happens when a conducting wall is rotated at high speeds around a stable or unstable plasma column? Can wall rotation stabilize the Resistive Wall Mode?

The hypothesis that the Resistive Wall Mode (RWM) can be stabilized by high-speed differentially rotating conducting walls is tested in the laboratory. This work is motivated by the fact that the RWM is a performance limiting instability, which can set the maximum achievable plasma pressure (β) or plasma current (I_p) in a magnetic confinement device. Understanding the impact of rotating walls on the plasma and its instabilities may thus contribute to the design of future devices, allow operation at higher performance levels, and provide insight to phenomena seen in existing experiments.

This Chapter will introduce the thesis as follows: In Section 1.1, the early period of RWM research is reviewed to give context to the work herein. Section 1.2 introduces the wall rotation approach to RWM stabilization, from which this work's central contribution to current research arises (as discussed in Section 1.4). For completion, other progress in RWM stabilization is briefly discussed in Section 1.3.[1] The work of the previous generation

[1]For further elaboration on the development of RWM physics a very thorough review was recently published [1].

of graduate students on the project is described in Section 1.5. Finally, a map of this thesis is given in Section 1.6.

1.1 Early Resistive Wall Mode Research

Experimental and theoretical study of the external kink (XK), and later resistive wall mode (RWM), has been an important part of the fusion research program since its inception. The earliest Z-pinch linear experiments quickly discovered that a plasma column was unstable to $m = 0$ ('sausage', where m is the axial wavenumber) instabilities. These instabilities terminated the plasma and precluded high performance operation. The sausage was found to be effectively stabilized by the addition of an axial guide field (B_z). This configuration, with both B_z and axial current (I_p), was termed the screw pinch. It was then found to be unstable to an $m = 1$ ('kink') instability.

Work in 1954 by Kruskal and Shafranov [2, 3], working independently, found that the screw pinch plasma column was indeed unstable to lateral ($m = 1$) displacements despite the presence of B_z. In their zero-pressure model, instability to the kink was found to be determined by the parameter $q = rB_z/RB_\theta$, and thus q is called the 'safety factor.' As devices generally operate at fixed B_z, instability was normally found as I_p is increased (q lowered). Further theoretical work around this period also found that several drives for instability exist. The sausage instability was found to be driven by plasma pressure, while the early kink was driven by I_p. The kink could also be destabilized by pressure, with both kink stability boundaries observed in toroidal devices.

Later theoretical work in 1984 (in toroidal geometry) by Troyon [4] arrived at the Troyon scaling for XK stability. This scaling stated that the stable operation range of the tokamak was a triangular region in β_T, I_p/aB_T space, where β_T is plasma pressure normalized to the toroidal field energy, a is device minor radius, and B_T is the toroidal

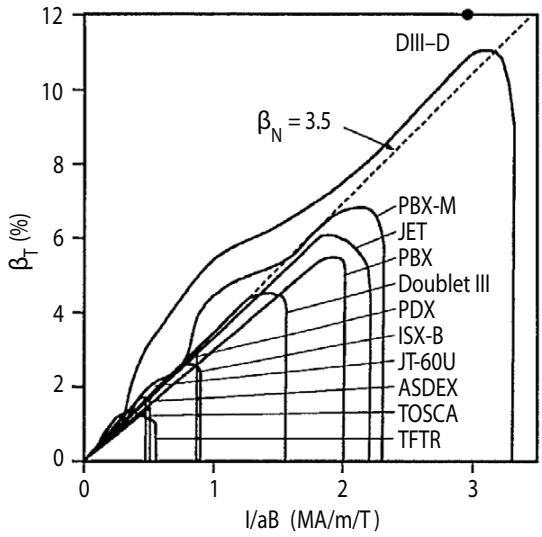

Figure 1.1: Stable operating range as of 1994 across a variety of devices in β_T, I_p parameter space. Results from all devices obey the Troyon scaling [4] though with $\beta_N \approx 3.5$. Taken from Strait et al. [5].

field. The Troyon result stated that critical β_T for instability scaled linearly with I_p/aB_T. Furthermore, the actual slope of the line β_N ($\equiv \beta_T aB_t/I_p$, or 'normalized beta') was predicted to be constant across devices at $\beta_N^{\text{Troyon}} = 2.8$.

Experimental work in the tokamak over the next decade (1984-1994) largely confirmed the picture presented by Troyon, and the view that the XK limited device performance became prevalent [5]. Figure 1.1 illustrates that the Troyon scaling was valid across a wide swath of devices in operation at the time. Even the numeric coefficient was found to be fairly accurate, with experiment giving $\beta_N = 3.5$ vs $\beta_N^{\text{Troyon}} = 2.8$. However, experimental results showed that when $\beta_N = 3.5$ was exceeded the resultant instability did not grow on the predicted Alfvenic time-scale, but rather much more slowly. As the work of Troyon and Kruskal-Shafranov did not include the conducting boundary and its induced eddy currents, the resistive wall effect was proposed to explain the discrepancy. Previous work by Pfirsch and Tasso had shown that such a wall could bring $\gamma \approx \tau_w^{-1}$ [6]. Here τ_w is the vertical field penetration time of the resistive wall, and is defined as $\tau_w \equiv \mu_0 \sigma_w \delta_w r_w$

(where σ_w, δ_w, and r_w are the conductivity, thickness, and radius of the wall). Notwithstanding, niether model predicted the correct stability limit, and sometimes growth was found to be even slower than τ_w^{-1}.

Concurrent research in the Reversed Field Pinch (RFP) also identified slowly growing instabilities with $\gamma \ll \tau_A^{-1}$. The first identification of the RWM in the RFP was made in the HBTX device [7]. There, for long discharges in which $\tau_{\text{pulse}} \gg \tau_w$, wall-locked ($\omega \approx 0$) modes (at $m = 1$, many simultaneous n) were detected on the edge magnetic sensors, and it was found that $\gamma \approx \tau_w^{-1}$. This result corroborated theoretical work that predicted inherent instability of a wide spectrum of RWMs in the RFP [8].

With an appreciation of the importance of the RWM firmly in place, several theoretical proposals to stabilize the RWM were presented around this time. Gimblett proposed stabilization via differentially rotating walls [9], Bondeson and Ward predicted RWM stability with plasma rotation [10], and Bishop proposed stabilization using active feedback coils [11]. Each method has garnered significant experimental and theoretical interest, and will now be explored sequentially. The proposal of Gimblett is the central subject of this thesis, and dedicated discussion is given in Section 1.2. For completion, progress in RWM stabilization via plasma rotation and active feedback is summarized in Section 1.3.

1.2 Resistive Wall Mode Stabilization by Rotating Conducting Walls

A novel proposal to stabilize the RWM was put forward in 1989 by Gimblett [9]. In this short work he showed that a non-rotating plasma otherwise unstable to the RWM could be made stable by allowing differential *wall* rotation. Essentially, stabilization is provided by persistent eddy currents sustained by induction in the two-wall system. The figure of merit for this approach is the magnetic Reynolds number of the wall (R_m), which

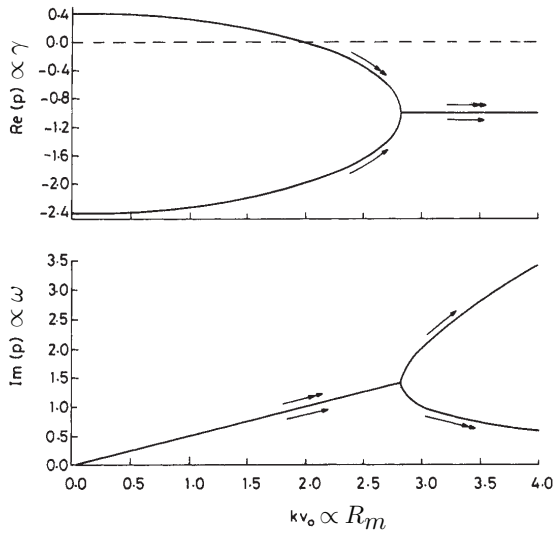

Figure 1.2: Gimblett first showed that differentially rotating walls could stabilize a growing instability. (a) Growth rate (γ) is shown to become negative at a critical value of R_m while (b) mode rotation (ω) continues to increase. Taken from Gimblett et al. [9].

is defined as $R_m \equiv \Omega_w \tau_w$ (where Ω_w is the angular rotation rate of the wall). In his scheme, the differential wall rotation would be provided by a static, inner vacuum vessel and associated mechanical supports, surrounded by a poloidally flowing liquid metal coolant. This scheme yielded the benefit of passive plasma stability without the need for momentum input to the plasma. Furthermore, stabilization should be fully robust once the engineering challenge of designing such a system is overcome. To illustrate this effect, Gimblett simply considered the behavior of the vacuum magnetic field across the static and rotating walls. By defining a perturbation that was unstable without wall rotation, he showed that the introduction of wall rotation brought the instability growth rate to a stable value, as is shown in Fig. 1.2. Further theoretical development of this scheme will be provided in Chapter 7.

The scheme of Gimblett was revisited by Freidberg et al. [14] and Umansky et al. [12] over a decade later. Freidberg considered rigid rotation of a liquid metal wall surrounding a static wall. It was found that this configuration was able to stabilize the RWM, though

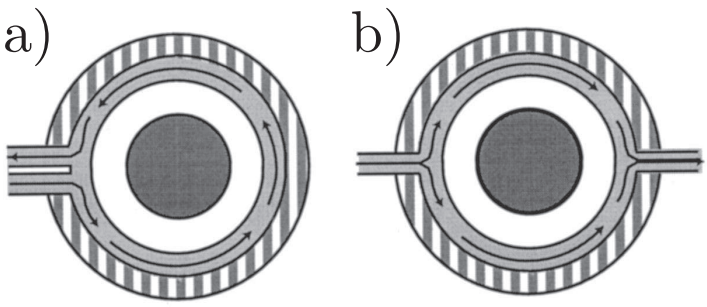

Figure 1.3: Stabilization of the RWM by flowing liquid metal walls was calculated using two different flow profiles. Solid walls can only generate the flow profile of (a). Taken from Umansky et al. [12].

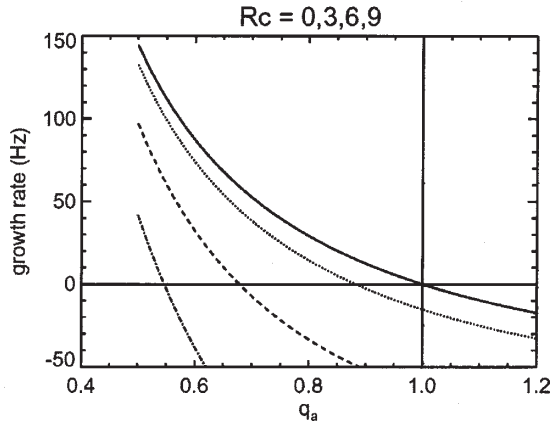

Figure 1.4: The Hegna model predicted that RWM growth rate should decrease as wall rotation ($R_c = \Omega_w \tau_w$) increased, and that the stable operation window should extend to lower safety factor ($\equiv q_a$). Taken from Hegna [13].

the required flow velocities were found to be larger than the single-wall RWM growth rate. Umansky extended the analysis by considering various flow profiles (shown in Fig. 1.3) and treated the liquid metal inlet and outlet, which required expansion to much larger azimuthal wavenumber m. As might be expected, a single flowing wall only Doppler shifted the resulting RWM rotation (ω) and did not provide stabilization. In contrast, a flowing wall in combination with a static wall provided robust stabilization. Interestingly, the two-stream flow of Fig. 1.3b was found to be much more effective, though both profiles required flows on the order of tens of m/s.

The experiment described in this thesis was preceded by a dedicated analytic study carried out in 2004 by Hegna [13], which gave predictions on required wall geometries and rates of rotation which then guided experimental construction. The geometry considered differs from past studies due to the line-tied boundary conditions expected for the device, in contrast to the periodic cylinder geometry used to model the torus. While the details of this work will be provided in Chapter 7, the central conclusions are presented. Hegna found that indeed the line-tied current-driven RWM could be stabilized up to the ideal-wall limit for sufficiently fast wall rotation. For device experimental parameters as they were defined in 2004, the predicted effect of wall rotation on the RWM growth rate is shown in Fig. 1.4. Experimentally achievable wall rotation rates were predicted to yield stabilization at up to $\approx 20-40\%$ lower q. Furthermore, the optimal spacing between the two walls was predicted to be $r_b \approx 1.2 r_a$, which further guided experiment design.

1.3 Other Progress in RWM Stabilization

1.3.1 Stabilization by Plasma Rotation

RWM stabilization by plasma rotation was placed on a firm theoretical footing by the seminal work of Bondeson and Ward [10]. In this work it was shown that with 1) a re-

sistive wall, 2) plasma rotation, and 3) plasma dissipation, the RWM could be stabilized at larger values of β than without these effects. Also introduced in the model was the definition of $\beta_N^{\text{no-wall}}$, the free-stability limit (equivalent to the Troyon calculation) and $\beta_N^{\text{ideal-wall}}$ the point where instability was present despite the conducting wall, dissipation, and rotation. The model predicted that with a rotating plasma β can exceed $\beta_N^{\text{no-wall}}$ (though not $\beta_N^{\text{ideal-wall}}$), and the resultant modes would have $\gamma \approx \tau_w^{-1}$ and a real frequency (ω) also $\approx \tau_w^{-1}$ despite the fact that the underlying plasma flow could be rotating much faster ($\Omega_\phi \gg \tau_w^{-1}$).

As with previous models [8], RWM stabilization could not occur without plasma dissipation, regardless of the value of Ω_ϕ. Thus, subsequent theoretical effort was directed at identifying and properly treating this dissipation. Bondeson and Ward's computational result employed coupling to sound waves and ion Landau damping. Later analytic theories proposed both sound wave coupling [15] and viscosity within an inertial later outside the plasma [16], although both models ultimately yielded similar final results. Around the same time a model proposed by Finn [17] showed that RWM stabilization could be achieved if plasma resistivity was included. In the Finn model resistivity allowed for a tearing-like response and the generation of magnetic islands, even though the (ideal) external kink was the underlying instability. All theories predicted Ω_ϕ to be a few percent of the Alfven speed (V_A) for RWM stabilization.

The Bondeson and Ward picture was found to be consistent with experimental observations at DIII-D [18], shown in Fig. 1.5. Here the plasma rotates rapidly due to imbalanced neutral beam injection imparting a large torque to the plasma. The plasma is stable to the RWM above $\beta_N^{\text{no-wall}}$ for many τ_w. Eventually, the plasma rotation decreases below a critical level ($\Omega_{\phi,\text{crit}}$) and the RWM is found to grow. For much of the next decade experimental and theoretical research were directed at measuring $\Omega_{\phi,\text{crit}}$, determining its scaling with plasma parameters, and developing a model for its prediction. As predicted,

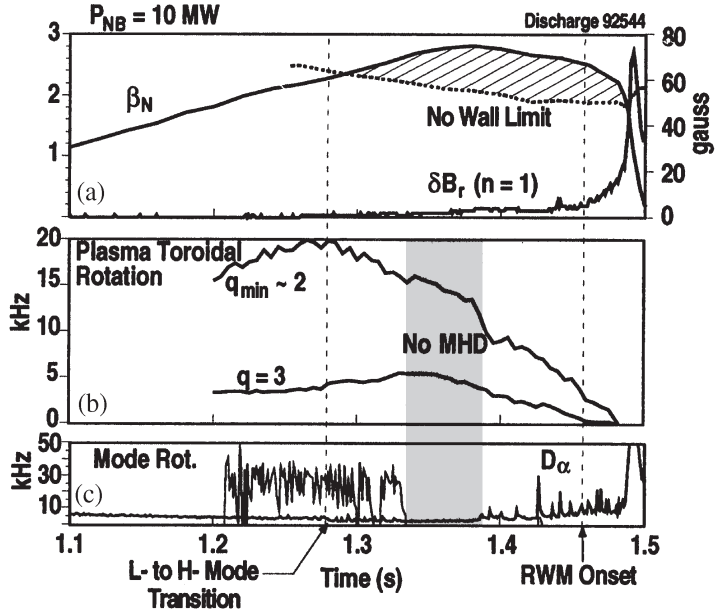

Figure 1.5: Stable operation above $\beta_N^{\text{no-wall}}$ until plasma rotation decreases below a critical value. Taken from Garofalo et al. [18].

$\Omega_{\phi,\text{crit}}$ was found to be a few percent of V_A.

In 2006, the introduction of balanced neutral beams at the DIII-D facility yielded for the first time the ability to independently change Ω_ϕ and β_N. Surprisingly, the plasma was found to be stable to the RWM down to a much lower value of Ω_ϕ than previously found [19]. Thus, two problems now existed. First, the old observations with unbalanced beams needed to be explained (ie, the old $\Omega_{\phi,\text{crit}} \approx 0.02 V_A$), and secondly the new results (which contradicted several theories) required explanation (ie, the new $\Omega_{\phi,\text{crit}} \approx 0.003 V_A$).

Mode-Locking Bifurcations

Study over the following few years identified the importance of the mode-locking bifurcation in setting $\Omega_{\phi,\text{crit}}$ for the unbalanced torque, large Ω_ϕ plasmas. A model put forward by Fitzpatrick [20] included the non-linear interaction of the RWM with its own eddy currents in the wall, and in so doing found that the plasma frequency could suddenly

transition from a quickly rotating (unlocked) state to a nearly stationary (locked) state as the RWM amplitude grew. This theory shared the same phenomenology as those put forward over the preceding decades to model tearing-mode physics [21, 22, 23, 24] and originally written for the induction motor [25].

Analysis of the experimental data with the Fitzpatrick model yielded better agreement with the stated values of $\Omega_{\phi,\text{crit}}$ [26]. Thus, a new interpretation for the data of Fig. 1.5 would be that the rotation associated with the growth of the RWM ($\Omega_{\phi,\text{crit}}$) was actually the rotation value at which the bifurcation to a low-rotation state took place. Thus, the true $\Omega_{\phi,\text{crit}}$ is somewhere between the mode locking threshold and the final, nearly zero rotation state.

It should also be noted that the magnetic perturbation leading to a mode-locking bifurcation need not arise from the instability itself. In fact, the perturbation could be applied from external coils as long as the resultant perturbation is of the same helicity as (resonates with) the instability. This resonant field might also be unintentional - ie, an 'error field.' Thus, the study of error fields is fundamentally important to the study of RWM stability. To complicate matters, the plasma itself can generate more fields (ie, move) as a result of an applied error field, a phenomenon called resonant (or error) field amplification (RFA or EFA) [27]. The RFA field also participates in setting the torque balance equilibrium. These themes are not unique to the torus, and will re-appear in the context of this thesis.

Stabilization by Kinetic Resonances

The much lower value of $\Omega_{\phi,\text{crit}}$ was theoretically explained by modifying the plasma dissipation models to include the effect of kinetic resonances with trapped particle drifts [29, 28, 30], which are important at low rotation. The most important drifts are the bounce frequency (time between poloidal extrema of the banana orbit) and precession

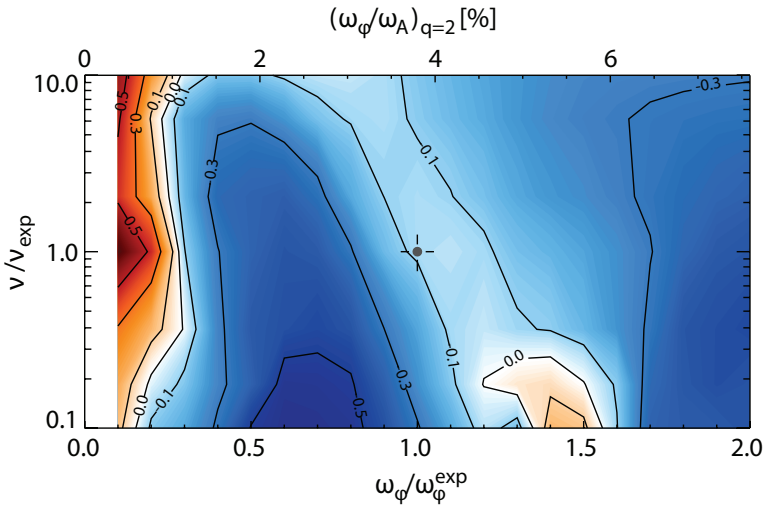

Figure 1.6: Predicted RWM growth rates as plasma rotation (ω_ϕ) and collisionality ν is varied from an experimental baseline. Blue indicates stability, while red is unstable. Taken from Berkery et al. [28].

drift frequency (toroidal transit time of banana orbit guiding center). When the plasma rotation is comparable to these frequencies, strong dissipation and thus stabilization is found. Figure 1.6 illustrates the result of a stability calculation including these kinetic effects. A non-monotonic dependence of the stability on Ω_ϕ is found, indicating that the simple $\Omega_{\phi,\mathrm{crit}}$ model is in fact insufficient to determine RWM stability.

Thus, a conclusion of the most recent works in RWM stabilization by plasma rotation is that the ideal MHD models used throughout RWM research are insufficient to yield predictive understanding of the RWM in future devices. In fact, a full drift-kinetic treatment of the plasma is required. Research along these paths is also ongoing.

1.3.2 Stabilization by Active Feedback

It was also realized early on that the flux leakage through the resistive wall due to a RWM could be actively replaced by a suitably designed active control system [11]. This line of effort forms another pillar of RWM research in the plasma physics community, especially

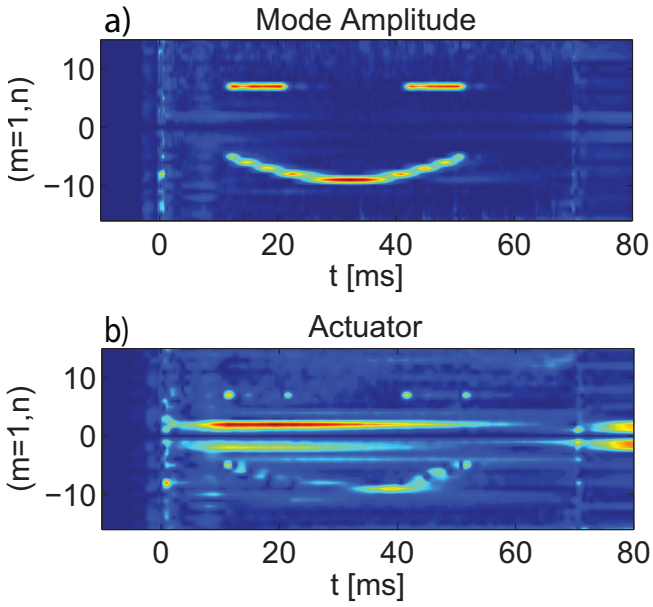

Figure 1.7: Simultaneous control of multiple RWMs ($m = 1$, various n) by active control coils as a function of time. Excitation (b) yields RWM amplitude (a). Taken from Olofsson et al. [31].

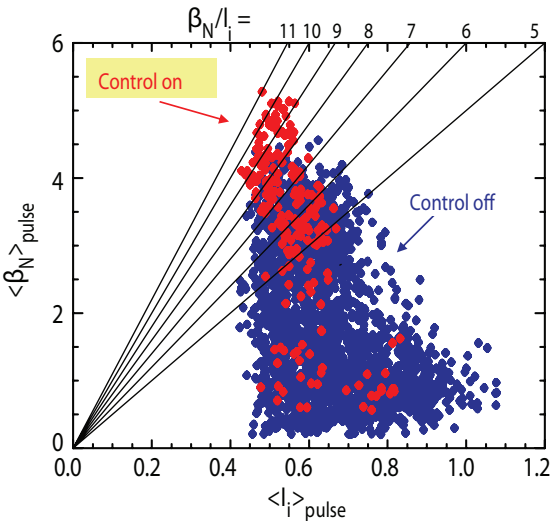

Figure 1.8: Demonstration of the achievement of higher performance plasmas (larger β, lower inductance l_i) with an active RWM controller. Taken from Sabbagh et al. [32].

in the RFP concept. In fact the feedback scheme described by Bishop has essentially been realized at RFX and EXTRAP-T2R in Italy and Sweden, respectively. While the details of the various active control schemes and modes of operation are beyond the scope of this thesis, Fig. 1.7 illustrates the maturity of this method in the RFP. After an appropriate control model of the RFP plasma is made, a deterministic set of excitation time traces (shown in Fig. 1.7b) can yield a controlled spectrum of RWMs (shown in Fig. 1.7a).

The situation for active control in the tokamak is generally less robust than that of the RFP. This is especially true of the advanced tokamak, where the self-generated bootstrap current plays a large role in the global dynamics of the discharge, leading to a very nonlinear system. That being said, advanced control schemes are in operation on most modern tokamak devices, and these control schemes have been proven to be able to expand the stable operation regime to higher values of β_N [32]. An example of improved performance is shown in Fig. 1.8, where for the NSTX device larger values of β_N are achieved with the control system on. Notwithstanding, in all devices discharges exist where RWMs have still been found to go unstable despite the presence of active control. RWMs have also

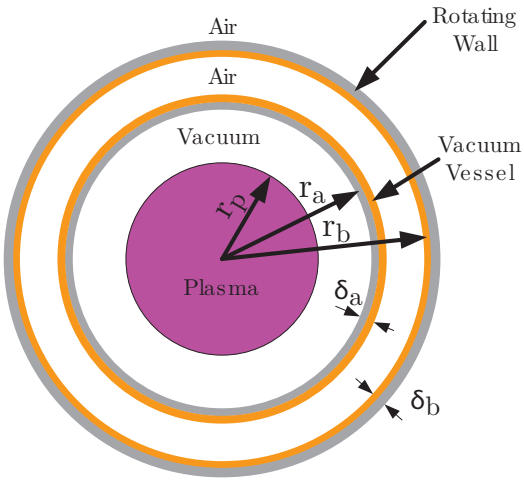

Figure 1.9: Experimental cross section realized in this thesis to test the RWM stabilization proposal of Gimblett [9].

been found to be non-linearly excited by other instabilities, such as fishbones, and these driven RWMs can also overcome the abilities of a control system [33]. Thus this area of research is also still very active.

1.4 Connections to Current Research

In contrast to the impressive progress seen with the schemes discussed in Section 1.3, the proposal put forth by Gimblett had never been experimentally explored prior to this work. Therein lies the central scope and contribution of this thesis. As will be discussed, the idealized geometry of Gimblett is reproduced in a dedicated experiment, the Rotating Wall Machine, whose cross section is shown in Fig. 1.9. The foremost contribution of this work will be the experimental verification of Gimblett's RWM stabilization scheme.

A solid rotating wall is topologically impossible in a torus - a flowing liquid metal is required. Design studies have included liquid metal walls for cooling, tritium breeding, or the first wall. However, important differences exist between a liquid metal and a solid conductor, most notably the fixed nature of the solid body rotation profile vs. the

more complex liquid metal flow. It is not known whether currents in the plasma could back-react onto the flow, producing a significant modification to the liquid metal flow profile and thus counteract the RWM stabilization. Furthermore, any turbulence present in the liquid metal flow could also hamper RWM stabilization by increasing the effective resistivity of the liquid metal. Addressing these effects is beyond the scope of this thesis.

Beyond testing Gimblett's hypothesis, this work extends beyond RWM stabilization and into issues of error field interactions and torque balance. While not considered at the outset of this work, these effects were found to be of profound importance to RWM stability in the device. Furthermore, striking parallels were found to the story of RWM stabilization by plasma rotation discussed in Section 1.3.1. The initially neglected role of error fields were quickly found to be critical in determining the dynamics of the RWM in the device, as is the case in the torus. Further, the device has proven to be a model system for the study of MHD mode-locking.

In summary, should a plasma device with a flowing metal boundary ever be constructed, this work will directly contribute to the general understanding of the complex and varied role of moving conductors at the boundary of a plasma device. Furthermore, the physical mechanisms discovered in this thesis share a remarkable parallel to the story of RWM stability in toroidal devices discussed in Section 1.3, thus furthering understanding in both configurations.

1.5 Past Results on the Device

This thesis builds on the work of two prior graduate students on the device, D. A. Hannum and W. F. Bergerson. A brief summary of their work will thus be presented to capture the level of understanding at the outset of this thesis. Exploration of magnetic reconnection in the experiment is being pursued by another graduate student (M. I. Brookhart) and is

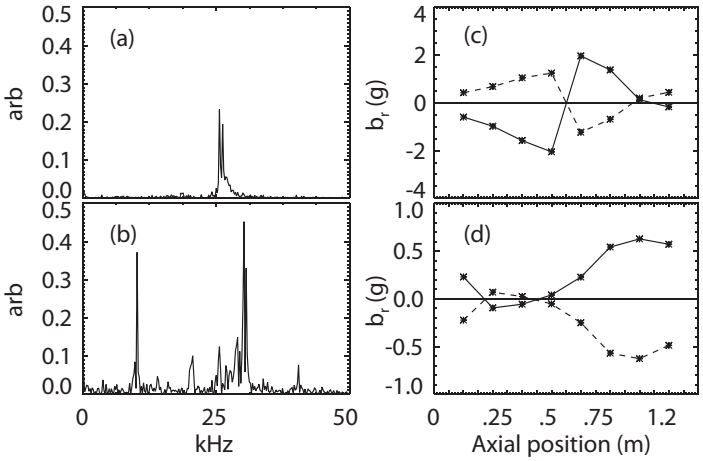

Figure 1.10: Measurements of both line-tied (a),(c) and perhaps non-line-tied (b),(d) high frequency modes robustly excited in the device. Taken from Bergerson et al. [34].

thus beyond the scope of this thesis.

Device Construction

D. A. Hannum and W. F. Bergerson completed the bulk of the device construction. It was under their tenure that the lab went from an empty room to first plasma. Vacuum systems, power supplies, and digitization hierarchy were all in place prior to 2008. Notwithstanding, with most equipment being several decades old, maintenance was continually required for all systems. For each successful run day, several more were lost to an unimaginably large array of failure modes. Additionally, as part of this thesis new measurements were added (internal probes, optical diagnostics, magnetic fluxloop arrays), power supplies upgraded (time-dependent control), and the rotating wall and associated sub-systems were designed, built, and operated.

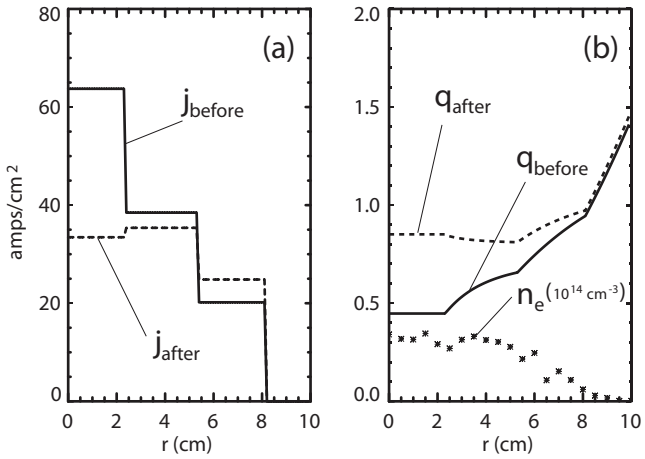

Figure 1.11: Observations of fast current profile re-distributions indicative of magnetic reconnection in the experiment. Note how the q-profile relaxes after one of these events. Taken from Bergerson et al. [34].

Identification of the Line-Tied Kink and Reconnection

The early work of Bergerson et al. [34] found that high frequency (several kHz) coherent MHD modes were robustly present in the device. As shown in Fig. 1.10, the magnetic fluctuations associated with these instabilities were largest at the device midplane and negligible at the electrodes. These modes were thus understood to be line-tied kink modes, and they were found to be destabilized when edge q dropped below approximately 1, as predicted by theory. At this time the vacuum vessel was made of insulating Pyrex, thus no wall stabilization effects were pursued.

Interestingly, the current profile was found to be susceptible to sudden re-distributions of current, shown in Fig. 1.11. These redistributions were interpreted to be manifestations of magnetic reconnection in the experiment, reminiscent of sawteeth in toroidal devices. Work independent of this thesis seeks to measure the internal structure of these reconnecting events using movable probes and stationary multi-probe arrays [35].

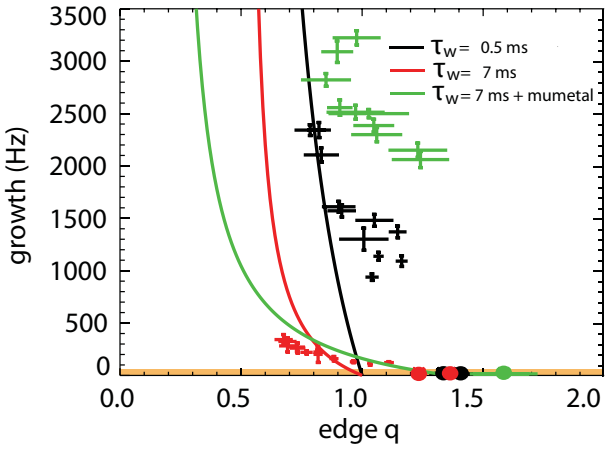

Figure 1.12: Early RWM observations in the device. Addition of ferritic material was found to destabilize the RWM while increasing the wall time was stabilizing. Taken from Bergerson et al. [36].

Identification of the Resistive and Ferritic Wall Mode

Later work by Bergerson et al. [36] focused on low frequency MHD instabilities present in the device. Again mode destabilization was cited to occur when edge $q < 1$. This mode was found to grow at approximately the resistive diffusion time of the wall (τ_w), and the growth rate was found to increase with I_p. Thus, this was the first identification of the RWM in the device. A novel scheme was also explored in which a MuMetal$^{\text{TM}}$ liner was added to the experiment. This was found to destabilize the RWM and allow it to grow when edge $q < 1.4$. The growth rate with the MuMetal$^{\text{TM}}$ liner was found to be significantly greater than the theoretical prediction, which in turn stimulated further theoretical effort [37]. These results are summarized in Fig. 1.12.

Plasma Characterization

The thesis of Hannum [38] extended the aforementioned studies by providing measurements of the plasma column via Langmuir probes. Single-tip Langmuir probes were used to measure electron temperature, ion density, floating potential, and plasma potential.

As these measurements have not been repeated, Langmuir probe data appearing in this thesis was collected by Hannum.

1.6 Thesis Outline

A brief outline of this thesis is presented. Throughout, the motivations and supporting theoretical work necessary are provided within each Chapter.

This introductory Chapter (Chapter 1) served to briefly summarize work relating to the RWM both on this device and in the field at large, as well as to motivate this thesis. Beyond that, this thesis is divided into two parts. Part I, comprising Chapters 2-4, describes the device and plasma. Part II, comprising Chapters 5-7 presents results from the rotating wall campaign. In more detail, Chapter 2 describes the experimental apparatus, and comments on the nature of the plasmas produced. Chapter 3 describes the MHD equilibrium of the device, beginning from the typical axisymmetric equilibrium, then moving to two-dimensional and finally three-dimensional helical equilibria as explored via internal and external probes. Chapter 4 describes the dynamics of the device cathode region, where measurements indicate a homogenized plasma column is formed from the discrete flux ropes of the plasma gun array. Chapter 5 describes the impact of the rotating wall on device error fields, both steady-state and time-dependent. Chapter 6 presents torque balance calculations and comparisons to experiment, including the observation of RWM wall-locking. The role of error fields is also further reinforced as they determine the regime for the RWM in the device. Chapter 7 presents the stabilization of the RWM by the rotating wall. Stabilization of both locked and born-locked modes are shown, along with the effect of the plasma flow. Chapter 8 provides concluding remarks and suggests future work.

Part I

Device and Plasma

Chapter 2

Device Overview and Operation

The Rotating Wall Machine is an experimental device which has been constructed to study the role of differentially rotating conducting walls on MHD instabilities. In this Chapter the device and its basic plasma properties are described. The design and mechanical performance of the rotating wall, as well as diagnostic capabilities are also discussed. The plasma is generated by an array of 19 plasma guns that produce high density plasmas and can be independently biased to allow spatial and temporal control of the current profile. Measurements from typical quiescent discharges show the plasma to be high β ($=< p > \frac{2\mu_0}{B_z^2}$), flowing, and collimated. Internal probe measurements show that the input current profile can be controlled by the plasma gun array.

A device has been constructed at the University of Wisconsin-Madison to investigate plasma dynamics with a rotating boundary. The Rotating Wall Machine, shown in Fig. 2.1, has the ability to excite resistive wall modes reproducibly, and has been topologically designed to allow for a rotating conducting boundary. The device has a screw pinch magnetic geometry with line-tying provided by thick conducting plates at the anode and by discreteness of the plasma source at the cathode. The characteristic τ_w of the anode is 200 ms, which is far longer than the discharge duration and thus provides effective line-tying.

The organization of this Chapter is as follows. Section 2.1 describes the design and operation of the device and associated subsystems such as vacuum maintenance, external magnets, plasma generation, and the rotating wall. Section 2.3 discusses diagnostic

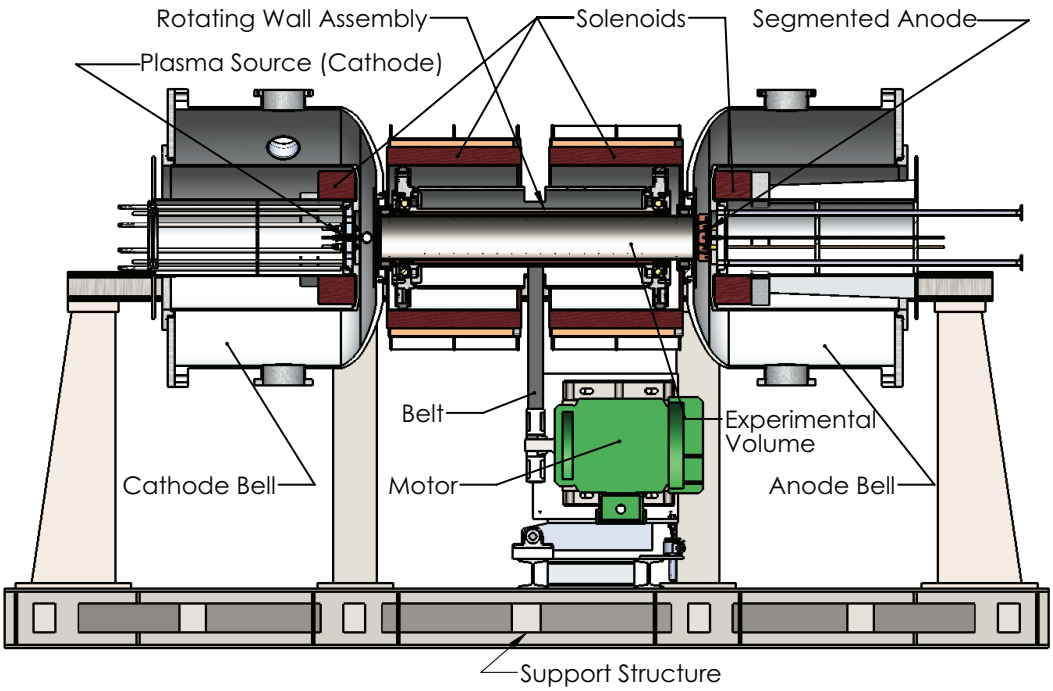

(a) Device cross section including structural elements.

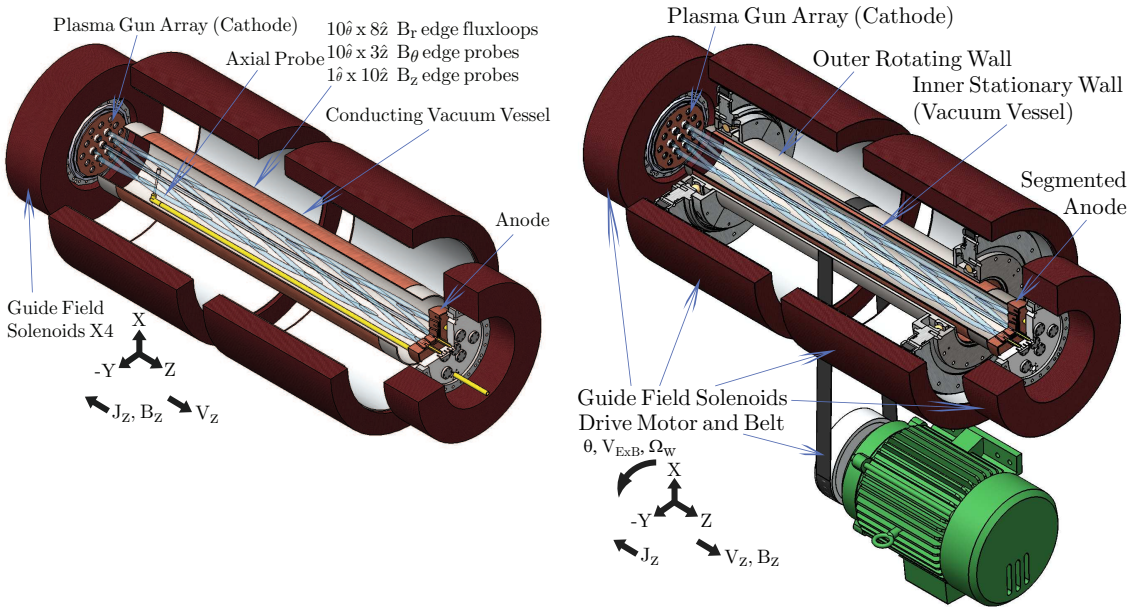

(b) Interior view illustrating physically relevant elements prior to rotating wall installation, corresponding to data from Part I.

(c) Interior view after device reconfiguration to allow for the rotating wall, corresponding to data from Part II.

Figure 2.1: The Rotating Wall Machine experimental geometry, illustrating device structural elements, vacuum vessel, and rotating wall hardware. As the device was modified to accept the rotating wall, interior views are shown before and after this modification.

systems employed on the device. Typical plasma parameter profiles and plasma controllability is explored in Section 2.4. General discussion of observed plasma parameters is discussed in Section 2.5.

2.1 Machine Description

The device experimental volume in which the plasma is formed is bounded by a 1.2 m long and 18 cm diameter cylinder, as shown in Fig. 2.1(a). The cylinder itself is interchangeable and experiments have been performed with Pyrex® [34] and various combinations of stainless steel, copper, and MuMetal™[36]. The rotating wall assembly is mechanically fixed to the device and is outside the vacuum vessel. It is important to note that there are two resistive walls, the inner static vacuum vessel and the outer rotating wall as shown in Fig. 1.9. At each end are large bell-shaped enclosures that house solenoid magnets, vacuum pumps, diagnostics, and the plasma source array. Including these bells the experiment is 3.3 m long and 1.5 m wide, and sits on a rigid stainless steel support structure.

The device was significantly modified during the course of this thesis to accept the rotating wall assembly. As such, views before (Fig. 2.1(b) and after (Fig. 2.1(c)) are provided. Specifically, the vacuum vessel radius was reduced from 10.2 cm to 7.6 cm to achieve better plasma-wall coupling, which prevented the use of internal probes. Thus, all data presented in Part I corresponds to the configuration of Fig. 2.1(b) while all data from Part II corresponds to the configuration of Fig. 2.1(c). Although the tube radius is different between the two configurations, the bulk plasma properties are set by the parallel dynamics and axial confinement of the device, which were left unchanged.

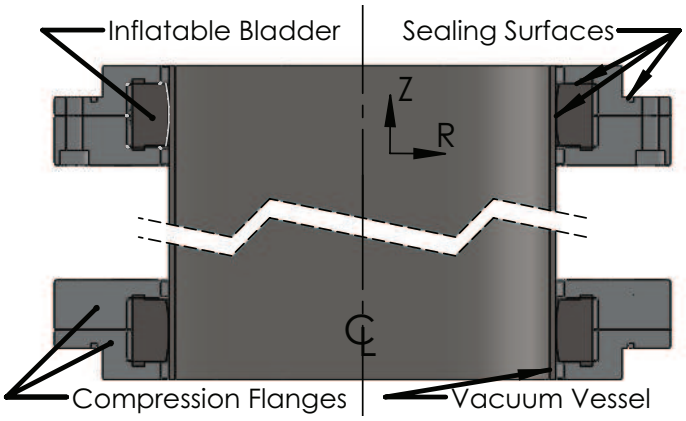

Figure 2.2: Cross section of the inflatable bladder seal assembly, with sealing surfaces shown. Overlap regions in the drawing indicate compression of the flexible inflatable bladder, both by the flange and by the vacuum vessel. The expansion of the bladder allows a range of vacuum vessel sizes to be accommodated.

2.1.1 Interchangeable Vacuum Vessels

To study the effect of different boundary conditions on MHD activity, the experiment has been designed to facilitate the exchange of the cylindrical vacuum vessel wall and liner with relative ease. Commercially available inflatable bladders, shown in Fig. 2.2, are used for both mechanical support and vacuum sealing. The bladders are compressed by a pair of large flanges and expanded by pressurized air at approximately 60 psi, forming two sealing surfaces. This expansion offers the added benefit of allowing the system to accommodate inner walls which vary in outer diameter by ± 1 cm. Several unique walls have been used on the device, as listed in Table 2.1.

2.1.2 Magnetic Geometry

The device employs a screw pinch magnetic geometry, with an externally imposed axial guide field (B_z) and azimuthal fields (B_θ) generated by the plasma current (I_p). The guide field is provided by four discrete solenoids, shown in Fig. 2.1. Solenoid power is provided by silicon-controlled rectifier (SCR) fired DC supplies capable of generating a 1

Description/ Material	Thickness δ_w, mm	Wall Time τ_w, ms	Rel. Permeability μ_r
Pyrex®	5	≈0	1
304SS	3	0.5	≈1
Static Copper	0.5	4	1
MuMetal™	0.2	0.006	1200
Moving Copper	0.7	7	1

Table 2.1: Table of wall parameters used on the device. The first two are vacuum vessels, the next two are liners wrapped around the 304SS, and only the final wall is capable of rotation.

kG field on-axis. In a typical discharge, the solenoids are energized several seconds before the plasma source becomes active, yielding a temporal decoupling of the magnetic fluxes arising from the plasma and from the external solenoids. Multiple power supplies yield independent control of the end and central solenoids, allowing variable mirror ratios to be achieved. The solenoids cover a large majority of the experimental volume, dramatically limiting the field ripple. Nonetheless, ripple of about 3.6% is experienced on-axis at the midplane gap and at the end gaps.

2.1.3 Plasma Generation and Current Control

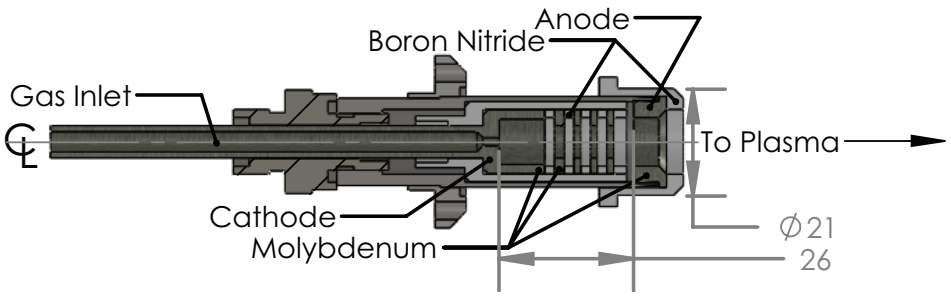

Figure 2.3: Cross section of a plasma gun: Gas is first puffed through the inlet, then a bias is established between the cathode and anode, yielding a high density arc plasma. Alternating boron nitride and molybdenum washers provide stability to the discharge. Dimensions are in mm.

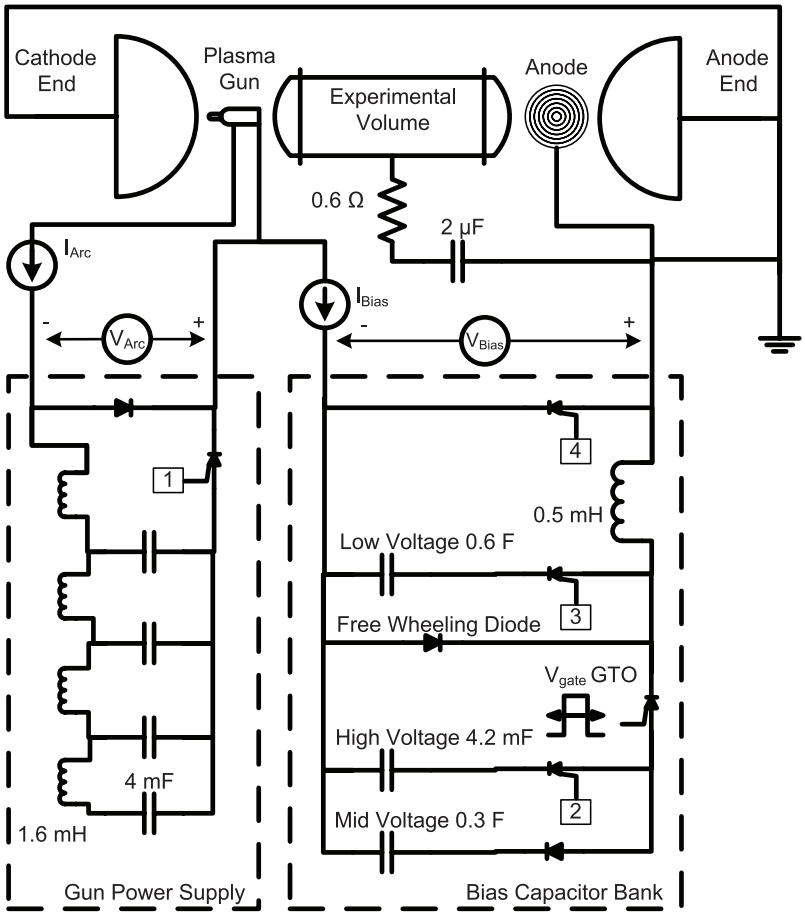

Figure 2.4: Illustration of the plasma generation circuit for each plasma source. The gun power supply's pulse forming network (PFN) is first discharged to create a high density plasma in the gun nozzle. High voltage banks then bias the gun relative to the external anode, striking the discharge and quickly bringing the current to the desired level and are then disengaged. The gate turn-off thyristor (GTO) timing circuit decides whether the low or mid voltage banks are active and thus controls the current. Boxes 1-4 are described in Section 2.1.3.

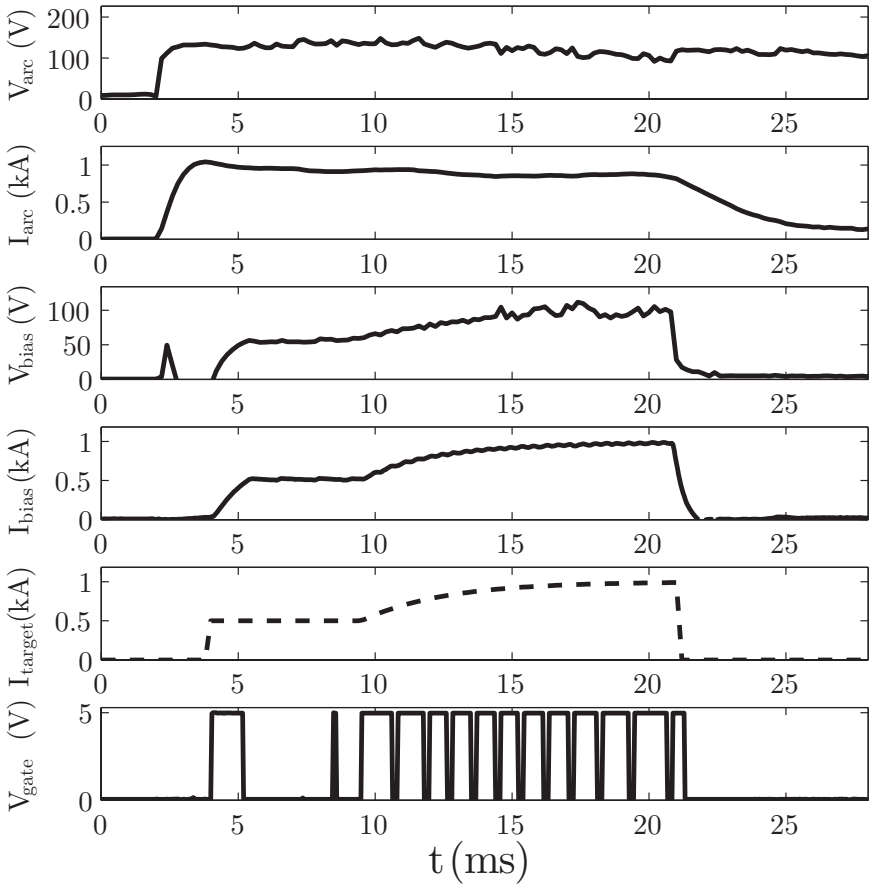

Figure 2.5: Typical plasma source time traces, illustrating source operation. The V_{gate} signal controls a GTO, yielding in this case a flat top followed by a slowly ramping current. I_{target} is the desired current waveform, while other measurements correspond to that shown in Fig. 2.4.

The device employs an array of 19 high current, high density plasma sources (guns) developed for helicity injection on the Madison Symmetric Torus [39, 40]. Each gun utilizes an alternating arrangement of molybdenum and boron nitride washers, shown in Fig. 2.3. The effective circuit of each source is shown in Fig. 2.4 and typical gun traces are shown in Fig. 2.5. The discharge begins by puffing gas into the plasma gun nozzle. The working gas is either hydrogen or helium. After 2 ms, the gun power supply Pulse Forming Network (PFN) is discharged (box 1 in Fig. 2.4) thus establishing a high density plasma within the plasma gun nozzle [39]. This discharge is maintained at 1.2 kA across 100 V for 20 ms by the PFN, as shown in the V_{arc} and $I_{\rm arc}$ traces of Fig. 2.5. Such large currents are possible due to the very high density plasma formed inside the gun nozzle which allows for large space-charge limited emission.

The next stage in the discharge begins when the gun is biased relative to the anode of the machine. The bias voltage ($V_{\rm bias}$) is established by independent capacitor banks, shown in Fig. 2.4. After 1 ms, a high voltage capacitor bank is discharged (box 2 in Fig. 2.4) to negatively bias the source with respect to the anode and quickly ramp the current. After 2 ms, a low voltage capacitor bank is enabled to continually supply the plasma current (box 3 in Fig. 2.4). Additionally, a feedback system based on pulse width modulation (PWM) begins to control the bias current ($I_{\rm bias}$ in Figs. 2.4-2.5) by switching on or off a mid voltage capacitor bank. A control signal ($V_{\rm gate}$ in Figs. 2.4-2.5) is determined by a comparator circuit which makes a decision based on the reference and actual $I_{\rm bias}$ waveform. If the measured current is above (below) the requested current waveform, the mid voltage capacitors will be disengaged (engaged), thus dropping (raising) the current. This system controls $I_{\rm bias}$ for the duration of the discharge, and after 20 ms a shorting SCR is triggered (box 4 in Fig. 2.4) which terminates the discharge. Due to cooling requirements the guns operate at a low duty cycle with discharges taking place approximately every three minutes.

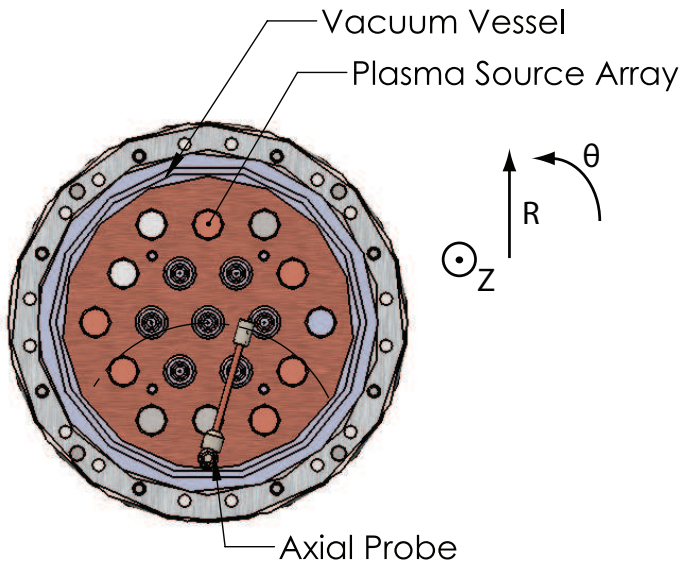

Figure 2.6: A face-on view of the plasma source (gun) array. There are 19 guns in the array though only the central seven are usually used. Varying the amount of current injected per gun allows spatial and temporal control of the current profile. The geometry of the internal probe is also shown in this view along with the trajectory it sweeps.

The feedback system described is unique to each plasma source thus allowing per-gun control of injected current. The device employs an array of plasma sources, which are arranged in a hexagonal array as shown in Fig. 2.6, to generate current profiles that can be controlled in both space and time as will be discussed in Section 2.4. This regulation not only provides for controllable and repeatable current waveforms but assures balanced current injection from each gun. Switching is achieved on the microsecond time scale through the use of Gate Turn-Off (GTO) thyristors. The use of the current controller is illustrated in Fig. 2.5, where the V_{gate} signal controls the capacitor bank and produces a ramped current profile.

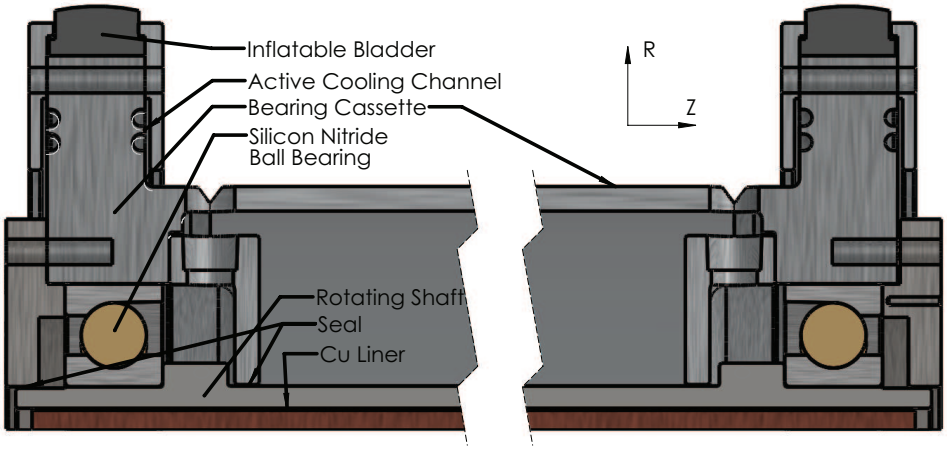

Figure 2.7: Cross sectional view of rotating wall assembly. The shaft is held in place by angular contact bearings and can rotate at a maximum speed of 280 km/h.

2.2 Rotating Wall Design and Operation

As discussed in Section 1.2, the device rotating wall must be able to achieve $R_m > 1$ to influence the stability of the resistive wall mode. The wall has been designed to reach $R_m \approx 5$ which necessitates rotation rates in excess of 6500 RPM or 240 km/h ($\Omega_w \approx 700$ rad/s), using a design τ_w of 7 ms.

The rotating wall is a precision-engineered product. A cross section schematic of the assembly is shown in Fig. 2.7, and installed in the device in Fig. 2.1. The rotating shaft has an outer diameter of 20 cm and is 1 m long and 1 cm thick. It is made of 304SS with a 1 mm thick copper liner on the inner diameter which was installed via a thermal interference fit. The copper provides electrical conductivity to increase τ_w while the 304SS provides mechanical strength. The shaft is held by two SKF 71940 hybrid angular contact ball bearings compressed against each other by Belleville spring loaded flanges, thus ensuring axial rigidity and radial load bearing capability. The balls are made of silicon nitride, which allows both greater maximum speeds and electrically isolates the shaft from the rest of the device thus preventing unwanted induced currents during the plasma discharge. The bearings are housed in a self-contained cassette that provides both

mechanical strength and modularity to the design. The assembly is mechanically coupled to the inner diameter of the central solenoids of the device by inflatable bladders in a process similar to that of Section 2.1.1, though all components are at atmosphere. Mechanical power is provided by a Reliance P25G4900 11 kW three-phase electric motor controlled by a Danfoss VLT6000HVAC variable frequency drive (VFD). A high-speed flat belt couples power from the motor to the shaft, as shown in Fig. 2.1. The motor is housed in a custom frame that allows fine tuning of motor yaw to maintain belt position. Bearing lubrication is provided by an SKF OLA05 oil-spot unit. Compressed air delivers a steady stream of Mobil Velocite 10 spindle oil to the bearings and provides active cooling.

The rotating wall has achieved a maximum speed of 7500 RPM, or 280 km/h, though maximum normal operation is closer to 6500 RPM, or 240 km/h. Speed is measured by an encoder on the motor and an optical tachometer on the shaft. During normal operation the bearings operate near 40-50°C, as measured by eight thermocouples on the end flanges which are also capable of localized measurements of any thermal excursions. The VFD provides power measurements and vibration sensors are located on both the wall and motor assemblies. The plasma discharge can also be triggered by the wall optical tachometer, allowing control of the wall phase trajectory during the discharge.

Typical Experimental Run

The operating characteristics of the rotating wall and a typical run day is briefly described. As stated in Section 2.2, vibration measurements are constantly logged on both the wall and motor assembly. As shown in Fig. 2.8a, vibration levels are generally larger for the motor assembly than the rotating wall, and vibration resonances appear to exist only for the motor assembly. Furthermore, the drive belt is shown to not significantly transmit vibrations from one assembly to the other. Beyond the resonance at 1300 RPM, the vibrations in the motor fall off slowly with periodic smaller peaks. The dotted line

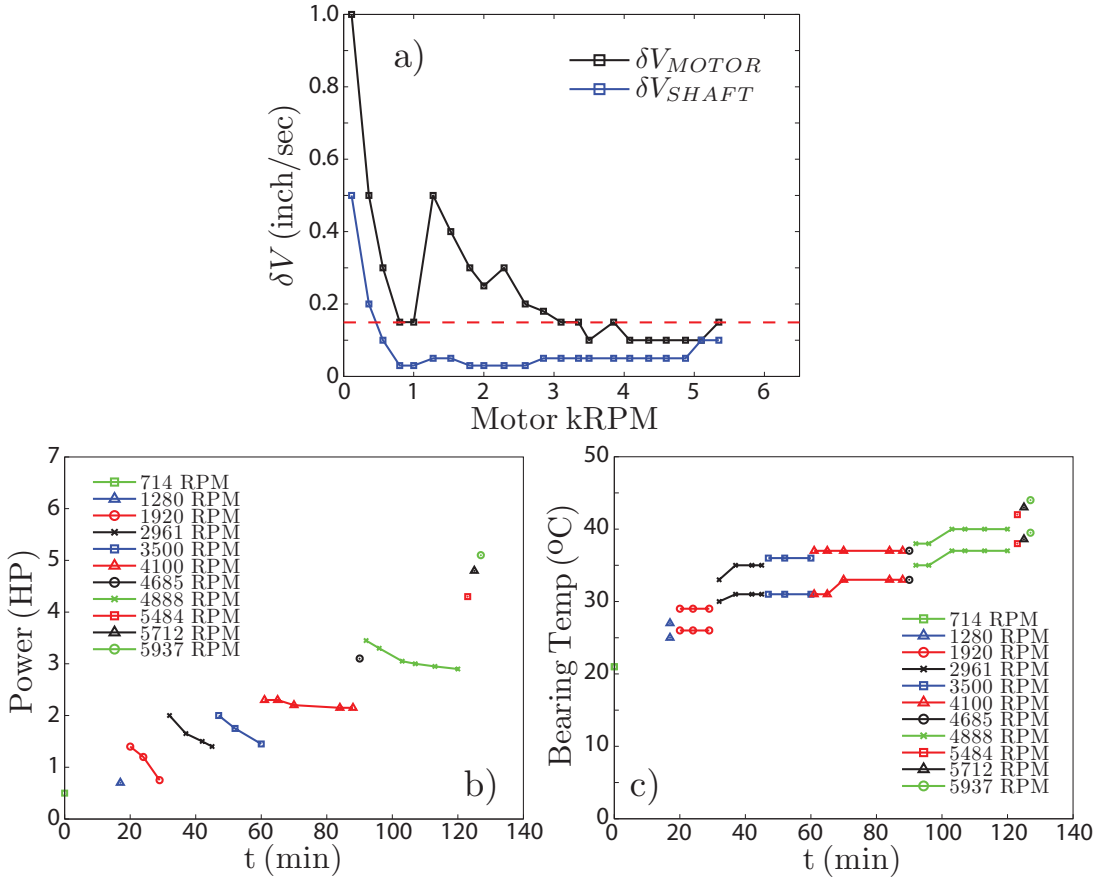

Figure 2.8: (a) Combined system vibration spectra, illustrating vibration resonances and defined safe operating limit for the shaft (dotted red line). (b)-(c) Evolution of rotating wall mechanical parameters during typical run day. (b) Displays required horsepower (HP $\equiv$ 0.75 kW) which (c) shows the bearing temperature.

in Fig. 2.8a constitutes the somewhat arbitrarily chosen 'safe' operation limit for the rotating wall (shaft only). During the entire experimental campaign this limit was not exceeded above 500 RPM.

Shown in Fig. 2.8b are the engineering parameters during a typical experimental run. Experiments are conducted by increasing the wall speed to the desired value, then forming plasma discharges until the required data is collected, which usually takes several hours. Following this, a new speed is set and experiments resume. Generally, the wall is taken from low to high speed during a run day. Figure 2.8b illustrates that the power requirements of the system are modest (<10 HP) and tend to peak immediately after a new speed is reached. Thermal equilibrium is reached when viscous heating of the oil equals conductive losses through the structure and advective losses as oil flows out of the system. As the viscosity decreases with increasing temperature, a stable equilibrium is reached under normal operating conditions. That power decreases over time while speed is constant is an important diagnostic of system health, as are the consistent temperatures shown in Fig. 2.8c. While this run lasted only approximately two hours, the wall has been operated for up to 12 hours at a time and is limited by operator stamina.

2.3 Plasma Diagnostics

A defining feature of the device geometry is the inaccessibility of the experimental volume from the radial direction, due to the topological constraint of the rotating wall. Thus, all diagnostics and feedthroughs must enter from either end of the machine.

2.3.1 Current Profile and Segmented Anode

The linear nature of the device allows for complete spatial and temporal accounting of the currents in the machine. Utilizing shunt resistors on the plasma source and bias capacitors

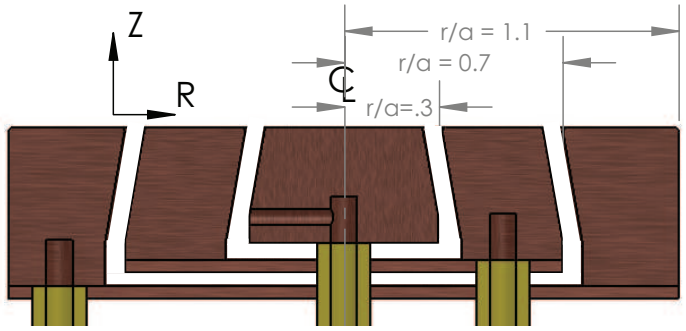

Figure 2.9: Cross section of the copper segmented anode, illustrating both the support scheme as well as the complete coverage of the target. The thickness of this section (5 cm), along with the highly conductive material used, maintains the line-tied condition at the anode.

(I_{arc} and I_{bias} in Fig. 2.4) the amount of current entering the machine is well known. Currents to the end bells and central tube of the machine are measured by Rogowski coils. The anode of the machine is comprised of a thick copper disk surrounded by two thick concentric rings, shown in Fig. 2.9. Rogowski coils are also placed on the leads exiting each anode segment, allowing all currents leaving the machine to be measured. Every discharge is checked to ensure that the current entering the plasma matches the current exiting the plasma at all times. The segmented anode also provides a three-point current profile measurement which can be related to the safety factor profile ($q(r)$).

2.3.2 Magnetic Field Measurements

For the study of MHD stability and to characterize MHD modes, arrays of fluxloops and coils are used. The device employs 30 B_θ coils, 10 B_z coils, and 80 B_r fluxloops at the edge of the experimental volume in a geometry shown in Fig. 2.10. Each signal is integrated by Sterling Scientific analog integrators prior to being simultaneously digitized at 0.5-1 MHz, allowing full resolution of all dynamics in the device. Simultaneous digitization also allows spatial Fourier decomposition of the azimuthal mode spectrum. Fourier decomposition in the z-direction is not amenable since two axial wavenumbers are required to satisfy the

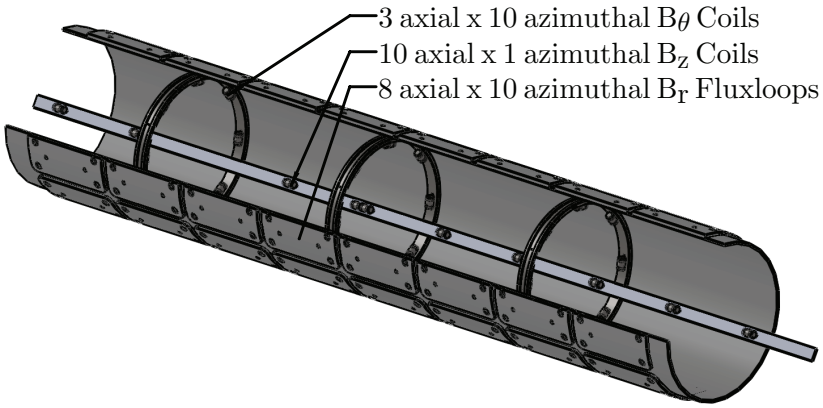

Figure 2.10: Cartoon illustrating location of the magnetic diagnostics on the device. There are 30 B_θ coils, 10 B_z coils, and 80 B_r fluxloops which together provide complete coverage of the experimental volume.

line-tied boundary conditions. Three fluxloops encircling the entire plasma cross section are also in place to measure the volume averaged diamagnetism. It should be noted that for the results of Part II only the B_r fluxloop was used.

2.3.3 Axial Probes and 2-D Drive Mechanism

The device plasma is well suited to internal probe work as the heat fluxes are tolerable and the discharges are highly reproducible. To access the vessel an axial probe drive mechanism is used that allows probe insertion from the anode of the machine. Due to geometric constraints of the probe feedthrough, inserted probes must have a diameter of no greater than 13 mm. A 90-degree articulating joint has been developed that allows the probe to swing into the radial direction once it has passed the feedthrough and entered the experimental volume, which is shown in Fig. 2.11. Using stepper motors, the articulated probe is able to sweep an arc in the (r,θ) plane, shown in Fig. 2.6. Assuming azimuthal symmetry, probe mobility in the axial (z) direction allows (r,z) contour maps of the plasma to be generated. This technique relies on the established shot-to-shot repeatability of the discharge when dealing with slow ($\leq$ 1 kHz) dynamics.

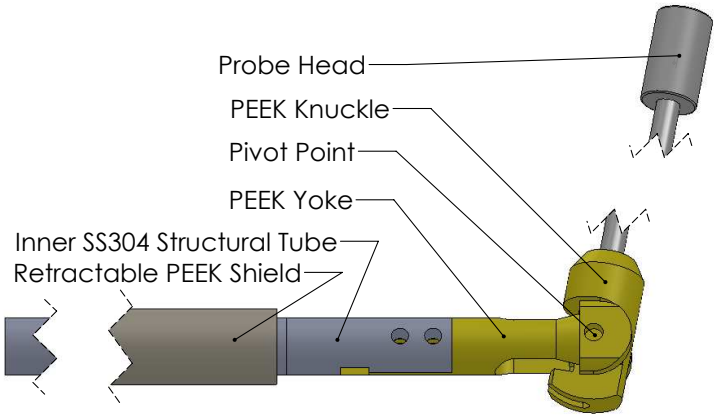

Figure 2.11: Cartoon illustrating the articulating knuckle used to position radial armature of probe after insertion through a 13 mm tube. The retractable polyether ether ketone (PEEK) thermoplastic shield slides flush with the semicircular section, locking the joint into a right angle. This is done in situ with a custom rod tool through a vacuum window.

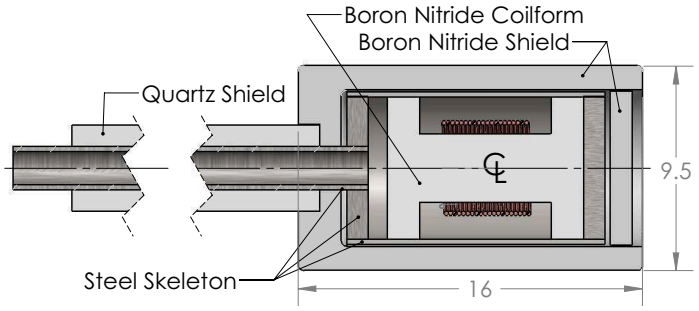

Figure 2.12: Magnetic probe cross section, illustrating the thermally fit, interlocking SS316 skeleton providing rigidity and electrostatic shielding, as well as the boron nitride and quartz plasma shielding. Dimensions are in mm.

Several probe heads utilize the same insertion and control system. A single-tip Langmuir probe is extensively used to characterize electron temperature, density, and plasma potential through I-V curve characterization. The Langmuir probe utilizes a tungsten wire of 0.4 mm diameter that is insulated from the plasma by a quartz stalk of 4 mm diameter that is filled with boron nitride powder. In addition, a three-axis magnetic fluctuation (B-dot) probe has been designed and deployed, shown in Fig. 2.12. The probe is constructed with a thermally fit stainless steel mechanical structure which also serves as an electrostatic shield, with boron nitride insulating the coil region and quartz insulating the stalk. The steel structure limits the high-frequency response of the probe to 100 kHz. Plasma parameters measured by these probes will be discussed in Section 2.4. A two-tip Mach probe is also used on the device to measure $\hat{z}$-directed flows. It is constructed by tightly fitting a 4 mm diameter quartz tube over a quartz rod with channels ground out for the 0.4 mm wire, which extends slightly above the tube. The rod extends beyond the wires to provide insulation between the tips.

2.3.4 Optical Spectroscopy

Optical diagnostics are also an important class of measurements performed on the device. For this purpose a 1.5 m focal length Czerny-Turner was retrofitted. Pre-existing photo-multiplier tubes were replaced with a modern linear charge-coupled device (CCD), allowing for diffraction-limited measurement of single spectral lines. Light was collected from the device using a custom-designed large aperture collimator, which was then routed through optical fibers to the spectrometer in an adjacent room. The system can collect spectra at 1 kHz, though longer integration times are generally used to improve the signal to noise ratio. A sample spectrum is shown in Fig. 2.13. This line (H_β) is dominated by Stark broadening and thus provides an accurate measure of electron density [41].

While Fig. 2.13 describes emission from an excited neutral atom, the system is also

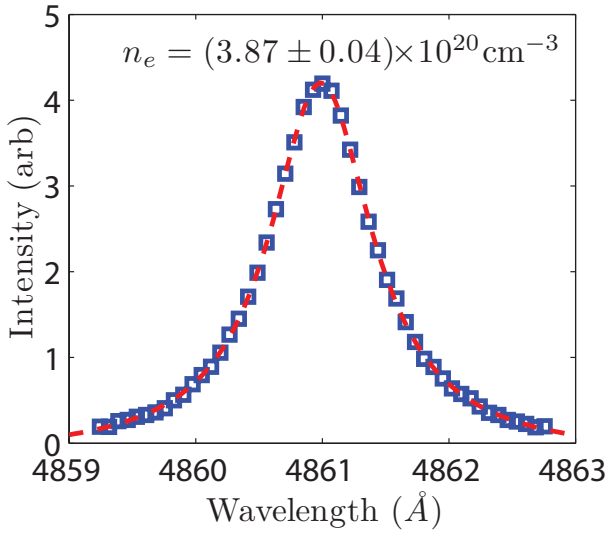

Figure 2.13: Sample H_β line from the Czerny-Turner spectrometer commissioned on the device to measure density, ion temperature, and flow. This spectrum is dominated by Stark broadening and thus measures line-integrated electron density to high accuracy.

intended to collect spectra from excited ion lines, the width and Doppler shift of which can yield ion temperature and flow respectively. Naturally, such lines are only emitted from non-hydrogenic species. Unfortunately, the device plasma is very cold (as will be discussed in Section 2.4) and it was found that excited ion lines (Helium II) were not of sufficient brightness to generate reliable spectra. Thus optical spectrometry on the device is currently limited to Stark effect measurements until a hotter plasma can be generated in the device, or a more sensitive cryogenic CCD is purchased.

2.4 Observed Plasma Parameters and Profile Control

The central parameters varied during experiments on the device are the axial guide field (B_z), plasma current density profile ($J_z(r,t)$), and the wall rotation (R_m). The resulting discharges are highly reproducible on a slow-time scale ($\tau \geq 1$ ms). This indicates that similar global MHD equilibria are achieved for similar input parameters. Some equilibria are prone to ideal [34] or resistive [36] MHD instabilities, while others are stable and quies-

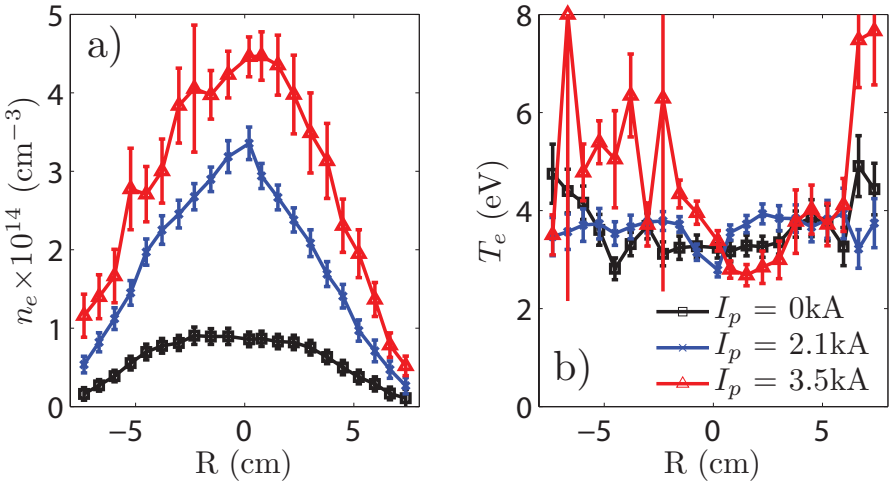

Figure 2.14: (a) Plasma density profiles from single-tip Langmuir probe for different injected gun currents. Increased gun injection current (ohmic heating) strongly increases the plasma density, while (b) T_e remains relatively constant. At the largest I_p the T_e measurements become unreliable due to MHD instabilities. Measurements were made by Hannum [38].

cent. To give a flavor of the plasmas produced by the device, measured plasma parameter profiles for different hydrogen gas equilibria are described in this section. Measurements are taken by the probes described in Section 2.3.3, with each spatial location corresponding to a single discharge. Plasma reproducibility allows both radial and axial profiles to be assembled with a standard grid spacing of 5 mm radially and 10 cm axially.

2.4.1 Kinetic Profile Control

Kinetic profiles (n_e, T_e) generated by the plasma source array are characterized by a monotonically decreasing in radius and very high density (n_e ≈1-5·10^{14} cm^{-3}) coupled with a cold and essentially uniform electron temperature (T_e ≈ 3.5 eV), shown in Fig. 2.14. The 0 kA case corresponds to the gun power supply circuit (shown in Fig. 2.4) discharging but with the bias capacitor bank disconnected. This configuration yields a low density, non-current-carrying plasma. As the plasma guns are biased to drive current, a dramatic increase in the plasma density is seen. The large amount of Ohmic heating

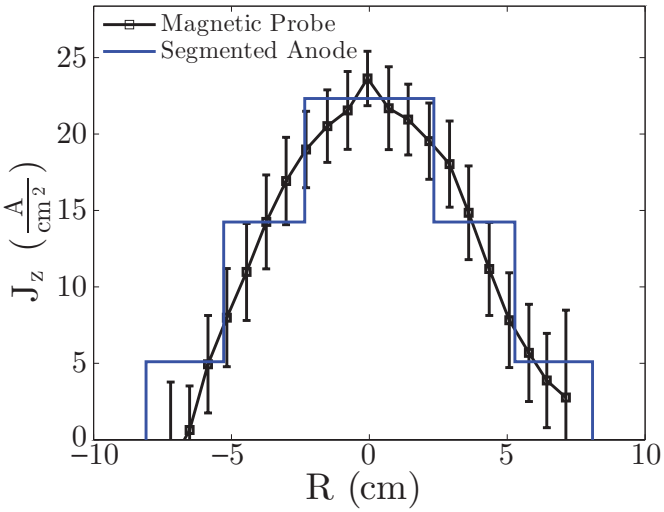

Figure 2.15: Axial current profile from internal magnetic probes utilizing ensemble averaging, illustrating a single collimated current channel. The discrete current filaments from the plasma source array have merged by this point in the discharge (Z=89 cm). The current measured by the segmented anode is also plotted and shows good agreement.

power ($P_{\text{Ohmic}} \approx$ 0.2-0.6 MW) from the bias capacitor bank is thus primarily ionizing new plasma particles. The electron temperature is relatively constant at 3-4 eV as gun current is increased, likely due to the fact that the poor axial confinement precludes the electrons from gaining much energy before they are lost to the ends. The plasma pressure can also be calculated, assuming quasi-neutrality and cold ions, as a product of these two values, yielding a volume averaged value of β approaching 10% for the profiles of Fig. 2.14.

2.4.2 Current Profile Control

The magnetic probe described in Section 2.3.3 is used to measure the equilibrium currents and magnetic fields in the device plasma. Using the differential form of Ampere's law ($\nabla \times \vec{B} = \mu_0 \vec{J}$), the radial profile of B_θ can be related to the axial current profile, assuming azimuthal axisymmetry. The current density profile shown in Fig. 2.15 is created with the central seven guns each producing an equal amount of current, yet the profile is strongly peaked. As a check of the probe measurement, the coarse current profile

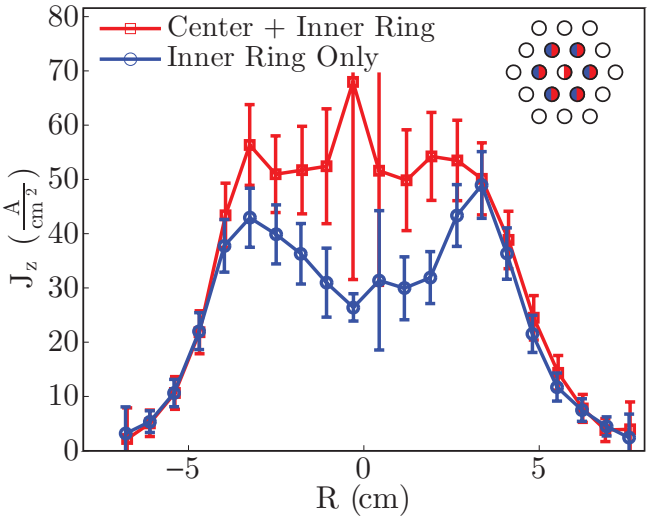

Figure 2.16: Current profile variation as measured by the internal magnetic probe described in Section 2.3.3. The case with all seven inner guns injecting current leads to a peaked current profile. When the central gun does not inject current, the profile is hollow. The measurement is taken at Z = 36 cm.

measured by the segmented anode is also shown in Fig. 2.15, illustrating good agreement between the two methods.

The current injected from each gun in the array can be controlled independently, giving a large degree of control over the input boundary condition for the plasma current profile in the device. As an illustration of spatial control, Fig. 2.16 illustrates two different current profiles. The first is from a discharge created with the central seven guns of the 19 gun array injecting current. This profile displays a peaked current density and a safety factor minimum on axis. The other profile shown in Fig. 2.16 pertains to a discharge in which the central gun was not discharged, leading to a hollow current profile and a correspondingly reversed-shear safety factor ($\frac{\partial q}{\partial r} < 0$) profile with a minimum off-axis. The peaked current profiles are well suited to excite internal kink modes while the hollow profiles are better suited to external kink mode study. Although the input boundary condition is well controlled, relaxation of the current profile tends to homogenize small-scale structures, as will be discussed in Chapter 4.

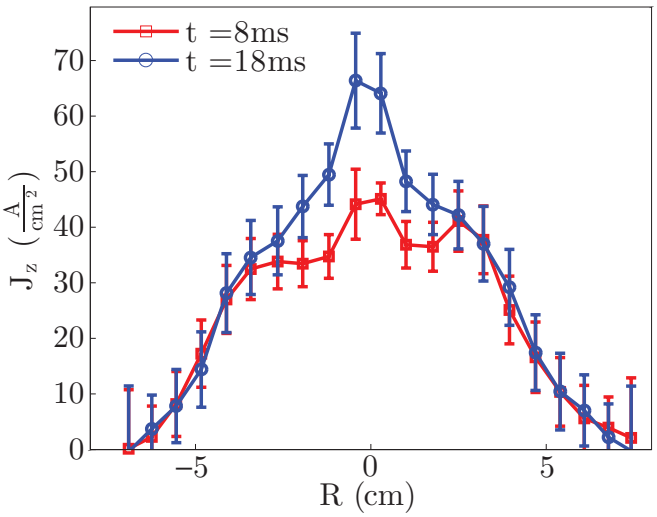

Figure 2.17: Current profile variation as central gun current is slowly increased from 500 A to 1000 A while inner ring delivers a constant 500 A/gun. This illustrates the device experimental capability of dynamic per-gun current profile control. This current profile is seen to become very peaked near the gun (where profile is taken) but diffuses outwards towards the anode (not shown).

The independent gun control also allows temporal control of the current profile. This is shown in Fig. 2.17, which illustrates current profiles at two distinct times during a discharge in which the central gun current was slowly increased from 500 A to 1000 A (as per Fig. 2.5), while the inner six guns were maintained at a constant current of 500 A each. The increased current injection is clearly visible as an increased central current density. Injected current from all guns can also be increased in tandem, allowing a more gradual transition through the critical current for MHD mode excitation.

2.4.3 Parallel Resistivity

The bias voltages applied to the guns ($V_{\text{bias}} \approx -(30-80)V$) results in large negative plasma potentials in the bulk with respect to the anode (ground), and consequently large plasma potential (V_P) gradients that can be measured with the single-tip Langmuir probe. Such a measurement is shown in Fig. 2.18a for a low bias voltage case ($V_{\text{bias}} \approx -30V$).

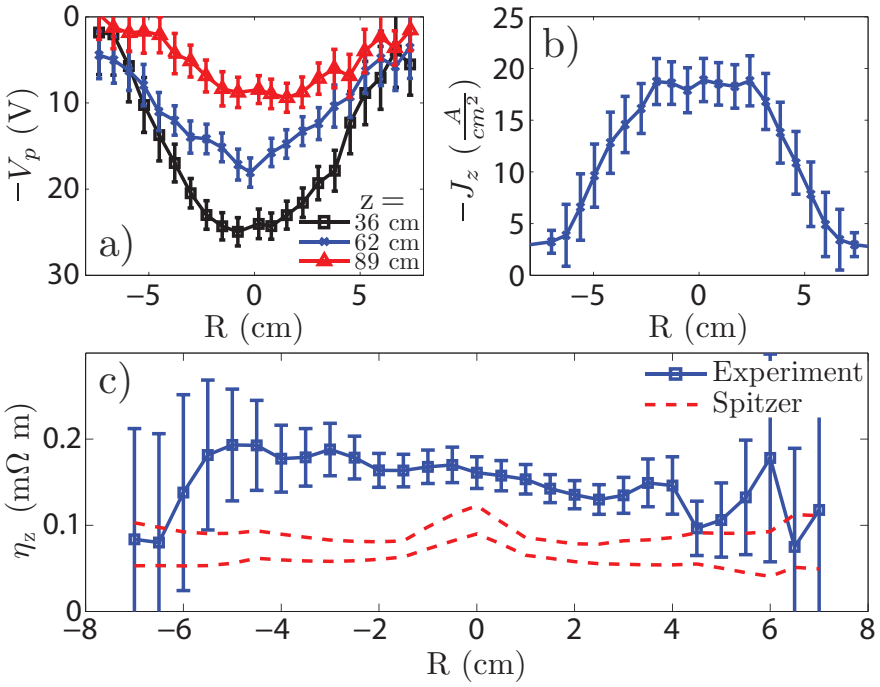

Figure 2.18: Axial resistivity is directly measured and compared to the Spitzer [42] value. (a) Axial gradients in the plasma potential V_p are measured by the single-tip Langmuir probe. (b) B-dot probe measurements of axial current J_z (negative convention) at Z = 62 cm. (c) Measurement of $\eta_z \approx \eta_{||}$ across the device, which is then compared to the Spitzer resistivity.

Using 3-point numerical derivatives, direct measurements of E_z in the plasma yield values on the order of -30 V/m, comparable to that of the bias voltage across the device length. Despite the resistive nature of the plasma, axial current densities (J_z) on the order of 20 A/cm^2 are drawn by this field. E_z and J_z can be measured in the bulk plasma to a good degree of accuracy due to their large amplitudes, as shown in Fig. 2.18a-b. Knowledge of these parameters allows a local, bulk plasma analysis of the axial Ohm's law, which is given by:

$$E_z + v_r B_\theta - v_\theta B_r \quad = \quad \eta_z J_z - \frac{1}{n_e e}\frac{\partial P_i}{\partial z} \tag{2.1}$$

where the plasma is assumed to be in MHD equilibrium. The pressure gradient term is measured to be negligible compared to the other terms of Eq. 2.1 by the single-tip Langmuir probe, as $T_i \leq T_e$ for the Ohmically heated plasma. Similarly, estimates of v_r and v_θ when multiplied by the known B_θ and B_r fields also yield negligible corrections, and vanish entirely at the magnetic axis. Figure 2.18c shows the η_z profile measured at the device midplane, as well as the upper and lower Spitzer estimates [42] computed from the Langmuir T_e profile with experimental uncertainties included.

The measurement yields resistivities higher than the Spitzer value by approximately a factor of two. While it is not understood why the measurement is anomalous, it is possible that a significant population of neutral particles could be raising the resistivity from the Spitzer estimate. A value of Z_{eff} (the average charge state of the plasma ions) greater than 1 could also account for the larger resistivity value, though the value of Z_{eff} has not been measured. However, the low T_e of the plasma suggests $Z_{\text{eff}} = 1$, as the plasma electrons would not have enough energy to strip the impurity ions of their more tightly bound electrons.

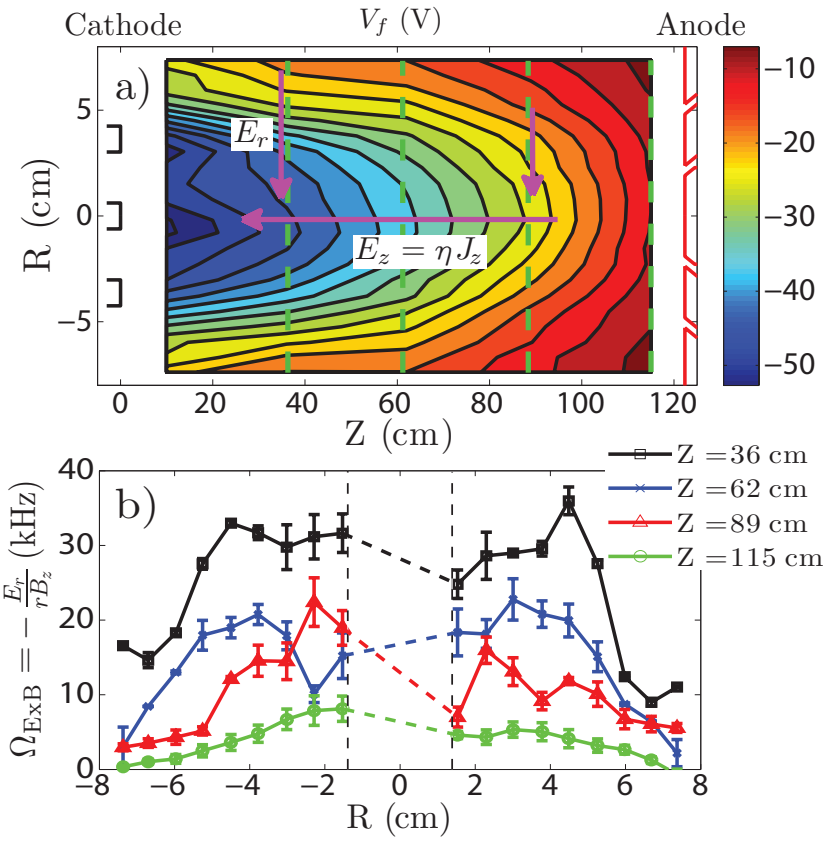

Figure 2.19: (a) Floating potential (V_f) measured as a function of radius at different axial locations. (b) Calculated ExB rotation profiles (Ω_{ExB}) from (a). Measurements are made with a single-tip sweeping Langmuir probe using shot-to-shot reproducibility. Other probe measurements indicate negligible radial current and uniform T_e, justifying equating gradients in V_f with E_r. Values at small r are skipped to avoid numerical singularities. Measurements were made by Hannum.

2.4.4 Plasma Flow

Potential gradients, and thus electric fields and ExB flows (shown in Fig. 2.19) are present in the device due to the large axial bias voltages (V_{bias}) applied to drive I_p in the relatively cold and resistive plasma. To understand this potential structure, note that in the axial direction $E_z \approx \eta_z J_z$. Figure 2.14b shows that T_e (and thus η_z) is constant throughout the device. However, J_z is strongly peaked as shown in Figs. 2.15-2.17. The potential at any point in the plasma is thus given by $\int_L^z \eta_z J_z dz$, which begins at the grounded

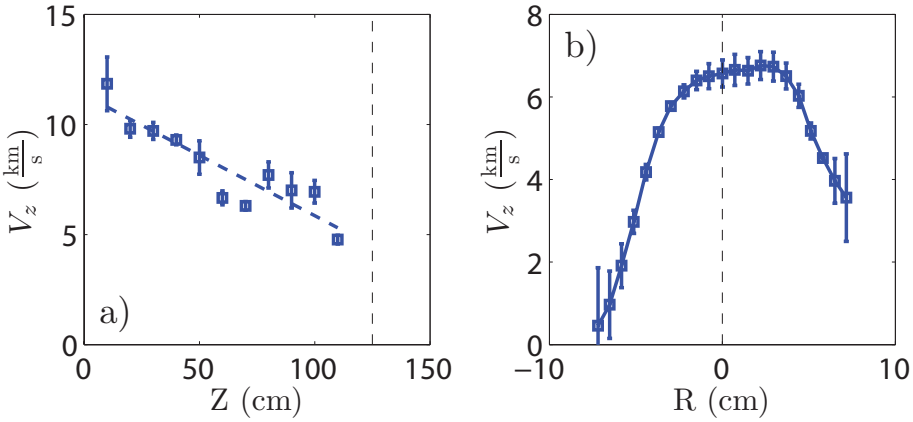

Figure 2.20: Axial flow (V_z) measured using a two-tip Mach probe. (a) Axial sweep at $R = 0$ cm indicates that significant flows are generated near the guns which then slow as they near the anode (dotted line is anode position). (b) Radial sweep at the midplane indicates that the axial flow is sheared radially at the edges. Measurements were made by Brookhart.

(equipotential) anode at $z = L$. Line integrals performed at the core of the device yield a large potential drop due to the large J_z, while line integrals at the edge of the device yield a small potential drop. As the field in the plasma is electrostatic, this directly results in the formation of a strong radial electric field (E_r).

This radial electric field (E_r), when crossed with the axial guide field (B_z) gives rise to ExB flow ($V_{\mathrm{ExB}} = -E_r/B_z$) throughout the plasma. In principle, E_r could instead drive radial currents (J_r) and reduce the ExB flow, but Bdot probe measurements to be discussed in Chapter 3 will show that J_r is very small. The resulting ExB flow profile (shown in Fig. 2.19b) is complex, with strong flows near the cathode and vanishing flows near the anode due to the equipotential at the highly conducting anode surface. Interestingly, the flow approximates a rigid rotor in the core, implying that the core plasma is very viscous. This flow profile will have important consequences for the study of MHD instabilities to be discussed throughout this thesis.

In addition to azimuthal ExB flow, a double-tip Mach probe was used to measure the axial flow (V_z) in the device. This flow profile, shown in Fig. 2.20, is also fairly complex.

The flow is measured to slow down monotonically as it leaves the cathode. This may be due to advective effects, as the plasma column is wider at the anode end than cathode end ($\vec{V} \cdot \nabla \vec{V}$ deceleration) or collisions with a neutral species which transfers momentum out of the plasma. The neutral fraction is not sufficiently well known to distinguish between the two effects, though at least some advective deceleration must occur. Radially, the V_z profile is shown to be peaked in the core, with significant slowing at the edges. Though present measurements are not conclusive, this radial shear could again this could be due to slowing down on the neutral fluid, balanced by plasma viscosity [43]. The asymmetry in the radial profile is artificial and due to the probe shadowing the flow.

2.5 Discussion

Probe measurements allow various plasma parameters and dimensionless numbers to be calculated, which are collected in Table 2.2. Due to the cold and dense nature of the plasma, the sound speed and the Alfven speed are comparable. The parallel Lundquist number, a ratio of the Alfven crossing time to the resistive diffusion time, is relatively low. The volume averaged plasma β is large, posing the question of whether or not β driven MHD modes can be observed in the device. This is as yet unresolved experimentally or theoretically in the line-tied geometry. As there is no confinement in the axial direction, the plasma confinement time τ_E is measured to be ≈ 10 μs, comparable to the sound transit time across the device length. The cold and dense nature of the plasma also assures the plasma is very collisional. This both validates the fluid picture used to interpret the results, but also placed the device in a parameter regime very different from toroidal magnetic confinement devices (which tend to be collisionless).

This chapter has described the device in great detail and detailed how it is ideal for the study of current-driven MHD instabilities and their interaction with moving conductors.

Parameter	Formula	Symbol	Value	
Axial Field		B_z	500	G
Plasma Current		I_p	2.1	kA
Electron (Elec.) Density		n_e	5E14	cm^{-3}
Elec. Temperature		T_e	3.5	eV
Spitzer Resistivity	$10^{-4}\log(\Lambda)T_e^{-\frac{3}{2}}$	η	230	$\mu\Omega$m
Elec. Thermal Speed	$(2k_bT_e/m_e)^{\frac{1}{2}}$	v_{Te}	110	km/s
Sound Speed	$(\gamma k_bT_e/m_i)^{\frac{1}{2}}$	C_s	24	km/s
Alfven Speed	$B_z/(n_im_i\mu_0)^{\frac{1}{2}}$	V_A	49	km/s
Mach Number	v_z/C_s	M	0.3	
Alfven Time	r/v_A	τ_A	2	μs
Resistive Diffusion Time	$r^2\mu_0/\eta$	τ_{res}	52	μs
Energy Confinement Time	W/P_{Ohmic}	τ_E	10	μs
Lundquist Number	$\tau_{\mathrm{res}}/\tau_A$	S	26	
Plasma Beta	$2\mu_0<\mathrm{p}>/B^2$	β	10	%
Volumetric Ohmic Heating	$\int \eta J^2 dV$	P_{Ohmic}	200	kW
Ion Mean Free Path (MFP)	$(n_i\sigma_i)^{-1}$	λ_i	3	μm
Electron MFP	$(n_e\sigma_e)^{-1}$	λ_e	500	μm
Ion Skin Depth	c/ω_{ci}	δ_i	13	mm
Elec. Skin Depth	c/ω_{ce}	δ_e	0.3	mm
Elec. Larmor Radius	v_{Te}/ω_{ce}	ρ_e	0.1	mm

Table 2.2: Table of plasma parameters for a typical device discharge (specifically the 2.1 kA constant-current discharge described in Section 2.4 utilizing the center and inner ring plasma guns). $L = 1.22$ m is the plasma length, $r \approx 10$ cm is the plasma diameter. k_b is Boltzmann's constant, γ is the adiabatic index, and Λ is the coulomb logarithm.

The discreteness of the plasma sources along with a sophisticated current control scheme allow current distributions to be programmed both in space and time, which gives a good degree of control and reproducibility in the excitement of MHD instabilities. For example, disengaging the central plasma source of the array tends to produce reverse-shear safety factor profiles which reduce internal mode activity but maintain external mode activity. A robust rotating wall has been built and shown to operate at the required speeds to meaningfully interact with the MHD instabilities of the device. Active control also assures the reproducibility of the discharge so that individual probe measurements taken at multiple locations over hundreds of discharges can be combined to form a cohesive picture of a single equilibrium.

Chapter 3

Plasma Equilibrium

This Chapter presents detailed MHD equilibrium measurements of the plasma column, from the bulk plasma 1-D equilibrium to a fully 3-D helical state found at high current. The line-tying condition is shown to provide a localized modification to the equilibrium in the presence of bulk plasma diamagnetism. Diamagnetic currents cannot flow near the conducting anode and are measured to disappear in a localized boundary layer, causing a weak magnetic mirror to form. For sufficiently large plasma currents, the paramagnetic nature of parallel current drives the equilibrium to paramagnetism and destroys the mirror effect. At a critical plasma current the axisymmetric equilibrium is found to transition to a long-lived, rotating, helical 3-D equilibrium state. Internal measurements of this state via multi-point correlation analysis techniques illustrate that it preserves the flux surfaces and pressure profile of the axisymmetric equilibrium.

3.1 Motivation

In order to understand the MHD instabilities present in the device, it is a prerequisite to have a thorough knowledge of the underlying MHD equilibrium. It is the purpose of this Chapter to describe what a 'typical' MHD equilibrium is for the device, using measurements from the internal probe system and interpreted via the simple 1-D screw-pinch MHD radial force balance model. Furthermore, during the course of this study, more ex-

otic properties of the equilibrium have been discovered. These equilibria will be described and shown to require an extension of the 1-D MHD model to include both axial gradients and in some cases fully 3-D treatments.

The 1-D MHD equilibrium of the screw-pinch is one of the most fundamental and well understood in magnetic confinement. However, the device contains an important departure from the more commonly treated periodic cylinder screw-pinch: line-tying. Line-tying requires the vanishing of electric fields tangent to a perfectly conducting surface, which in the ideal MHD limit corresponds to zero plasma displacement as the plasma is frozen into the magnetic field. Line-tying has been both inferred [34] and mechanically enforced [44] in past experiments using planar and conical conducting anodes, respectively. Conducting anodes have also been found to provide incomplete line-tying [45] due to finite sheath resistivity at the anode surface [46]. In this Chapter the effect of line-tying by a planar anode will be directly measured for certain MHD equilibria. The line-tying condition will be shown to break the assumptions of the canonical 1-D MHD force balance in a narrow boundary layer and thus require a 2-D treatment of the equilibrium.

The plasma will also be shown to transition to a helical equilibrium at large plasma current (I_p). This equilibrium is reminiscent of persistent helical states observed in otherwise axisymmetric systems, such as RFX-mod [47], MST [48], JET [49], NSTX [50], and MAST [51]. Such states have also been theoretically predicted for straight cylinders [52] and seen in computational studies [53] despite the presence an axisymmetric boundary condition. This Chapter reports the experimental observation of such a 3-D helical state in the device and uses internal probe analysis to explore its structure. Measurements are not sufficient to determine whether the state is line-tied or not.

The organization of this Chapter is as follows: Section 3.2 discusses the theory and analysis method utilized within this Chapter. Section 3.3 details 1-D equilibrium in the bulk plasma, as well as the direct verification of the line-tying condition at the anode and

resultant 2-D modifications to the equilibrium. Section 3.4 discusses analysis of coherent fluctuations present in the device and their interpretation as a 3-D helical equilibrium. Section 3.5 provides additional discussion of the aforementioned topics.

3.2 Theory and Analysis Method

To interpret the magnetic measurements on the device, MHD equilibrium theory is briefly reviewed. MHD force balance in a flowing plasma is given in vector form by [54]:

$$\nabla P = \vec{J} \times \vec{B} - \rho \left(\vec{V} \cdot \nabla \vec{V} \right) \tag{3.1}$$

where $\vec{V}$ is the plasma flow, ρ is the mass density, P is the pressure, $\vec{J}$ is the current density and $\vec{B}$ is the magnetic field. In the canonical 1-D cylindrical form (only gradients in $\hat{r}$ allowed), Ampère's law $\left(\nabla \times \vec{B} = \mu_0 \vec{J} \right)$ expands Eq. 3.1 to become, in the radial direction:

$$\frac{\partial P}{\partial r} = -\frac{\partial}{\partial r}\left(\frac{B_z^2}{2\mu_0}\right) - \frac{B_\theta}{\mu_0 r}\frac{\partial}{\partial r}\left(r B_\theta\right) + \rho \frac{V_\theta^2}{r} \tag{3.2}$$

where $V_r = 0$ is assumed, and $B_r = 0$ by necessity. The pressure gradient is supported by the Θ-pinch and Z-pinch term (first and second term on the RHS of Eq. 3.2). The centrifugal term (third term on the RHS of Eq. 3.2) is often ignored, though for large enough ρ or V_θ it can lead to a meaningful reduction of the pressure gradient. Expanding Eq. 3.1 into a 2-D equilibrium is achieved by including gradients in $\hat{z}$ (which were neglected in Eq. 3.2) yielding:

$$\frac{\partial P}{\partial r} = -\frac{\partial}{\partial r}\left(\frac{B_z^2}{2\mu_0}\right) - \frac{B_\theta}{\mu_0 r}\frac{\partial}{\partial r}\left(r B_\theta\right) + \frac{B_z}{\mu_0}\frac{\partial B_r}{\partial z} + \rho\left[\frac{V_\theta^2}{r} - V_z\frac{\partial V_r}{\partial z} - \frac{\partial}{\partial r}\left(\frac{V_r^2}{2}\right)\right] \tag{3.3}$$

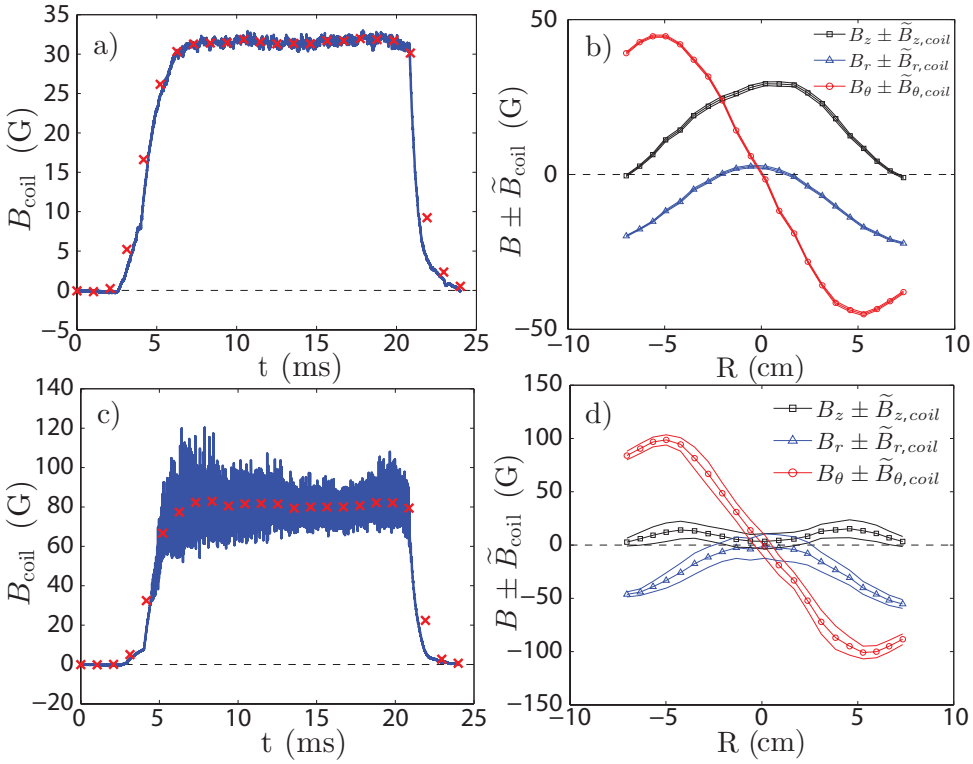

Figure 3.1: Raw (integrated) signal from the B-dot probe under (a) quiescent and (c) fluctuating conditions. The crosses are 1 ms-bin time-averages of the signal, which are well-defined despite the large fluctuations present. Radial profiles of 1 ms-bin time-averages are displayed in (b) for the quiescent and (d) for the fluctuating case, along with the relative fluctuation amplitude, illustrating the ability of shot-to-shot repeatability at the ms level to resolve well-defined spatial information.

where axial gradients can thus sustain or degrade the pressure gradient. $V_r = 0$ is no longer enforced in Eq. 3.3, adding an additional term.

This Chapter will utilize the canonical 1-D axisymmetric equilibrium of Eq. 3.2 to describe the bulk plasma. However, it will be shown that the 2-D form of Eq. 3.3 must be used to adequately describe a boundary layer at the anode where the line-tying condition generates significant axial gradients. As plasma current is increased, the axisymmetric equilibrium transitions to a rotating, highly coherent, helical state. This state is shown to be a fully 3-D helical equilibrium described by the vector form of MHD force balance given by Eq. 3.1.

Measurements for this Chapter are conducted by the edge magnetic arrays described in Section 2.3.2 as well as the internal probes described in Section 2.3.3. Though the internal probe system does not capture full 3-D maps of the plasma column, it can resolve up to $m = 1$ structures. Profiles in (r, θ, z) space are built up using extensive shot-to-shot repeatability as the probe is fixed at a single position during a discharge. Figure 3.1a,c illustrates an integrated signal from a single B-dot probe coil along with 1 ms-bin time average values. As shown, even discharges with strong fluctuation levels have well-defined mean values from which radial profiles can be created. As all components of $\vec{B}$ are measured (shown in Fig. 3.1b,d) a direct measurement of the axial and azimuthal (approximately the parallel and perpendicular) currents using Ampère's law is possible. Using Eq. 3.2, local spatial gradients in $\vec{B}$ are related to the plasma pressure gradient which is then integrated to calculate a radial pressure profile. This integration is carried out from the plasma edge to the core from each direction, allowing a rough gage of the error by noting the degree of core pressure mismatch. Pressure integration is valid for time scales longer than the Alfvén time τ_A ($\approx 2\ \mu s$), a condition easily met by the 1 ms time binning utilized.

3.3 Axisymmetric Equilibrium

3.3.1 High-q Diamagnetic Equilibrium

Weakly biasing the plasma guns ($I_{\text{discharge}} > I_p$) generates a strongly diamagnetic, high q ($\approx$ 3-4) plasma in which the pressure gradient is primarily supported by the $\frac{\partial}{\partial r}(\frac{B_z^2}{2\mu_0})$ term of Eq. 3.2, as shown in Fig. 3.2. Equivalently, the contribution to $J_\perp$ is primarily from J_θ over J_z. This indicates that the equilibrium is Θ-pinch like, and as such is robustly stable to MHD instabilities. The large diamagnetism ($\delta B_z \equiv B_{z,\text{guide}} - B_{z,\text{observed}} < 0$) also lowers the q profile by reducing the local B_z, and this effect can be significant at

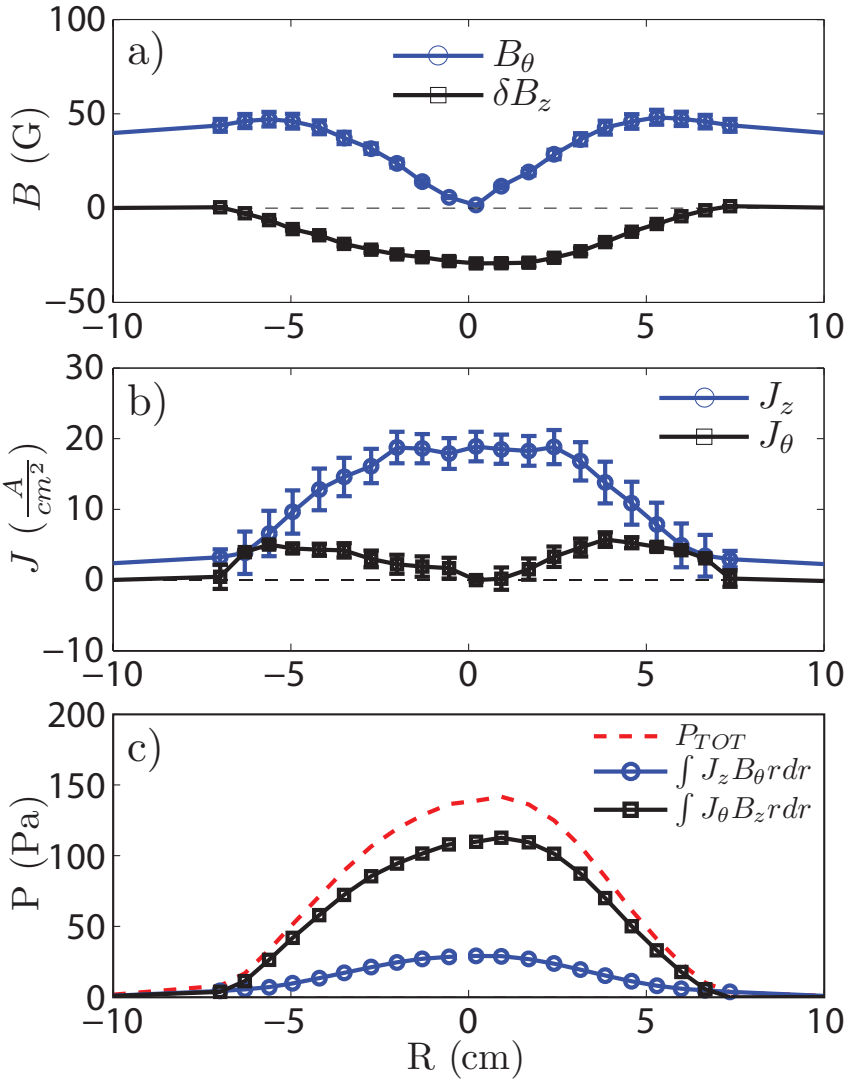

Figure 3.2: 1-D Screw-pinch equilibrium under low plasma current operation illustrating the strongly diamagnetic nature of the equilibrium. (a) δB_z is the perturbation to the axial guide field by (b) currents internal to the plasma. (c) The pressure gradient is supported primarily by diamagnetic currents, with the resultant equilibrium similar to that of a Θ-pinch. The boundary condition is provided by edge probe array measurements.

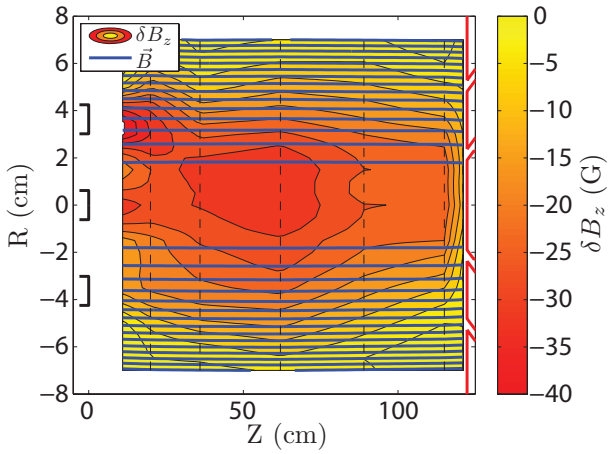

Figure 3.3: The perturbation to the guide field (δB_z) by diamagnetic currents exists throughout the bulk of the plasma. Near the anode, δB_z is much reduced. The axial scale length of this phenomena is seen to be ≤ 5 cm, the resolution of which is limited by the finite axial spacing of the probe sweeps. Dashed lines indicate the axial location of probe sweeps of 21 radial points.

weak guide fields. The magnitude of the pressure gradient is also large, yielding a core β ($\equiv \frac{2\mu_0 P_0}{B_z^2}$) of 15% for this plasma, illustrating that the force-free approximation used to describe screw-pinch equilibria may not be applicable to this plasma. The absence of a force-free current profile can be understood by noting that though the current profile is stationary in time, it is strongly sourced and sinked by the guns and anode respectively.

3.3.2 Two-Dimensional Equilibrium and Anode Mirroring

The large δB_z of the high-q equilibrium shown in Fig. 3.2 also allows a unique and direct confirmation of anode line-tying to be performed for this plasma. At the highly conducting anode surface, any ΔB_z in time interval $\Delta t < \tau_{\text{res}}$ is forbidden as the line-tying condition requires $E_t = 0$. It would thus be expected that $\delta B_z = 0$ at the anode surface, leading to a weak magnetic mirror. Experimental observations, shown in Fig. 3.3, clearly display this behavior, though measurements at the exact surface of the anode are impossible due to finite probe size. This constitutes a direct measurement of magnetic fieldline

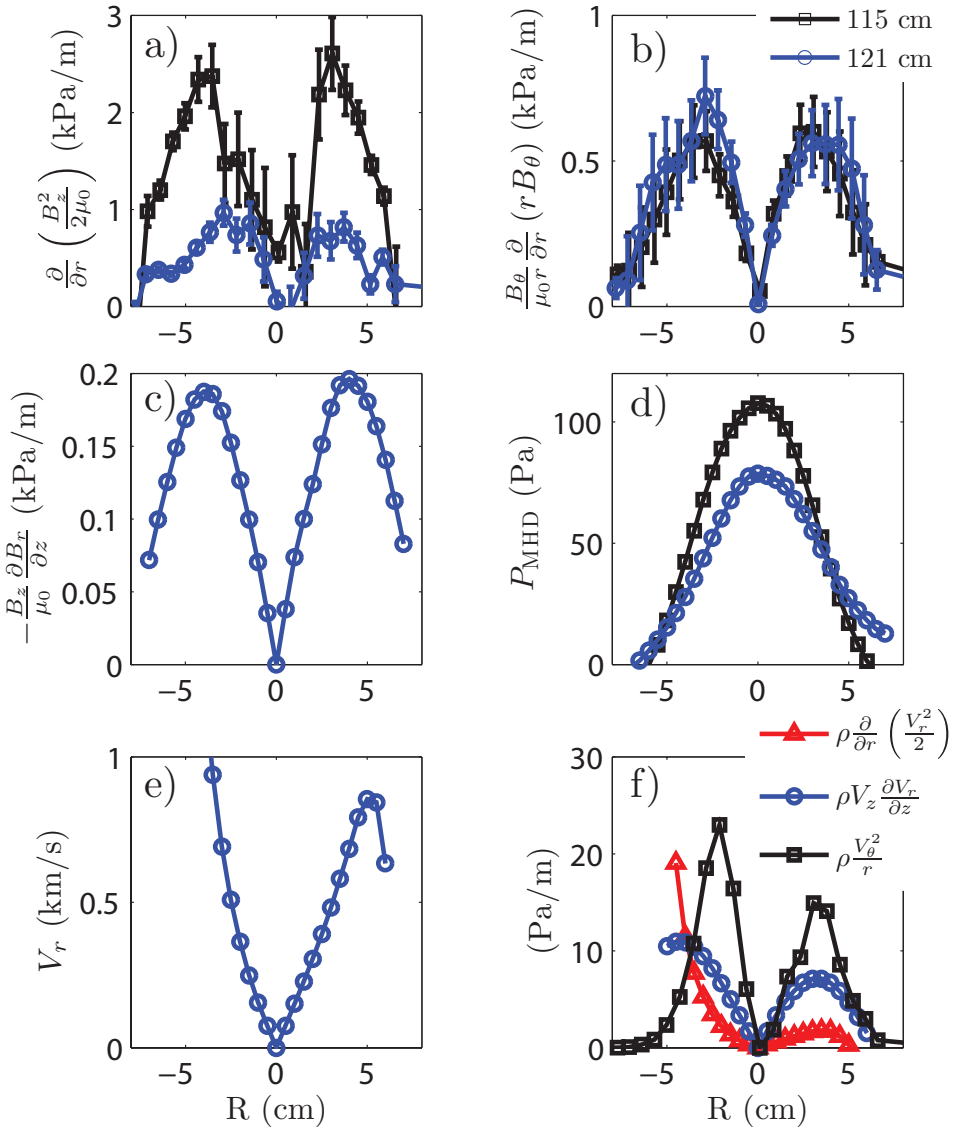

Figure 3.4: Analysis of Eq. 3.3 in the anode boundary layer (ABL). Measurements at Z = 115 cm are in the bulk plasma (where Eq. 3.2 applies) while measurements at Z = 121 cm are partway into the ABL. The anode is at Z = 123 cm. (a) The diamagnetic term is much reduced in the ABL while (b) The Z-pinch term is unaffected. (c) The 2-D nature introduces a new term into radial force balance. (d) Pressure profiles from the integration of the $\vec{J}\times\vec{B}$ forces illustrate the reduced pressure from the weakened diamagnetic term, which is partially offset by the new axial term. (e) Radial flow V_r approximated from the incompressible continuity equation using the $P_{\rm MHD}$ profiles. (f) The remaining flow terms of Eq. 3.3 using the V_r of (e).

tying in a plasma by a conducting anode and illustrates that its effects are highly localized.

The nature of MHD radial force balance is significantly altered in a narrow anode boundary layer (hereafter called the ABL) as the dominant contribution to Eq. 3.2 (the $\frac{\partial}{\partial r}(\frac{B_z^2}{2\mu_0})$ term) is much reduced in the ABL. This requires a transition from the 1-D form of Eq. 3.2 to the 2-D form of Eq. 3.3 in the ABL. To analyze the 2-D equilibrium in this region, plasma parameters presented in Section 2.4 are used. The B-dot probe is capable of directly measuring the magnetic field terms of Eqs. 3.2 and 3.3, and results are shown in Fig. 3.4a-c. Measurements at Z = 115 cm are in the bulk plasma, where Eq. 3.2 is expected to hold, while measurements at Z = 121 cm are partway into the ABL, and the anode is at Z = 123 cm. The reduction in δB_z leads to a large reduction in the $\frac{\partial}{\partial r}\left(\frac{B_z^2}{2\mu_0}\right)$ term in the ABL. This imbalance must be compensated for by other terms in Eq. 3.3. The $\frac{B_\theta}{\mu_0 r}\frac{\partial}{\partial r}(rB_\theta)$ term is unaffected by the transition into the ABL. The $\frac{B_r}{\mu_0}\frac{\partial B_z}{\partial z}$ term, not present in Eq. 3.2, is present in the ABL, but is insufficient to account for the force imbalance in the ABL. Thus, the total magnetic body force is reduced and must be compensated for by either reducing the pressure gradient or accelerating large flows or both.

An approximate analysis is carried out in the ABL by first neglecting the flow terms of Eq. 3.3 and integrating the resultant pressure profile ($\int J \times B dl \equiv P_{\mathrm{MHD}}$), shown in Fig. 3.4d. For the bulk plasma, P_{MHD} is a very good approximation to the true pressure as V_r, $B_r = 0$ is expected and the inferred values of V_θ are taken from Section 2.4.4. This indicates that the $\rho\frac{V_\theta^2}{2}$ term is negligible at the anode. For the ABL, it is not possible to *a priori* neglect the V_r terms, though as they contribute to sustaining the pressure gradient the Z = 121 cm P_{MHD} profile is thus a lower limit. P_{MHD} exhibits a strong parallel pressure gradient and loss of plasma particles from Z = 115 cm to 121 cm. As T_e is measured to be spatially uniform, the spatial variation in P_{MHD} arises from density gradients and these gradients are used to calculate the V_r necessary to satisfy the incompressible continuity

equation without particle sources or sinks, where V_z is measured and was discussed in Section 2.4.4. This limiting case V_r is then used to compute the remaining flow terms in Eq. 3.3, which are shown to be small (Fig. 3.4f). As the P_{MHD} profile utilized is a lower limit and as V_r arises from this pressure decrease, the V_r limit is thus an upper one and the neglect of the flow terms is thus justified in the original approximation. Confirmation of these estimates naturally requires a direct measurement of the radial flow (V_r) profile, as the assumption of incompressibility may be inaccurate. Particle sources and sinks, however, are not thought to play an important role as the mean free paths of ionization and recombination are much larger than the spatial scales relevant to the ABL. Furthermore, measurements are limited to Z = 121 cm by the spatial scale of the probe. It is expected that the force imbalance of Fig. 3.4a will become more pronounced closer to the anode, leading to larger axial gradients. It is further speculated that the observed lack of density pile-up at the anode despite the large V_z is due to the pumping effect of V_r. If particles retain radial momentum after recombination, neutral and plasma particles alike would be driven into the expansion volume at the anode end.

The axial scale length of the ABL is set by the competition between advection and diffusion of the magnetic field as axial flows (V_z) present in the device tend to advect field perturbations downstream while diffusion allows perturbations to move upstream. The parallel magnetic field diffusion coefficient ($D = \eta/\mu_0$) is calculated to be 120 m^2/s using the measurement of η from Section 2.4.3. From the induction equation, $D \approx (\Delta Z)V_z$, where measured $V_z \approx 6$ km/s sets a scale length (ΔZ) of ≈ 2 cm, consistent with the observed scale length.

3.3.3 Transition to Paramagnetic Equilibrium

As more $J_{||}$ ($\propto I_P$) is injected into the plasma by increasing the bias voltage on the plasma guns, the diamagnetic equilibrium transitions to paramagnetism and the anode boundary

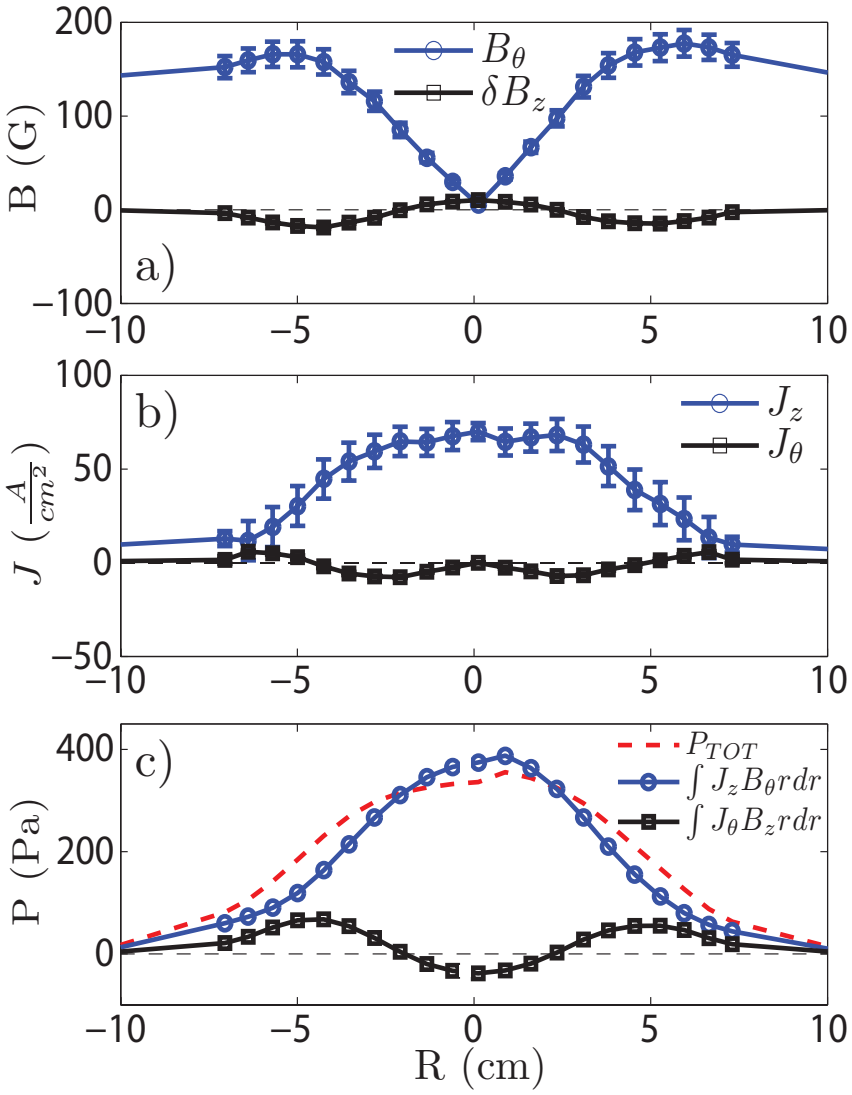

Figure 3.5: 1-D equilibrium magnetic fields during high current operation. (a) The diamagnetism is shown to be greatly reduced in this case as (b) increasing $J_{||}$ is strongly paramagnetic. (c) The pressure gradient is primarily balanced by gradients in B_θ, unlike the low current discharge of Section 3.3.1, and the resulting equilibrium is Z-pinch like.

layer effect is lost. This is because the magnetic field unit vector exhibits a greater pitch thus giving a solenoidal component to $J_{||}$ and contributing positive (paramagnetic) δB_z to the core. This effect is counter to the J_θ currents produced by the plasma gun itself. Thus, increasing I_P transitions the core plasma from diamagnetic to paramagnetic in nature, and eliminates the anode mirror effect described in Section 3.3.2. The nature of the canonical 1-D radial MHD-force balance of Eq. 3.2 is also altered by the paramagnetic effect, with the $J_z B_\theta$ drive becoming dominant over the $J_\theta B_z$ term, as shown in Fig. 3.5. This geometric effect is well known [55] but is rarely demonstrated experimentally due to the fact that $\delta B_z \ll B_{z0}$ in low β devices.

3.3.4 Role of Plasma Sourcing and Ohmic Heating

The precise effect of the plasma source on the canonical screw pinch equilibrium can be studied by selectively disengaging single guns from the plasma source array and observing the resultant MHD equilibrium. Figure 3.6 illustrates three equilibria generated with the central gun of the plasma source off, unbiased, and biased equal to the surrounding guns. For all cases the outer ring of guns were discharged and biased equally, and profiles are taken at the midplane of the device.

With the central plasma gun off, no diamagnetic currents exist in the core, yielding a flat pressure profile. In this case, only $J_{||}$ is observed to diffuse into the core plasma, yielding a force-free state ($\nabla \times \vec{B} = \lambda \vec{B}$) in the core. The Taylor parameter λ is found to be constant to within 5% across the core region (to R = 3 cm), though beyond this point it is strongly varying. Thus, while a global fully relaxed Taylor state [56, 57] is not achieved, there is a large force-free region in the core of the plasma.

Discharging the central gun without biasing it is found to drive no additional $J_{||}$ as compared to the gun off case, though the gun still sources plasma which in turn carries a pressure gradient. The core of the plasma thus now contains finite $J_\perp$ and the resultant

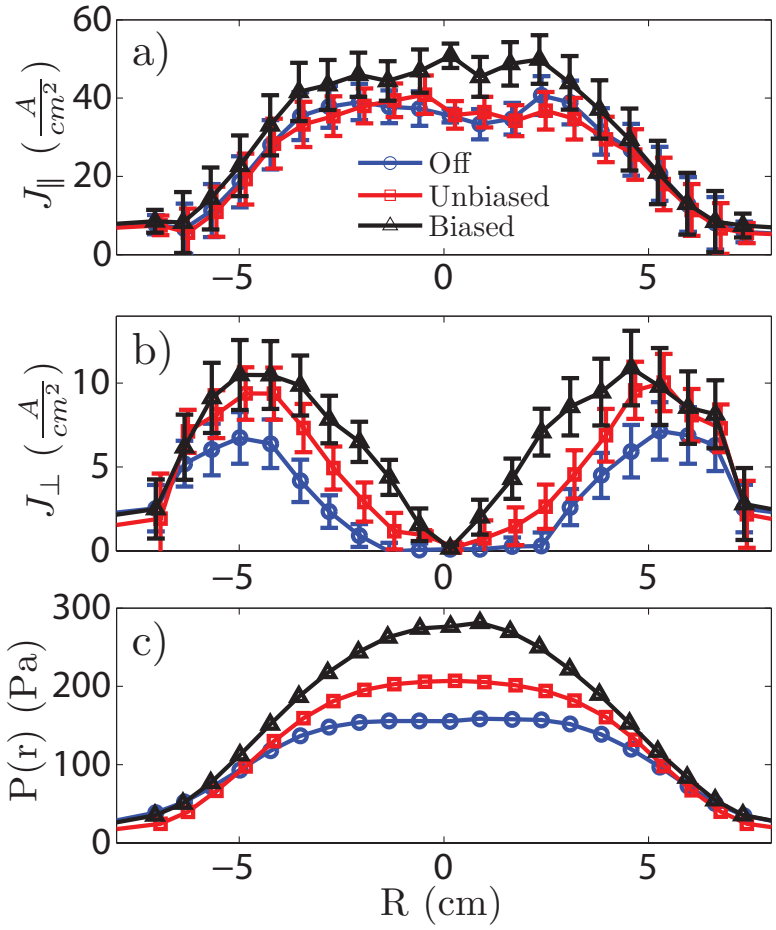

Figure 3.6: Disparate MHD equilibria are achieved depending on whether the central plasma gun is turned off, discharged but left unbiased, and biased. (a) The off and unbiased case display identical $J_{||}$ profiles, while the biased case clearly adds to the $J_{||}$ profile. (b) $J_{\perp}$ profiles indicate that the unbiased gun still contains significant perpendicular currents which leads to an increase in the pressure profile (c). Biasing the central gun also raises the level of $J_{\perp}$ and P.

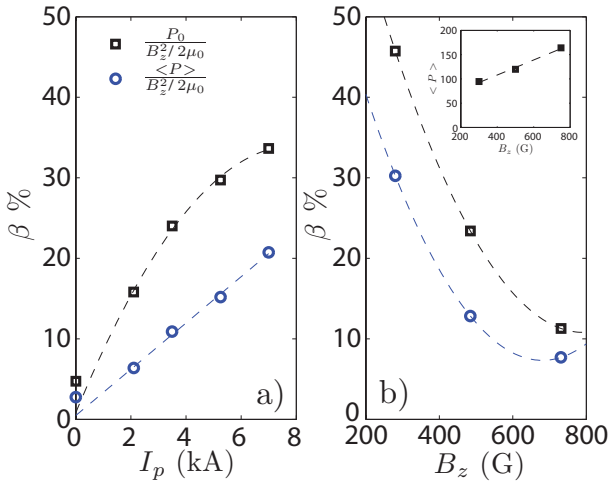

Figure 3.7: Scaling of peak and volume averaged plasma $\beta = P/(B_z^2/2\mu_0)$ with plasma current I_P and guide field B_z. (a) A linear dependence on I_P is seen for volume averaged β which breaks down in the limit of zero I_P, while diamagnetism in B_z breaks this trend for core β. (b) $B_z \propto P$ as B_z increases confinement, though the B_z^{-2} dependence in the definition of β yields a $\beta \propto B_z^{-1}$ final scaling. Simple trend lines are also shown. P_0 and $<P>$ are computed by integrating the 1-D radial force balance of Eq. 3.2.

core equilibrium is no longer force-free. As the $J_{||}$ profile is identical between the off and unbiased case, the additional heating to increase $J_\perp$ is not simply Ohmic heating ($\eta J_{||}^2$) in the bulk plasma. Instead, $J_\perp$ likely originates from Ohmic heating inside the plasma gun that has been advected by the axial flow.

Biasing the central gun clearly drives additional $J_{||}$ but also increases $J_\perp$, indicating that additional Ohmic heating has contributed to sustaining a larger pressure gradient and thus a larger core pressure. As described in Section 2.4.1, this additional heating primarily increases n_e while leaving T_e relatively unchanged.

3.3.5 Confinement Scaling of Axisymmetric Equilibria

Figure 3.7 illustrates that increasing the plasma current (I_P) and guide field (B_z) are found to both lead to higher core pressure (P_0) though differing effects on $\beta = \langle P \rangle / (B_z^2/2\mu_0)$ are seen. The large amount of Ohmic heating from $I_P \propto J_{||}$ results in a very high value

of β, both in a peak and volume averaged sense. A linear dependence of volume-averaged β on I_P is seen, though Ohmic power scales like $P \propto \eta I_P^2$ (where η is the resistivity and is $\propto T_e^{-\frac{3}{2}}$) and measurements indicate T_e and thus η are insensitive to I_P. This is reconciled by noting that for open ended devices, particle flux Γ (and thus power loss) is overwhelmingly directed to the end plates giving $\Gamma \propto n_e C_s$, where C_s is the sound speed and is $\propto T_e^{\frac{1}{2}}$. Measurements preesnted in Section 2.4 have shown that $n_e \propto I_P$, while T_e is insensitive to I_P. Thus, while $P \propto I_P^2$, $\Gamma \propto I_P$, resulting in the observed $\beta \propto I_P$ scaling. In the limit of zero I_P (unbiased plasma), the plasma guns still produce plasma, which leaks along the guide field while maintaining ambipolarity, yielding the finite β values observed when $I_p = 0$. Core β deviates from linearity with I_p due to diamagnetism (δB_z) significantly modifying B_z in the core. Guide field scaling ($B_z \propto \langle P \rangle$) illustrates that reduced Larmor radii are effective in increasing confinement even in open ended devices, though the B_z^{-2} dependence in the definition of β yields a final scaling of $\beta \propto B_z^{-1}$.

3.4 Helical Equilibrium State

The lower q ($\approx$ 1-2), higher (I_p) equilibria discussed in Section 3.3.3 are also characterized by the appearance of long-lived coherent fluctuations in the magnetic and kinetic profiles. Typical magnetic field measurements for this mode are shown in Fig. 3.8. It is exceptionally coherent and dominantly $m = 1$ with a helical twist. The mode is global, but with the largest amplitudes observed at the anode end. It is also a global mode of the device with a single frequency present throughout. Detailed internal measurements illustrate that mode is a helical equilibrium state, as will be discussed in the following Sections.

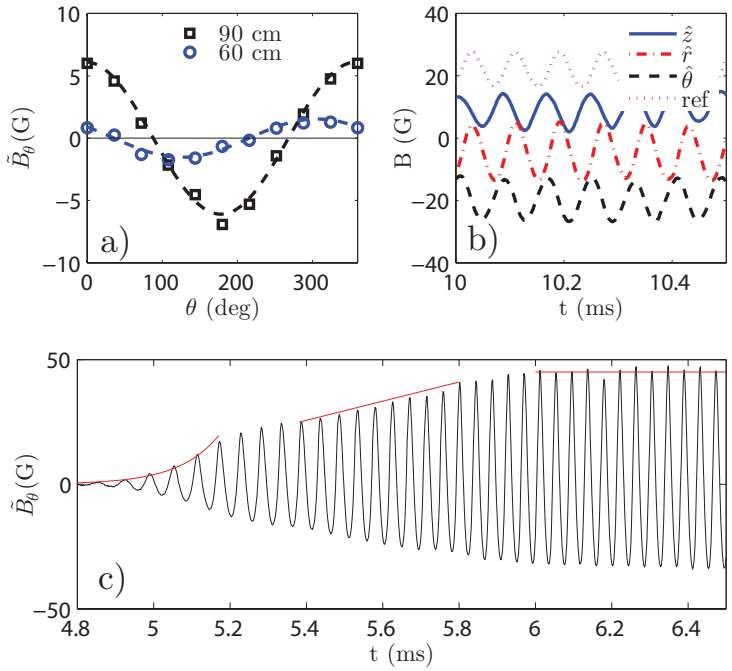

Figure 3.8: (a) Edge B_θ probes illustrate the presence of an $m = 1$ perturbation that has a helical twist. (b) B-dot probe signals illustrating the exceptional coherence and single-harmonic structure of the fluctuation. The directions of the signals refer to the probe frame, which is distinct from the cylindrical frame as seen in Fig. 2.1(b). An edge B_θ probe is also shown (ref). (c) High-pass filtered edge B_θ coil illustrates that onset of the perturbation is characterized by an exponential growth phase, followed by a linear growth phase indicating non-linear interactions, until a saturation amplitude is reached.

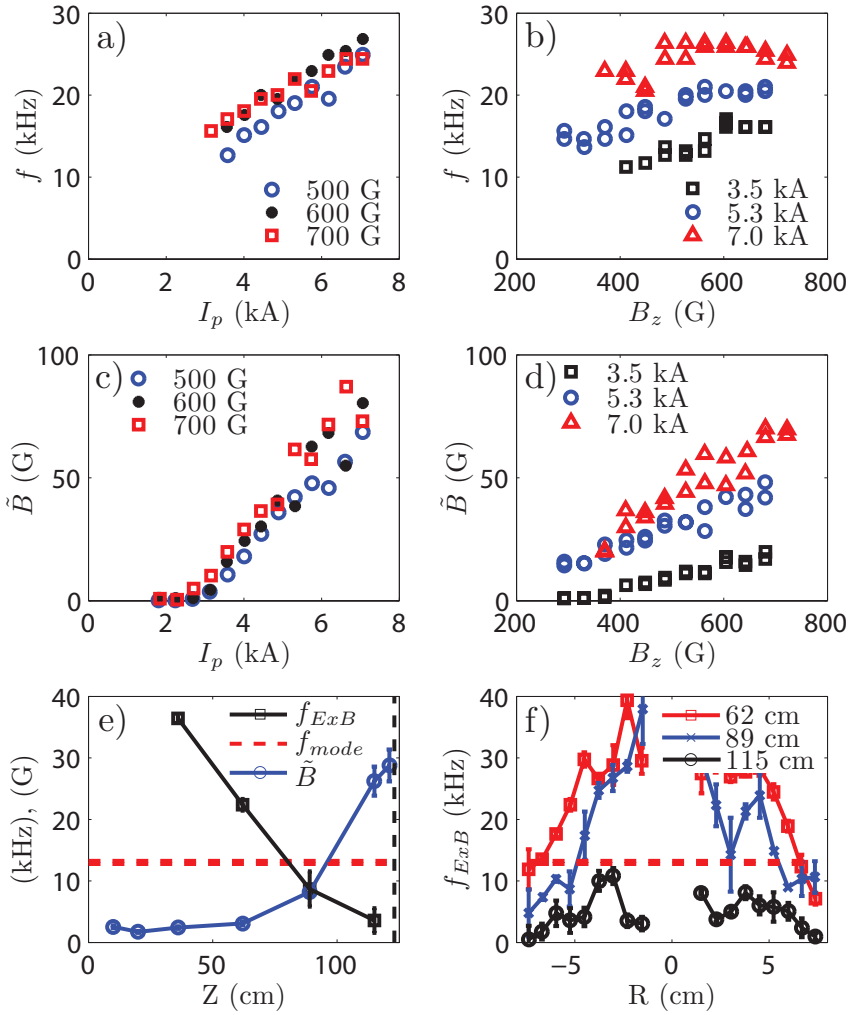

Figure 3.9: (a) The coherent mode of Section 3.4 is shown in (a) to linearly increase in frequency as plasma current (I_p) is increased. (b) Frequency dependence on B_z is increasing at lower I_p but static at higher I_p. (c) Mode amplitude ($\tilde{B}$) increases linearly with I_p, and the critical current for excitation is not found to occur at a single value of safety factor q. (d) $\tilde{B}$ also counter-intuitively increases with increasing B_z. (e) Axial structure of the ExB frequency and $\tilde{B}$ for the 500G, 3.5 kA case. Mode amplitude is largest where $f_{\mathrm{mode}} < f_{\mathrm{ExB}}$. (f) Significant radial shear in f_{ExB} also exists, requiring a mode-weighted volume average to relate f_{ExB} to f_{mode}.

3.4.1 Scaling and Onset

Coherent mode scaling with I_p and B_z is complex, as shown in Fig. 3.9a-d. Onset occurs at a critical plasma current I_p (equivalent to a critical $J_{||}$), though this critical current is seen to vary weakly with the axial magnetic field B_z. This is inconsistent with a critical safety factor (q) for excitation expected by external kink theories [58, 3]. Furthermore, the mode can be excited by increasing the guide field (B_z), which would tend to be stabilizing to the external kink mode. The current profile is modified and becomes somewhat more peaked as B_z is increased, but measurements using the segmented anode (not shown) indicate that the $q \propto B_z$ nonetheless. The frequency of the mode is increased as I_p or B_z is increased, but this dependence is weak with B_z. The growth rate (γ) for the mode in the exponential phase (shown in Fig. 3.8c) is found to be in the 6-10 kHz range. A weak $\gamma \propto I_p$ scaling is observed, while no dependence on B_z is seen. As the experimental scatter in γ is great due to the short duration of the exponential phase, no analysis of this scaling is presented.

The observed mode frequency (f_{mode}) at a single coil is simply that of the Doppler shift of the rotating $m = 1$ perturbation. f_{mode} is large enough that the conducting vacuum vessel appears ideal and thus $\tilde{B}_r = 0$ at the wall. Analysis discused in Section 3.4.2 will show that the typical radial scale size of the oscillation is ≈ 5 cm, which allows conversion from f_{mode} (13 kHz for the Section 3.4.2 case) to a mode azimuthal velocity (V_{mode}), which is found to be ≈ 4 km/s, and directed in the ExB direction. This velocity is sub-Alfvénic and sub-sonic as these speeds are ≈ 75 and 25 km/s respectively.

Figure 3.9e-f illustrates that an axially and radially sheared ExB flow (V_{ExB}) profile exists in the device, as discussed in Section 2.4.4. Despite the sheared V_{ExB} profile, a single, global f_{mode} is observed, shown by the dotted lines in Fig. 3.9e-f. Though the process by which a global mode frequency is selected in a sheared flow is not fully understood, it can be intuitively inferred that a volume-weighted average is taken to select the mode velocity.

With this hypothesis, scaling with I_p is easily understood as $V_{\mathrm{ExB}} \propto E_r \propto E_z \propto I_p$, though scaling with B_z is more complex. Mode axial extent increases toward the cathode with increasing B_z (and I_p) and begins to inhabit regions of larger V_{ExB}. Thus, as the volume-weighting includes regions of larger V_{ExB}, larger frequencies would be observed, consistent with observations. Mode amplitude is largest when $V_{\mathrm{mode}} > V_{\mathrm{ExB}}$, indicating that V_{ExB} may be setting the axial scale size of the mode in addition to its frequency. Alternatively, the large V_{ExB} may be stabilizing the mode in the cathode region.

3.4.2 Internal Analysis

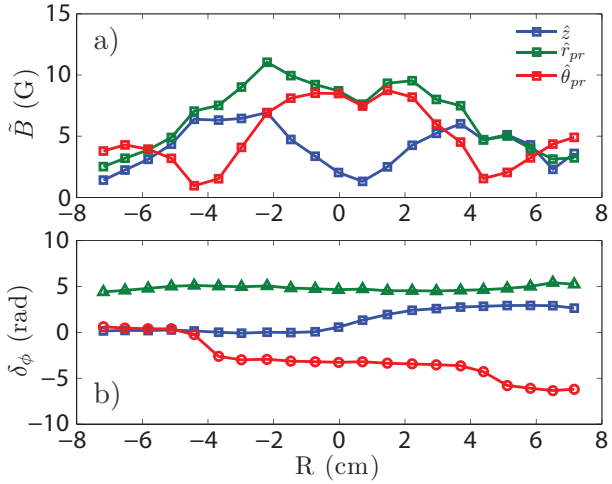

Figure 3.10: Using an edge B_θ signal as a reference (or click), relative phase shifts from different discharges can be directly compared and radial profiles built of both fluctuation amplitude ($\tilde{B}$) and relative phase (δ_ϕ) using simple FFT based algorithms. This method relies on the exceptional coherence of the signals and on the shot-to-shot reproducibility of the discharge.

The exceptional coherence of the raw magnetic signals (samples shown in Figs. 3.1a,c and 3.8b) allows the use of a reference signal (an edge B_θ coil) to clock signals across different discharges, thus enabling internal profiles of the fluctuating field to be constructed. Each magnetic field component has a well-defined phase shift (δ_ϕ) from the reference signal, and δ_ϕ can be measured at different spatial locations. In this way, utiliz-

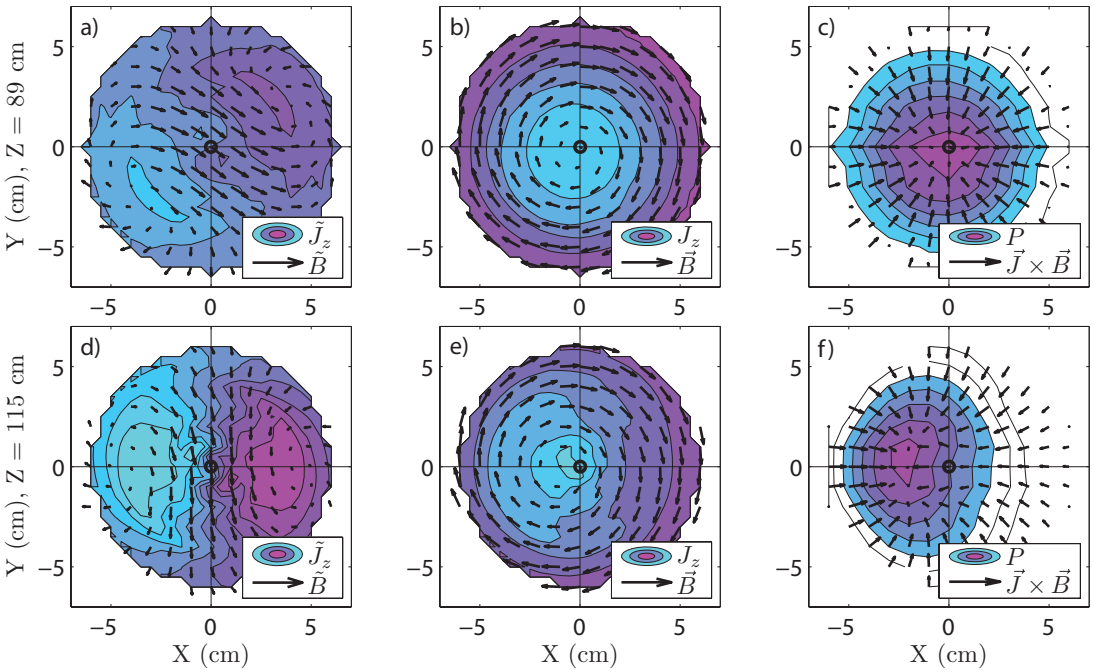

Figure 3.11: Fluctuating and total contributions to Ampère's Law and radial MHD force balance for the helical equilibrium state at two axial locations to indicate the helical twist. (a) and (d) illustrate the fluctuating fields leading to a rigid shift in the current centroids, shown in (b) and (e). Integrating $\vec{J} \times \vec{B}$ also indicates the pressure centroid is shifted, shown in (c) and (f). All parameters are decomposed into mean-field and fluctuating components, using the notation $\vec{B} = B_0 + \tilde{B}$.

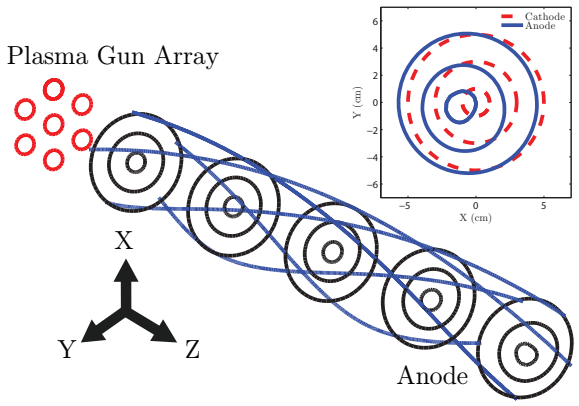

Figure 3.12: Helical equilibrium fieldline and flux surface mapping throughout the device, illustrating that circular flux surfaces are maintained. The inset illustrates the offset of the circular flux surfaces between cathode and anode, indicating that flux surfaces wander at the anode.

ing shot-to-shot repeatability, radial and axial profiles of δ_ϕ can be obtained, as shown in Fig. 3.10b. A fast Fourier transform (FFT) based algorithm is used, as cross-correlation techniques are unnecessary due to the dominantly single-mode time-dependence. Mode amplitudes are trivially extracted from the FFT, as shown in Fig. 3.10a.

Full 3-D maps of each component of the fluctuating magnetic field can be constructed using the decomposition:

$$\tilde{B}(r,\theta,z,t) \quad = \quad \tilde{B}(r,z)\cos\left(\omega t - m\theta - \delta_\phi(r,z)\right) \tag{3.4}$$

where global mode frequency (ω) is taken to be an average for all discharges in the series ($\delta\omega/\omega \approx 2\%$ over the > 100 discharges used to create a map). The azimuthal mode number (m) is taken to be 1 throughout the profile based on edge measurements by the B_θ array shown in Fig. 3.8a. The phase shift (δ_ϕ) is also a function of probe position and desired component, as is the fluctuation amplitude ($\tilde{B}$). As all parameters in Eq. 3.4 are known, the 3-D (r,θ,z) space can be populated. For the following measurements, the measurement grid is 5-7 axial locations by 11 radial locations, corresponding to a spacing of ≈ 20 cm and 5 mm respectively.

The 3-D fields constructed using Eq. 3.4 illustrate that the mode is global in nature, existing throughout the plasma core and with significant internal structure. All parameters are decomposed into mean-field and fluctuating components, using the notation $\vec{B} = B_0 + \tilde{B}$. Ampère's law is similarly decomposed, with Fig. 3.11a,d illustrating fluctuating contributions and Fig. 3.11b,e illustrating total, instantaneous fields. The fluctuating axial current $\tilde{J}_z$ exhibits a peak at r = 5 cm, which when summed to the equilibrium J_{z0} causes a rigid shift in the current channel, shown in Fig. 3.11b,d. Time dependence is a simple rigid rotation of the fluctuating profiles shown in Fig. 3.11a,b.

As $1/\tau_A \ll \omega$, radial MHD force balance is still upheld throughout the oscillation.

Equation 3.1 is also decomposed into mean-field and fluctuating components, yielding:

$$J_0 \times B_0 + J_0 \times \tilde{B} + \tilde{J} \times B_0 + \tilde{J} \times \tilde{B} \;\; = \;\; \nabla P + \nabla \tilde{P} \tag{3.5}$$

where flow has been ignored as measurements are taken away from the anode boundary layer of Section 3.3.2. As shown in Fig. 3.11c,f, summing all terms in Eq. 3.5 yields a force profile that is dominantly radial, while each individual contribution from Eq. 3.5 is not. Furthermore, the force null is now offset from the geometric axis of the device. The contribution to this perturbed force profile is equally shared between the second and third terms of Eq. 3.5. The Maxwell stress ($\tilde{J} \times \tilde{B}$) is found to be vanishingly small, indicating that $\tilde{J}$ is fully out of phase with $\tilde{B}$, as $\left|\tilde{J}\right| \left|\tilde{B}\right|$ is large. This force profile can be integrated and generally circular pressure contours are found, shown in Fig. 3.11c,f. As with Fig. 3.11b,e, a rigid shift is seen of the pressure maximum. Thus, the fluctuating currents and fields act to offset the plasma centroid while maintaining its overall structure. Figure 3.12 illustrates using fieldline mapping that the flux surfaces are also maintained throughout the plasma, consistent with equilibrium being maintained. The flux surfaces are also seen to be offset at the anode and are found to trace a circular pattern around the geometric axis. The validity of the line-tying condition in this context will be discussed in Section 3.5.

3.5 Discussion

This Chapter has described the MHD equilibrium properties of the Rotating Wall Machine plasma. The plasma is found to be either diamagnetic or paramagnetic, depending on the strength of the plasma current. The plasma guns are found to provide the dominant source of diamagnetic currents, allowing the plasma to reach very high values of β despite its poor axial confinement. The large flows found in the device also give rise

to MHD modes that rotate with the plasma and thus possess significant real frequencies when Doppler shifted into the lab frame.

The direct observation of the line-tying of magnetic fieldlines by a conducting anode discussed in Section 3.3.2 is in contrast to other results in which sheath resistance is found to break the line-tying condition at a conducting boundary [59, 45]. This not inconsistent with a recent theory [46] as the non-dimensional κ parameter (Eq. 49 in Ref. 8) which gauges the importance of sheath resistance (where $\kappa \gg 1$ indicates strong sheath effects) is found to be ≈ 0.05 as opposed to $\kappa \approx 15$ cited for an experiment in which significant sheath effects are observed [59, 45]. Physically, this corresponds to a lower total sheath resistance due to larger plasma density and consequently smaller sheath axial dimensions (electron and ion Debye lengths are 0.2 and 0.9 μm respectively).

As with the axisymmetric case, a dramatic reduction in $\tilde{B}_z$ and δB_z very near the anode is observed for the helical equilibrium of Section 3.4. In contrast, $\tilde{B}_{r,\theta}$ reaches its maximum amplitude at the anode, a result which (in addition to an off-axis emissivity maximum) has been previously interpreted as imperfect line-tying [60, 44]. This discrepancy may be explained by introducing finite bulk plasma resistivity, which when expanding the resistive Ohm's law ($\vec{E} - \vec{V} \times \vec{B} = \eta \vec{J}$) at the anode surface can allow for finite $\tilde{V}$ and $\tilde{B}$ while maintaining $\tilde{E} = 0$. In fact, in a perfectly conducing and flowing plasma finite $\vec{V}_t$ is permitted as long as $\vec{V} \times \vec{B} = 0$ [61]. Either way, as E_t is not measured at the anode surface, existing measurements cannot conclusively determine if line-tying is upheld in the helical equilibrium state.

It is possible that the kink instability initiates the transition from the axisymmetric to helical state. In this sense, an alternative framework for understanding the helical equilibrium of Section 3.4 is that of a saturated kink. Notwithstanding, observations of the helical state onset indicate that there is no critical safety factor q at which the helical equilibrium is found, in contrast to established external kink theory [62, 13]. Internal

kinks, however, have no such critical q [62], nor presumably would cases in which the distinction between internal and external kinks is inappropriate due to a poorly defined plasma boundary. Furthermore, onset as described in Section 3.4.1 is also consistent with a pressure-driven onset, as $P \propto I_p$, B_z, and both were found to be destabilizing. A β driven onset is not consistent with the observations, due to the inverse scaling of β with B_z. As the topic of pressure-driven modes in the finite length screw-pinch is largely unexplored, no comparison to theoretical predictions is attempted.

Chapter 4

Flux Rope Merger and Column Formation

Individual flux-ropes injected from the plasma gun array are observed to merge without time-dependence. In the presence of collimated axial flow, spatial gradients can be related to time steps in the plasma frame, thus forming a Fick's law for the merging assuming the plasma flow slips from the ExB flow. Measurements indicate that a slip of only $\approx 1\%$ is required to explain the flux-rope merger. Neutral drag, plasma viscosity, or flow shear could be responsible for this offset, though present measurements are unable to clearly identify a single source. Particle diffusion rates are found to be consistent with classical predictions, and current diffusion is comparable to the particle diffusion rate.

4.1 Motivation

Modeling of MHD instabilities in this experiment assumes a homogeneous axisymmetric plasma column [13]. However, plasmas are injected into the device as discretized, elongated structures called flux ropes. Whether or not these flux ropes merge into a homogeneous plasma (and if so in what axial distance) is thus of critical importance to the confident application of existing theories to the device plasma. While homogeneous, axisymmetric profiles shown in Chapters 2-3 supported this treatment of the plasma, the

process by which axisymmetry was achieved was not described.

Furthermore, flux ropes form the fundamental building blocks of many terrestrial and astrophysical plasma structures. When flux ropes interact, a rich set of dynamics has been observed [63]. Depending on the underlying plasma parameters, flux ropes can twist around their center of mass [64], become unstable [34], merge [65], or even bounce [66].

In this Chapter, internal probe measurements of flux rope merger in the device are presented. Flux ropes are observed to radially diffuse into one another as a function of axial distance from the guns, generating a homogeneous bulk plasma with no small-scale internal structure. This is despite the fact that cross-field particle transport is intrinsically ambipolar in the ideal MHD approximation, formally preventing any such radial current channel expansion. However, finite plasma resistivity can break this condition as long as the plasma azimuthal flow (V_θ) slips from the ExB velocity ($\vec{V}_{\mathrm{ExB}}$), which in turn requires an additional torque arising from non-ideal effects. This chapter will both present measurements of flux-rope merger on the device as well as identify the possible physical mechanisms at play. Though flux rope merger has generally been discussed and studied in the context of impulsive magnetic reconnection events [67], measurements are here shown for which all merging is time-independent.

The organization of this Chapter is as follows. Section 4.2 details model equations used to compare to experiment. Section 4.3 presents measurements of the radial and azimuthal flux rope merger. Section 4.4 derives a cross-field current diffusion equation, and Section 4.5 discusses possible physical mechanisms responsible for this diffusion. Section 4.6 provides additional interpretation for the aforementioned topics.

4.2 Diffusion Ansatz and Model Equation

Plasma Density

To model flux rope merger of the plasma density, particles are assumed to follow the standard advection diffusion equation:

$$\frac{\partial \rho}{\partial t} = -\rho \nabla \cdot \vec{V} - \vec{V} \cdot \nabla \rho + D_\rho \nabla^2 \rho \tag{4.1}$$

where D_ρ ($\approx (\Delta x)^2/\nu$) is a generic diffusion coefficient for a random walk step size Δx and collision frequency ν. This method necessarily further assumes that D_ρ is a global parameter, when in fact it may be highly local. All experimental data considered in this Chapter will be from the steady-state flat-top phase of the discharge, thus all $\frac{\partial}{\partial t}$ terms are eliminated. The first term of the RHS of Eq. 4.1 is removed due to incompressibility, which is a good approximation for the sub-sonic flows present in the device. The large aspect ratio approximation is used to allow $\nabla^2 \approx \nabla_\perp^2$ by neglecting weak axial gradients. Assuming axisymmetry, allowing the axial flow to be collimated such that $\vec{V} = V_z \hat{z} + V_\theta \hat{\theta}$ (where V_z is constant), and expanding $\rho = m_i n_i = m_i n_e$ yields:

$$V_z \frac{\partial n_e}{\partial z} = D_\rho \nabla_\perp^2 n_e \tag{4.2}$$

A purely diffusive equation is thus recovered, where the $V_z \frac{\partial}{\partial z}$term has taken the place of the $\frac{\partial}{\partial t}$ term found in a standard diffusion equation. Thus, this can be thought of as a diffusive process in a frame moving axially with the plasma flow. Note that V_θ does not enter into Eq. 4.2 in the axisymmetric limit. Using these approximations, a spatial step along the device axis is related to a time step in the frame of the moving plasma. This relation allows direct measurement of the diffusion coefficient D_ρ necessary to fit the observed axial profiles, as will be shown in Section 4.3.

Current Density

A similar advective diffusive ansatz is made for the plasma axial current density (J_z). Once again, a Galilean transformation is used to move axially with the plasma at speed V_z. In this frame, all cross field current transport is transport is assumed to obey a Fick's law, yielding the following relation:

$$V_z \frac{\partial J_z}{\partial z} = D_J \nabla_\perp^2 J_z \tag{4.3}$$

The diffusion coefficient above is defined as $D_J \equiv \epsilon \frac{\eta}{\mu_0}$, where a small parameter ϵ has been introduced. While Eq. 4.3 has been provided as an ansatz, a derivation is also provided in Section 4.4, in which ϵ can be shown to arise from a slippage between V_θ and V_{ExB}. The physical origin of this slippage is in turn discussed in Section 4.5.

Model Equation

The solution to Eqs. 4.2 & 4.3 with a delta-function initial condition at Z = 0 cm is, in Cartesian geometry:

$$Q(x,y,z) = \sum_{i=1}^{[6,7]} A \exp\left(-\frac{(x-x_i)^2 + (y-y_i)^2}{4D_Q(\Delta Z)/V_z}\right) \tag{4.4}$$

Where Q can be n_e or J_z, ΔZ is the axial step size between measurements, V_z is the axial flow, D_Q is either D_ρ or D_J depending on the measurement, and A is a constant related to the total n_e or J_z. The centroid locations $\{x_i, y_i\}$ are well known from the plasma gun array geometry. The index i sums over all the guns discharged in a particular experiment. Thus, measurements taken at discrete axial locations are fit to solutions of these equations in Cartesian coordinates. Each axial location can yield a measurement for $\{D_x, A\}$.

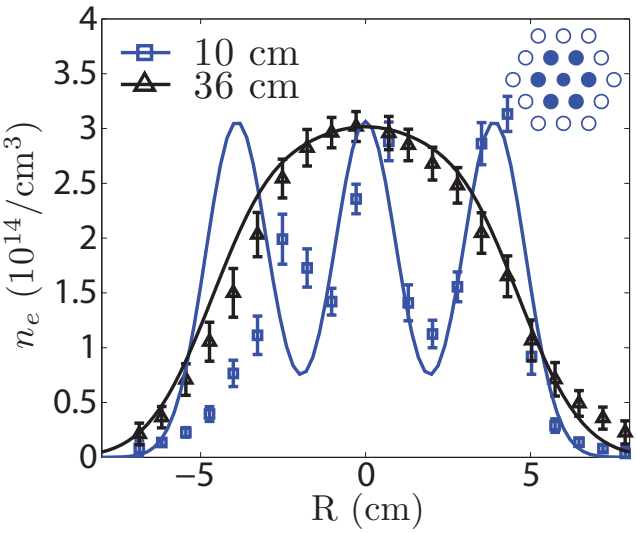

Figure 4.1: Langmuir probe measurements of electron density (n_e) and fits to Eq. 4.4, illustrating complete merger by Z = 36 cm. The central seven guns are discharged.

4.3 Flux Rope Merger Measurements

4.3.1 Radial Merger

Plasma Density

The discretized plasma source array shown in Fig. 2.6 allows flux rope merger to be experimentally studied under a variety of geometries. The guns are separated by 3.6 cm, and the full-width at half-maximum (FWHM) of a single gun plasma gun has been previously reported to be 3 cm at an axial distance of 25 cm from the guns [39]. Thus, the radial separation of each source is comparable to the individual flux rope size and merging is expected to occur. Figure 4.1 displays Langmuir probe data in which the transition from discretized flux ropes to homogeneous plasma is clearly present. Each profile includes a fit to Eq. 4.4, where each flux rope has been modeled as a delta function at Z = 0 cm. Left-right asymmetry in the Z = 10 cm profile is due to the pitch of the fieldlines, which bring the left (right) flux rope into (out of) the path of the probe, as expected by Fig. 2.6.

This can also be thought of as aliasing of the $m = 6$ gun array onto the $m = 1$ resolution of the probe sweep. Furthermore, as the Z = 36 cm profile appears fully merged, it is unclear whether the merger was complete much before the Z = 36 cm plane. Thus, the D_ρ measured for this case only provides a lower bound. Conversely, assuming a delta function density profile at Z = 0 cm can provide an upper bound for D_ρ. Both of these results are comparable and results are listed in Table 4.1.

Axial Current

For merger of the axial current, several configurations are studied by selectively engaging and disengaging the discrete elements of the plasma gun array. The first configuration studied is the discharging and biasing the central 7 guns of the array equally, shown in Fig. 4.2a. Monotonic profiles are achieved by Z = 36 cm, which corresponds to 30% of the distance from cathode to anode. Although Langmuir data from Z = 20 cm is missing, it appears that merging of n_e and J_z occurs on similar spatial scales. Fits to Eq. 4.4 extract a diffusion coefficient (D_J) for the axial current in this configuration, which is given in Table 4.1.

The second configuration studied is generated by biasing only the inner ring of 6 plasma sources and leaving the central gun either discharged but unbiased or off altogether. This creates a ring-like current profile, as merging in the azimuthal direction will be shown in Section 4.3.2 to be required by magnetic shear. The core of the ring-like plasma is either a current-free plasma (if the gun is discharged but left unbiased) or vacuum (if the gun is left off). In both cases, the axial ring current profile is shown to diffuse inwards until a monotonic current profile is generated, as shown in Fig. 4.2b. As the radial separation between guns is larger than in the 7 gun configuration, radial merging occurs over a longer axial length in this case. The centroid of each individual current channel is maintained throughout the merger, indicating $\vec{J} \times \vec{B}$ body forces do not draw the channels together,

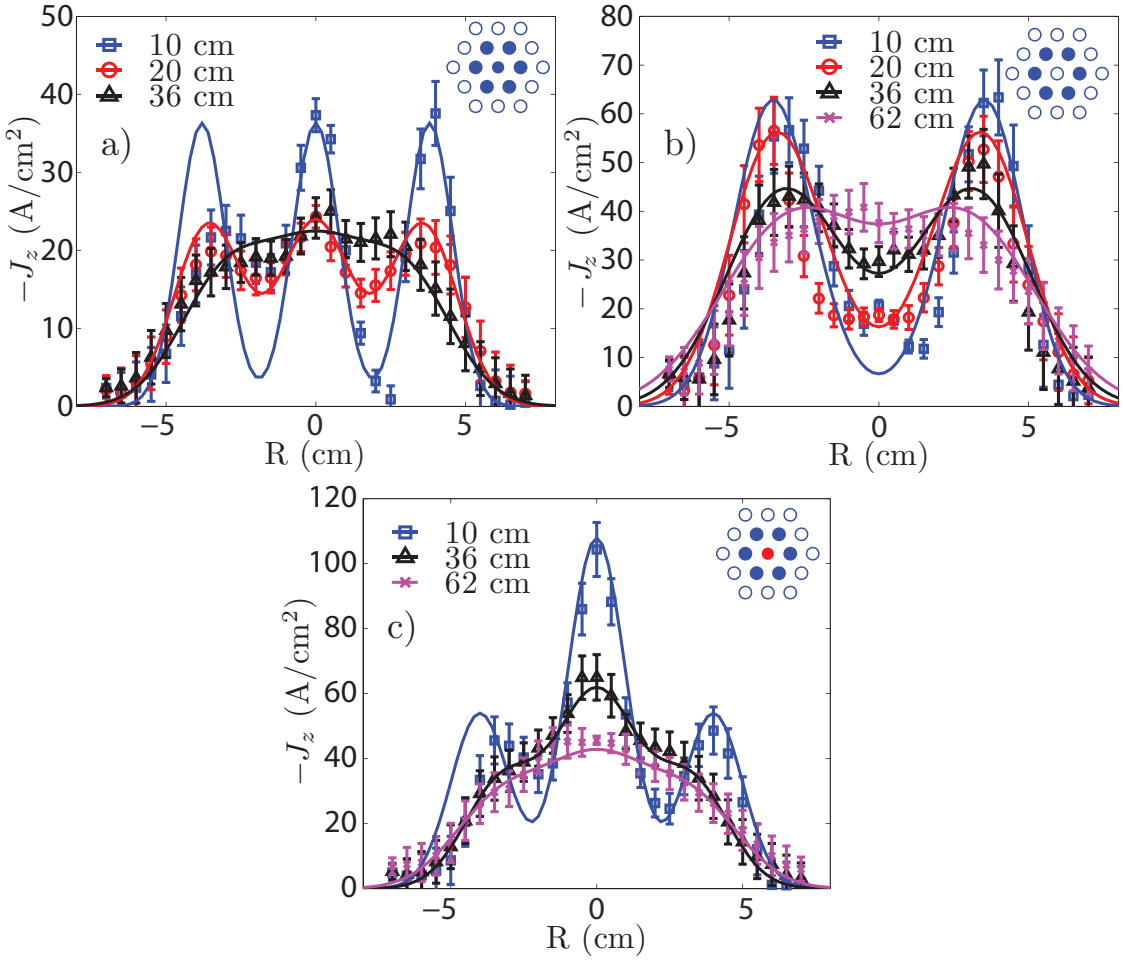

Figure 4.2: B-dot probe measurements of axial current (J_z) profiles at different axial locations for three different gun configurations, and fits to Eq. 4.4 (a) Central 7 guns biased. (b) Inner ring of sources biased. (c) The central gun is biased to double the current of the surrounding guns.

Description	Definition	Theoretical D_x [m^2/s]	Experimental D_x [m^2/s]	ϵ [%]
Classical	$\eta_\perp n_e k_B T_e / B^2$	11 ± 4		
Bohm	$\frac{1}{16}\frac{k_B T_e}{eB}$	7 ± 1		
Ambipolar	$\frac{\mu_{\perp i} D_{\perp e} + \mu_{\perp e} D_{\perp i}}{\mu_{\perp i} + \mu_{\perp e}}$	2 ± 1		
n_e (Fig. 4.1)			4.5 ± 1	
Magnetic Field	$\eta_\perp / \mu_0$	235 ± 80		
J_z, (Fig. 4.2a)			3.5 ± 0.5	1.5 ± 0.5
J_z, (Fig. 4.2b)			3.0 ± 0.5	$1.3 \pm .5$
J_z, (Fig. 4.2c)			4 ± 2	1.7 ± 1

Table 4.1: Summary of experimental measurements of D_x from fits to Eq. 4.4 and comparison to theoretical estimates. Uncertainties in experimental values come from scatter in fit parameters from different axial profiles, while uncertainties in theoretical values are propagated from errors in the underlying experimental measurements.

as will be further discussed in Section 4.6.

The final configuration studied is that of a current spike generated by quickly increasing the bias current of the central plasma gun, as shown in Fig. 4.2c. This configuration begins with the central 7 guns biased equally and brought to steady-state, similar to the case of Fig. 4.2a. From this point the bias current to the central gun is doubled over 7 ms using the plasma source pulse width modulation (PWM) controller as per the time trace shown in Fig. 2.5. Figure 4.2c illustrates that this current spike is only apparent near the plasma gun, and by the device midplane (Z = 62 cm) the spike has fully diffused into the surrounding current profile. As the diffusion coefficient D_J of the initial equilibrium before this spike is the same as the first configuration, new diffusion coefficients are only found for the current spike itself once it reaches steady-state. This coefficient is also shown in Table 4.1.

Each experimental flux rope merger case has yielded a measurement of the diffusion coefficients ($\{D_\rho, D_J\}$) and slippage parameter (ϵ) as will be defined in Section 4.4. These parameters are summarized in Table 4.1. Results indicate that diffusion is occurring with characteristic D_x all in the vicinity of 3-5 m^2/s, for both particles and current density. The

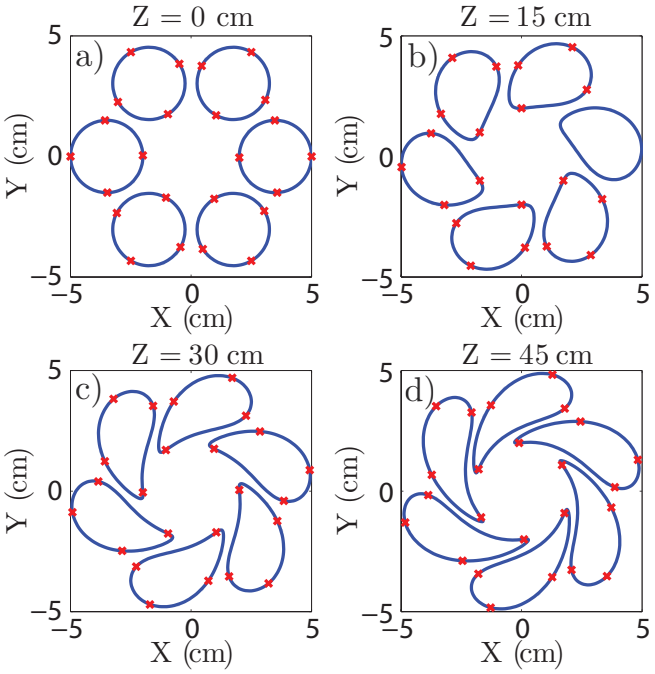

Figure 4.3: Cartoon illustrating azimuthal phase mixing of flux rope magnetic surfaces. (a)-(d) map an originally circular magnetic surfaces for each flux rope across consecutive axial steps, illustrating their deformation. Single fieldlines are marked by red crosses.

diffusion in density is found to be slightly larger than the classical ambipolar prediction utilizing Spitzer resistivity, though less than the Bohm prediction. For the collisionality (ν) and guide field (B_z) regime of the device plasma neither the strongly magnetized nor weakly magnetized regime is valid and the full ambipolar diffusion form must be used. This intermediary regime also exhibits a linear dependence of D_ρ on the guide field, instead of the standard classical scaling ($D_\rho \propto B_z^{-2}$). Current diffusion measurements indicate that the ϵ parameter is small for all experimental configurations. The physical origin for ϵ will be discussed in Section 4.5. It is also interesting that comparable rates of diffusion are found for both current and density.

4.3.2 Azimuthal Merger

While experimental observation of the azimuthal merger of the flux ropes is beyond the resolution of the internal probe, there is strong grounds to believe azimuthal flux rope merging takes place on similar axial scales. This process can be understood as being due to phase mixing arising from the magnetic shear in the experiment, illustrated qualitatively in Fig. 4.3. Fieldlines from the inner radius of an outer flux rope will map through a smaller azimuthal step ($\Delta\theta$) than an outer radius fieldline over the same axial step (ΔZ). When current is driven from the central gun larger magnetic shears are generated and mixing occurs in a smaller axial step size. Further azimuthal mixing would be expected to arise from azimuthal ExB flow shear, which may in fact be dominant, though the $m = 6$ component of the ExB flow has not yet been measured.

4.4 Derivation of Current Diffusion

In this Section the axial current diffusion equation (Eq. 4.3) is derived and it is shown to critically depend on the degree of slippage between V_θ and V_{ExB}, quantified by the ϵ parameter. Beginning with the resistive Ohm's law:

$$\vec{E} + \vec{V} \times \vec{B} = \eta \vec{J} \tag{4.5}$$

where η is the bulk plasma resistivity. Justification of neglected Ohm's law terms will be discussed in Section 4.6. It is clear that in contrast to Eq. 4.1, axisymmetric ExB flows ($\vec{V}_{\mathrm{ExB}} = \vec{E} \times \vec{B}/B^2$) can no longer be ignored as they could be for particle transport. This is because $\vec{V}_{\mathrm{ExB}}$ is established to reduce the plasma-frame radial electric field, and this in turn impedes magnetic diffusion. The azimuthal flow is now assumed to be nearly that of $\vec{V}_{\mathrm{ExB}}$, except for a small parameter ϵ ($\ll 1$), which quantifies the degree of slippage

between V_θ and V_{ExB}. Thus $\vec{V} = V_z\hat{z} + (1-\epsilon)\vec{V}_{\mathrm{ExB}}$, where V_z is the axial flow. The physical origin of this slippage will be discussed in Section 4.5. That ϵ is a constant coefficient constitutes another simplifying assumption of this treatment. Inserting this definition of $\vec{V}$ into Eq. 4.5 yields a modified Ohm's law:

$$\vec{E} + (\vec{V}' \times \vec{B}) = \eta' \vec{J} \tag{4.6}$$

where $\vec{V}' \equiv \frac{1}{\epsilon} V_z \hat{z}$ and $\eta' \equiv \frac{\eta}{\epsilon}\left((\epsilon - 1)\frac{J_{||}}{J} + 1\right)$ are modified flow speeds and resistivities. The magnetic probe measurements of Chapter 3 show $J_{||} \approx J$, thus $\eta' = \eta$ is taken throughout the remainder of this Chapter. The curl of Eq. 4.6 is taken to yield a modified advection diffusion equation for the magnetic field:

$$\frac{\partial \vec{B}}{\partial t} = \nabla \times \vec{V}' \times \vec{B} + D_B \nabla^2 \vec{B} \tag{4.7}$$

where diffusivity D_B in this case is η/μ_0 and is taken to be a global parameter as $\eta \propto T_e^{-\frac{3}{2}}$ and Fig. 2.14 shows the plasma is isothermal. The ratio $J_{||}/J$ in the definition of η' is not local, however, although it is approximated as so for this analysis. Following the derivation of Eq. 4.2, a steady-state solution is found by setting $\frac{\partial}{\partial t} \mapsto 0$, and expanding the second term of the LHS of Eq. 4.7:

$$0 = \vec{B} \cdot \nabla \vec{V}' - \vec{V}' \cdot \nabla \vec{B} - \vec{B} \nabla \cdot \vec{V}' + D_B \nabla^2 \vec{B} \tag{4.8}$$

The third and first terms of Eq. 4.8 are eliminated by noting all flows are subsonic and thus incompressible and by assuming weak axial gradients in $\vec{V}'$ and small B_r respectively. Letting $\vec{V}' = V_z' \hat{z}$, the same form as Eq. 4.2 is recovered:

$$V_z \frac{\partial \vec{B}}{\partial z} = \epsilon D_B \nabla^2 \vec{B} \tag{4.9}$$

Once again, the result is analogous to purely diffusive transport of magnetic field in a Galilean frame moving axially with the plasma. This analysis is expanded to axial currents (J_z) by taking the curl of Eq. 4.9 and isolating the $\hat{z}$ component. The vector relation $\nabla^2\vec{B} = -\nabla\times\nabla\times\vec{B}$, valid for all divergence-free fields (including $\vec{J}$), expands the $\nabla\times\nabla^2\vec{B}$ term, from which $\vec{J}$ is easily isolated by Ampere's law. The same vector identity then collapses the expanded form to that of Eq. 4.9 with J_z in the place of $\vec{B}$. The advection term is also expanded:

$$\nabla\times\left(V_z'\frac{\partial\vec{B}}{\partial z}\right) = V_z'\left(\nabla\times\frac{\partial\vec{B}}{\partial z}\right) + \nabla V_z'\times\frac{\partial\vec{B}}{\partial z} \tag{4.10}$$

Assuming no radial and azimuthal gradients in V_z' (collimated flow profile) removes the $\nabla V_z'$ term in the $\hat{z}$ component of Eq. 4.10. The divergence-free condition on both $\vec{B}$ and $\vec{J}$ in addition to Ampère's law yields a condition on $B_{x,y}$, such that $\frac{\partial}{\partial z}\frac{\partial}{\partial x}B_y = \frac{\partial}{\partial x}\frac{\partial}{\partial z}B_y$ and $\frac{\partial}{\partial z}\frac{\partial}{\partial y}B_x = \frac{\partial}{\partial y}\frac{\partial}{\partial z}B_x$. This relation allows $\left[\nabla\times\frac{\partial\vec{B}}{\partial z}\right]_z$ to become $\frac{\partial}{\partial z}\left[\nabla\times\vec{B}\right]_z$, which is then trivially related to J_z. Again, the large aspect ratio approximation allows $\nabla^2\approx\nabla_\perp^2$, yielding:

$$V_z\frac{\partial J_z}{\partial z} = D_J\nabla_\perp^2 J_z \tag{4.11}$$

Where $V_z' = \frac{1}{\epsilon}V_z$ has been used and $D_J \equiv \epsilon\frac{\eta}{\mu_0}$. This is the result shown in Section 4.2.

4.5 Physical Mechanisms for Cross-Field Current

In the preceding Sections it was shown that a slight slippage of the plasma azimuthal velocity (V_θ) to the ExB velocity (V_{ExB}) could, under certain assumptions, lead to a spatial diffusion of the current profile. This slippage was parametrized by the ϵ coefficient which was later measured. However, parameterizing the flow in terms of a slippage pa-

rameter ϵ was not justified, and this will be the topic of this Section. Once again, a velocity profile of the form $\vec{V} = V_z\hat{z} + (1-\epsilon)\vec{V}_{\mathrm{ExB}}$ is taken, where $\vec{V}_{\mathrm{ExB}} \equiv \vec{E} \times \vec{B}/B^2$, and $(1-\epsilon)\vec{V}_{\mathrm{ExB}} = V_\theta\hat{\theta}$. Insertion of this relation into the radial component of the resistive Ohm's law ($E_r + V_\theta B_z = \eta_\perp J_z$) yields $J_r = \left(\frac{\epsilon}{\epsilon-1}\right)\frac{B_z}{\eta_\perp}V_\theta$. Note that Hall terms and electron-neutral collisions have been neglected, as will be discussed in Section 4.6.

The ϵ parameter implies an imperfect cancellation of E_r in the Ohm's law and thus a finite J_r and azimuthal torque. In equilibrium, this torque must be balanced by another term in the (axisymmetric) azimuthal force balance:

$$\rho\left(\vec{V}\cdot\nabla\vec{V}\right)_\theta = \left(\vec{J}\times\vec{B}\right)_\theta - \rho\nu_{in}V_\theta + \mu\left(\nabla^2\vec{V}\right)_\theta \tag{4.12}$$

where ν_{in} is the ion-neutral collision rate, μ is the viscosity, and ρ is the density. Were azimuthal forces not in equilibrium, V_θ would adjust itself on an inertial time scale until equilibrium was found. It is challenging to measure all of the terms in Eq. 4.12 directly and with sufficient accuracy. This is especially true of the second derivatives in the viscous term. Note that a scalar viscosity ν is used as opposed to the viscous stress tensor due to the relatively weak magnetization of the ions in the device. Nevertheless, Eq. 4.12 can be simplified with the following assumptions, already used in Section 4.2. First, $\{B_r, V_r\} = 0$, yielding:

$$\rho V_z\frac{\partial V_\theta}{\partial z} = -J_r B_z - \rho\nu_{in}V_\theta + \mu\nabla^2 V_\theta \tag{4.13}$$

and upon insertion of the relation for J_r this becomes:

$$\left(\frac{\epsilon}{1-\epsilon}\right)\frac{B_z^2}{\eta_\perp}V_\theta = \underbrace{\rho V_z\frac{\partial V_\theta}{\partial z}}_{\text{flow shear}} + \underbrace{\rho\nu_{in}V_\theta}_{\text{neutral drag}} - \underbrace{\mu\nabla^2 V_\theta}_{\text{viscosity}} \tag{4.14}$$

with the physical mechanisms balancing the ϵ parameter indicated. Note that the flow

shear term is the plasma-frame polarization drift as $V_\theta \approx \vec{V}_{\mathrm{ExB}}$. As the relative contribution of each of the terms of Eq. 4.14 have not been measured to significant accuracy, this is the current state of understanding concerning current diffusion in the device. Notwithstanding, limits of Eq. 4.14 can be taken.

Neutral Drag Limit

In the limit that the only term balancing J_r in Eq. 4.14 is the neutral drag ($\{V_z, \nu\} = 0$), a prediction of the ionization fraction can be made.

$$n_n = \left(\frac{\epsilon}{1-\epsilon}\right) \frac{B_z^2}{\rho \eta_\perp (\sigma V_{\mathrm{Ti}})} \tag{4.15}$$

where $\nu_{in} = n_n \sigma V_{\mathrm{Ti}}$ has been expanded, and n_n is the neutral density, σ is the neutral collision cross-section, and V_{Ti} is the ion thermal velocity. Using parameters for the device (see Table 2.2), the fractional ionization is found to be $\approx 95\%$, which is a reasonable number, though as yet unconfirmed by measurements. Note also that this physical mechanism for cross-field current transport is the Pedersen current [68, 69].

Flow Shear Limit

In the limit of negligible neutral drag and viscosity ($\{\nu_{in}\mu\} = 0$), a new, anti-diffusive Fick's law can be formulated. Returning to Eq. 4.13, which in this limit becomes:

$$\rho V_z \frac{\partial V_\theta}{\partial z} = -J_r B_z \tag{4.16}$$

As ϵ is a small correction, $V_\theta \approx \vec{V}_{\mathrm{ExB}} = -E_r/B_z$. Furthermore, axial gradients in B_z and B are taken to be small. Thus, $\frac{\partial V_\theta}{\partial z} \approx \frac{\partial E_r}{\partial z} = \frac{\partial E_z}{\partial r}$, where the steady-state (electrostatic) condition has been used to relate E_z and E_r. Using $E_z = \eta_{||} J_z$, valid for B_r, $V_r = 0$, Eq.

4.16 is converted to:

$$\frac{\rho V_z \eta_{||}}{B_z}\frac{\partial J_z}{\partial r} = J_r B_z \tag{4.17}$$

Eq. 4.17 indicates that transport of J is related to spatial gradients in J, a situation characteristic of (anti-)diffusive phenomena. Eq. 4.17 thus can be used to generate a global Fick's law. Both sides are multiplied by $\frac{1}{r}\frac{\partial}{\partial r}r$, and gradients in $\eta_{||}$, V_z, ρ are necessarily neglected to obtain an approximate global anti-diffusivity. Using $\nabla \cdot J = \frac{1}{r}\frac{\partial}{\partial r}(rJ_r) + \frac{\partial J_z}{\partial z} = 0$, and maintaining axisymmetry, a Fick's law is found:

$$V_z \frac{\partial J_z}{\partial z} = -D_{\text{fs}} \nabla_{\perp}^2 J_z \tag{4.18}$$

where $D_{\text{fs}} \equiv \frac{\rho V_z^2 \eta_{||}}{B_z^2}$. Global J_z profile anti-diffusion via flow shear can thus be approximately characterized by a simple parameter, D_{fs}. It should also be noted that the flow-shear mechanism is identically the plasma-frame polarization current. Interestingly, this diffusion parameter is of the same magnitude as the experimental diffusion coefficient, though the experimental observation is decisively diffusive, not anti-diffusive. For this reason, this is not expected to be the appropriate limit for the experiment. Thus, neutrals and viscosity are critical to explain experimental results, though they remain to be measured to sufficient accuracy.

4.6 Discussion

In deriving the theoretical model for fitting the flux rope merger measurements of Section 4.2, a resistive Ohm's law was used. This Ohm's law neglected the Hall, electron pressure, and electron inertia terms present in the generalized Ohm's law [70]. Electron inertia terms are easily shown to be negligible for the steady-state phenomenon here stud-

ied. The steady-state requirement also implies that the plasma is in MHD force balance, thus reducing the hall and electron pressure term into a single ion pressure tensor term. Taking the curl of this term results in contributions of the form $\nabla n_e \times \nabla T_i$ (thermal electromotive force, or Biermann battery) which are negligible for the isothermal plasma. Thus, the resistive Ohm's law of Eq. 4.5 is appropriate for use in this study.

The diffusive model of discrete current channel merger also ignores the possible role of fast magnetic reconnection [67]. Fast reconnection is generally invoked when the typical resistive diffusion time (τ_{res}) of the plasma is too long to account for the observed time-scales of magnetic field profile modification. In contrast, for the mergers discussed in Section 4.3, the measured profile evolution times (in the plasma frame) are longer than τ_{res} - the opposite limit. Thus, fast reconnection need not be invoked. Observations of fast current profile modification events have been made in the device [34], though for the parameters of this study all measured quantities are steady-state and no impuslive phenomena are observed.

Another consideration in flux rope merger studies is the role of $\vec{J} \times \vec{B}$ body forces, which are non-diffusive. Data presented in Section 4.3 clearly illustrates that the large, bulk radial accelerations expected by $\vec{J} \times \vec{B}$ body forces are not present, an observation corroborated in other experiments [64]. Furthermore, for the ring-like current profile discussed in Section 4.3, there is no enclosed current inside the ring and thus no $J_z \times B_\theta$ force to bring the centroids together. Notwithstanding, for the case where 7 guns are discharged, mm-scale radial shifts to the centroid are observed, possibly due to $\vec{J} \times \vec{B}$ body forces, although diffusive profile broadening is still dominant.

This Chapter also illustrates that although the plasma source array can provide tailored axial current input boundary conditions ($J_z(r,t)|_{Z=0}$), diffusive phenomena limits the degree to which the current profile ($J_z(r)$) can be controlled throughout the entire device length. As long as D_J remains $\mathcal{O}(1\ \text{m}^2/\text{s})$ diffusion will homogenize any imposed

radial structure in $J_z(r,t)$ over a relatively short axial distance. That being said, profile homogenization is required to produce a bulk, axisymmetric plasma for which theoretical treatments are more easily formulated. Thus, a truly ideal MHD plasma throughout the whole device length may be undesirable as it would never become axisymmetric.

The conclusion of this Chapter marks the end of Part I. Results up to this point (Part I, Chapters 3-4) were conducted in the device prior to the installation of the rotating wall. This configuration, shown in Fig. 2.1(b), had a larger ($\approx$ 20 cm diameter) vacuum vessel and thus allowed the use of the internal probe. Beyond this point, (Part II, Chapters 5-7) describe results with the rotating wall, and this device configuration is shown in Fig. 2.1(c). This configuration used a smaller ($\approx$ 16 cm diameter) vacuum vessel to yield better plasma-wall coupling. As discussed in Section 2.1, this geometry prevented the use of the internal probe system. Thus, results with the rotating wall primarily use the edge magnetics array. Although the tube radius is different between the two configurations, the bulk plasma properties are set by the parallel dynamics and axial confinement of the device, which are left unchanged. Thus, the exploration of the plasma in the first configuration is thought to be applicable to the rest of this thesis.

Part II

Rotating Wall Results

Chapter 5

Error Field Interactions with the Rotating Wall

The interaction of error fields with the rotating wall apparatus is studied analytically and compared to experimental data. Wall rotation causes eddy currents to persist indefinitely, attenuating and rotating the original error field. Superposition of error fields from external coils and plasma currents are found to break the symmetry in wall rotation direction. The error field penetration time is found to decrease as wall rotation increases.

5.1 Motivation

Attention is now turned to results from the device with the high-speed rotating wall present. A natural place to begin is to discuss the interaction of the rotating wall with non-axisymmetric fields. As these fields are normally unintentional, they are termed 'error fields' (EFs). In fact, all magnetic confinement devices tend to possess EFs to varying degrees, and their mitigation is an important part of optimizing the performance of a given device. This is because the EFs tend to affect the torque balance, slowing plasma and MHD mode rotation with generally deleterious effects.

In Chapter 6, it will be shown that the EF is of critical importance in determining the behavior of the RWM in the device. This demands a thorough understanding of the EF and its interaction with the rotating wall. These requirements motivate this Chapter. Here, the interaction of the EF with a differentially rotating system of conducting walls is studied analytically and compared to experimental data from the device. Wall rotation is shown to permanently shield EFs from the plasma and to induce a phase shift from the applied field orientation. Superposition of EFs from distinct sources is also found lead to asymmetry in wall rotation direction, with the potential for one direction of rotation to overcome the effect of shielding and increase the apparent EF. Using normal mode analysis it is also shown that the vertical field penetration time is decreased as wall rotation increases.

The organization of this Chapter is as follows: Section 5.2 defines the relevant geometries and derives the relations used throughout this Chapter. Section 5.3 examines the $t \mapsto \infty$ solution, as rotation induces persistent eddy currents that permanently alter the magnetic field structure. Section 5.4 illustrates that vacuum eigenmodes of the rotating wall system can be found, and studies the influence of rotation on these modes. Further discussion is provided in Section 5.5.

5.2 Analytical and Experimental Geometry

In this study several wall geometries are considered. These are: a single rotating wall (Fig. 5.1a), two walls with the outer wall rotating (Fig. 5.1b), and three walls with the middle wall rotating (Fig. 5.1c). The single wall geometry is useful as it forms the building block of the multi-wall systems. The two-wall geometry contains the relevant rotating wall physics, while the three-wall geometry is required to match the experiment (whose parameters are displayed in Table 5.1). In the device, the third wall represents the

Wall	Radius [cm]	Wall Time [ms]
Vacuum Vessel	$r_a = 7.71$	$\tau_a = 3.5$
Rotating Wall	$r_b = 9.16$	$\tau_b = 7.0$
Mechanical Structure	$r_c = 17.30$	$\tau_c = 41.3$
Measurement Array	$r_{\mathrm{m}} = 8.00$	N/A

Table 5.1: Experimental parameters for each cylindrical wall of the Rotating Wall Machine. For all walls, the aspect ratio (radius/length) ≈ 10.

mechanical structure used to support the rotating wall. Measurements herein are made using the 8 axial by 10 azimuthal B_r fluxloop array described in Section 2.3.2.

Experimentally, two classes of symmetry-breaking current sources are available. The first is applied from outside the rotating wall through conductors far from the walls, as shown in Fig. 5.2a. Current through this coil provides a predominantly $m = 1$ field (where m is the azimuthal wavenumber) and is hereafter called $\vec{B}_{\mathrm{ext}}$. The second current source is that of equilibrium plasma currents whose centroid is offset from the wall geometric axis (hereafter called $\vec{B}_{\mathrm{eq}}$). This offset would arise from the misalignment of the magnetic axis to the geometric axis. $\vec{B}_{\mathrm{eq}}$ is produced either with a current-carrying plasma or with a solid conducting rod located at radius r_{r} and angle η, as shown in Fig. 5.2. The field produced by this configuration is not spectrally pure, though only $m = 1$ is treated as this is the only component resonant with the kink mode in the device. Small imbalances in the resistance of conductors used to return plasma currents in the linear device can also source $\vec{B}_{\mathrm{ext}}$, shown in (c). Note that although the return conductors are far from the vacuum vessel, imbalances can still result in significant $m = 1$ perturbations within the vacuum vessel.

5.2.1 Vacuum Region Solution and Boundary Conditions

In the vacuum regions outside and between the rotating walls the Laplace equation ($\nabla^2\Phi = 0$, where Φ is the magnetostatic potential) in cylindrical geometry is used to

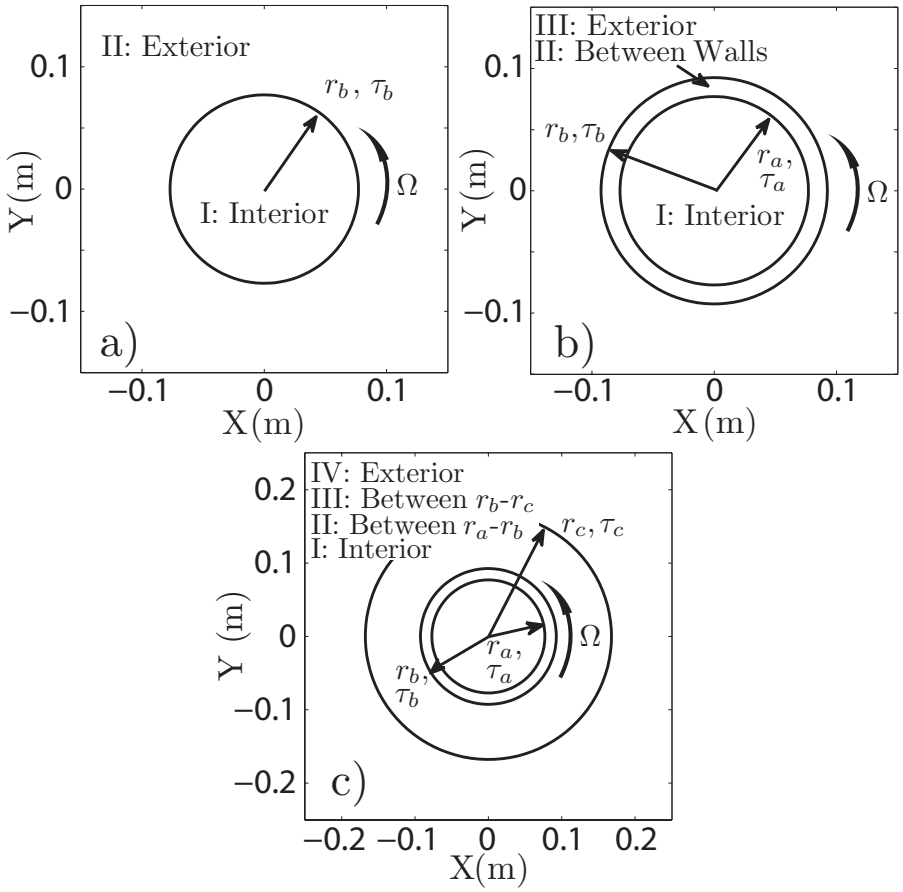

Figure 5.1: Wall geometries examined in this Chapter with scale set to experimental parameters. (a) Single rotating wall geometry, (b) two-wall geometry, and (c) three-wall geometry.

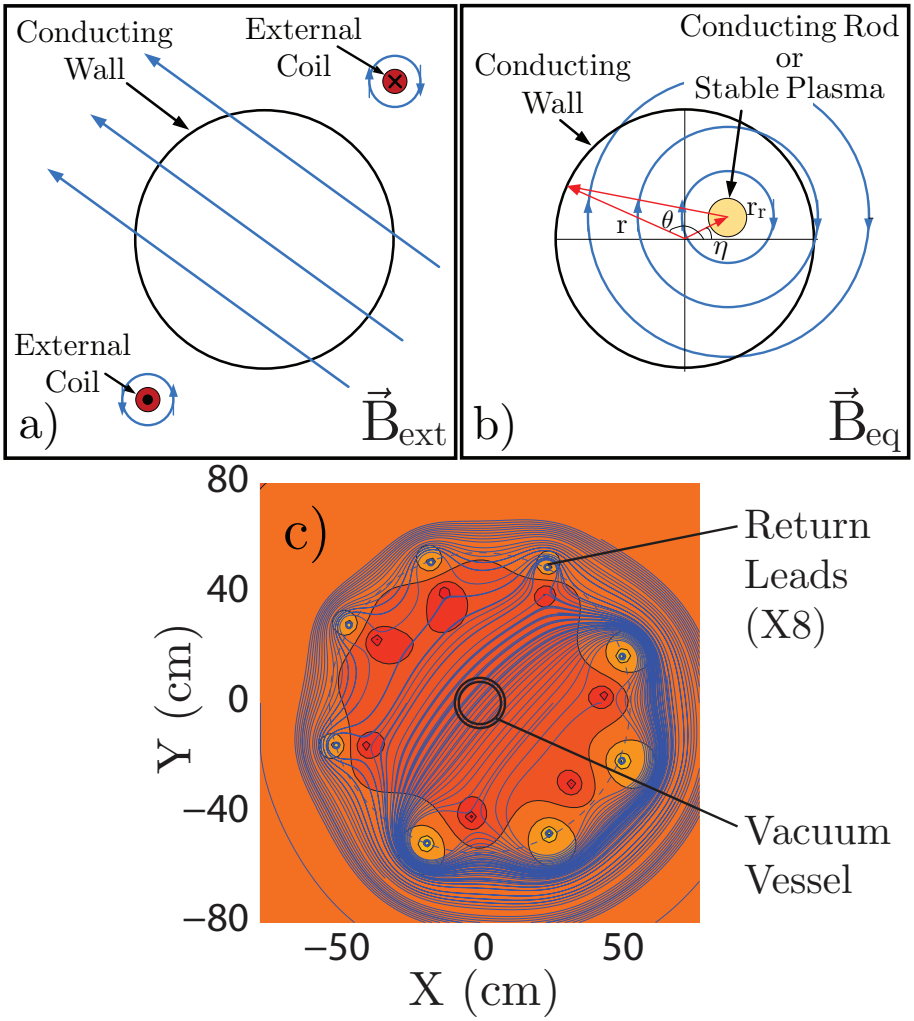

Figure 5.2: (a) An externally applied error field ($\vec{B}_{\rm ext}$) is driven by a coil external to the conducting walls. (b) Current is applied through a conducting rod or stable plasma within the interior of the conducting walls (located at radius r_p and angle β), producing $\vec{B}_{\rm eq}$. (c) Fieldlines illustrating the intrinsic external error field, which arises when currents returning through eight return leads are not properly balanced.

calculate the magnetostatic fields. The displacement current is neglected, and the long-cylinder approximation removes all variation in $\hat{z}$. As $\vec{B} = -\nabla\Phi$,

$$\begin{aligned} B_r(r,\theta) &= \Re\left[(A_j - A_k r^{-2})e^{-i\theta}\right] \\ B_\theta(r,\theta) &= \Re\left[\left(-i(A_j + A_k r^{-2})\right)e^{-i\theta}\right] \end{aligned} \tag{5.1}$$

where the guide field (B_z) is neglected. A_j, A_k are constant (complex) coefficients, and time-dependence has been left unspecified. If a current source of the form of Fig. 5.2a is present, the solution as $r \mapsto \infty$ is $\vec{B}_{\text{ext}}$. Thus, in this case simply $A_j = B_{\text{ext}}$, where the coordinate system is aligned with $\vec{B}_{\text{ext}}$. If $\vec{B}_{\text{eq}}$ (of the form of Fig. 5.2b) is present, then the field inside the innermost conductor has a term like $B \propto r^{-2}$. The matching used is to let $A_k = b_{\text{eq}}$, where $b_{\text{eq}} = B_{\text{eq}} r^2 = -i\frac{\mu_0 I_p r_{\text{r}}}{2\pi}\exp(-i\eta)$ and has units of [T m^2] and is thus left lowercase. I_p is the current driven (into the page) through the plasma or conducting rod at radius r_{r} and angle η.

5.2.2 Matching through Rotating Conducting Walls

In the rotating/static walls the magnetic field obeys the induction equation:

$$\frac{\partial \vec{B}}{\partial t} = \underbrace{\nabla \times \vec{V} \times \vec{B}}_{\text{advection}} + \underbrace{\frac{1}{\mu_0 \sigma}\nabla^2 \vec{B}}_{\text{diffusion}} \tag{5.2}$$

where σ is the (constant) conductivity of the wall. The radial projection of this vector equation is used. Enforcing $\vec{B} \propto \exp(-\gamma t)$ allows the first term in Eq. 5.2 to be linear in γ. For this work, γ is complex and $\equiv \gamma^{\text{r}} + i\omega$. Note that $\gamma^{\text{r}} > 0$ is a decay constant, while $\gamma^{\text{r}} < 0$ is a growth rate. The wall velocity is that of rigid rotation, $\vec{V} = r\Omega_w\hat{\theta}$. For the final term the long-cylinder identity $\left[\nabla^2\vec{B}\right]_{\hat{r}} = \frac{1}{r}\nabla^2(rB_r)$ is used, after which Eq. 5.2

becomes:

$$(\gamma + i\Omega_w)\, B_r = -\frac{1}{\mu_0 \sigma}\frac{1}{r}\nabla^2(rB_r)$$

This equation is now integrated from $r_w^- \equiv r_w - \frac{\delta_w}{2}$ to $r_w^+ \equiv r_w + \frac{\delta_w}{2}$, where r_w, δ_w are the radius and thickness respectively of any wall. The thin-wall approximation is used which states that B_r and r_w are constant across δ_w. For this to be accurate the wall thickness δ_w must be much less than the skin depth for a given γ such that $\gamma\mu_0\sigma\delta_w^2 \ll 1$. This is easily satisfied for the experiment as $\gamma\tau_w \ll r_w/\delta_w \approx 100$. Here, $\tau_w \equiv \mu_0\sigma r_w\delta_w$ is called the 'wall time'. Appendix C develops the equivalent thick-wall calculation. The integration yields:

$$\delta_w(\gamma + i\Omega_w)B_r = -\frac{1}{\mu_0\sigma}\frac{1}{r_w}\frac{\partial}{\partial r}(rB_r)|_{r=r_w^-}^{r=r_w^+}$$

$\nabla \cdot \vec{B} = 0$ yields $\frac{\partial}{\partial r}(rB_r) = -\frac{\partial B_\theta}{\partial \theta} = iB_\theta$. The final matching conditions are presented:

$$B_r|_{r=r_w^-}^{r=r_w^+} = 0 \tag{5.3}$$

$$B_\theta|_{r=r_w^-}^{r=r_w^+} = i(\gamma + i\Omega_w)\tau_w B_r \tag{5.4}$$

These conditions must be upheld at each wall, with $\Omega_w = 0$ if the wall is static. Note that if both $\gamma = 0$ and $\Omega_w = 0$ the field is not affected by the wall.

5.3 Steady-State Error Field Interactions

Steady state field solutions ($\gamma = 0$) are strongly affected by wall rotation (Ω_w). The fields arising from currents external to the conducting walls ($\vec{B}_{\text{ext}}$, as in Fig. 5.2a) and equilibrium plasma currents internal to the conducting walls ($\vec{B}_{\text{eq}}$, as in Fig. 5.2b) will

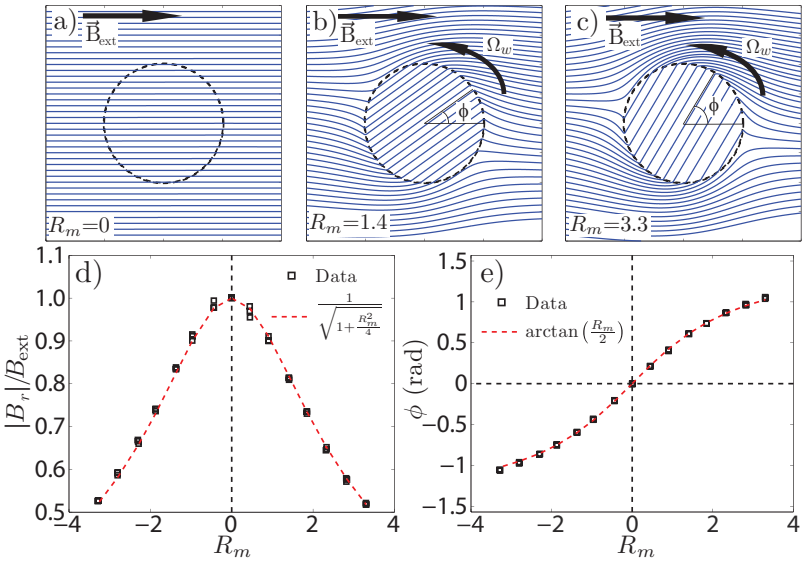

Figure 5.3: (a)-(c) Fieldlines of the steady-state field created by the application of an external $m = 1$ field ($\vec{B}_{\text{ext}}$) with all static walls omitted for clarity. The field within the rotating wall is observed to be (d) excluded and (e) phase shifted by the persistent eddy currents in the rotating wall.

be first treated independently then linearly superimposed. Solutions will be calculated and compared to experimental measurements using solid conductors or a stable plasma. When $\gamma = 0$, static conducting walls do not play a role. Thus, the single wall geometry of Fig. 5.1a is used.

5.3.1 External Error Fields

Forcing from currents external to the rotating wall (as in Fig. 5.2a) requries that as $r \mapsto \infty$, $\vec{B} \mapsto \vec{B}_{\text{ext}}$. The following functional form of $\vec{B}$ must be upheld:

$$
\begin{aligned}
I &: B_r(r,\theta) = \Re\left[A_0 e^{-i\theta}\right] \\
II &: B_r(r,\theta) = \Re\left[(B_{\text{ext}} - A_1 r^{-2}) e^{-i\theta}\right]
\end{aligned}
\tag{5.5}
$$

and where the divergence-free condition can be used to find B_θ. Using the matching conditions of Eqs. 5.3-5.4, the following matrix equation is generated:

$$\begin{bmatrix} 1 & r_b^{-2} \\ iR_m - 1 & r_b^{-2} \end{bmatrix} \begin{bmatrix} A_0 \\ A_1 \end{bmatrix} = \begin{bmatrix} B_{\text{ext}} \\ -B_{\text{ext}} \end{bmatrix} \tag{5.6}$$

where $R_m \equiv \Omega_w \tau_b$. Eq. 5.6 is non-homogeneous, and upon inversion yields a unique solution for A_n. The ratio of the field amplitude within the rotating wall (B_r) to the applied B_{ext} field is given by:

$$\frac{|\vec{B}_r|}{B_{\text{ext}}} = \frac{1}{\sqrt{1 + \frac{R_m^2}{4}}} \tag{5.7}$$

Wall rotation permanently shields the region within the rotating wall from error fields, an effect termed 'flux exclusion' and clearly illustrated by the density of the fieldlines within the wall in Figs. 5.3a-c. Figure 5.3d compares this calculation to experimental data ($t \mapsto \infty$ limit in Fig. 5.11a) and the agreement is excellent. Wall rotation also introduces a phase shift (ϕ) between the applied $\vec{B}_{\text{ext}}$ and $\vec{B}_r$. This is calculated using Eq. 5.6 to be:

$$\phi = \arctan\left(\frac{R_m}{2}\right) \tag{5.8}$$

In the thin-wall limit, ϕ cannot exceed $\pm\pi/2$. Figure 5.3e compares this calculation to experimental data and agreement is found to be excellent. The superb agreement of Fig. 5.3 gives confidence that the experiment can be used to test the more complex configurations presented in the remainder of this Chapter.

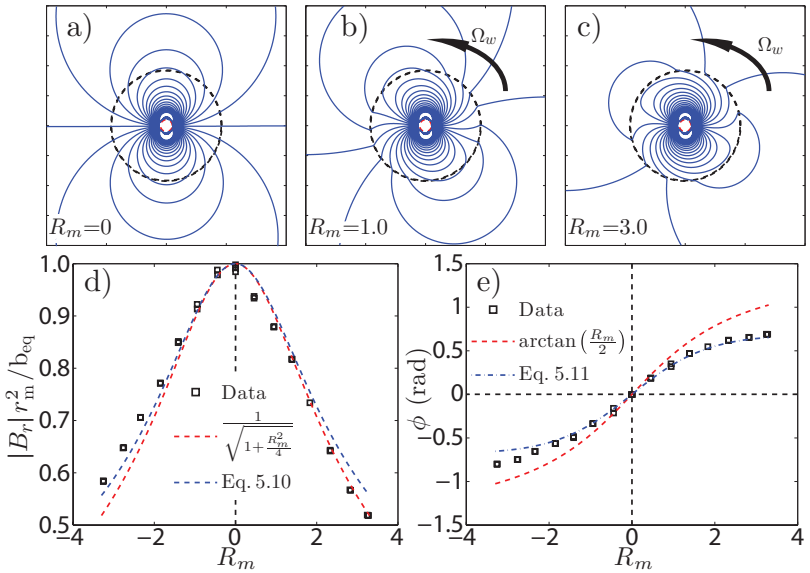

Figure 5.4: (a)-(c) Fieldlines of the $m = 1$ component of the steady-state field created by currents in a conducting rod or stable plasma within the rotating wall ($\vec{B}_{\rm eq}$) with all static walls omitted for clarity. Field penetration through the rotating wall is found to be (d) reduced and (e) phase shifted by the persistent eddy currents in the rotating wall. Data in (d) and (e) is from the conducting rod.

5.3.2 Equilibrium Plasma Currents or Conducting Rod

Forcing from currents internal to the rotating wall (from the offset conducting rod or equilibrium plasma currents, as shown in Fig. 5.2b) requires that the portion of the field decaying as r^{-2} be uniquely specified by the current source. Utilizing the single wall geometry, the following functional form of $\vec{B}$ must be upheld:

$$I : B_r(r,\theta) = \Re\left[(A_0 - b_{\rm eq} r^{-2})e^{-i\theta}\right]$$
$$II : B_r(r,\theta) = \Re\left[(-A_1) r^{-2} e^{-i\theta}\right]$$

This is similar to Eq. 5.5 though with the source term $b_{\rm eq}$ located in the interior solution as discussed in Section 5.2.1. Using the matching conditions of Eqs. 5.3-5.4, the following

matrix equation is generated:

$$dev \begin{bmatrix} r_b^2 & 1 \\ r_b^2 & iR_m - 1 \end{bmatrix} \begin{bmatrix} A_0 \\ A_1 \end{bmatrix} = \begin{bmatrix} b_{\mathrm{eq}} \\ -b_{\mathrm{eq}} \end{bmatrix} \tag{5.9}$$

Equation 5.9 is non-homogeneous, and upon inversion yields a unique solution for A_n. Solution fieldlines at various R_m are shown in Fig. 5.4a-c. Flux exclusion again occurs, though its form is modified from Eq. 5.7 and a dependence on r_{m} (the measurement radius) is introduced:

$$\frac{|B_r|}{b_{\mathrm{eq}} r_{\mathrm{m}}^{-2}} = \frac{1}{1 + \frac{R_m^2}{4}} \sqrt{\left(1 + \alpha_{\mathrm{m}} \frac{R_m^2}{4}\right)^2 + \frac{R_m^2}{4} \left(1 - \alpha_{\mathrm{m}}\right)^2} \tag{5.10}$$

where $\alpha_{\mathrm{m}} \equiv \frac{r_b^2 - r_{\mathrm{m}}^2}{r_b^2}$ has been defined and is 0.23 in the experiment. Though similar in form to Eq. 5.7, correction terms of $\mathcal{O}(\alpha_{\mathrm{m}})$ exist. In the limit of $r_{\mathrm{m}} \mapsto r_b$, $\alpha_{\mathrm{m}} \mapsto 0$, Eq. 5.10 is identical to Eq. 5.7. Comparison to experimental data, shown in Fig. 5.4d, is found to be good. The departure from the perfect agreement of Section 5.3.1 will be discussed in Section 5.3.3. The observed phase shift is distinct from Eq. 5.8 and now also depends on r_{m}:

$$\phi = \arctan\left(\frac{R_m}{2}\left(\frac{1 - \alpha_{\mathrm{m}}}{1 + \alpha_{\mathrm{m}} \frac{R_m^2}{4}}\right)\right) \tag{5.11}$$

Again corrections of $\mathcal{O}(\alpha_{\mathrm{m}})$ exist, and these tend to reduce the amount of phase shift observed. Similarly, in the limit of $r_{\mathrm{m}} \mapsto r_b$, Eq. 5.11 is identical to Eq. 5.8. Excellent agreement of Eq. 5.11 with experimental data is shown in Fig. 5.4e. Unlike the case of external forcing, the effect of the rotating wall on Eqs. 5.10-5.11 depends on r_{m} and is most pronounced at $r_{\mathrm{m}} = r_b$. Also note that this field contains a finite electromagnetic torque if $R_m \neq 0$.

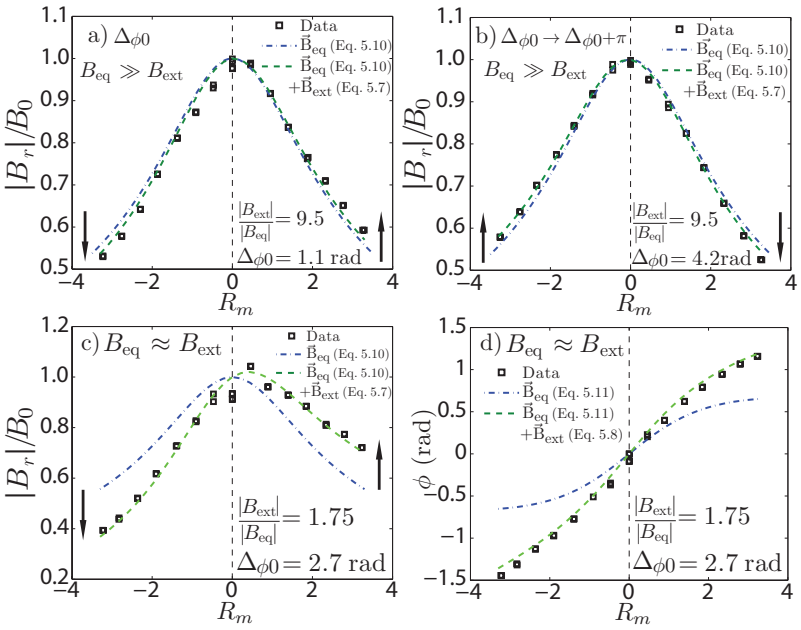

Figure 5.5: Asymmetry in R_m in (a) flux exclusion in the presence of both $\vec{B}_{\text{eq}}$ (conducting rod only) and $\vec{B}_{\text{ext}}$. For a given $\Delta_{\phi 0}$, flux exclusion is reduced at $R_m > 0$ while (b) changing $\Delta_{\phi 0} \mapsto \Delta_{\phi 0} + \pi$ reverses the asymmetry. (c)-(d) With suitably chosen $\vec{B}_{\text{ext}}$, $\vec{B}_{\text{eq}}$, and $\Delta_{\phi 0}$, the asymmetry can become very large and overwhelm the shielding effect of wall rotation.

5.3.3 Superposition of Error Fields and Asymmetric Response

The difference between the response to $\vec{B}_{\text{ext}}$ and $\vec{B}_{\text{eq}}$ in flux exclusion (Eq. 5.7 vs Eq. 5.10) and phase shift (Eq. 5.8 vs Eq. 5.11) gives rise to an asymmetry in wall rotation direction. To illustrate this simply, the linear superposition of $\vec{B}_{\text{ext}}$ and $\vec{B}_{\text{eq}}$ is checked for parity. $\vec{B}_{\text{ext}} = B_{\text{ext}} \exp\left(i(\phi_e(R_m) - \phi_{0e})\right)$ and $\vec{B}_{eq} = B_{\text{eq}} \exp\left(i(\phi_i(R_m) - \phi_{0i})\right)$, where $\phi_e(R_m)$ is Eq. 5.8 and $\phi_i(R_m)$ is Eq. 5.11. All amplitude information (Eqs. 5.7 and 5.10) is ignored for simplicity and both source terms are separated at $R_m = 0$ by an angle

$\Delta_{\phi 0} \equiv \phi_{0e} - \phi_{0i}$. Parity at $+R_m$ and $-R_m$ is checked:

$$\begin{aligned} &= \left|\vec{B}_{\text{ext}} + \vec{B}_{eq}\right|^2_{+R_m} - \left|\vec{B}_{\text{ext}} + \vec{B}_{eq}\right|^2_{-R_m} \\ &= 2B_{\text{ext}}B_{\text{eq}}\left(\cos\left(\Delta_\phi - \Delta_{\phi 0}\right) - \cos\left(-\Delta_\phi - \Delta_{\phi 0}\right)\right) \\ &= 4B_{\text{ext}}B_{\text{eq}}\sin\left(\Delta_\phi\right)\sin\left(\Delta_{\phi 0}\right) \end{aligned} \tag{5.12}$$

where $\Delta_\phi \equiv \phi_e(R_m) - \phi_i(R_m)$ is the difference between Eqs. 5.8 and 5.11. Since $\Delta_\phi \neq 0$, Eq. 5.12 is non-zero. Asymmetry in R_m is maximized when $\Delta_{\phi 0} = \pm\frac{\pi}{2}$.

This asymmetry is demonstrated experimentally by pulsing $\vec{B}_{\text{ext}}$ and $\vec{B}_{\text{eq}}$ simultaneously. Inclusion of both $\vec{B}_{\text{ext}}$ and $\vec{B}_{\text{eq}}$ using the full vector superpositions of Eqs. 5.6-5.11 is shown in Fig. 5.5a-b for two different $\Delta_{\phi 0}$, each separated by π. Changing $\Delta_{\phi 0}$ by π is done by repositioning the conducting rod (changing the angle η in Fig. 5.2b). The resultant asymmetry in flux exclusion is captured by the model, as is the asymmetry reversal as $\Delta_{\phi 0} \mapsto \Delta_{\phi 0} + \pi$. Note that Fig. 5.5b shows the same data of Fig. 5.4d, where much better agreement is found when $\vec{B}_{\text{ext}}$ is included. Although in Fig. 5.5a-b this asymmetry is a small correction, it can be made large if $B_{\text{eq}} \approx B_{\text{ext}}$, as shown in Fig. 5.5c-d. If $B_{\text{eq}} \approx B_{\text{ext}}$ and $\Delta_{\phi 0} \approx \pi$, as would be the case if external currents were used to correct the misalignment of the magnetic axis [71], increasing R_m would increase the error field significantly.

5.3.4 Asymmetric Response in Plasma Discharges

Strong asymmetry in R_m is also observed when the conducting rod is replaced with a stable plasma. Low current, stable plasmas are used to isolate the interaction of equilibrium currents ($\vec{B}_{\text{eq}}$) with $\vec{B}_{\text{ext}}$ without considering MHD instabilities. Figure 5.6 illustrates large asymmetry in plasma discharges. The scatter in the data is also larger due to the poorer reproducibility of the plasma discharge. Figure 5.6a-b illustrates a response

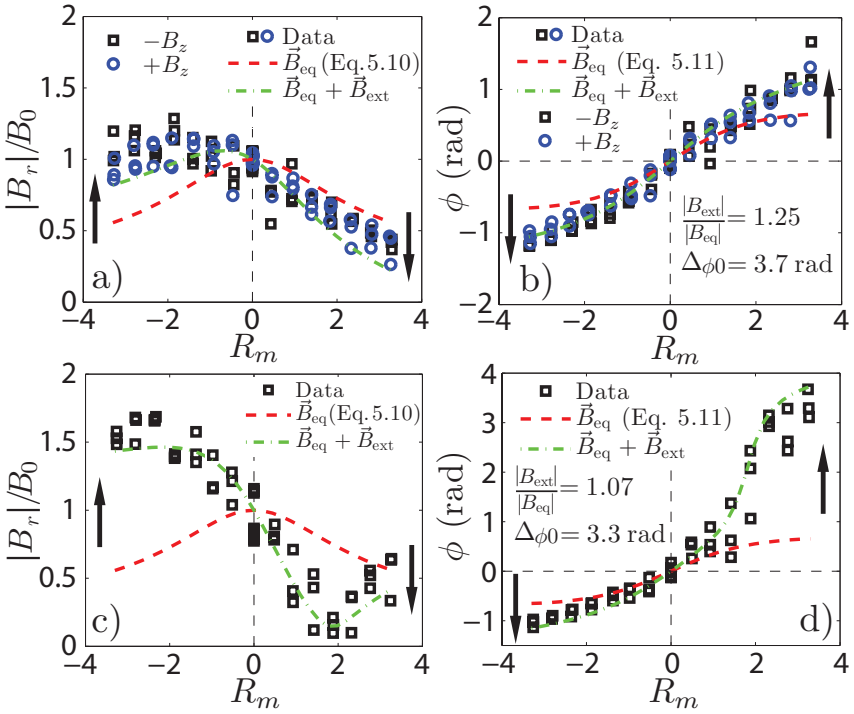

Figure 5.6: Error field asymmetries in R_m in stable plasma discharges. Amplitude (a) and phase (b) of the total error field is found to be asymmetric in R_m, and the asymmetry is invariant to B_z reversal. Amplitude (c) and phase (d) indicate that extreme asymmetries are possible depending on the alignment of $\vec{B}_{ext}$ to $\vec{B}_{eq}$.

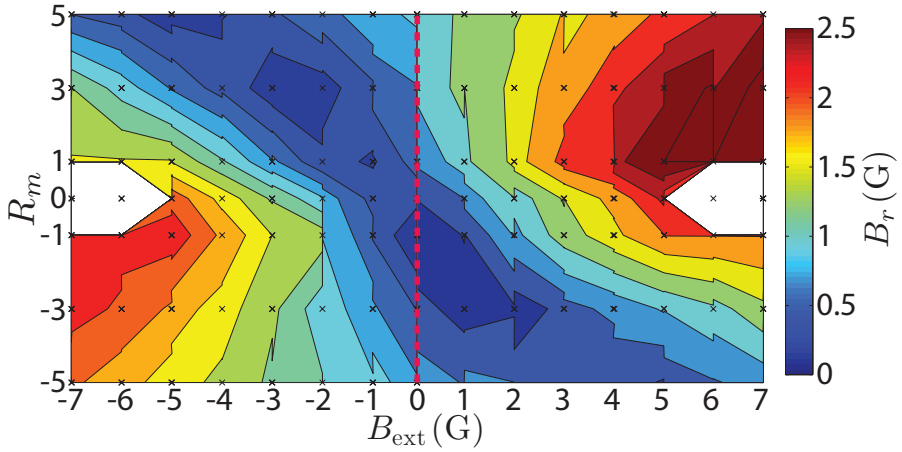

Figure 5.7: Contour plot of measured radial magnetic field (B_r) as B_{ext} and R_m are varied. The error field asymmetry in R_m is inverted upon B_{ext} reversal. Operation limits prevented data collection at large B_{ext} and low R_m.

approaching linearity in R_m, and the interactions of the error fields with the rotating wall is clearly a zeroth order effect. The error field asymmetry is found to be invariant with guide field (B_z) reversal, thus ruling out plasma drift effects. Figure 5.6c-d illustrates another plasma case where the constructive and destructive interference between $\vec{B}_{\text{ext}}$ and $\vec{B}_{\text{eq}}$ is dramatically demonstrated. A minimum in the total amplitude occurs at $R_m \approx 2$, which the model can capture with suitable selection of free parameters $B_{\text{ext}}/B_{\text{eq}}$ and $\Delta_{\phi 0}$. A wide family of curves can be generated depending on the values of $B_{\text{ext}}/B_{\text{eq}}$ and $\Delta_{\phi 0}$.

Figure 5.7 illustrates the odd parity of the asymmetric interaction with R_m and $\vec{B}_{\text{ext}}$. While the asymmetry in R_m is present at all B_{ext}, its sense (or parity) is inverted as $\vec{B}_{\text{ext}}$ is reversed. That the asymmetry was not reversed upon inversion of B_z, yet was inverted with $\vec{B}_{\text{ext}}$ gives confidence that even in the presence of a (stable) plasma, the error field interaction can be well described by the linear superposition of B_{ext} and B_{eq}. That is, the stable plasma (Fig. 5.6) can be described by the same model as the conducting rod (Fig. 5.5). The unstable plasma will be treated in Chapter 7 and the effectiveness of this model will be further discussed in Section 5.5.

5.4 Vacuum Field Eigenmodes and Vertical Field Penetration

Normal mode analysis is used to derive the time-dependent behavior of the device error fields and corroborates the experimental observation that the vertical field penetration time (τ_{vfp}) decreases as R_m increases. As all equations used in Section 5.2 are linear in $\vec{B}$, the system can be expressed as an eigenvalue equation with corresponding eigenvalues and eigenvectors (normal modes) in the absence of any forcing (current sources). The normal modes of multiple wall systems will be considered, beginning with the limiting cases of a single wall and static double walls, then proceeding to the differentially rotating system

and concluding with the three-wall system necessary to match experimental data.

To solve the normal modes of the system, a matching problem is carried out in a similar style to that of Section 5.3, where now exponential time dependence is introduced ($Q(t) \propto Qe^{-\gamma t}$, for any Q). The two-wall geometry of Fig. 5.1b is used. The field solutions are:

$$\begin{aligned} I &: B_r(r,\theta,t) = \Re\left[A_0 e^{-i\theta}\right] \\ II &: B_r(r,\theta,t) = \Re\left[(A_1 - A_2 r^{-2})e^{-i\theta}\right] \\ III &: B_r(r,\theta,t) = \Re\left[(-A_3 r^{-2})e^{-i\theta}\right] \end{aligned}$$

The matching conditions of Eqs. 5.3-5.4 yields a 4x4 matrix equation for the 4 unknown parameters:

$$\begin{bmatrix} -1 & 1 & -r_a^{-2} & 0 \\ \gamma\tau_a - 1 & 1 & r_a^{-2} & 0 \\ 0 & 1 & -r_b^{-2} & r_b^{-2} \\ 0 & r_b^2 & 1 & (\gamma + i\Omega_w)\,\tau_b - 1 \end{bmatrix} \begin{bmatrix} A_0 \\ A_1 \\ A_2 \\ A_3 \end{bmatrix} = 0 \tag{5.13}$$

Setting the determinant of the matrix of Eq. 5.13 to zero yields the characteristic equation:

$$(\tau_a\tau_b\alpha)\,\gamma^2 - (2\,(\tau_a + \tau_b) - i\Omega_w\tau_a\tau_b\alpha)\,\gamma + 2\,(-2 + i\Omega_w\tau_b) = 0 \tag{5.14}$$

where defining $\alpha \equiv \frac{r_b^2 - r_a^2}{r_b^2}$ replaces the geometry of the problem with a normalized mutual inductance. Two normal modes exist, and a single equation for the roots of Eq. 5.14 can

be written:

$$\gamma = \frac{\tau_a + \tau_b}{\tau_a \tau_b \alpha} - i\frac{\Omega_w}{2} \pm \frac{1}{\tau_a \tau_b \alpha}\left[(\tau_a + \tau_b)^2 - 4\tau_a\tau_b\alpha - \frac{\Omega_w^2}{4}(\tau_a\tau_b\alpha)^2 + i\Omega_w\tau_a\tau_b\alpha(\tau_b - \tau_a)\right]^{\frac{1}{2}} \tag{5.15}$$

decomposing into real and imaginary terms:

$$\gamma^{\mathrm{r}} = \frac{\tau_a + \tau_b}{\tau_a\tau_b\alpha} \pm \frac{(\kappa_r^2 + \kappa_i^2)^{\frac{1}{4}}}{\tau_a\tau_b\alpha}\cos\left(\frac{1}{2}\arctan\left(\frac{\kappa_i}{\kappa_r}\right)\right) \tag{5.16}$$

$$\omega = -\frac{\Omega_w}{2} \pm \frac{(\kappa_r^2 + \kappa_i^2)^{\frac{1}{4}}}{\tau_a\tau_b\alpha}\sin\left(\frac{1}{2}\arctan\left(\frac{\kappa_i}{\kappa_r}\right)\right) \tag{5.17}$$

$$\kappa_r \equiv (\tau_a + \tau_b)^2 - 4\tau_a\tau_b\alpha - \frac{\Omega_w^2}{4}(\tau_a\tau_b\alpha)^2$$

$$\kappa_i \equiv \Omega_w\tau_a\tau_b\alpha(\tau_b - \tau_a)$$

To explore the behavior of Eqs. 5.15-5.17, limiting cases with respect to rotation (Ω_w) and mutual inductance (α) are explored separately.

5.4.1 Single Wall Limit

The simplest case to consider is that of Fig. 5.1a, with only a single wall which is allowed to rotate. This is achieved by letting $\tau_a \mapsto 0$ in Eq. 5.15. In this limit, only a single root remains, which is given by:

$$\gamma = \frac{2}{\tau_b} - i\Omega_w \tag{5.18}$$

The real part of this eigenvalue ($\Re[\gamma] \equiv \gamma^{\mathrm{r}} \equiv \frac{1}{\tau_{\mathrm{vfp}}} = \frac{2}{\tau_a}$) is the unique time constant characterizing eddy current decay (and thus vertical field penetration) in the single wall system. Furthermore, γ^r does not depend on Ω_w; wall rotation in the single wall case merely transforms the normal mode into a rotating frame with $\omega = \Omega_w$. The eigenfunction

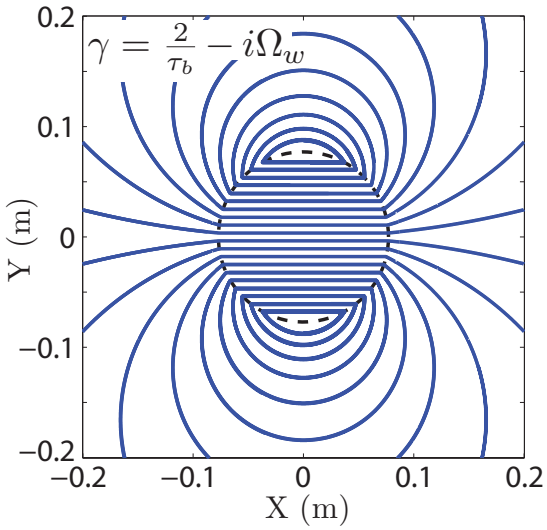

Figure 5.8: Fieldlines of $\vec{B}$ produced by the eddy current eigenfunction in a single wall. Current flows into and out of the page as $J_z \propto \delta(r - r_w)\exp(-i\theta)$, producing a constant field within the wall and dipolar field beyond. This structure is independent of rotation for the single wall case.

(field structure) is given by: $A_0 = A_1 = -r_b^{-2}A_3, A_2 = 0$, which yields a dipole-like solution as shown in Fig. 5.8. As this is an infinite-length model, the wall eddy currents flow purely into and out of the page, while in a finite-length wall these currents must close at the ends giving rise to fringing fields.

5.4.2 Static Double Wall Limit

In the limit of no rotation ($\Omega_w \mapsto 0$), Eq. 5.15 becomes:

$$\gamma = \frac{1}{\tau_a\tau_b\alpha}\left[\tau_a + \tau_b \pm \left[(\tau_a + \tau_b)^2 - 4\alpha\tau_a\tau_b\right]^{\frac{1}{2}}\right] \tag{5.19}$$

To begin, the large gap limit of $\alpha \mapsto 1$, $r_b \gg r_a$ is also taken. In this limit, $\gamma = \left\{\frac{2}{\tau_a}, \frac{2}{\tau_b}\right\}$ and each normal mode is independently tied to its own wall and has the single wall time constant of Eq. 5.18. Thus, α behaves as a mutual inductance between the two walls. Fig. 5.9 shows the behavior of γ as $\alpha \neq 1$. Both γ diverge from their decoupled values and

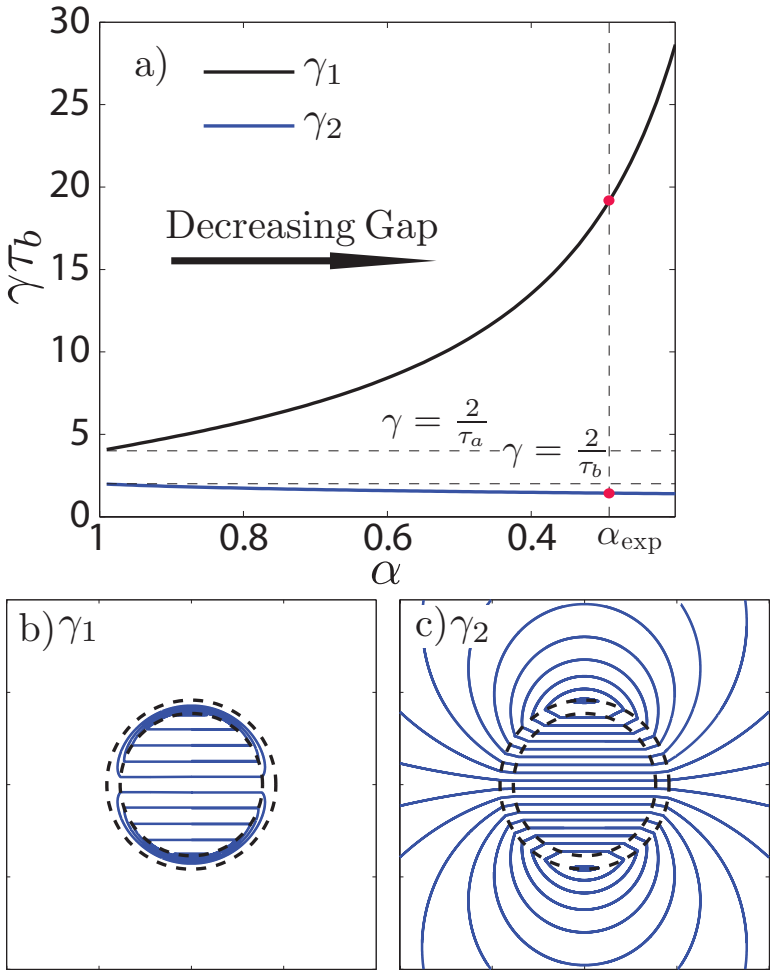

Figure 5.9: (a) Time constants (eigenvalues) of the static two-wall normal modes as the coupling parameter α varies. (b)-(c) Eigenstructure of the normal modes of (a). The fast (slow) root field structure does not (does) extend beyond the outer wall and thus represents counter- (co-) directed currents within each wall respectively.

a fast and slow root develops. For experimental parameters, $\gamma_1 \approx 10\gamma_2$. The asymptote of strong coupling (small gap, $\alpha \mapsto 0$) corresponds to the same solution as a single wall system with $\tau = \tau_a + \tau_b$ and the fast root decaying infinitely quickly.

For weak coupling ($\alpha \mapsto 1$), the eigenfunctions are the same as Fig. 5.8. Eigenfunctions with the coupling parameter set to that of the experiment ($\alpha_{\text{exp}} = 0.3$) are next considered. As shown in Fig. 5.9b-c, the γ_1 (fast) eigenfunction is confined to within the two-wall system, while the γ_2 (slow) eigenfunction is dipolar everywhere. In terms of induced eddy currents, the γ_1 currents are counter-aligned in each wall, while the γ_2 currents are co-aligned, thus they can be thought of as opposing and reinforcing dipoles, respectively. Qualitatively, this is reminiscent of the coupled oscillator, whose eigenmodes are symmetric and anti-symmetric oscillations.

5.4.3 Effect of Wall Rotation

Wall rotation is now reintroduced, necessitating the full form of Eqs. 5.16-5.17 and yielding complex eigenvalues ($\gamma \equiv \gamma^{\text{r}} + i\omega$). The value of Ω_w now affects both γ^{r} as well as ω, as shown in solutions for experimental parameters plotted in Fig. 5.10a. Increasing R_m brings the two eigenvalues toward each other. Eigenfunctions are shown in Fig. 5.10b-c for the intermediate rotation case. Rotation is seen to phase shift the eigenfunctions in opposite directions. As with the static solution, one eigenfunction penetrates the outer wall while the other does not.

With $\Omega_w \mapsto \infty$ in Eqs. 5.16-5.17, $\gamma = \left\{ \frac{2}{\tau_a \alpha}, \frac{2}{\tau_b \alpha} - i\Omega_w \right\}$. The corresponding eigenfunctions are shown in Fig. 5.10d-e. The γ_1 eigenfunction is found to decay at a geometrically weighted τ_a timescale, and does not extend into the rotating wall. Similarly, the γ_2 eigenfunction does not see the static wall, and as such it rotates at $\omega = \Omega_w$ and decays at a geometrically weighted τ_b timescale. The phase shifts have also reached an asymptotic limit of $\phi = \frac{\pi}{2}$. The fast rotation limit is thus seen to decouple the two walls, acting oppo-

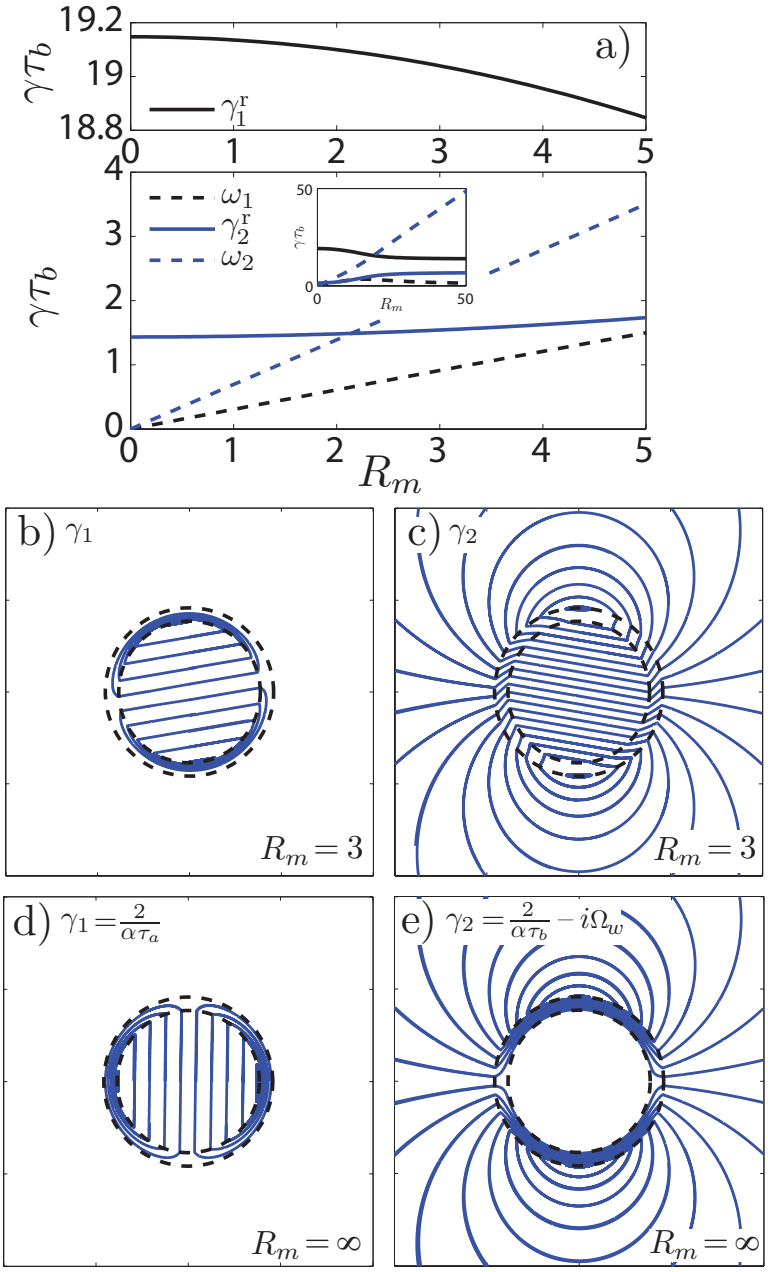

Figure 5.10: (a) Real (γ^r) and imaginary (ω) time constants of the two-wall normal modes with $\Omega_w \neq 0$ ($R_m \equiv \Omega_w \tau_b$). Eigenfunctions of (b) the fast root and (c) the slow root at intermediate R_m. Eigenfunctions of (d) the fast root and (e) the slow root as $\Omega_w \mapsto \infty$.

site to the coupling parameter α. The α parameter splits the eigenvalues into a slow and fast branch, while rotation brings both branches back to their (geometrically weighted) single wall values.

5.4.4 Three-Wall Eigenmodes and Comparison to Experiment

As discussed in Section 5.2, a three-wall system is required to adequately capture experimental vertical field penetration data. The geometry (to scale) is presented in Fig. 5.1c, with the third (outermost) wall corresponding to the mechanical support structure. Fields for this geometry must be of the form:

$$
\begin{aligned}
I : B_r(r,\theta,t) &= \Re\left[A_0 e^{-i\theta}\right] \\
II : B_r(r,\theta,t) &= \Re\left[(A_1 - A_2 r^{-2}) e^{-i\theta}\right] \\
III : B_r(r,\theta,t) &= \Re\left[(A_3 - A_4 r^{-2}) e^{-i\theta}\right] \\
IV : B_r(r,\theta,t) &= \Re\left[(-A_5 r^{-2}) e^{-i\theta}\right]
\end{aligned}
$$

the matching conditions of Eqs. 5.3-5.4 are applied, which then forms a 6X6 matrix equation for the unknown A_n. For brevity, only the characteristic equation yielded by setting the determinant to zero is shown:

$$
\begin{aligned}
0 &= a\gamma^3 + b\gamma^2 + c\gamma + d \qquad (5.20) \\
a &= \tau_a\tau_b\tau_c\alpha_1\alpha_2 \\
b &= 2\left(\tau_a\tau_b\alpha_1 + \tau_b\tau_c\alpha_2 + \tau_a\tau_c\alpha_{12}\right) + i\Omega_w\tau_a\tau_b\tau_c\alpha_1\alpha_2 \\
c &= 4(\tau_a + \tau_b + \tau_c) + i2\Omega_w\left(\tau_a\tau_b\alpha_1 + \tau_b\tau_c\alpha_2\right) \\
d &= 4(-2 + i\Omega_w\tau_b)
\end{aligned}
$$

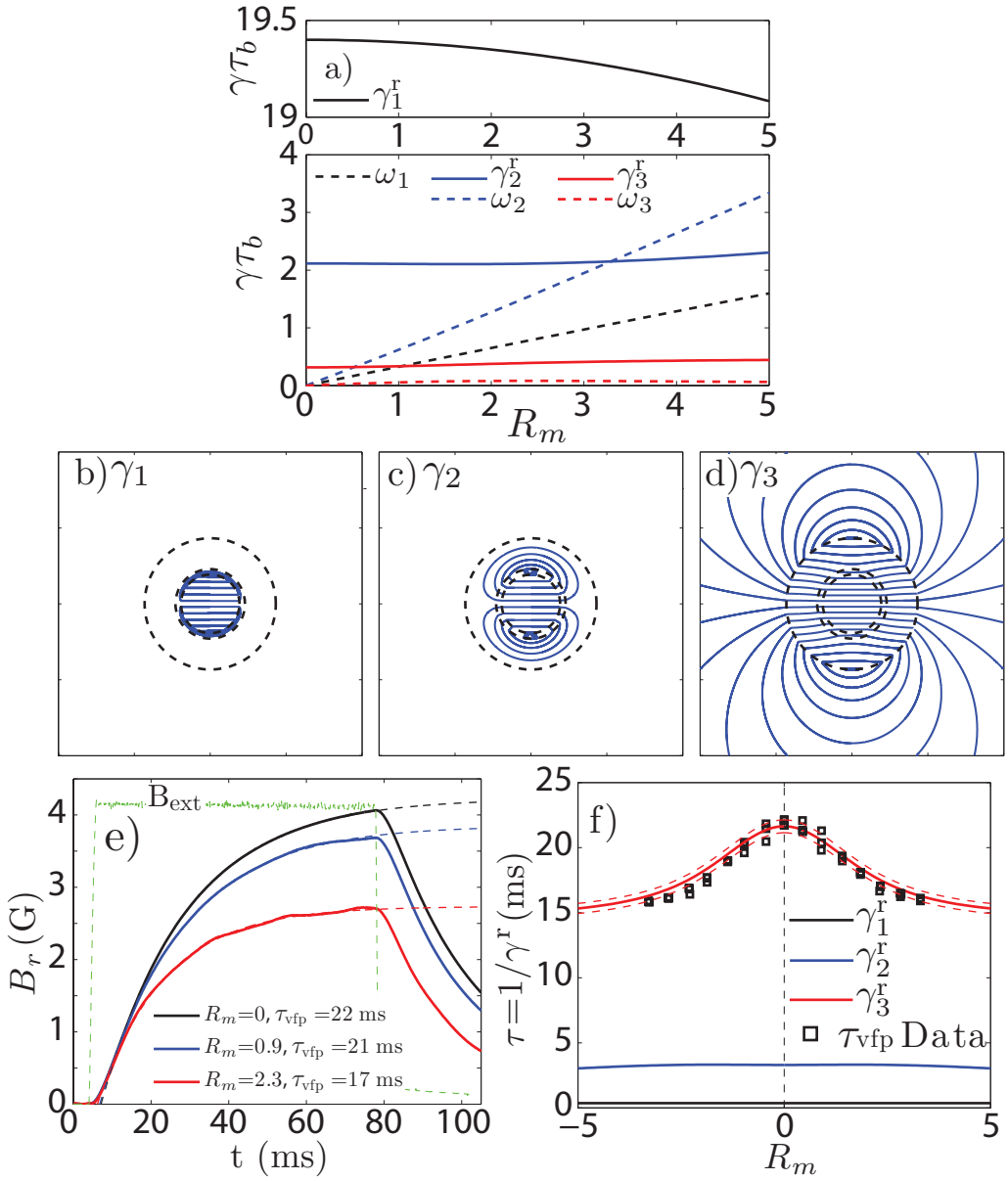

Figure 5.11: (a) Eigenvalues of the three-wall normal modes. (b)-(d) Eigenfunctions of each root with $\Omega_w = 0$. (e) Experimental excitation of the normal modes pulsing $\vec{B}_{\text{ext}}$ and resultant measurement of the vertical field penetration time (τ_{vfp}). (f) Comparison of τ_{vfp} with γ_3^{r} evaluated using the experimental parameters of Table 5.1. Dotted lines in (f) are evaluated with $\tau_c \pm 2\%$.

Again, coupling parameters are defined which simplify the geometry: $\alpha_1 \equiv \frac{r_a^2 - r_b^2}{r_b^2}$, $\alpha_2 \equiv \frac{r_b^2 - r_c^2}{r_c^2}$, $\alpha_{12} \equiv \frac{r_a^2 - r_c^2}{r_c^2}$. Beyond these simplifications, analytic forms for the three roots of Eq. 5.20 are prohibitively lengthy and are not shown. Solutions of Eq. 5.20 are shown in Fig. 5.11a and indicate that rotation affects the three-wall eigenvalues in broadly the same manner as the two-wall eigenvalues of Section 5.4.3. For experimental parameters, there is one fast root which decreases as R_m increases, and two slow roots which increase as R_m increases. Eigenfunctions at $R_m = 0$ are shown in Fig. 5.11b-d and illustrate that the fastest root γ_1 does not penetrate the second (rotating) wall, the middle root γ_2 does not penetrate the third wall, while the slowest root γ_3 penetrates all walls.

The inclusion of the third wall permits quantitative comparison to experiment. The normal modes are experimentally excited by the application of a square-wave B_{ext} pulse, yielding the time-traces of Fig. 5.11e. The steady-state response created by this excitation has already been discussed in Section 5.3.1. Focusing on the time-dependent behavior shows that the vertical field penetration time (τ_{vfp}) decreases as R_m increases. As γ_3 is the most persistent eddy current, it dominates the measurement a short time after the current pulse turn-on. Figure 5.11f confirms the counter-intuitive result that increasing wall rotation (Ω_w) *decreases* τ_{vfp}. The slowest root of Eq. 5.20 matches the τ_{vfp} data very closely despite the fact that there are no free parameters. The dotted lines in Fig. 5.11f plot the γ_3^r root with τ_c varied by $\pm$ 1 ms (or 2%), which is sufficient to bound the data.

5.5 Discussion

This Chapter used the long-thin approximation to derive analytic relationships for device error fields which experiment then confirmed. The error field from external conductors and equilibrium plasma currents are found to behave differently, giving rise to potentially significant asymmetries in wall rotation direction. Later Chapters will show that error

field interactions (and their asymmetries) were the zeroth order effect of wall rotation on plasma dynamics, complicating instability studies and necessitating an alignment campaign to minimize the intrinsic error fields. In fact, this asymmetry was initially misinterpreted as asymmetric stabilization of the kink instability in the device, until experiments with the conducting rod revealed their independence from the plasma. Although toroidal effects are not included here, it is likely that future devices with flowing liquid metals may also exhibit similar asymmetries. A treatment of the same problem while relaxing the thin-wall approximation is found in Appendix C.

Section 5.3.4 illustrated that the model developed to treat rigid conductors was also successful in capturing the asymmetries observed in stable plasma discharges. Vacuum superposition of $\vec{B}_{\text{ext}}$ and $\vec{B}_{\text{eq}}$ assumes that the two are independent of one-another. This is not a-priori guaranteed as the plasma can respond (move) due to $\vec{B}_{\text{ext}}$ while the rigid rod cannot. That the vacuum superposition is valid for the stable plasma as well as the rigid conducting rod reinforces the point that there is no appreciable modification of the error field by the stable plasma.

The result that the vertical field penetration time decreases as wall rotation increases is counterintuitive. Although infinite wall rotation yields a 'perfectly conducting' wall, it does not simply increase the effective wall time. This Chapter has shown that careful consideration of the multi-wall couplings is essential to build intuition on the effect of differential rotation on field eigenmodes. In the limit of an infinite number of walls, these results are reminiscent of the flowing liquid metal dynamo problem, where expected growth/decay constants are very sensitive functions of the flow profiles [72]. It is also clear that the success of the simple model to capture the experimental τ_{vfp} data indicates that the long-thin cylinder approximations made are very good.

With the impact of the rotating wall on device error fields well understood, it is possible to begin to discuss the problem of RWM stability in the presence of both an

error field and the rotating wall. To do this, several experiments were done at 'constant error field'. This utilized the understanding of this section to tailor the current in the error field coil such that the apparent error field felt by the plasma was constant. The following Chapters will stress the importance of this technique to elucidate the varied effects of the rotating wall on RWM stability.

Chapter 6

Torque Balance and Mode-Locking of the External Kink

Wall-locking of an MHD mode is found for the first time in a linear device. The effect of the rotating wall on mode-locking is studied experimentally and compared to a torque balance model which has been extended to include differential wall rotation. Wall rotation is predicted to asymmetrically affect the mode-unlocking threshold, with fast rotation eliminating the locking bifurcation. Static error fields are observed to lock the resistive wall mode (RWM) variant of the current driven kink instability by modifying the electromagnetic torque.

6.1 Motivation

Resistive wall modes (RWMs) often grow from a flowing plasma, and this experiment is no exception. Plasma flow is important to RWM stability, as RWMs entrained in a rapidly flowing plasma can rotate with frequency $\omega \gg \tau_w^{-1}$ and be passively stabilized by the wall [10, 18], as was discussed in Chapter 1. In certain regimes, the RWM discontinuously transitions from a rotationally stabilized RWM to a stationary ($\omega \approx 0$) 'locked' RWM followed by subsequent fast growth with $\gamma^{-1} \propto \tau_w$ [73]. For this reason, experimental

observations of RWM onset conditions are often convolutions of RWM stability criteria and mode-locking thresholds [26]. Thus, in order to understand RWM onset in the device it is also necessary to explore the process by which mode-locking occurs including the effect of the rotating wall.

In this Chapter, the effect of physically rotating walls on mode-locking is tested experimentally and interpreted using a torque balance model that accounts for both errors fields and wall rotation. Plasma rotation yields a kHz-scale rotating RWM which must be slowed or locked to observe the interaction of the instability with the rotating wall. Braking and locking is shown to be achieved with static $m = 0$ and $m = 1$ error fields, yielding the first observation of MHD mode-locking in a linear device. These effects are interpreted with a commonly used torque balance model [21, 22, 23] which is adapted to this experiment. This model is further extended to treat differential wall rotation using the thin-wall, long-cylinder approximation. Wall rotation is found to Doppler shift the mode-locking threshold. However, a much larger effect is predicted for the mode-unlocking threshold, and asymmetry in wall rotation direction is also predicted. The extended model is then used to fit mode-locking observations in the presence of the rotating wall.

The structure of this Chapter is as follows: Section 6.2 derives and describes the torque balance equation used to model mode-locking in the experiment. Section 6.3 applies this model to describe experimental observations of mode-locking by $m = 0$ and $m = 1$ static error fields. Mode-locking in the presence of wall rotation is treated in Section 6.4. Discussion of results is presented in Section 6.5.

6.2 Mode-Locking Model and Free Parameters

In order to model azimuthal RWM rotation in the experiment, total torques on a rigidly rotating plasma are calculated. As described in Section 2.4, the device plasma is very cold and dense. Thus, its collisionality is very large and the MHD mode is taken to be fully entrained in the plasma flow such that the mode frequency ω is equal to the plasma rotation frequency. To simplify the analysis, the plasma is taken to be a rigid-rotor, such that everywhere the plasma rotates at a single frequency ω and $V_\theta = r\omega$. Data presented in Section 2.4.4 showed that this was a satisfactory approximation in the core of the device. Rigid-body rotation is also indicative of a large viscosity, as will be discussed in Section 6.5. The total torques on the plasma can thus be evaluated:

$$\hat{z} \cdot \int_{\mathcal{V}} \vec{r} \times \left[\rho \left(\frac{\partial \vec{V}}{\partial t} + \vec{V} \cdot \nabla \vec{V} \right) \right] d\mathcal{V} = \hat{z} \cdot \int_{\mathcal{V}} \vec{r} \times \left[-\nabla p - \nabla \cdot \bar{\bar{\Pi}} + \nabla \cdot \bar{\bar{T}} \right] d\mathcal{V} \tag{6.1}$$

where ρ is the density, p is the pressure, and $\bar{\bar{\Pi}}$ and $\bar{\bar{T}}$ are the viscous and Maxwell stress tensors. The integral is performed over a cylindrical volume $\mathcal{V}$ enclosed by a surface $\mathcal{S}$ of length L and radius r_a outside of the plasma but just inside the first wall. As $r_a/L \approx 10$, the large aspect ratio approximation allows the end-caps to be neglected due to their small contribution to $\mathcal{S}$. As $\mathcal{S}$ is outside the plasma, the pressure and viscous stress terms vanish. Using the rigid-rotor approximation, the advection term also vanishes. The inertial term is equal to $I_{zz}\dot{\omega}$, where I_{zz} is the moment of inertia of the rigidly rotating plasma, and can be shown to be small relative to the remaining electromagnetic term. Using the divergence theorem and as the end caps are neglected in $\mathcal{S}$, the remaining term in Eq. 6.1 can be written:

$$0 = r_a \int_{\mathcal{S}} \hat{\theta} \cdot \frac{1}{\mu_0} \left[\vec{B}\vec{B} - \frac{1}{2} B^2 \bar{\bar{I}} \right] \cdot d\mathcal{S} \tag{6.2}$$

and as $\hat{\theta} \perp d\mathcal{S}$ the second term vanishes. The magnetic field is written as $\vec{B} = \vec{B}_0 + \vec{B}_{\text{ext}} + \tilde{B}_{\text{mode}} \exp(-i\phi)$, where $\vec{B}_0$, $\vec{B}_{\text{ext}}$, $\tilde{B}_{\text{mode}}$ is the equilibrium, error, and RWM field respectively, and $\phi \equiv \int_0^t \omega(t')dt' + \phi_0$. $\vec{B}_0$ is taken to be axisymmetric ($m = 0$) while the $\vec{B}_{\text{ext}}$ and $\tilde{B}_{\text{mode}}$ are non-axisymmetric ($m = 1$). Each magnetic field source produces a contribution to the torque balance relation, and these are calculated in Secs. 6.2.1-6.2.3. Summing these contributions results in a torque balance equation of the form:

$$0 = \underbrace{A_{\text{res}}(\Omega_0 - \omega)}_{\Gamma_{\text{res}}} + \underbrace{A_{\text{ext}} \sin(\phi)}_{\Gamma_{\text{ext}}} - \underbrace{A_{EM} \frac{R_a R_b^2 \alpha^2 + 4\left(R_a + R_b(\alpha+1)\right)}{(4 + R_a R_b \alpha)^2 + 4(R_a + R_b)^2}}_{-\Gamma_{EM}} \tag{6.3}$$

where Γ_{res}, Γ_{ext}, and Γ_{EM} are electromagnetic torques arising from the restoring torque to a 'natural' frequency Ω_0, the mode-error field interactions, and the the mode-wall interactions, respectively. Within Γ_{EM}, $R_a \equiv \omega\tau_a$, $R_b \equiv (\omega - \Omega_w)\tau_b$, $\alpha \equiv (r_a^2 - r_b^2)/r_b^2$, and τ_a, r_a, τ_b, r_b are the wall time and radius of the inner and outer wall respectively and Ω_w is the wall angular velocity. Γ_{ext} and Γ_{EM} can be measured using magnetic flux-loops [74], leaving Ω_0 and A_{res} as the free parameters in the model. Equation 6.3 is quintic in ω and will be shown to be multi-valued, with rotating $\omega \approx \Omega_0$ and locked $\omega \approx 0$ solutions as well as bifurcations (mode-locking) between the two occurring at a critical ω_{lock} which can also be measured. The combined measurements of ω_{lock}, Γ_{EM} and Γ_{ext} are sufficient to uniquely determine both Ω_0 and A_{res}, thus these parameters are not fit but rather calculated for a given discharge.

6.2.1 Derivation of Two-Wall Electromagnetic Torque

The electromagnetic torque from interactions of the RWM mode fields with the resistive wall is treated rigorously and can be directly measured experimentally [74, 75]. The non-axisymmetric part of $\vec{B}$ in Eq. 6.2 will be considered and subsequently cycle-averaged. Cycle-averaging eliminates cross terms like $\vec{B}_{\text{ext}}\tilde{B}_{\text{mode}}$ and these will be considered sepa-

rately in Sec. 6.2.2. The integral to be evaluated is thus:

$$\Gamma_{EM} = \frac{r_a^2 L}{\mu_0} \int_0^{2\pi} \left\langle \tilde{B}_{\mathrm{mode},\theta} \tilde{B}_{\mathrm{mode},r} \right\rangle d\theta \tag{6.4}$$

where $\langle \cdots \rangle$ denotes a cycle-average. Note that integration in θ would drop terms that scale like $\vec{B}_0 \vec{B}_{\mathrm{ext}}$ or $\vec{B}_0 \tilde{B}_{\mathrm{mode}}$. To compute Eq. 6.4, Laplace's equation in the long-cylinder approximation is solved, showing that the magnetic field in the vacuum region between the plasma and the wall must take the form:

$$\begin{aligned} B_r(r,\theta) &= \Re\left[(A_j - A_k r^{-2}) e^{-i\theta}\right] \\ B_\theta(r,\theta) &= \Re\left[(-i(A_j + A_k r^{-2})) e^{-i\theta}\right] \end{aligned} \tag{6.5}$$

where A_j, A_k are complex coefficients. Computing Eq. 6.4 with this field structure yields:

$$\Gamma_{EM} = \frac{r_a^2 \pi L}{\mu_0} \Im\left[\left(A_j - A_k r_a^{-2}\right)\left(A_j^* + A_k^* r_a^{-2}\right)\right] \tag{6.6}$$

Note that there can be no torque unless there both A_j and A_k are non-zero, and there must be a phase shift between them. The phase shift between B_r and B_θ at the wall must thus differ from $\pi/2$, which is accomplished by eddy currents induced in the wall when $\omega \neq 0$. Note that for this reason terms arising from non-axisymmetric static fields like $\vec{B}_{\mathrm{ext}} \vec{B}_{\mathrm{ext}}$ in Eq. 6.2 yield no net torque. To evaluate Eq. 6.6, the coefficients A_j, A_k must be determined from knowledge of the geometry of the experiment. A matching problem is carried out, where the fields in regions inside (I), in between (II), and outside (III) the

inner and outer wall are solved. From Eq. 6.5, these field structures are:

$$
\begin{aligned}
I : B_r(r,\theta) &= \Re\left[(A_0 - \tilde{b}r^{-2})e^{-i\theta}\right] \\
II : B_r(r,\theta) &= \Re\left[(A_1 - A_2 r^{-2})e^{-i\theta}\right] \\
III : B_r(r,\theta) &= \Re\left[(-A_3)r^{-2}e^{-i\theta}\right]
\end{aligned}
$$

where the B_θ component can be obtained from Eq. 6.5 for each region. A_n are complex coefficients and a fluctuating mode source $\tilde{b} \equiv \tilde{B}_{\text{mode}} r^2$ [T m^2] is the non-homogeneous part of the equation. Matching across the thin walls at r_a and r_b is accomplished using the well known thin-wall jump conditions obtained by integration of the induction equation across the wall at r_w, derived in Section 5.2.2.

$$
\begin{aligned}
B_r\big|_{r=r_w^-}^{r=r_w^+} &= 0 \\
B_\theta\big|_{r=r_w^-}^{r=r_w^+} &= -\Omega_w \tau_w B_r
\end{aligned}
$$

As $r_w/\delta_w \approx 100$ for both walls, the thin-wall approximation is valid for a wide range of ω in the experiment. Applying these conditions at r_a and r_b a matrix equation is formed for the unknown coefficients:

$$
\begin{bmatrix}
r_a^2 & -r_a^2 & 1 & 0 \\
-r_a^2 & (1+iR_a)r_a^2 & (1-iR_a) & 0 \\
0 & r_b^2 & -1 & 1 \\
0 & r_b^2 & 1 & (iR_b - 1)
\end{bmatrix}
\begin{bmatrix} A_0 \\ A_1 \\ A_2 \\ A_3 \end{bmatrix}
=
\begin{bmatrix} \tilde{b} \\ \tilde{b} \\ 0 \\ 0 \end{bmatrix}
$$

where $R_a \equiv \Omega_a \tau_a$, and $R_b \equiv \Omega_b \tau_b$. Inverting this matrix yields a unique solution for A_0, which upon substitution of $\{A_0, \tilde{b}\}$ for $\{A_j, A_k\}$ in Eq. 6.6 yields Γ_{EM} for the differentially

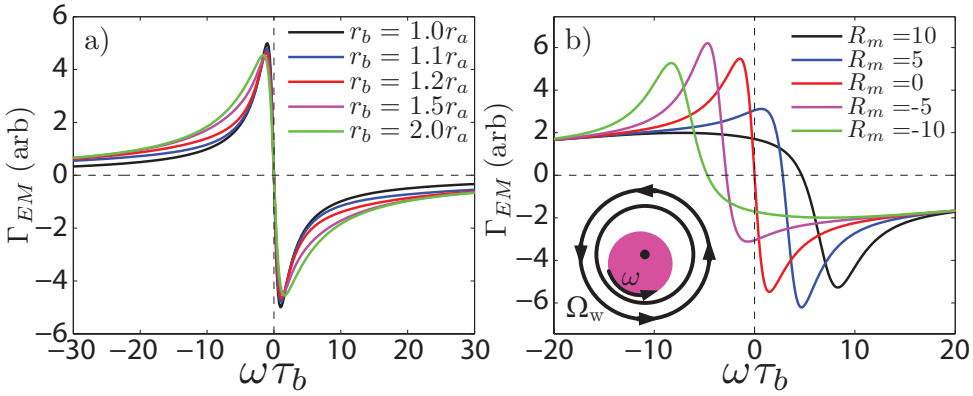

Figure 6.1: (a) Wall-induced electromagnetic torque (Γ_{EM}) plotted vs. plasma rotation normalized to the wall time ($\omega\tau_b$) for a variety of inter-wall spacings for equal τ_w walls ($\tau_a = \tau_b$). (b) Modifications to Γ_{EM} for co- and counter-rotation for a variety wall speeds (R_m) utilizing experimental values for τ_a, $\tau_b = 2\tau_a$, r_a, and $r_b = 1.2r_a$. $\hat{R}_m$ is set by the direction of the natural frequency (Ω_0).

rotating two-wall system:

$$\Gamma_{EM} = -4\left(\frac{\tilde{b}^2\pi L}{r_a^2\mu_0}\right)\frac{R_a R_b^2\alpha^2 + 4\left(R_a + R_b(\alpha+1)\right)}{(4 + R_a R_b\alpha)^2 + 4(R_a + R_b)^2} \tag{6.7}$$

which was first given in Eq. 6.3. The coefficient A_{EM} is thus identified to be $A_{EM} \equiv 4\left(\frac{\tilde{b}^2\pi L}{r_a^2\mu_0}\right)$ and is $\mathcal{O}(10^{-2})$ [N m] in the experiment. Eq. 6.7 is able to capture any combination of mode, inner wall, and outer wall rotation by suitable selection of Ω_a and Ω_b.

Properties of Two-Wall Electromagnetic Torque

The general double-wall torque of Eq. 6.7 can be easily transformed to a single-wall torque by letting $R_b \mapsto 0$. In this limit, Eq. 6.7 becomes:

$$\Gamma_{EM} = -\left(\frac{\tilde{b}^2\pi L}{r_a^2\mu_0}\right)\frac{\omega\tau}{1 + (\frac{\omega\tau}{2})^2} \tag{6.8}$$

which is a well known relation derived elsewhere [22, 23, 76, 74]. The change in Γ_{EM} as the gap between walls (α in Eq. 6.7) is increased is shown in Fig. 6.1a, with $\tau_a = \tau_b$ for simplicity (experimentally, $\tau_b = 2\tau_a$). For wall spacings beyond $r_b = 2.0r_a$, little change is seen in Γ_{EM}, indicating the weak coupling limit has been reached. It is found that for the wall spacing corresponding to the experiment ($r_b = 1.2r_a$), the single-wall model is a good approximation at low frequencies but becomes inaccurate at higher frequencies. This can be explained by noting that as $\omega\tau_b \gg 1$, only the inner wall participates as little flux penetrates to the outer wall, so $\Gamma_{EM} \propto (\omega\tau_a)^{-1}$. In general this is larger than the zero-gap limit where both walls participate, yielding a larger τ and smaller Γ_{EM}. Generally, the i^{th} element (with wall time τ_i) of multi-conductor systems can significantly increase Γ_{EM} in a local region around $\omega\tau_i \approx 1$, for example with discrete tiles lining a vacuum vessel [75].

The experimentally relevant effect of outer wall rotation on Γ_{EM} is explored by setting $\Omega_a = \omega$ and $\Omega_b = \omega - \Omega_w$. The result is shown in Fig. 6.1b, where now $R_m \equiv \Omega_w\tau_b$. While rotation of the single-wall model would rigidly Doppler-shift the curves of Fig. 6.1b, differential rotation is found to both Doppler-shift the curves and asymmetrically alter their shape. Co-rotation ($\hat{\Omega}_w = \hat{\omega}$) yields a larger peak in Γ_{EM} at the Doppler-shifted frequency. Conversely, counter-rotation ($\hat{\Omega}_w = -\hat{\omega}$) weakens the peak in Γ_{EM}, until eventually no non-monotonic behavior is seen. As $R_m \mapsto \infty$, the shielding effect becomes dominant and Γ_{EM} is reduced for all frequencies, with only the static inner wall participating weakly. The consequences of differential wall rotation on mode-locking will be discussed in Section 6.2.5.

6.2.2 Derivation of Error Field Torque

Derivation of the torque due to the static error field (Γ_{ext}) is similar to that of the mode-wall electromagnetic torque, where now terms that scale like $\vec{B}_{\text{ext}}\tilde{B}_{\text{mode}}$ are considered in Eq. 6.2. Using similar arguments as Eqs. 6.4-6.6, the torque from the static error field is

found to be:

$$\Gamma_{\text{ext}} = \frac{2Lr_a^2}{\mu_0}\int_0^{2\pi} \vec{B}_{\text{ext},\theta}\tilde{B}_{\text{mode},r}\exp\left(-i\phi\right)d\theta \tag{6.9}$$

where no cycle-averaging is carried out. Due to the $\exp\left(-i\phi\right)$ and $\exp\left(-i\theta\right)$ dependence, the cross-power is of a different form and the torque is found to be:

$$\Gamma_{\text{ext}} = 2\left(\frac{L\pi}{\mu_0}\right)B_{\text{ext}}\tilde{b}\sin\phi \tag{6.10}$$

here ϕ ($\equiv \int_0^t \omega(t')dt' + \phi_0$) is the complementary angle between $\vec{B}_{\text{ext}}$ and $\tilde{B}_{\text{mode}}$. Thus A_{ext} is identified in Eq. 6.3 as $A_{\text{ext}} \equiv 2B_{\text{ext}}\tilde{b}\left(\frac{\pi L}{\mu_0}\right)$ and is $\mathcal{O}(10^{-3})$ [N m] in the experiment. A similar term is present in other treatments [22, 76] though as no net torque is generated by Γ_{ext} over a rotation in ϕ it is often neglected.

As $\vec{B}_{\text{ext}}$ is applied from external conductors, it is also a function of wall rotation. Rotation shields $\vec{B}_{\text{ext}}$ such that $\left|\vec{B}_{\text{applied}}\right| / \left|\vec{B}_{\text{ext}}\right| = \sqrt{1 + R_m^2/4}$ as was derived in Section 5.3.1. However, this effect is purposely excluded from Eq. 6.10 as it is experimentally compensated by applying more current to the error field coil as wall rotation increases.

6.2.3 Estimation of Phenomenological Restoring Torque

In order for the torque balance relation of Eq. 6.2 to capture mode-locking phenomenology a restoring torque to an offset frequency is required. Most simply, this torque takes the linear form of $\Gamma_{\text{res}} = A_{\text{res}}(\Omega_0 - \omega)$ (where Ω_0 is an offset rotation) though higher order dependencies on ω could also yield bifurcations. In this Section, it is shown that Γ_{res} could arise from electromagnetic torques forcing the plasma to its 'natural' ExB frequency, Ω_{ExB}. The origin of this flow was discussed in Section 2.4.4. This flow profile is well described by the rigid-rotor approximation within the core, though this approximation becomes less accurate at the edge. The rigid-rotor approximation, however, is not able to capture the

effects of the axial shear present in the device. To estimate the restoring torque, the plasma rotation ω is allowed to deviate by δ_ω from Ω_{ExB}, such that $\omega \equiv \Omega_{\mathrm{ExB}} + \delta_\omega$. Upon insertion of $V_\theta = r\omega$ into the radial resistive Ohm's law, $E_r + V_\theta B_z = \eta_\perp J_r$ (where $\eta_\perp$ is the cross-field resistivity and $V_z = 0$), E_r cancels $r\Omega_{\mathrm{ExB}}$ and it is found that $J_r = \frac{rB_z}{\eta_\perp}(\omega - \Omega_{\mathrm{ExB}})$, where J_r is axisymmetric. Note in the open-ended system this does not require charge build up. Taking only the axisymmetric contribution to Eq. 6.2:

$$\begin{aligned}\Gamma_{\mathrm{res}} =& \hat{z} \cdot \int_{\mathcal{V}} r \times \left(\vec{J}_0 \times \vec{B}_0\right) d\mathcal{V} \\ =& -L \int_0^{2\pi} d\theta \int_0^{r_p} r^2 J_r B_z dr \\ =& \frac{\pi}{2} \frac{L B_z^2 r_p^4}{\eta_\perp} (\Omega_{\mathrm{ExB}} - \omega)\end{aligned} \tag{6.11}$$

where r_p, L is the plasma radius and length, B_z is the (constant) guide field and $B_r = 0$. From Eq. 6.11 $A_{\mathrm{res}} \equiv \frac{\pi}{2}\frac{LB_z^2 r_p^4}{\eta_\perp}$ and $\Omega_0 \equiv \Omega_{\mathrm{ExB}}$ are identified. For experimental parameters, $A_{\mathrm{res}} \approx \mathcal{O}(10^{-5})$ [N m s/rad], and $\Omega_0 \approx \mathcal{O}(10^4)$ [rad/s]. In Section 6.5 it will be shown that this estimate is within an order of magnitude of experimental measurements, which is encouraging considering the rudimentary arguments used to arrive at Eq. 6.11. Note that more complete versions of Ohm's law could be used with a suitable redefinition of $\delta\omega$ and Ω_{ExB} and thus A_{res} and Ω_0.

6.2.4 Wall-Locking: Bifurcations in Torque Balance

Solutions of Eq. 6.3 are explored first with $R_m = 0$ and $\Gamma_{\mathrm{ext}} = 0$ for simplicity, with results similar to earlier treatments despite the inclusion of a second wall [21, 22, 23, 76]. Fig. 6.2a-d illustrates the various regimes of Eq. 6.3 possible when scanning Ω_0 while holding A_{EM} and A_{ext} fixed. As will be discussed in Section 6.3, this is the experimentally relevant treatment. For large Ω_0, shown in Fig. 6.2a, there is only one root at $\omega \approx \Omega_0$ which is dynamically stable and is termed the fast branch. As Ω_0 is decreased, as in

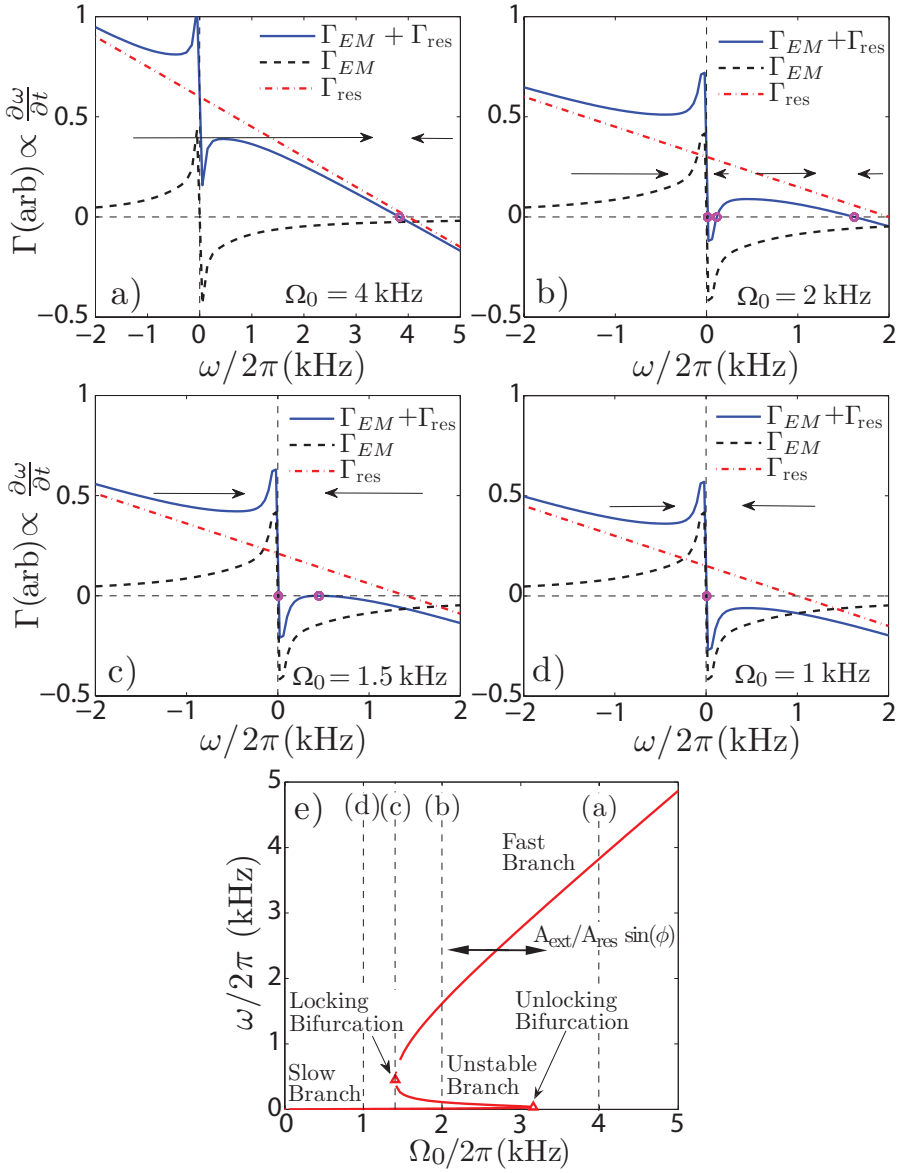

Figure 6.2: (a)-(d) Net electromagnetic torque (Γ) as a function of plasma rotation (ω) decomposed into electromagnetic ($\Gamma_{\rm EM}$) and restoring ($\Gamma_{\rm res}$) contributions for various values of natural frequency (Ω_0). Other variables in Eq. 6.3 are held constant. Arrows in (a)-(d) indicate the direction of net torque and thus point to the stable solutions. (e) This bifurcation diagram is made by plotting the torque balance equilibrium points (solutions of Eq. 6.3) while varying Ω_0, illustrating the locking and unlocking bifurcation points.

Fig. 6.2b, 3 roots are found - the fast branch, a new stable slow branch, and an unstable branch. Lowering Ω_0 further the locking bifurcation point is reached, shown in Fig. 6.2c, where the fast and unstable branches merge. Below this critical value of Ω_0, only the slow branch remains, as shown in Fig. 6.2d. Figure 6.2e summarizes the solutions of Eq. 6.3. Locking bifurcations thus occur when Ω_0 is lowered past the bifurcation point and the mode transitions discontinuously from $\omega \approx \omega_{\text{lock}} \mapsto 0$ on an inertial time-scale, which is sub-ms for the experiment. Another possible bifurcation is mode unlocking, in which raising Ω_0 past the unlocking threshold transitions the mode from the slow to fast branch. As expected, hysteresis is present.

The effect of Γ_{ext} on the picture of Fig. 6.2 is only important near the bifurcation point as over a cycle there is no net torque and the roots of Eq. 6.3 are not modified. Within each cycle, Ω_0 effectively oscillates at $\approx \omega$ such that $\Omega_0(t) = \Omega_0 + \tilde{\Omega}_0 \sin\phi$, where $\tilde{\Omega}_0 \equiv A_{\text{ext}}/A_{\text{res}}$, as shown in Fig. 6.2e. Near the bifurcation, this excursion in Ω_0 can induce a bifurcation at $\Omega_0 = \Omega_{0,\text{lock}} + \tilde{\Omega}_0$, which would be observed as a lock at higher frequency than predicted in the absence of an error field. In Section 6.3 and 6.4 it will be shown that this correction is necessary to interpret the observed data.

6.2.5 Bifurcations with Differential Rotation

The bifurcations of Eq. 6.3 are now explored with the inclusion of differential wall rotation. Figure 6.3a illustrates the modification of the roots of Eq. 6.3 by wall rotation. The fast branch is largely unaffected by rotation, while the slow branch is shifted to $\omega \approx \Omega_w/2$. The unstable branch, and thus the bifurcations, are strongly affected by rotation as summarized in Fig. 6.3b. The locking bifurcation at ω_{lock} is monotonically Doppler shifted by rotation, while the natural frequency required to lock the mode ($\Omega_{0,\text{lock}}$) is insensitive to wall rotation. The unlocking bifurcation at ω_{unlock} is also Doppler shifted, though a very dramatic effect on $\Omega_{0,\text{unlock}}$ is found. For co-rotation ($R_m > 0$), $\Omega_{0,\text{unlock}}$ is found

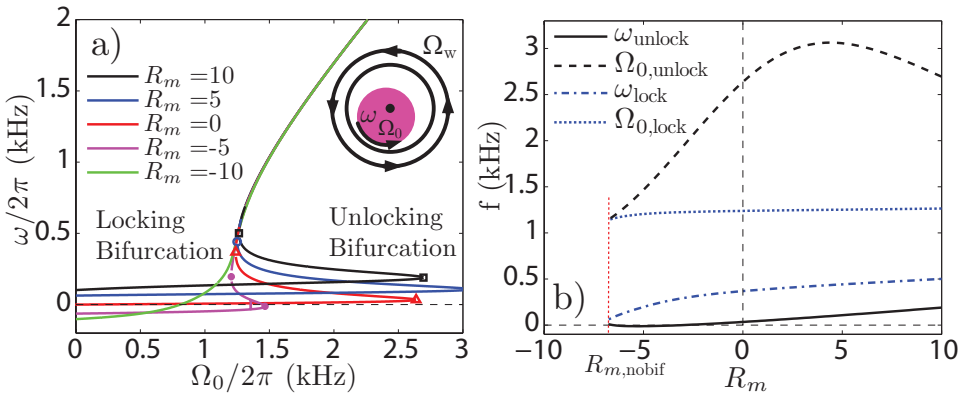

Figure 6.3: (a) Bifurcation diagram illustrating torque balance equilibrium points (solutions of Eq. 6.3) as Ω_0 is varied for various values of differential wall rotation (R_m). (b) Dependence of the locking and unlocking bifurcation frequencies (ω_{lock},ω_{unlock}) and natural frequencies ($\Omega_{0,\text{lock}}$,$\Omega_{0,\text{unlock}}$) as R_m is varied. Beyond $R_{m,\text{nobif}}$ the bifurcation is lost.

to increase, thus requiring more torque to unlock a locked mode, until at fast rotation shielding weakens this effect. In contrast, counter-rotation ($R_m < 0$) dramatically decreases $\Omega_{0,\text{unlock}}$ until both bifurcations are completely lost at $R_m = R_{m,\text{nobif}}$. Thus, for fast counter-rotation mode-locking is not predicted to occur and a mode could transition unimpeded from slow to fast rotation. Wall rotation above $R_{m,\text{nobif}}$ has thus removed the ability of the mode to lock to any wall.

The locking asymmetry in R_m reverses as $\Omega_0 \mapsto -\Omega_0$, justifying the definition of co- and counter-rotation by Ω_0. Were $\Omega_0 = 0$, there would be no asymmetry, though the only solution to Eq. 6.3 would be the locked branch at $\omega \approx \Omega_w/2$, precluding bifurcations. Lastly, as the rotating wall is a realization of a perfect active control system with a single value of complex gain [16], active control of MHD modes would alter the torque balance in an equivalent manner. Thus, in addition to directly reducing the mode amplitude, active control may also stabilize modes by altering their unlocking bifurcations. This topic is treated separately in Appendix D.

6.3 Static Wall Mode-Locking

The model developed in Section 6.2 will be shown to capture the effects of both $m = 0$ and $m = 1$ error fields with the rotating wall left stationary for simplicity. All static error fields are applied as part of the vacuum field configuration well prior to plasma formation and flux-loop integration and thus are not directly detected.

6.3.1 Slowing of Plasma Rotation by Guide Field Ripple

The application of axially localized, steady-state $m = 0$ fields (guide field ripple, $\tilde{B}_z$) is found to have a strong effect on the observed mode frequency ω. This is shown in Fig. 6.4a, where other plasma parameters are held constant. At low $\tilde{B}_z$ the mode is always in the fast branch and $\Omega_0 \approx \omega$. As a characteristic fast slow-down followed by modest increase in ω is typical of all discharges in the device, as shown in Fig. 6.4b, $\Omega_0(t)$ will be fit to the following analytic form:

$$\Omega_0(t) = a_1 + a_2 \left(1 - \exp\left(-\frac{t}{a_3}\right)\right) + a_4 \exp\left(\frac{t}{a_5}\right)$$

where a_n are positive definite coefficients. Specifically, $a_n \approx [1, 2, 2.5, .2, .01, 2.5]$ [kHz, kHz, ms, kHz, ms] respectively is found to well match the data for the discharges of this study. The physics behind the evolution of $\Omega_0(t)$ is highly complex, as it involves J_z profile evolution, T_e evolution, and possible neutral pile-up effects. Nonetheless, $\Omega_0(t)$ is an input to the model and its self-consistent evolution is beyond the scope of this work. Measurements of A_{ext} and A_{EM} (not shown) are found to be remarkably constant in time for these discharges, indicating that the rotating RWM amplitude ($\tilde{B}_{\text{mode}}$) is constant and stabilized by plasma rotation. As the flux-loops are located outside the static wall, all amplitude variations in Fig. 6.4a are due to the shielding effect of the wall on the measurement of $\tilde{B}_{\text{mode}}$. The interpretation of field ripple variations in terms

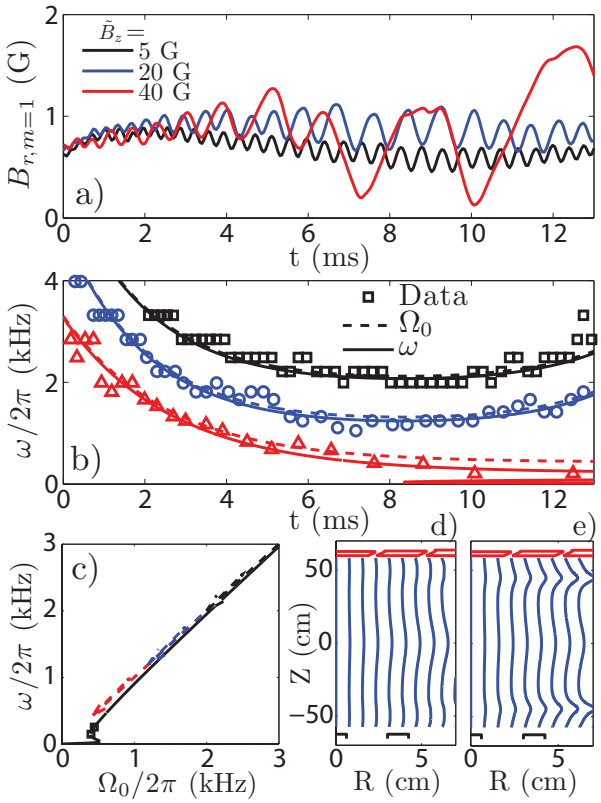

Figure 6.4: (a) Time-trace of radial magnetic field ($B_{r,m=1}$) as guide field ripple ($\tilde{B}_z$) is increased. (b) Measurements of mode frequency (ω) for the discharges of (a). For Figs. 6.4-6.10, $\Omega_0(t)$ is fit (according to Eqs. 6.3, 6.12) such that $\omega(t)$ matches the data, holding other parameters in Eq. 6.3 constant. (c) Bifurcation diagram (roots of Eq. 6.3) calculated using data from the fits of (b). (d)-(e) The calculated alteration of the guide field by the $\tilde{B}_z$ coil is shown, where panel (d) is for $\tilde{B}_z = 5$ G while panel (e) is for $\tilde{B}_z = 40$ G. The red, black outlines in (d)-(e) indicate the position of the segmented anode and plasma guns respectively. $t = 0$ is when the bias voltage to drive I_p is applied.

of the bifurcation picture of Section 6.2.4 is shown in Fig. 6.4c for constant $A_{\rm res}$ and measured $A_{\rm ext}$, A_{EM}. Increasing $\tilde{B}_z$ causes Ω_0 to plunge further towards the bifurcation point as a function of time. While the largest ripple case did not lock, the very low ω and continually slowing time-dependence indicate it neared the locking threshold. Figure 6.4d-e illustrates the modification of the vacuum fieldlines by $\tilde{B}_z$. While the ripple coils are axially localized, they have a global effect on the mode frequency. It is speculated that $\tilde{B}_z$ is hollowing the $J_z(r)$ profile, whose radial gradient is thought to set E_r and thus Ω_0, as discussed in Section 2.4.4.

6.3.2 Mode-Locking by Vertical Error Fields

Increasing the static, vertical ($m = 1$, $k_z = 0$) error field ($\equiv \vec{B}_{\rm ext}$) is found to lock the RWM at progressively higher frequencies, giving rise to three distinct regimes as shown in Fig. 6.5. First, at low $\vec{B}_{\rm ext}$, the RWM does not lock for the duration of the discharge, and is termed a rotating RWM. At intermediate $\vec{B}_{\rm ext}$, the RWM initially rotates and locks during the discharge. As indicated in Fig. 6.5b, for the $B_{\rm ext} = 2$ (3) G case, the mode frequency abruptly jumps to zero at $t \approx 2$ (5) ms. This is termed a locked RWM. For large $\vec{B}_{\rm ext}$ no oscillations are seen and the mode is termed born-locked. Increasing $\vec{B}_{\rm ext}$ both increases $B_{\rm eq}$ and modifies $\omega_{\rm lock}$, as shown in Fig. 6.5b. This illustrates that the error field is critical in determining the RWM regime present in the experiment. Furthermore, as was discussed in Chapter 5, the error field is also dependent on R_m. The implications of this additional interaction will be deferred to Chapter 7.

Using the model of Eq. 6.3 with measurements of the $\omega_{\rm lock}$, $A_{\rm ext}$ and A_{EM} as inputs, curves of the form of Fig. 6.5c are generated. Ω_0 decreases throughout the discharge until the modified locking condition $\Omega_0 = \Omega_{0,\rm lock} + A_{\rm ext}/A_{\rm res}$ is reached. An intermediate amount of $\tilde{B}_z$ is also applied to bring Ω_0 closer to the locking threshold, as suggested by Fig. 6.4. At fast ω, $\vec{B}_{\rm ext}$ is observed to have no effect whatsoever on the $\omega(t)$ trace

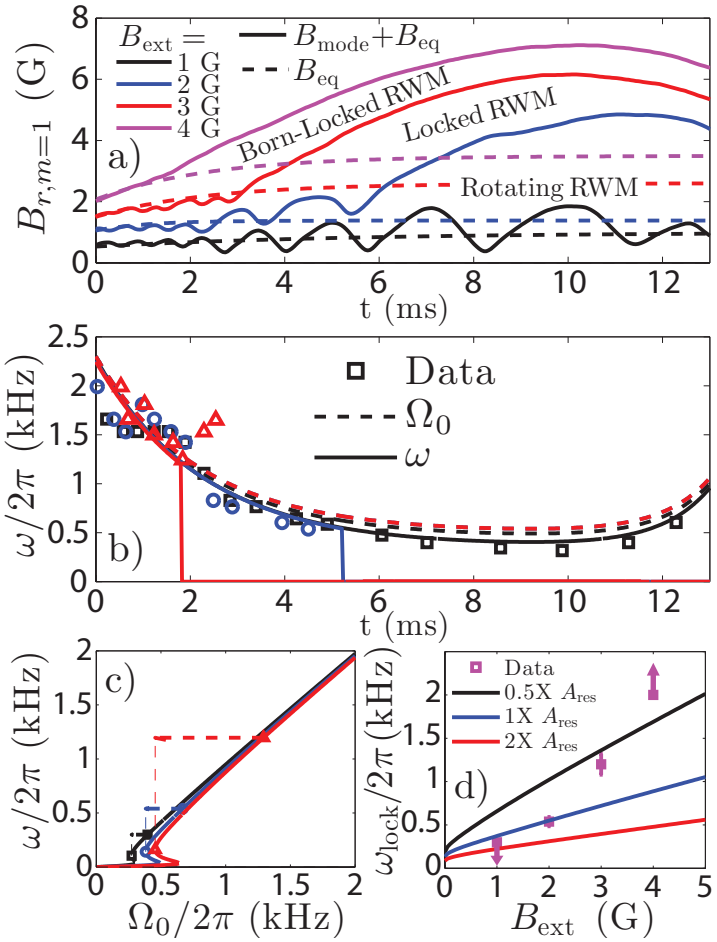

Figure 6.5: (a) Time-traces of radial magnetic field ($B_{r,m=1}$) as $m = 1$ error field (B_{ext}) is increased, yielding mode locking. (b) Mode rotation (ω) and resultant fits to the model of Eqs. 6.3, 6.12. (c) Bifurcation diagrams (solutions of Eq. 6.3) using the fit parameters of (b). (d) Expected locking frequencies (ω_{lock}) as B_{ext} is increased and comparison to data. Arrows in (d) indicate that no locking bifurcation was observed, thus ω_{lock} must be in the direction shown. Like $\tilde{B}_z$, $\vec{B}_{ext}$ is applied prior to plasma formation and flux-loop integration and thus is not directly measured. However, $\vec{B}_{ext}$ forces the resulting equilibrium to be centered off-axis, thus causing an $m = 1$ component to the equilibrium field ($\equiv B_{eq}$) that is detected.

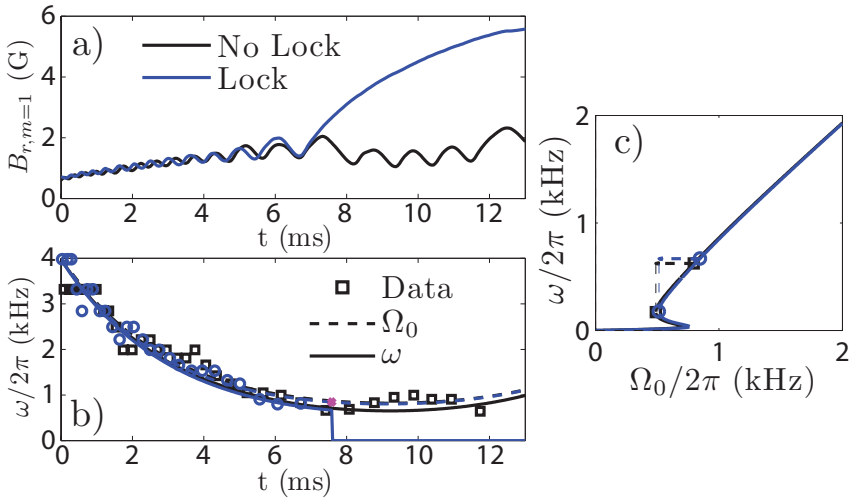

Figure 6.6: (a) Radial magnetic field ($B_{r,m=1}$) time-traces for two sequential discharges. (b) Mode rotation (ω) and fits to Eqs. 6.3, 6.12 for the discharges in (a). (c) Bifurcation diagram (solutions of Eq. 6.3) using fits from (b).

(not shown), confirming that $\vec{B}_{\text{ext}}$ does not modify the torque balance when integrated over a cycle. The model of Section 6.2 predicts a roughly linear increase in ω_{lock} with increasing $\vec{B}_{\text{ext}}$ if all other parameters are held constant. However, as shown in Fig. 6.5d, the observed increase in ω_{lock} is larger than the prediction. Allowing A_{res} to vary as $\vec{B}_{\text{ext}}$ is increased yields better agreement, indicating that $\vec{B}_{\text{ext}}$ may be altering the torque balance beyond simply modifying the static error field torque. Nonetheless, the model of Eq. 6.3 captures the trend in ω_{lock}, and captures the discontinuous nature of the locking transition. The fact that locking occurs at the same phase (ϕ) also reinforces the idea that Γ_{ext} is responsible for locking.

6.3.3 Near-Threshold Effects

Sensitivity to Input Conditions

The sensitivity of the locking bifurcation to input conditions is shown in Fig. 6.6, which compares two successive discharges where no change was made to the experimental control

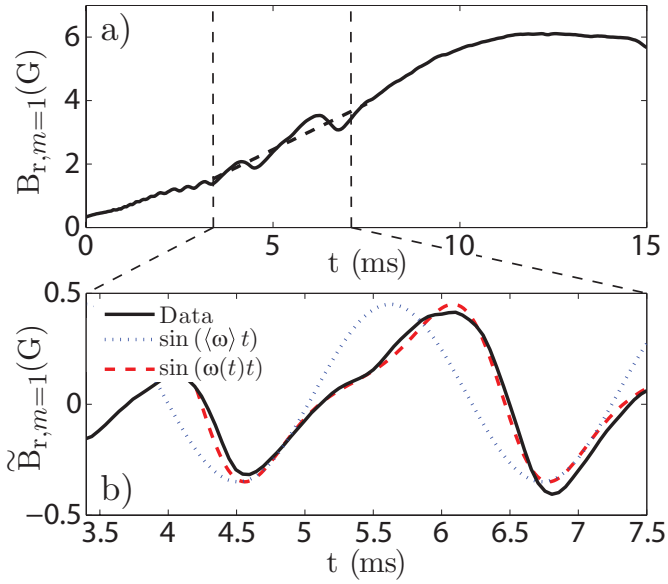

Figure 6.7: (a) Radial magnetic field ($B_{r,m=1}$) for a discharge where locking occurred (at $t \approx 7$ ms) after a longer final oscillation. (b) Enlargement of this final oscillation, with fits to a single frequency model ($\sin(\omega t)$) and one in which $\omega(t) = \langle\omega\rangle + \tilde{\omega}\sin\langle\omega\rangle t$.

parameters. Very different outcomes were obtained as the second discharge locked while the first did not, as would be expected of the behavior of Eq. 6.3 near the locking threshold. Holding $\Omega_0(t), A_{EM}, A_{\text{ext}}$ constant and allowing A_{res} to vary by 8% is sufficient to differentiate between a discharge that is predicted to lock and one that is not, further reinforced by the small difference in the solutions to Eq. 6.3 shown in Fig. 6.6c. Variations of A_{res} at this level are thus thought to define the level of repeatability attainable in the experiment.

Non-uniform Rotation

As discussed in Section 6.2.4, the effect of Γ_{ext} is to oscillate the effective Ω_0 such that $\Omega_0(t) = \Omega_0 + A_{\text{ext}}/A_{\text{res}}\sin\phi$. Letting $\phi \equiv \int_0^t \omega(t)dt \approx \langle\omega\rangle t$ shows that this should in principle result in an oscillation of ω at $\approx \langle\omega\rangle$ as well, such that $\omega(t) \approx \langle\omega\rangle + \tilde{\omega}\sin\langle\omega\rangle t$, where $\tilde{\omega}$ depends on the nature of the other torques in the system. At low ω the deviation

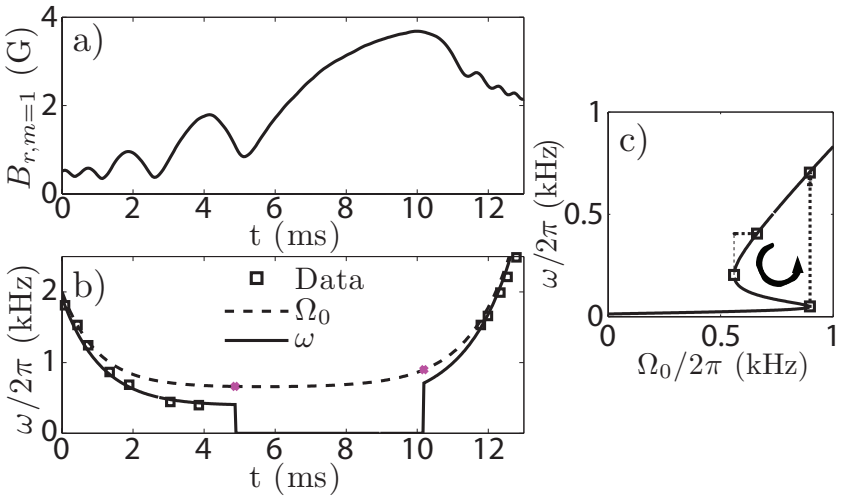

Figure 6.8: (a) Time-trace of radial magnetic field ($B_{r,m=1}$) for a discharge illustrating mode-unlocking. (b) Mode rotation (ω) with fits to Eqs. 6.3, 6.12 for the same discharge. (c) Bifurcation diagram (solutions of Eq. 6.3) using fits from (b) illustrating mode-locking and mode-unlocking bifurcations at constant A_{res}, A_{ext} and A_{EM}.

from $\langle\omega\rangle$ throughout a cycle can be observed in the experiment. Figure 6.7 illustrates a sample discharge where a long oscillation prior to locking is observed. Removing the approximate error field by a linear fit isolates the oscillation. It is clear that the oscillation is inconsistent with a single, constant $\langle\omega\rangle$. Introducing $\tilde{\omega}$ into the form of $\omega(t)$ yields much better agreement, with a curve characteristic of nested sinusoids observed. The best fit is found for $\tilde{\omega} = 0.7\,\langle\omega\rangle$, which supports the significant role of Γ_{ext} in the observed mode-locking. The exact form of the curve also depends sensitively on the initial conditions (ω_0 and ϕ_0), with different shapes seen in different discharges.

Hysteresis in Mode-Unlocking

The model of Section 6.2 also predicts a second bifurcation when a locked mode's natural frequency (Ω_0) exceeds a critical value ($\Omega_{0,\text{unlock}}$), thus allowing the mode to discontinuously unlock. The discharge shown in Fig. 6.8 exhibits mode-locking occurring at $t \approx 5$ ms followed by mode-unlocking at $t \approx 10$ ms. The frequency immediately after the

mode-unlocking is clearly larger than that immediately before the lock, thus illustrating hysteresis. Figure 6.8c illustrates the discharge evolution in terms of the bifurcation diagram of Section 6.2.4, showing both the locking and unlocking transitions. For simplicity, this is done assuming constant A_{res}, A_{ext} and A_{EM} before and after locking, which may account for the discrepancy in the predicted frequency after mode-unlocking. It should be noted that mode-unlocking is a rare phenomenon in the experiment, with locked modes almost always remaining locked throughout the discharge. This is thought to be because Ω_0 does not normally reach a sufficiently large value at the end of the discharge to unlock the mode. As discussed, the self-consistent evolution of Ω_0 is complex and not well understood.

6.4 Mode-Locking with Differential Wall Rotation

Mode-locking in discharges with differential wall rotation are compared to the predictions of Section 6.2.5, with wall rotation found to affect mode-locking asymmetrically. As shown in Fig. 6.3, mode-locking is expected to occur at higher frequency for co-rotation and lower frequency for counter-rotation. For all discharges examined in this Section the error field ($\vec{B}_{\text{ext}}$) is held approximately constant by applying more error field current as wall rotation is increased to overcome the natural shielding effect of the rotating wall.

The co-rotation case is shown in Fig. 6.9, with locking observed at higher ω as wall rotation is increased. Figure 6.9c illustrates the solutions to Eq. 6.3 with increasing wall rotation. To better match the data, A_{res} has been allowed to vary, though $\Omega_0(t)$ has been held nearly constant. As shown in Fig. 6.9d, the observed increases in ω_{lock} are greater than that expected by the constant A_{res} model, indicating that wall rotation may be affecting other parameters in the simple model of Eq. 6.3, though the data is contained within a fairly narrow band of A_{res}.

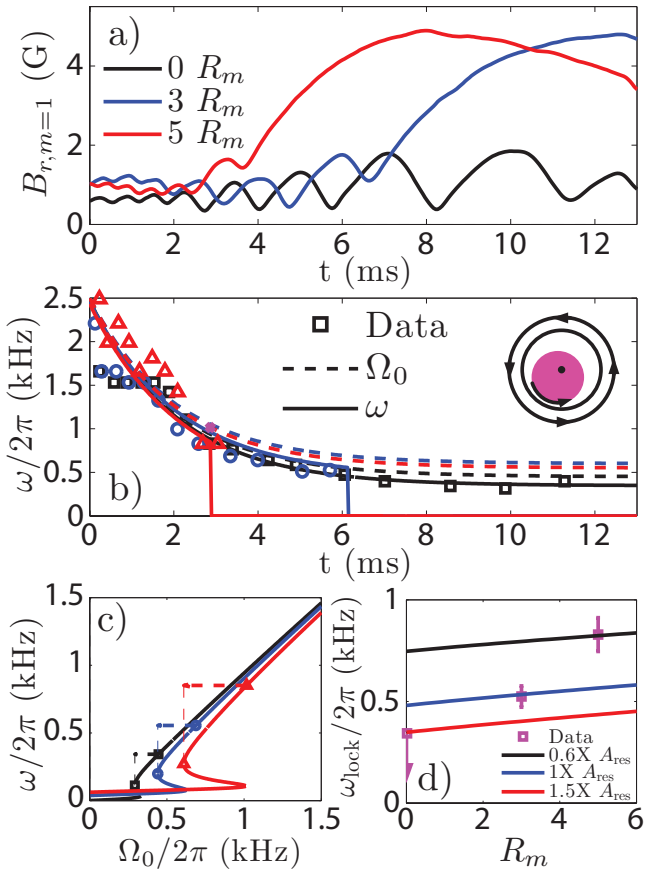

Figure 6.9: (a) Radial magnetic field ($B_{r,m=1}$) traces illustrating mode-locking at higher frequency due to wall co-rotation ($R_m > 0$). (b) Mode rotation (ω) traces and corresponding fits to Eqs. 6.3, 6.12. (c) Bifurcation diagram (solutions of Eq. 6.3) for fit parameters from (b). (d) Comparison of theoretical and experimental locking bifurcation frequency ($\omega_{\rm lock}$) as R_m is varied for a range of values of $A_{\rm res}$.

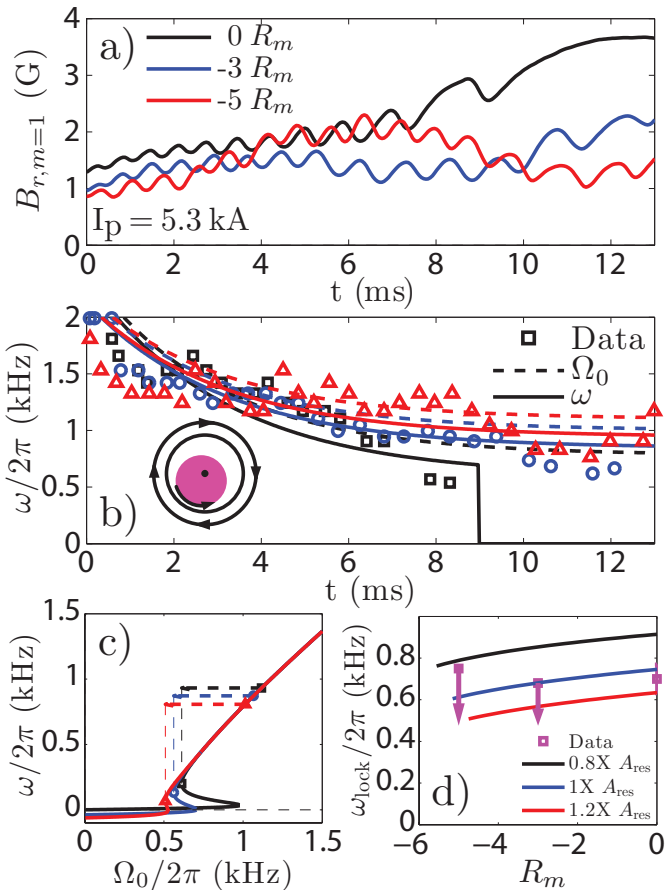

Figure 6.10: (a) Radial magnetic field ($B_{r,m=1}$) traces illustrating mode-locking at lower frequency due to wall counter-rotation ($R_m < 0$). (b) Mode rotation (ω) traces and corresponding fits to Eqs. 6.3, 6.12. (c) Bifurcation diagram (solutions of Eq. 6.3) for fit parameters from (b). (d) Comparison of theoretical and experimental locking bifurcation frequency (ω_{lock}) as R_m is varied for a range of A_{res}. As a lock is only observed for $R_m = 0$, only the upper bound of ω_{lock} is known.

Inhibited locking by counter-rotation is shown in Fig. 6.10. For only these discharges, I_p has been lowered from 6.0 to 5.3 kA in order to alter ω_{lock} and lock at $R_m = 0$ with low $\vec{B}_{\text{ext}}$. Note the modification of ω_{lock} as plasma parameters are varied is beyond the scope of this study. While at early time $\Omega_0(t)$ is constant between discharges, the $R_m = 0$ case slows and locks while the $R_m < 0$ cases continue unlocked throughout the discharge. Figure 6.10c shows the modifications to the solutions of Eq. 6.3 for experimental parameters, and Fig. 6.10d summarizes the results by noting the expected change in ω_{lock} as R_m is varied.

6.5 Discussion

Several points are raised by the functional equivalence of Eq. 6.3 to the established torque balance models [21, 22, 23, 24, 20]. These models are fundamentally layer theories, with ideal MHD violated either at a rational surface or in a thin inertial layer. Some form of dissipation, or violation of ideal MHD, is necessary for the electromagnetic torque to exist [22], as in ideal MHD $\nabla \cdot \bar{\bar{T}} = \nabla P$ which vanishes over surface integration. In this model, the two main sources of dissipation are resistivity and viscosity. Resistivity in the wall is explicitly used in the calculation of Γ_{EM} in Eq. 6.7, while resistivity in the plasma is invoked to approximate Γ_{res} in Eq. 6.11. Though viscosity does not explicitly appear in this study, the use of the rigid-rotor approximation implies it is the dominant term in setting the rotation profile. The flow profiles of Section 2.4.4 support this in the core of the device, though at the edge this is less clear. It is thus not surprising that electromagnetic body torques are present in the experiment despite their absence in ideal MHD.

The role of the error field ($\vec{B}_{\text{ext}}$) in the torque balance model is contained entirely in the Γ_{ext} term of Eq. 6.3 and $\vec{B}_{\text{ext}}$ is shown to exert no net torque over a cycle in

Description	$\langle A_{\text{res}} \rangle * 10^6$	$\langle A_{EM} \rangle * 10^2$	$\langle A_{\text{ext}} \rangle * 10^3$
m = 0 fields (Fig. 6.4)	0.4 ± 0.2	0.5 ± 0.2	0.2 ± 0.1
m = 1 fields (Fig. 6.5)	1.6 ± 0.7	1.9 ± 0.7	$1 - 4$
Sensitivity (Fig. 6.6)	0.5 ± 0.1	1.0 ± 0.3	1.0 ± 0.3
Unlocking (Fig. 6.8)	1.1 ± 0.5	2.5 ± 0.5	0.7 ± 0.2
Co-ω (Fig. 6.9)	0.9 ± 0.5	0.6 ± 0.2	0.7 ± 0.2
Counter-ω (Fig. 6.10)	0.3 ± 0.1	1.3 ± 0.5	1.4 ± 0.4

Table 6.1: Measured values of A_{EM}, A_{ext}, and calculated values of A_{res} from the discharges of this study. Errors are estimated from the deviations between and within discharges.

ϕ. In the long-cylinder model, the error field is resonant with the mode as $k_z = 0$ for both. Experimentally, however, the cylinder is finite and bounded by highly conducting electrodes, thus requiring at least two $k_z \neq 0$ for the RWM, and more k_z in the presence of magnetic shear [77]. Thus, the error field is not obviously resonant in the experiment. Nonetheless, $\vec{B}_{\text{ext}}$ is observed to strongly affect mode-locking phenomenology and alter the locking frequency ω_{lock} as discussed in Section 6.3.2. It is speculated that either the resonance condition is relaxed by the strong dissipation everywhere in the plasma, or that some k_z are sufficiently small that they are effectively resonant with $\vec{B}_{\text{ext}}$. The relationship between $\tilde{B}_{\text{mode}}$ and $\vec{B}_{\text{ext}}$ has also been neglected in this model. This in contrast to the treatment of tearing modes, where $\vec{B}_{\text{ext}}$ is responsible for driven reconnection which introduces $\tilde{B}_{\text{mode}}$. However, for the experimental geometry it is not evident that $\tilde{B}_{\text{mode}}$ would be affected by $\vec{B}_{\text{ext}}$, thus justifying their independence in the model.

Each observation of mode-locking in this study has yielded a measurement of A_{res}. An equation to solve for the locking bifurcation point $[\omega_{\text{lock}}, \Omega_{0,\text{lock}}]$ is readily obtained as bifurcation occurs where the discriminant of Eq. 6.3, written as a polynomial in ω, vanishes. In the aforementioned discharges $\Gamma_{EM}, \Gamma_{\text{ext}}$, and ω_{lock} are experimentally measured by the flux-loop array, giving a unique prediction for A_{res}. For the discharges of this study, measured values of A_{EM}, A_{ext} and calculated values of A_{res} are shown in Table 6.1. Despite the wide range of discharges used in each comparison, $A_{\text{res}} \approx \mathcal{O}(10^{-6})$ for all cases.

This is smaller than the $\mathcal{O}(10^{-5})$ estimate of Section 6.2.3. This level of disagreement is acceptable as several approximations were used to arrive at Eq. 6.11, specifically the simplification of the rotation profile of Section 2.4.4 to simple rigid-rotation and the neglect of other terms in the radial Ohm's law. Furthermore, though a possible mechanism has been identified for the restoring torque in Section 6.2.3, other mechanisms could be occurring in conjunction. Torques from neutral collisions [69], direct losses [78], turbulent stresses [79], or other anomalous torques can generally be lumped into the parametric form of $A_{\text{res}}(\Omega_0 - \omega)$ as long as they are linear in ω, and thus they would alter the prediction of Γ_{res}.

In this Chapter and the preceding one, the groundwork for studying the stabilization of the RWM was laid. This Chapter illustrated the critical importance of the error field in determining the RWM regime present in the device, for example as shown in Fig. 6.5. Chapter 5, on the other hand, presented the tools necessary to understand and model this error field. To study the interaction of the RWM with the rotating wall, locked or born-locked RWMs must be used as otherwise $\omega \gg \Omega_w$ and in the plasma frame only a small relative change in wall velocity is felt. Furthermore, the same RWM regime must be maintained while R_m is varied, which in turn requires the error field to be held constant. With both the mode-locking phenomenon and error field interactions relatively well understood, attention can now be turned to the interaction of the locked and born-locked RWMs with the rotating wall.

Chapter 7

Stabilization of the RWM

Stabilization of the resistive wall mode (RWM) by high-speed differentially rotating conducting walls is demonstrated in the experiment. To observe stabilization, only locked RWMs must be considered. Wall rotation is found to reduce the locked RWM growth rate, with both wall-locked and slowly rotating RWMs observed depending on the alignment of wall to plasma rotation. Asymmetries in the error fields lead to RWM stabilization or destabilization depending on the wall rotation direction. At high wall rotation rates, born-locked RWM onset is found to occur at larger plasma currents, thus increasing the RWM-stable operation window. This is found to be symmetric in wall rotation direction.

The study of resistive wall mode (RWM) stability in a device with a rotating wall constituted the original motivation for this work. As such, an introduction to this topic has been provided in Chapter 1 and is not here repeated. In this Chapter experimental data is presented that demonstrates the stabilizing effect of the rotating wall on the RWM.

The structure of this Chapter is as follows: Section 7.1 presents the theoretical model used to interpret experimental observations. Section 7.2 presents the effect of the error field on the locked RWM and associated asymmetry in wall rotation direction. Section 7.3 presents the stabilization of the locked RWM by wall rotation, and Section 7.4 shows the extension of the RWM-stable operation window. Section 7.5 shows measured RWM eigenfunctions and discussion is provided in Section 7.6.

7.1 Theoretical Model

7.1.1 Plasma Dispersion Relation

To predict the stability of the RWM in the line-tied cylinder, a model for the plasma column must be developed. The plasma model used is that of Hegna [13], which is briefly summarized here. A screw-pinch equilibrium is first defined, in which the equilibrium field, $B_0 = B_{z0}(r)\hat{z} + B_{\theta 0}(r)\hat{\theta}$ is axisymmetric and invariant in $\hat{z}$. The plasma is taken to be force free, such that $\nabla p_0 = 0$, and $\nabla \times B_0 = \frac{\lambda(r)}{\mu_0} B_0$. The equilibrium plasma is taken to have a radius r_p, and the current profile is taken to be constant within this radius and zero outside, such that:

$$\lambda(r) = \begin{Bmatrix} \lambda_0 & r < r_p \\ 0 & r > r_p \end{Bmatrix} \tag{7.1}$$

where $J_0(r) \equiv \frac{\lambda(r)}{\mu_0} B_0(r)$. For this simple equilibrium, the safety factor $q(r)$ is constant inside the plasma and is given by:

$$q(r) = \begin{Bmatrix} q_0 & r < r_p \\ q_0 \left(\frac{r}{r_p}\right)^2 & r > r_p \end{Bmatrix} \tag{7.2}$$

Where $q_0 = \frac{4\pi}{\lambda_0 L}$, which is equivalent to the conventional definition of $q(r) = \frac{rB_z}{RB_\theta} = \frac{4\pi^2 r^2 B_z}{\mu_0 I_p(r) L}$ for the line-tied cylinder of length L. An eigenvalue approach is taken to solve for the unstable modes of the system. Taking the time dependence of perturbations to the equilibrium to be $\propto e^{-\gamma t}$ (where γ is complex, and $\gamma < 0$ is an unstable mode), the

momentum and induction equations are linearized, yielding:

$$\gamma^2 \rho_0 \tilde{\xi} = \tilde{J} \times B_0 + \frac{\lambda}{\mu_0} B_0 \times \tilde{B} - \nabla \tilde{p} \tag{7.3}$$

$$\tilde{B} = \nabla \times (\tilde{\xi} \times B_0) \tag{7.4}$$

where ρ_0 is the (constant) mass density, and the displacement vector $\tilde{\xi}$ is introduced. Note the lack of bulk flow in Eq. 7.4. The differential equations of Eqs. 7.3-7.4 are made algebraic by simplification of spatial gradients. However, due to the line-tied property of the device Fourier decomposition is only allowed in θ. Hence, $\tilde{\xi}$ and $\tilde{B}$ can be written $\tilde{\xi} = \tilde{\xi}(r,z)e^{-i\theta}$ and $\tilde{B} = \tilde{B}(r,z)e^{-i\theta}$ (only $m = 1$ kink modes are treated). In this simplified equilibrium radial gradients in Eqs. 7.3-7.4 only exist at r_p. Thus, the radial derivative is substituted with algebraic 'jump parameters,' given as:

$$\Delta_\xi = \frac{1}{\tilde{\xi}_{r_p}} \frac{d}{dr} (r\tilde{\xi}_r)_{r=r_p^-} \tag{7.5}$$

$$\Delta_- = \frac{1}{\tilde{B}_{r_p}} \frac{d}{dr} (r\tilde{B}_r)_{r=r_p^-} \tag{7.6}$$

$$\Delta_+ = \frac{1}{\tilde{B}_{r_p}} \frac{d}{dr} (r\tilde{B}_r)_{r=r_p^+} \tag{7.7}$$

Solutions of the resultant partial differential equation yield two allowable Fourier modes in z ($f(z) \propto e^{ik_z z}$). Equations 7.3-7.4 thus result in a quadratic equation for k_z, whose solutions are:

$$k_{z,\{1,2\}} = -\frac{B_{\theta r_p}}{r_p B_{z0}} + \frac{\lambda_0}{2(1-\Delta_+)} \pm \sqrt{\frac{\lambda_0^2}{4(1-\Delta_+)^2} + \frac{\gamma^2}{V_A^2(1-\Delta_+)}} \tag{7.8}$$

where $V_A \equiv B_{z0}^2/\mu_0\rho_0$ and Δ_+ is the only remaining jump condition. The boundary condition of line-tying relates these two k_z to one another, forming the dispersion relationship. Line-tying requires that $\tilde{\xi}_r(z=0) = \tilde{\xi}_r(z=L) = 0$. Thus, $\tilde{\xi}$ must be a linear combi-

nation of two $e^{ik_z z}$ axial wavenumbers (or two propagating waves), whose relationship is quantized:

$$k_{z1} - k_{z2} = \frac{2n\pi}{L} \tag{7.9}$$

With this quantization, the ideal MHD displacement vector takes the form:

$$\tilde{\xi}(r,\theta,z) = f(r)e^{i\theta + i(k_{z1}+k_{z2})z/2} \sin\left(\frac{n\pi z}{L}\right) \tag{7.10}$$

Which clearly satisfies the line-tying condition. Furthermore, the quantization yields a dispersion relation for the RWM / XK in the device:

$$n = \sqrt{\frac{4}{(q(r_p))^2(1-\Delta_+)^2} + \frac{4\gamma^2\tau_A^2}{1-\Delta_+}} \tag{7.11}$$

where $\tau_A \equiv L/2\pi V_A$. As the resistive instabilities of interest have $\gamma \approx \tau_w^{-1}$, and $\tau_w \gg \tau_A$, then $\gamma\tau_A \ll 1$. Thus, the second term in Eq. 7.11 is negligible and the dispersion relation (for $n = 1$) is simply:

$$1 - \Delta_+ = \frac{2}{q(r_p)} \tag{7.12}$$

Thus the stability problem has been reduced to a determination of the jump parameter, Δ_+. The full device geometry, including rotating walls, is now required.

7.1.2 Matching Problem for RWM Stability

The model geometry is that of plasma within r_p, static vacuum vessel wall at r_a, and rotating wall at r_b, as shown in Fig. 7.1. From the discussion of Section 5.2.1 The

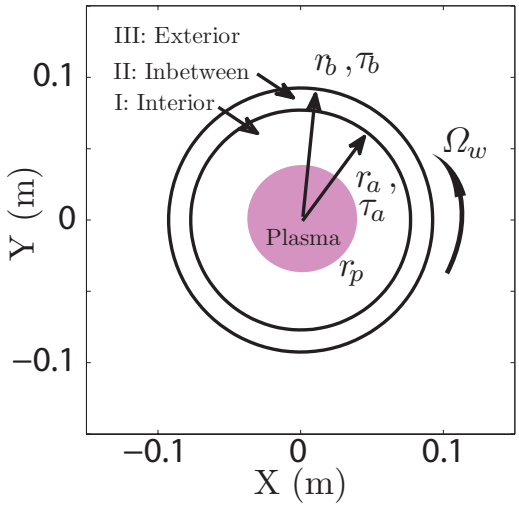

Figure 7.1: Geometry used for the RWM stability calculation. r_p, r_a, r_b denote the plasma, inner static wall, and outer rotating wall radii respectively. The regions between the walls and plasma are taken to be at vacuum.

functional form of the vacuum fields in these regions is given by:

$$\begin{aligned} I &: B_r(r,\theta,t) = \Re\left[(A_0 - A_1 r^{-2})e^{-i\theta}\right] \\ II &: B_r(r,\theta,t) = \Re\left[(A_2 - A_3 r^{-2})e^{-i\theta}\right] \\ III &: B_r(r,\theta,t) = \Re\left[(-A_4 r^{-2})e^{-i\theta}\right] \end{aligned} \tag{7.13}$$

where A_n are complex coefficients and $\nabla \cdot \vec{B} = 0$ can be used to find B_θ. To treat the walls the induction equation is integrated across each wall, whose thickness is taken to be thin. As this has been presented in Section 5.2.2, it is not repeated. The matching conditions at r_a, r_b are:

$$B_r|_{r=r_w^-}^{r=r_w^+} = 0 \tag{7.14}$$

$$B_\theta|_{r=r_w^-}^{r=r_w^+} = -(i\gamma + \Omega_w)\tau_w B_r \tag{7.15}$$

where $\Omega_w = 0$ for $r_w = r_a$. The jump condition Δ_+ can be defined in terms of the coefficients of Eq. 7.13, yielding:

$$\begin{aligned} \Delta_+ &= \frac{1}{\tilde{B}_{r_p}} \frac{d}{dr}(r\tilde{B}_r)_{r=r_p{}^+} \\ \Delta_+ \left(A_0 - A_1 r_p^{-2}\right) &= A_0 + A_1 r_p^{-2} \\ r_p^2 \delta A_0 &= A_1 \end{aligned} \tag{7.16}$$

where shorthand notation $\delta \equiv -\left(\frac{1-\Delta_+}{1+\Delta_+}\right) = \frac{1}{1-q(r_p)}$ is introduced. Note that while A_n are complex coefficients, Δ_+ must be purely real. Eq. 7.16 constitutes another matching condition, to be used in conjunction with Eqs. 7.14-7.15. The matrix equation for A_n constructed from the matching conditions of Eqs. 7.14-7.16 is:

$$\begin{bmatrix} r_p^2\delta & -1 & 0 & 0 & 0 \\ 1 & -r_a^{-2} & -1 & r_a^{-2} & 0 \\ \gamma\tau_a + 1 & r_a^{-2}(1-\gamma\tau_a) & -1 & -r_a^{-2} & 0 \\ 0 & 0 & r_b^2 & -1 & 1 \\ 0 & 0 & r_b^2 & 1 & (i\Omega_w - \gamma)\tau_b - 1 \end{bmatrix} \begin{bmatrix} A_0 \\ A_1 \\ A_2 \\ A_3 \\ A_4 \end{bmatrix} = 0 \tag{7.17}$$

As the matrix is sparse, it can be reduced to an equivalent coupled differential equation, where the time dependence has been left in generalized form:

$$\underbrace{\begin{bmatrix} \left(\frac{2r_a^2 r_p^2 \delta}{r_a^2 - r_p^2\delta}\right) & \left(\frac{-2r_a^2}{r_a^2 - r_p^2\delta}\right) \\ r_b^2(2 - iR_m) & iR_m \end{bmatrix}}_{\bar{\bar{M}}} \underbrace{\begin{bmatrix} A_2 \\ A_3 \end{bmatrix}}_{\vec{A}} + \underbrace{\begin{bmatrix} -r_a^2\tau_a & \tau_a \\ -r_b^2\tau_b & \tau_b \end{bmatrix}}_{\bar{\bar{D}}} \frac{\partial}{\partial t} \begin{bmatrix} A_2 \\ A_3 \end{bmatrix} = \underbrace{\begin{bmatrix} 0 \\ 2B_{\text{ext}} r_b^2 \end{bmatrix}}_{\vec{B}_{\text{ext}}} \tag{7.18}$$

where $A_0 = \frac{A_2 r_a^2 - A_3}{r_a^2 - r_p^2\delta}$, $A_1 = r_p^2\delta\left(\frac{A_2 r_a^2 - A_3}{r_a^2 - r_p^2\delta}\right)$, and $A_4 = B_{\text{ext}} r_b^2 - A_2 r_b^2 + A_3$ can be used to find the remaining coefficients. This equation can now be solved both for the normal modes

(by setting $\vec{B}_{\text{ext}} = 0$) and for steady-state error field amplification (by setting $\frac{\partial}{\partial t} = 0$).

7.1.3 Plasma Normal Modes (Kink Instabilities)

Equation 7.18 shows that for a given Δ_+ a unique set of eigenmodes is present, allowing a prediction for the growth rate ($\Re[\gamma] \equiv \gamma^{\text{r}}$) and rotation frequency ($\Im[\gamma] \equiv \omega$). To find the eigenmodes of the system the forcing ($\vec{B}_{\text{ext}}$) is set to zero and the characteristic equation for γ is formed by solving $\det\left(\bar{\bar{M}} + \gamma\bar{\bar{D}}\right) = 0$ in Eq. 7.18, yielding:

$$
\begin{aligned}
0 =& a\gamma^2 + b\gamma + c \\
a =& \tau_a\tau_b(1-\alpha_b)(1-\alpha_p\delta) \\
b =& -2[\tau_a\alpha_b(1-\alpha_p\delta) + \tau_b(\alpha_b - \alpha_p\delta)] - i\tau_a R_m(1-\alpha_b)(1-\alpha_p\delta) \\
c =& -4\alpha_b + i2R_m(\alpha_b - \alpha_p\delta)
\end{aligned}
\tag{7.19}
$$

whose solution is given by:

$$
\begin{aligned}
\gamma =& \frac{1}{\tau_b}\left(\frac{\alpha_b}{1-\alpha_b}\right) + \frac{1}{\tau_a}\left(\frac{(\alpha_b - \alpha_p\delta)}{(1-\alpha_b)(1-\alpha_p\delta)}\right) + i\frac{\Omega_w}{2} \pm \left[\frac{1}{\tau_a^2}\left(\frac{(\alpha_b - \alpha_p\delta)}{(1-\alpha_b)(1-\alpha_p\delta)}\right)^2 - \frac{\Omega_w^2}{4}\right. \\
&\left. + \frac{1}{\tau_b^2}\left(\frac{\alpha_b}{1-\alpha_b}\right)^2 + \frac{2\alpha_b}{\tau_a\tau_b}\left(\frac{2-\alpha_b-\alpha_p\delta}{(1-\alpha_p\delta)(1-\alpha_b)^2}\right) - i\left(\frac{\Omega_w}{1-\alpha_b}\right)\left[\frac{1}{\tau_a}\frac{\alpha_b-\alpha_p\delta}{(1-\alpha_p\delta)} - \frac{\alpha_b}{\tau_b}\right]\right]^{\frac{1}{2}}
\end{aligned}
\tag{7.20}
$$

decomposing into real and imaginary terms:

$$\gamma^{\mathrm{r}} = \frac{1}{\tau_b}\left(\frac{\alpha_b}{1-\alpha_b}\right) + \frac{1}{\tau_a}\left(\frac{(\alpha_b-\alpha_p\delta)}{(1-\alpha_b)(1-\alpha_p\delta)}\right) \pm \left(\eta_r^2+\eta_i^2\right)^{\frac{1}{4}} \cos\left(\frac{1}{2}\arctan\left(\frac{\eta_i}{\eta_r}\right)\right) \tag{7.21}$$

$$\omega = \frac{\Omega_w}{2} \pm \left(\eta_r^2+\eta_i^2\right)^{\frac{1}{4}} \sin\left(\frac{1}{2}\arctan\left(\frac{\eta_i}{\eta_r}\right)\right) \tag{7.22}$$

$$\eta_r \equiv \frac{1}{\tau_b^2}\left(\frac{\alpha_b}{1-\alpha_b}\right)^2 + \frac{1}{\tau_a^2}\left(\frac{(\alpha_b-\alpha_p\delta)}{(1-\alpha_b)(1-\alpha_p\delta)}\right)^2 + \frac{2\alpha_b}{\tau_a\tau_b}\left(\frac{2-\alpha_b-\alpha_p\delta}{(1-\alpha_p\delta)(1-\alpha_b)^2}\right) - \frac{\Omega_w^2}{4}$$

$$\eta_i \equiv -\left(\frac{\Omega_w}{1-\alpha_b}\right)\left[\frac{1}{\tau_a}\frac{\alpha_b-\alpha_p\delta}{(1-\alpha_p\delta)} - \frac{\alpha_b}{\tau_b}\right]$$

where non-dimensional coupling terms $\alpha_b \equiv \frac{r_b^2}{r_a^2}$ and $\alpha_p \equiv \frac{r_p^2}{r_a^2}$ have been used. As Eq. 7.20 is lengthy, limiting cases are considered.

Single Wall Limit

The single wall limit (shown in Fig. 5.1a) is found by letting $\tau_a \mapsto 0$ in Eqs. 7.21-7.22. There is now only one solution for γ, given by:

$$\gamma = \left(\frac{2}{\tau_b}\right)\frac{1-q(r_p)}{1-\alpha_p-q(r_p)} - i\Omega_w \tag{7.23}$$

where $\delta \equiv (1-q(r_p))^{-1}$ has been used. The behavior of $\Re[\gamma] \equiv \gamma^{\mathrm{r}}$ as a function of $q(r_p)$ is plotted in Fig. 7.2a. The instability threshold is at $q(r_p) = 1$, matching the Kruskal-Shafranov [2, 3] condition. The ideal-wall stability limit is also found (at $q(r_p) = 0.5$ for sample parameters) beyond which the neglect of the final term of Eq. 7.11 is invalid. Wall rotation is shown to be ineffective at stabilizing the mode in the single wall case as it does not modify γ^{r} in Eq. 7.23. Eigenfunctions at a few values of $q(r_p)$ are shown in Fig. 7.2b-d. Unstable ($q(r_p) < 1$) eigenfunctions are dipolar and inhibited from exiting the wall. The marginally stable ($q(r_p) = 1$) eigenfunction does not feel the wall at all, and stable ($q(r_p) > 1$) eigenfunctions have fieldlines which are inhibited from entering the

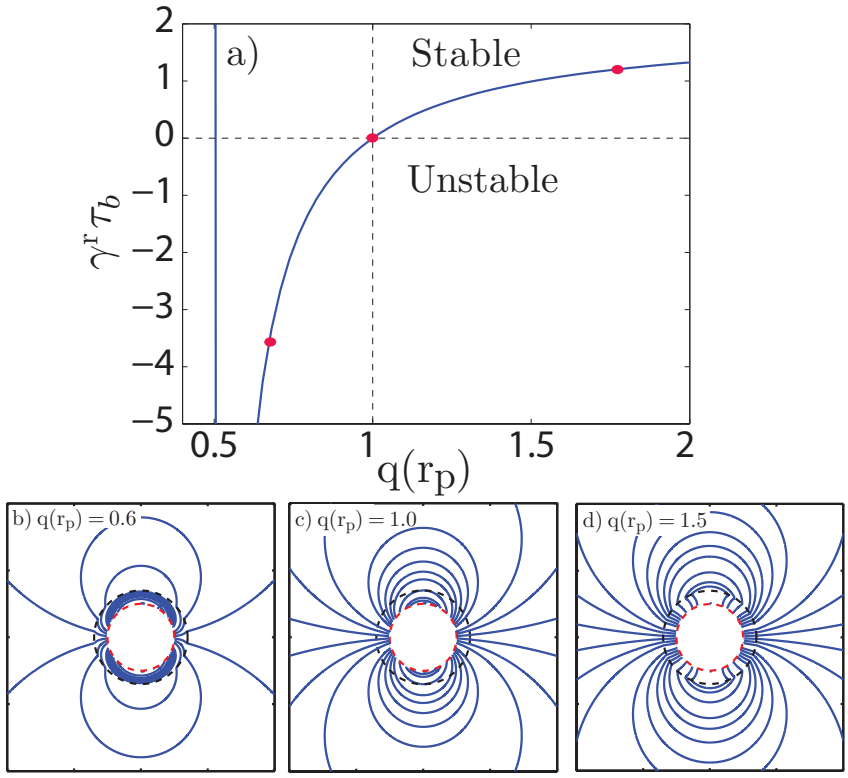

Figure 7.2: (a) Time constants (eigenvalues) of the exponentially forced single-wall system, with forcing specified in terms of the edge safety factor $q(r_p)$. Field structures (eigenfunctions) at (b) $q(r_p) < 1$, (c) $q(r_p) = 1$, and (d) $q(r_p) > 1$.

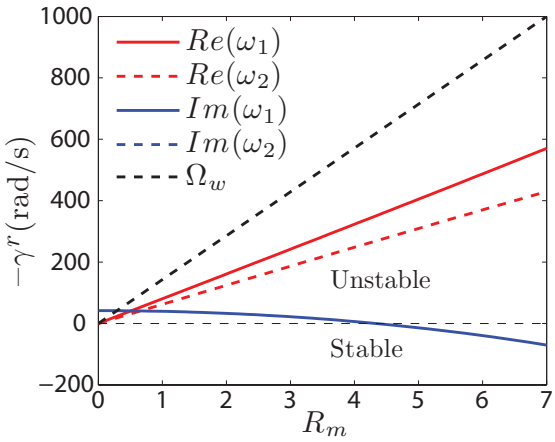

(a) Dispersion relation for the RWM in the Hegna model.

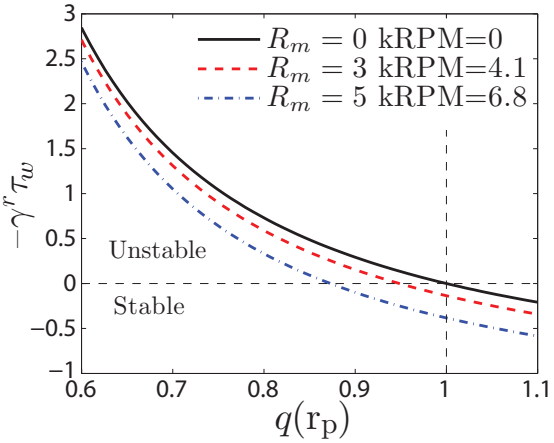

(b) RWM growth rates with wall rotation in the Hegna model.

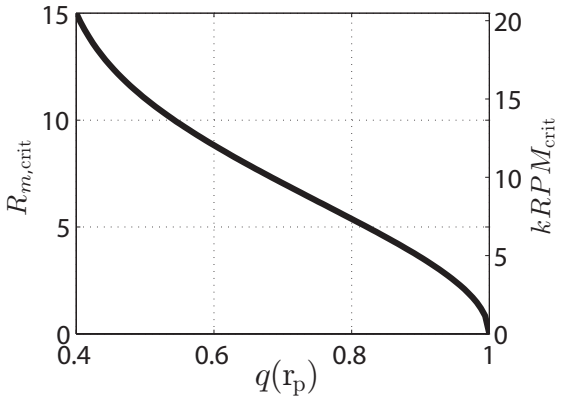

(c) Critical wall rotation for RWM stabilization in the Hegna model.

Figure 7.3: Predictions for RWM stability in the Hegna model [13].

wall. All cases are consistent with the condition $\gamma\tau_A \ll 1$.

7.1.4 Kink Stabilization by Wall Rotation

The model is thus able to predict a complex eigenvalue γ for a given $R_m, r_p, q(r_p)$. The behavior of the full Eq. 7.22 is now discussed. As the model current profile is top-hat like, a well-defined r_p exists and stability is uniquely determined by $q(r_p)$. First, the dispersion relation for a fixed equilibrium (single value of $q(r_p)$ and r_p) is explored, as shown in Fig.

7.3(a). A real frequency (rotation) is introduced to the RWM as Ω_w increases. As Eq. 7.22 predicts two roots (two modes), though one is always stable. The unstable root, however, is shown to become more stable as R_m is increased. At a critical R_m ($\equiv R_{m,\text{crit}} \approx 5$ for this equilibrium) the growth rate becomes negative and the RWM is stabilized. This is equivalent to Gimblett's original prediction shown in Fig. 1.2.

Figure 7.3(b) illustrates the dependence of the unstable mode γ^r as $q(r_p)$ is varied for a few R_m. For all R_m, decreasing $q(r_p)$ (increasing I_p or decreasing B_z) destabilizes the RWM. However, as R_m is increased, the stability curves are shifted such that a lower $q(r_p)$ can be achieved for the same level of stability (same γ^r). That is, more I_p or lower B_z could be used in a device without becoming unstable to the RWM. Figure 7.3(b) also illustrates that a critical $q(r_p)$ is required for RWM stabilization. For $R_m = 0$, this value is $q(r_p) = 1$, the Kruskal-Shafranov condition for the line-tied cylinder [2, 3].

This condition can be inverted, such that for a given $q(r_p) < 1$ a critical rotation ($R_{m,\text{crit}}$) is required to maintain stability to the RWM. This condition is given by:

$$R^2_{m,\text{crit}} = \frac{4\alpha_a(1-q(r_p))}{(\alpha_a-\alpha_b)(q(r_p)-1+\alpha_b)}\left[1+\left(\frac{\tau_b}{\tau_a}\right)\frac{q(r_p)-1+\alpha_b}{q(r_p)-1+\alpha_a}\right]^2 \tag{7.24}$$

where $\alpha_a \equiv (r_p/r_a)^2$, $\alpha_b \equiv (r_p/r_b)^2$. As $q(r_p)$ is decreased, faster rotation is required to maintain stability. Furthermore, coupling to the rotating wall, and thus stabilization, is found to be more effective as r_p approaches r_a ($\alpha_a \mapsto 1$).

The full two-wall dispersion relation of Eq. 7.20 illustrates a scaling very reminiscent of the two-wall vacuum field eigenmodes of Section 5.4.3. Once again, the introduction of rotation tends to bring the two eigenmodes to a more common value, slowing the fast root and speeding up the slow root. However, now $\gamma^r = 0$ lies between the two roots, thus raising the slow root requires it to transition through the stability threshold. Thus, stabilization of kink modes by wall rotation can also be thought of in terms of coupling the stable and unstable eigenmodes of the two-wall system. This was the theoretical result

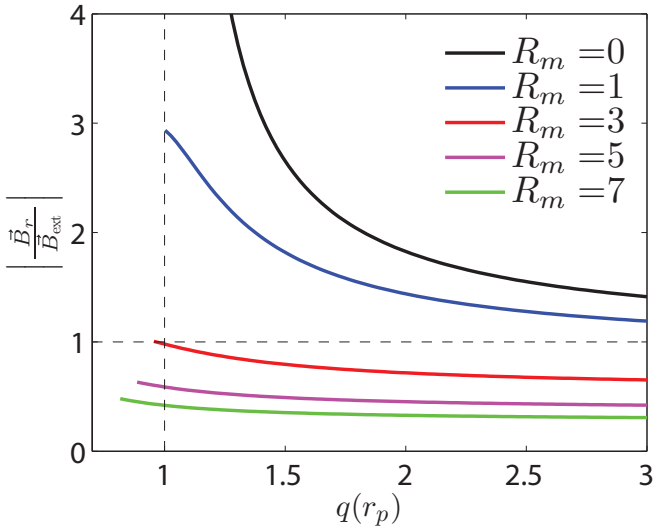

Figure 7.4: The amount of error field amplification (EFA) is shown as a function the safety factor ($q(r)$) and wall rotation R_m. At high $q(r_p)$ the error field is simply shielded, while at low $q(r_p)$ the wall rotation greatly reduces the amount of EFA.

was first conceptualized by Gimblett [9].

7.1.5 Error Field Amplification

With the linear stability solved, attention is now turned to the driven stable modes predicted by Eq. 7.18. Error field amplification (EFA, or also called resonant field amplification) is calculated by finding the steady-state ($t \mapsto \infty$) solution of Eq. 7.18 while allowing the forcing $\vec{B}_{\rm ext}$ to be finite. In the steady-state, $\frac{\partial}{\partial t} \mapsto 0$ and $\vec{A}$ is found by simple inversion of Eq. 7.18, such that $\vec{A}_{\rm EFA} = \left(\bar{\bar{M}}^{-1}\right)\vec{B}_{\rm ext}$, yielding:

$$\vec{A}_{\rm EFA} = \frac{2B_{\rm ext}}{2 - iR_m\left(\frac{r_p^2}{r_b^2}\left(\frac{1}{1-q(r_p)}\right) - 1\right)}\begin{bmatrix} 1 \\ \frac{r_p^2}{1-q(r_p)} \end{bmatrix} \tag{7.25}$$

which gives the field structure in all regions after using the definitions for A_n given after Eq. 7.18. To evaluate the magnitude of the EFA, the predicted total field $\vec{B}_{\rm EFA}|_{r=r_{\rm m}}$ at a measurement location $r_{\rm m}$ (taken to be just outside r_p in region I) is normalized to the

applied error field amplitude ($|\vec{B}_{\text{ext}}|$). This yields:

$$\frac{|B_{r,\text{EFA}}|}{B_{\text{ext}}} = \frac{\left|1 - \frac{r_p^2}{r_{\text{m}}^2}\left(\frac{1}{1-q(r_p)}\right)\right|}{\sqrt{1 + \frac{R_m^2}{4}\left(\frac{r_p^2}{r_b^2}\left(\frac{1}{1-q(r_p)}\right) - 1\right)^2}} \tag{7.26}$$

As the fields are steady state, only the rotating wall interacts with the error field and thus Eq. 7.26 has no dependence on the inner wall parameters. Figure 7.4 illustrates the behavior of the EFA as R_m and $q(r_p)$ is varied. When $R_m = 0$, as $q(r_p) \mapsto 1$ (the stability threshold) the EFA amplitude diverges. However, unbounded growth breaks the steady-state assumption and thus the full treatment of Eq. 7.18 is required [80]. Nonetheless, the EFA can be expected to approach large values in this regime.

Finite R_m modifies this picture. First, shielding of B_{ext} occurs, such that in the high-$q(r_p)$ (stable plasma) limit Eq. 7.26 is identically equal to the vacuum field result of Eq. 5.7. This has not been neglected as it was in the calculation of Γ_{ext} in Section 6.2.2. Second, the linear stability threshold is brought to lower $q(r_p)$ as R_m increases, thus finite EFA is present at lower $q(r_p)$ whereas otherwise instability would result. Note the EFA is not calculated where the kink is unstable ($\gamma^{\text{r}} < 0$) as a steady state cannot be reached. Third, and most importantly, the actual amplitude of the EFA is decreased. This is thought to be because of a poorer overlap of the kink eigenmode to the applied error field at large R_m. As $R_m \mapsto \infty$, the EFA vanishes.

It should also be noted that another model has been developed to predict EFA [81, 82, 80] which predicts that the amplification factor scales as $\frac{\gamma_{\text{vac}}}{\gamma_{\text{kink}}}$ (Eqs. 16-18 in Ref. [82]), where γ_{kink} would be the eigenvalue of the kink mode given by Eq. 7.20 and γ_{vac} would be the vacuum field eigenvalue given by Eq. 5.15. While the EFA as derived in Section 7.1.5 varies somewhat depending on which r_{m} is chosen, both methods yield broadly similar results for the impact of wall rotation on the EFA. In the model of Ref [81], the reduction in amplification can be seen to be due to the imaginary parts of both

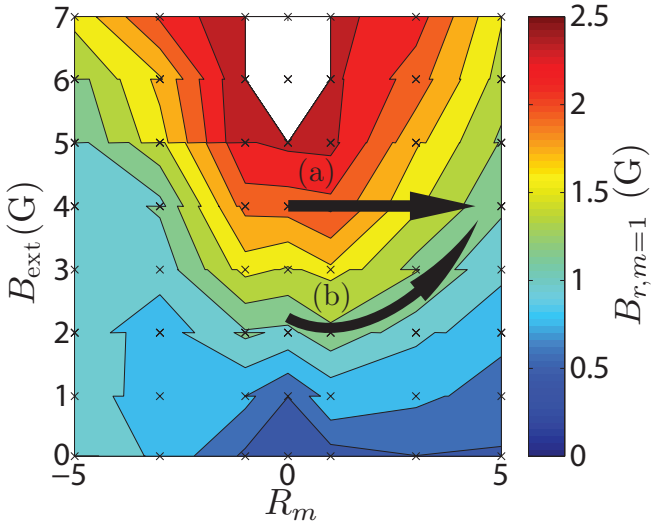

Figure 7.5: Contours of the measured $B_{r,m=1}$ field after 1-2 ms in the experiment, before the RWM becomes large. Increasing B_{ext} increases error field amplitude, while R_m decreases the error field through shielding. Arrow (a) indicates an experiment in which effective error field was variable although B_{ext} held fixed, in contrast to arrow (b) in which the effective error field was constant.

γ_{vac} and γ_{kink}, present when $R_m \neq 0$. Inclusion of a finite imaginary component removes the divergence at marginal stability ($\gamma^r_{\text{kink}} \mapsto 0$). Additionally, the study of Ref [80] is distinct from that treated herein due to the presence of differential wall rotation (multiple walls). Differential rotation precludes the use of Doppler shifts, and introduces non-linear Ω_w dependencies to both γ_{vac} and γ_{kink}.

7.2 Error Field Mitigation for Locked Discharges

As discussed in Chapters 5-6, the error field is of critical importance in the experiment. However, it was not included in the linear theory of Section 7.1. Furthermore, the error field cannot simply be minimized in the experiment, as that leads to rotating modes that do not lock during the discharge, as suggested by Fig. 6.5. It is clear that some amount of error field is necessary to lock the RWM. In turn, locked modes are necessary to observe

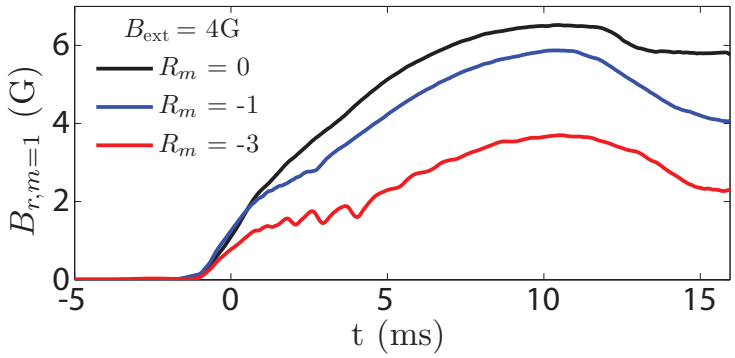

Figure 7.6: Increasing R_m while holding error field current constant reduces the effective error field and allows the RWM to remain unlocked for more of the discharge. This experiment corresponds to trajectory (a) in Fig. 7.5.

stabilization, as otherwise $\omega \gg \Omega_w$ and the wall would change speeds only very slightly in the plasma frame.

The experiment is further complicated by the fact that the error field is profoundly affected by wall rotation, as was detailed in Chapter 5. Figure 7.5 illustrates the dependence of the error field strength on the applied error field B_{ext} and wall rotation R_m, after a campaign of minimizing intrinsic error fields. This should be contrasted with Fig. 5.7, where a combination of B_{eq} and B_{ext} yielded large asymmetries in R_m.

For the rest of this Chapter beyond this Section, the complicating effect of the error field is minimized by performing discharges at constant effective error field while R_m is increased. This is done by tracing a diagonal trajectory in B_{ext} and R_m, corresponding to curve (b) in Fig. 7.5. Larger error field currents (larger B_{ext}) are applied at high R_m to yield the same effective error field. In this way, the time-traces of discharges are nearly identical for the first few ms, before the RWM amplitude becomes large.

Asymmetry in Wall Rotation due to Error Field Interactions

The importance of keeping the error field constant as R_m is increased is illustrated by way of contrast with experiments where this was not done. Figure 7.6 illustrates three

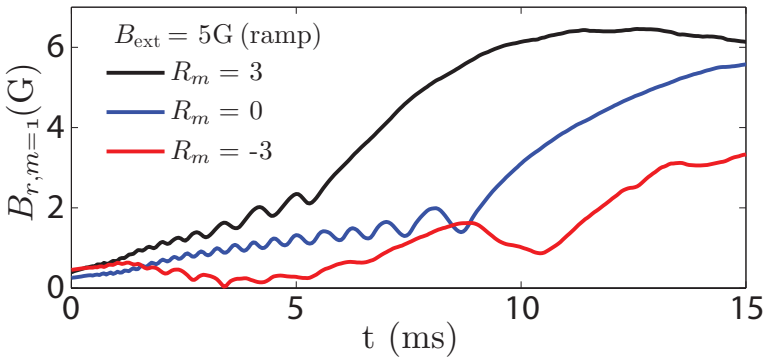

Figure 7.7: The effect of asymmetries in error field amplitude with R_m (discussed in Section 5.3.4) results in apparant asymmetric stabilization of the RWM in the experiment. Increasing error fields ($+R_m$) leads to earlier locking while -R_m leads to incomplete locking. Error fields are of the form of Fig. 5.7 for these discharges.

discharges where the current in the error field coil was held constant while R_m was increased, corresponding to trajectory (a) in Fig. 7.5. Clearly, the zeroth order effect is that the mode is allowed to remain unlocked for a longer duration as the error field has been reduced. This figure should be contrasted with Fig. 6.5, where similar effects are seen by directly reducing $B_{\rm ext}$.

Figure 7.7 illustrates the effect of changing R_m while holding $B_{\rm ext}$ constant in the presence of large error field asymmetries in R_m, as might be expected from Fig. 5.7. For $R_m = 3$, a larger error field is found and RWM locking and destabilization happens earlier. In contrast, $R_m = -3$ reduces the error field and again allows the mode to remain unlocked for a longer duration. Note that the $R_m = -3$ illustrates more complex dynamics in both amplitude and phase and is seen to never fully lock during the discharge. Again, for both directions, the zeroth order effect of the rotating wall on the RWM is indirect. The rotating wall modifies the error field, which in turn modifies the RWM dynamics. It is for this reason that all subsequent results are obtained with the effective error field as constant as possible.

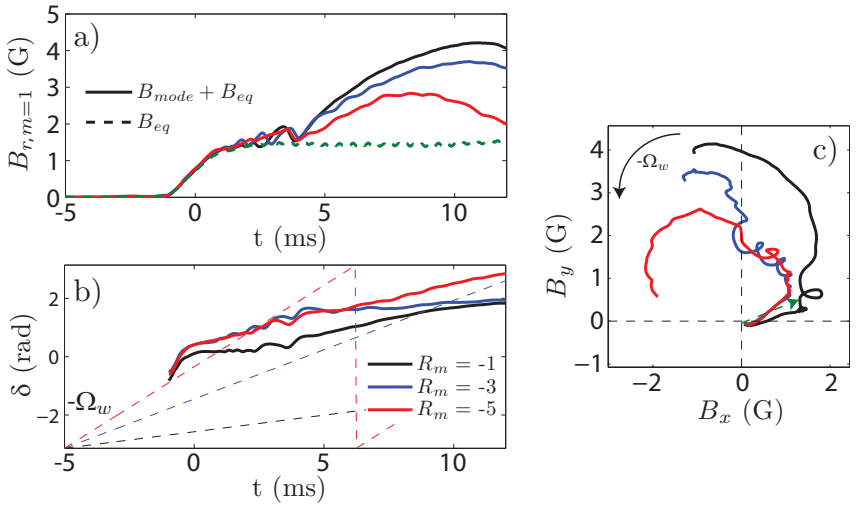

Figure 7.8: Time-traces of (a) amplitude, (b) phase, (c) hodogram of the $m = 1$ component of B_r at different wall rotation rates (R_m), while holding B_{ext} and B_{eq} constant. Dotted lines in (b) indicate the rate of wall rotation. This experiment corresponds to trajectory (b) in Fig. 7.5.

7.3 Locked Mode Stabilization by Wall Rotation

The stabilizing effect of wall rotation on the RWM is most clearly demonstrated for discharges which lock during the discharge lifetime, shown in Fig. 7.8. Holding the error field constant (as described in Section 7.2) in a regime where the RWM locks during the discharge lifetime allows the stabilizing effect of the wall to be isolated. This corresponds to trajectory (b) in Fig. 7.5. It is found that increasing $|R_m|$ both reduces the growth rate of B_{mode} from the B_{eq} baseline and imparts rotation (ω) to the locked mode. Qualitatively, these results are in agreement with the theory of Section 7.1 as will be described.

It is important to note that the displayed error field traces (B_{eq} in Fig. 7.8) are experimentally obtained by minimizing $\tilde{B}_z$ such that the mode rotates very quickly (kHz scale, irrespective of B_{ext}) as suggested by Fig. 6.4. B_{mode} is thus shielded from the flux-loop array by the conducting walls and only B_{eq} is measured. This technique is imperfect, as can be seen from both the slight deviation of B_{eq} from the mean of $B_{\text{mode}} + B_{\text{eq}}$ from 0-4

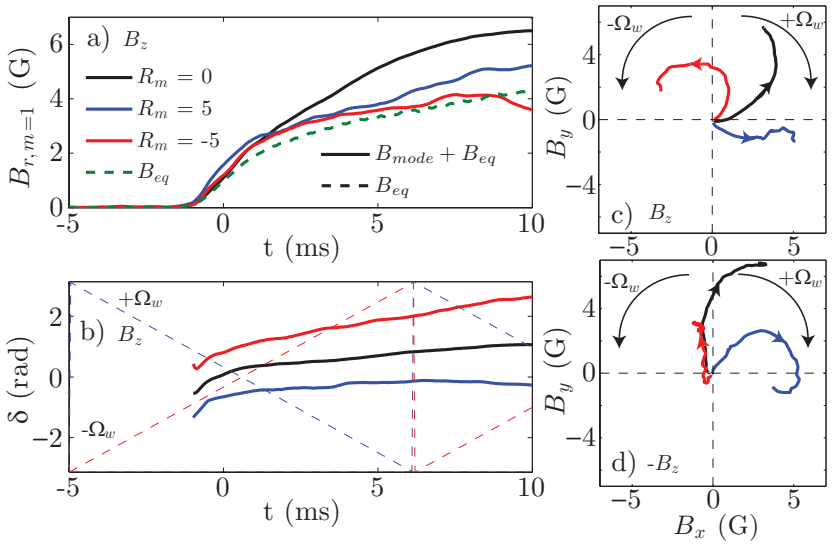

Figure 7.9: Time-traces of locked-mode (a) amplitude, (b) phase, (c) hodogram of the $m = 1$ component of B_r at different wall rotation rates (R_m), while holding B_{ext} and B_{eq} constant. Dotted lines in (b) indicate the rate of wall rotation. (d) Hodogram at similar R_m, B_{eq}, and B_{ext} though with B_z reversed.

ms, as well as the difference between B_{eq} from $R_m = 0$ to $R_m = -5$.

Hodograms (Fig. 7.8c) clearly illustrate the discontinuous behavior at the locking bifurcation, which occurs just after the final circular motion. Progressively larger locked mode real frequencies (ω) are also observed as R_m is increased. The locked mode rotation is found to be roughly consistent with the theoretical prediction of $\omega \approx \Omega_w/2$ given in Eq. 7.22, though measurements are complicated by the fact that ω is not constant during the locked mode evolution. It is also clear that the low R_m locked mode is not exactly at $\omega = 0$, but that a small residual rotation is present. This will be shown to lead to an observed asymmetry in R_m.

Asymmetry in Wall Rotation due to Residual Mode Rotation

The residual locked mode rotation (ω) is found to lead to a modest asymmetry in wall rotation direction. Inspection of Fig. 6.5c illustrates that even in the $R_m = 0$ case a

low level residual mode rotation remains whose direction is opposite to the initial plasma ExB rotation. This requires an additional anomalous torque (Γ_{anom}) which does not vanish when $\omega = 0$ and is oppositely directed to the ExB restoring torque (Γ_{res} in Chapter 6). This torque is not included in the analysis of Chapter 6. However, as the residual ω (and thus Γ_{anom}) is very small, Γ_{anom} is thought to be unimportant in the mode locking bifurcation itself thus the conclusions of Chapter 6 are still valid.

Figure 7.9 illustrates the consequences of Γ_{anom} once the mode is locked: wall rotation with Ω_w counter-aligned to Γ_{anom} decreases the residual rotation, yielding mode-locking roughly to the static wall (vacuum vessel). Discharges with Ω_w co-aligned to Γ_{anom} increases the residual rotation, bringing ω closer to Ω_w. To confirm that Γ_{anom} arises from plasma phenomenon (as opposed to error field interactions), the residual rotation is examined upon reversal of B_z. This is found to reverse this asymmetry (shown in Fig. 7.9d), thus confirming the importance of the relative rotation of the wall with respect to all plasma drifts. This should be contrasted with Fig. 5.6, where B_z reversal was found to not affect the error field asymmetry with R_m.

Despite the asymmetry in R_m, reductions in the growth rate and mode amplitude are seen in both directions. The two traces are not identical however, though the level of discrepancy is not large and thus no conclusions are drawn. The possibility of asymmetry in R_m in RWM stabilization will be treated in Section 7.4 using born-locked modes.

7.4 Born-Locked Mode Stabilization by Wall Rotation

Experiments utilizing born-locked modes allow the demonstration that $|R_m| > 0$ operation increases the window of RWM-stable operation, as shown in Fig. 7.10. Discharges are carried out at constant B_z and B_{ext}, such that RWM onset is found as I_p is increased

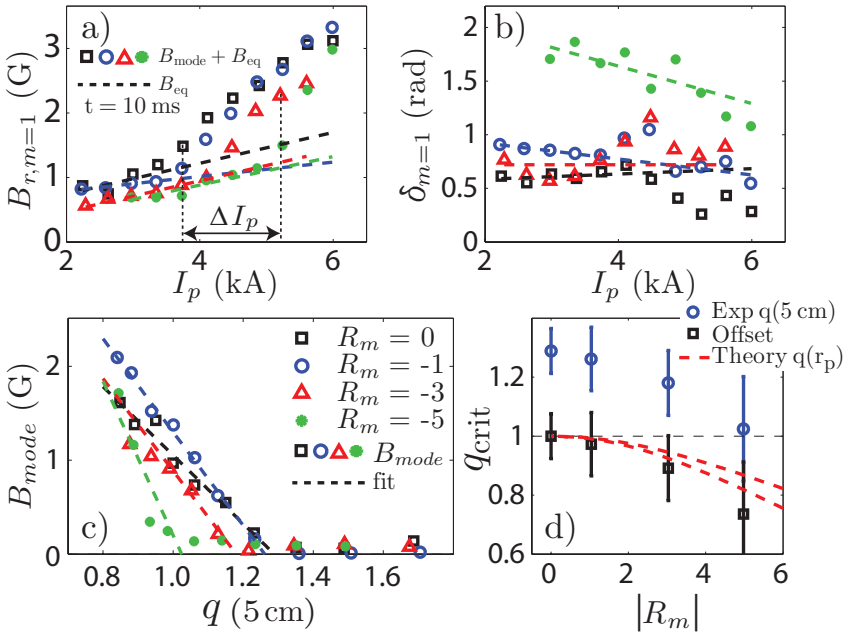

Figure 7.10: (a) $B_{r,m=1}$ amplitude diverges from $B_{\rm eq}$ at a critical I_p which is raised as R_m increases. (b) Phases of B_{mode} + $B_{\rm eq}$ also vary as I_p increases. (c) B_{mode} amplitude as a function of q as measured by the anode ring at $r = 5$ cm. (d) Comparison of experimental data and theoretical predictions of the critical q ($q_{\rm crit}$) for instability . The squares in (d) have been offset such that $q_{\rm crit} = 1$ for $R_m = 0$.

($q(r)$ decreased). Shot-to-shot reproducibility is used to scan I_p as each data point in Fig. 7.10 is a separate discharge. Born-locked modes (largest amplitude region of Fig. 7.5) are used to avoid confusion between locking thresholds and RWM onset conditions [26]. This is especially important given that wall rotation also modestly alters the locking threshold (ω_{lock}), as discussed in Section 6.4.

Onset is determined by noting where $B_{\text{mode}} + B_{\text{eq}}$ diverges from the B_{eq} baseline as I_p is raised, as shown in Fig. 7.10a,b. As B_{ext} is not directly measured and B_{eq} arises from plasma equilibrium currents, B_{eq} is linear in I_p. A subtraction of a linear fit to B_{eq} is carried out to isolate the RWM signature, B_{mode}. Figure 7.10c illustrates B_{mode} amplitude, with higher $|R_m|$ operation yielding mode onset at lower $q(r)$ as measured by the 5 cm radius anode ring of the segmented anode. The resultant critical q for RWM onset (q_{crit}) as $|R_m|$ is increased is shown in Fig. 7.10d and compared to the theoretical prediction. Specifically, the experimental q_{crit} is taken from the zero-crossing of the fits in Fig. 7.10c with errors derived from the confidence intervals of this fit. Theoretical curves are directly calculated from Eq. 7.24, taking $r_p = 6.5$, 7.5 cm for the upper, lower curve respectively and using the parameters of Table 5.1. Defining a single r_p for the experimental plasma is ambiguous and thus a source of uncertainty. Also note the model q profile is constant for $r < r_p$. The experimental q_{crit} is larger than the theoretical prediction for all R_m, as will be discussed in Section 6.5. Offsetting the experimental data such that $q_{\text{crit}} = 1$ when $R_m = 0$, the change in q_{crit} as $|R_m|$ increases ($\equiv \Delta q_{\text{crit}}$) is found to be in agreement with theory. Similar agreement is found if the data is scaled rather than offset. It is also found that the stabilizing effect is relatively modest until high R_m is achieved, consistent with the quadratic scaling of Eq. 7.24. Furthermore, although $q(5\text{ cm})$ has decreased by $\approx 25\%$ ($I_p(5\text{ cm})$ increased by $\approx 25\%$), total current ΔI_p has increased by $\approx 35\%$ as shown in Fig. 7.10a. Larger I_p plasmas are thus less peaked and have a larger plasma radius r_p, providing a second-order stabilizing effect.

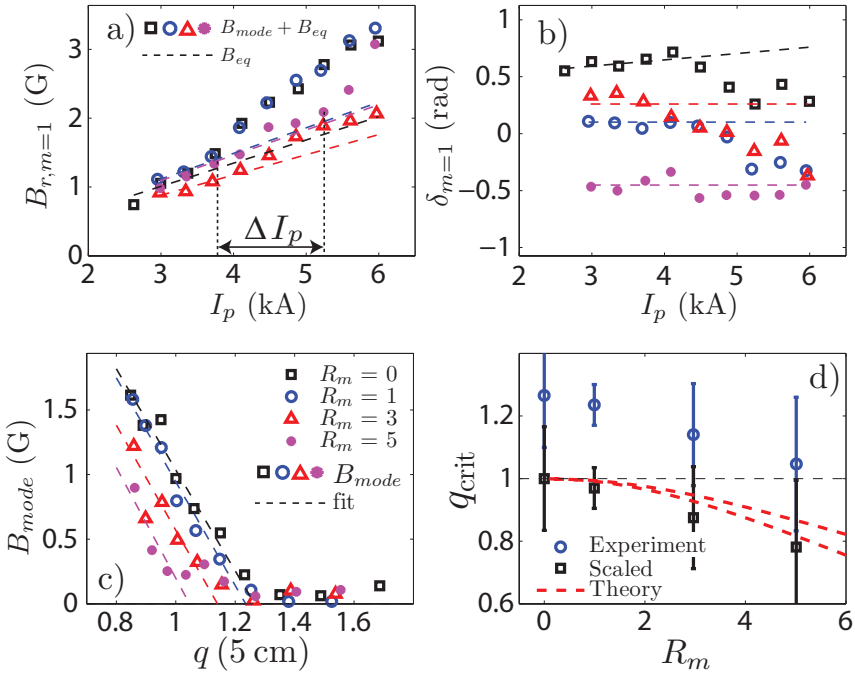

Figure 7.11: Stabilization of the born-locked RWM with co-rotation.

Symmetry in Wall Rotation

Born-locked mode stabilization with wall rotation in the co-rotation direction ($+R_m$) is explored and contrasted with counter-rotation. Using the same experimental procedure as before, RWM onset with co-rotation is shown in Fig. 7.11. RWM Onset is once again determined by noting where $B_{\text{mode}} + B_{\text{eq}}$ diverges from the B_{eq} baseline as I_p is raised. Subtracting B_{eq} from the signals, the residual B_{mode} is found to appear at lower $q(r_p)$ as R_m is increased. Figure 7.11d contrasts the experimental observation with the theoretical prediction of Eq. 7.24. Once again, the onset is found to be above $q(r_p) = 1$ at $R_m = 0$. Scaling the data such that $q_{\text{crit}} = 1$ when $R_m = 0$, it is also once again found that the scaled experimental data is somewhat below the theoretical prediction, though the large error bars preclude definitive conclusions. Error bars are larger at high R_m due to the availability of fewer points in the fits of Fig. 7.11c. The confidence intervals of these fits are the stated error bars.

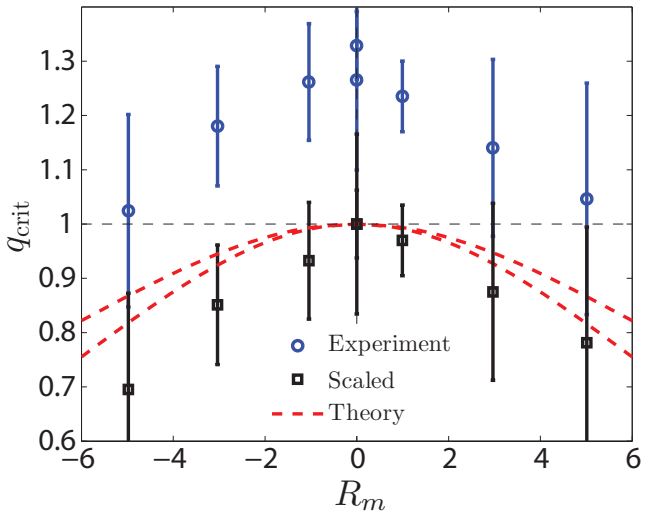

Figure 7.12: Locked mode stabilization in both directions of R_m

A summary of born-locked mode onset for the range of R_m studied in this experiment is shown in Fig. 7.12. Both directions are found to be stabilizing, and both directions showed the onset of instability above $q(r_p) = 1$. Thus, while asymmetries in R_m have been found with error field interactions (Section 5.3.4) and mode-locking (Section 6.2.5), no asymmetries in born-locked mode stabilization are found at the level of precision of the experiment. As the error field has been held constant, the only likely remaining source of asymmetry in this study is the plasma flow. Thus, as no asymmetry is found it can be inferred that any residual plasma flow in the born-locked mode is unimportant.

7.5 Locked Mode Eigenfunction

Large locked modes in the experiment yield clear measurements of the eigenstructure of the RWM. As all channels of the B_r fluxloop array are digitized simultaneously, the structure is also known as a function of time. Furthermore, using the theory of Section

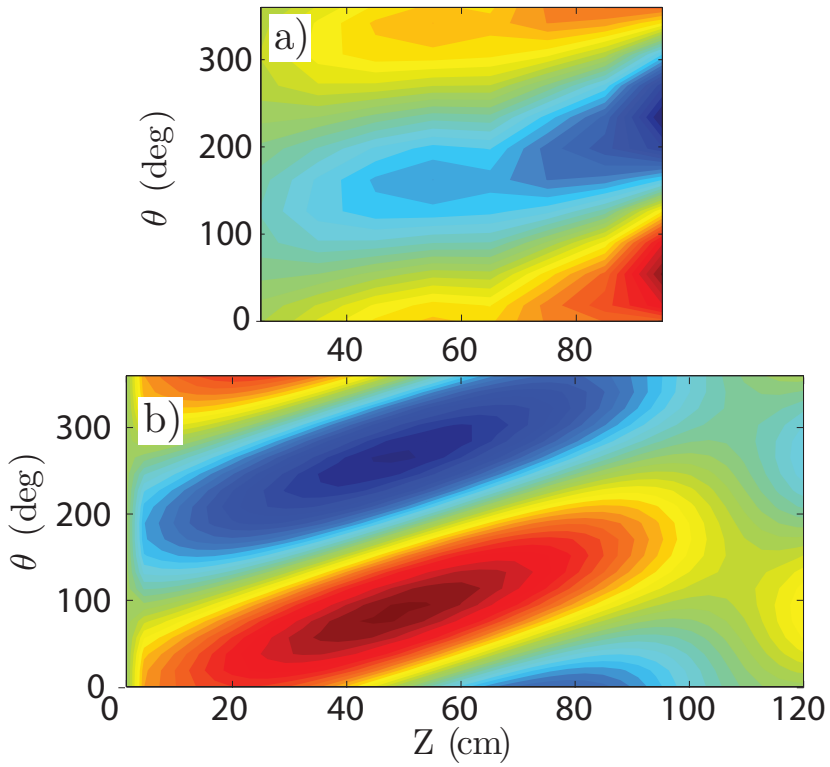

Figure 7.13: Contour maps of (a) experimental vs (b) theoretical mode eigenfunctions (B_{mode}) as measured by the B_r fluxloop array. Distances are measured from the cathode while the anode (not shown) is at Z = 123 cm. The smaller size of (a) reflects the axial extent of the fluxloop array.

7.1, a prediction for the eigenmode structure is possible:

$$\tilde{\xi}(r,\theta,z) = f(r)e^{i\theta+i(-\frac{B_\theta r_p}{r_p B_{z0}}+\frac{\lambda_0}{2(1-\Delta_+)})z}\sin\left(\frac{n\pi z}{L}\right) \tag{7.27}$$

$$\tilde{B} = \nabla\times(\tilde{\xi}\times B_0) \tag{7.28}$$

Experimental RWM eigenfunctions (shown in Fig. 7.13a) are found to be anode localized in contrast to theoretical predictions of Eq. 7.28 (shown in Fig. 7.13b). While the cause of this cathode-anode asymmetry is not fully understood, it is possible that significant axial flows (V_z) measured in the device (discussed in Section 2.4.4) are advecting the RWM eigenfunction away from the device midplane. This effect has been predicted by the theory of Ryutov which treated the plasma as a rigid, infinitely long conducting wire [46]. However, as axial flow is not included in the theory of Hegna (Section 7.1), this effect is not captured in Fig 7.13b. Also important to match theory to experiment would be the proper treatment of the axial flows at the line-tied boundary. Some treatments [61] allow this flow to be sinked at the boundary (presumably due to surface recombination) while others enforce it to zero. Interestingly, these same studies have found that the flow can be either stabilizing or destabilizing, depending on the relative strength of V_z to V_A. Furthermore, the azimuthal flow and flow shear, which is especially strong in the cathode region (Z $<$ 60 cm) as shown experimentally in Section 2.4.4, has not been treated. This flow shear may be locally stabilizing the mode in the cathode region, thus also contributing to the asymmetry. Note that structure in the cathode side of Fig. 7.13a is without helicity and is dominated by $\vec{B}_{\rm eq}$. Further measurements of the flow profile in the locked mode and comparison with a computational stability calculation would be required to elucidate the dynamics of the locked-mode eigenfunction. It should also be noted that although detailed internal studies were not made of the eigenfunction, it shares basic similarities with the structure of the mode leading to the helical equilibrium state

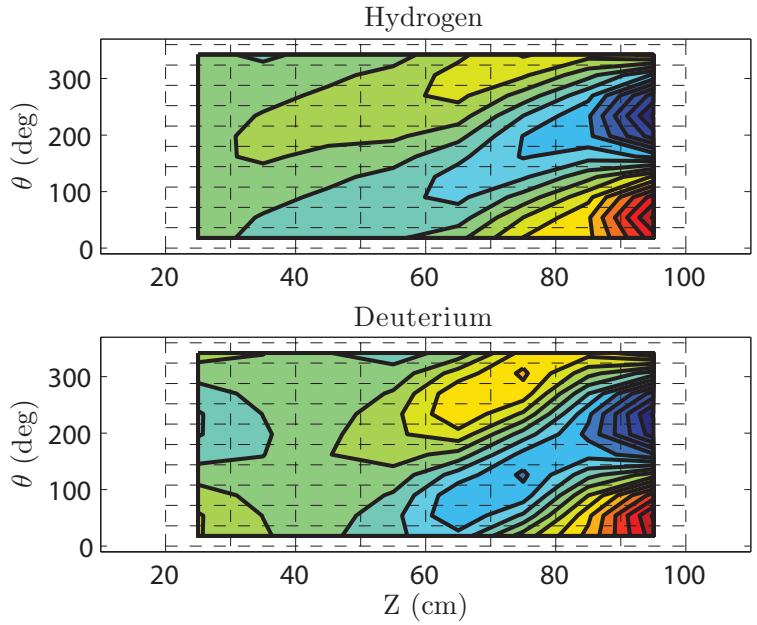

Figure 7.14: Comparison of hydrogen and deuterium locked mode eigenfunctions

described in Chapter 3. However, while the eigenfunction is similar, the mode leading to the helical equilibrium was not stabilized by increasing B_z, unlike the mode described in this Chapter.

Role of Ion Mass

While the device cannot directly control the axial flow, different isotopes of hydrogen can be used in the device to attempt to slow down the dynamical timescales. For example, fuel gas is injected into the plasma guns at the local sound speed, which is naturally a function of the ion (molecular) mass. Comparing hydrogen (H) and deuterium (D) discharges it was found that hydrogen plasmas tended to exhibit faster unlocked mode rotation (ω) and consequently were more difficult to lock. Not enough data was collected to systematically compare this difference in all discharge scenarios, though it was found that approximately an extra 10 G of $\tilde{B}_z$ was required to achieve the same rotation rates in H as in D, using the notation of Section 6.3.1.

Locked mode eigenfunctions of hydrogen (H), the nominal gas used throughout this thesis, and deuterium (D) are shown in Fig. 7.14. Interestingly, the anode localization is less pronounced in D plasmas than H plasmas, potentially supporting the notion that the localization is related to the axial flow. Notwithstanding, further flow measurements and comparison with computation are required to confidently understand this observation.

7.6 Discussion

Locked mode stabilization in the device has shown qualitative agreement with the theory of Section 7.1, with wall rotation increasing the RWM stability window, decreasing the mode growth rate, and imparting rotation to the RWM. Notwithstanding, several discrepancies remain. Exponential growth is not observed, likely due to the inherent nonlinearities present in the mode-locking bifurcation. The neglected effect of plasma flow is also thought to be the cause of the anode localization of the RWM eigenfunction, the residual locked mode rotation, and the subsequent asymmetry in wall rotation direction seen in the experiment.

The error field amplification calculation presented in Section 7.1.5 raises an interesting question regarding the born-locked mode observations of Section 7.4. In fact, the born-locked mode results could equally well be interpreted as a reduction in the error field amplification due to wall rotation (compare Fig. 7.4 to Fig. 7.10c). It is likely beyond the reach of a short pulse device to definitively state whether or not the born-locked mode observation represents a 'true instability' as opposed to an amplification of the error field. In the tokamak, these two effects were differentiated by pulsing the error field on and off and noting whether or not the mode signature grew or decayed [83, 84, 85]. Nonetheless, for both phenomena the same underlying physics is at play - it is wall stabilization that both reduces the error field amplification and extends the stability window.

Further, although Δq_{crit} is found to be in fairly good agreement, q_{crit} is measured to be larger in experiment ($q(5\text{ cm}) = 1.3$) than in theory ($q(r_p) = 1.0$). This disagreement is most likely explained by non-ideal MHD effects neglected in the model used to derive Eq. 7.24. Here again the flow profile may be to blame if it alters the underling MHD stability [61]. Also not included is the role of resistivity [86], and pressure [87]. Additionally, as the experimental current profile does not resemble the top-hat model, a more accurate treatment of the current profile and magnetic shear [77] is likely required to reach better agreement. Any deviation from the line-tying boundary condition would also increase q_{crit} [46].

Experimentally, the coarseness of the $q(r)$ measurement also introduces uncertainty, which is also related to the presence of significant magnetic shear in the device. Furthermore, the addition of guide field ripple ($\tilde{B}_z$) discussed in Section 6.3 introduces significant axial structure to the plasma column. Thus, the 1-D formulation of $q(r)$ strictly speaking no longer applies, and 2-D corrections calculated by integration of the full 2-D equilibrium would be required to accurately determine the instability criteria. This problem would likely be tractable only through computation.

Chapter 8

Conclusion

This thesis is structured such that discussion of results is provided within each Chapter. As such, only a summary view of the thesis is here provided, along with suggested avenues of future work on the device. Also note that much of the content of this thesis has already appeared in the peer-reviewed literature [88, 89, 90, 91, 92].

8.1 Summary of Thesis

This thesis has measured the magnetic structure of the Rotating Wall Machine plasma and detailed the various means by which a rotating conducting wall interacts with the plasma column and its MHD instabilities.

The design, manufacture, and implementation of a high-speed rotating wall was carried out successfully. The rotating wall achieved speeds of ≈ 300 km/h, or $R_m > 5$, in a safe, consistent, and routine manner. The entire device was also nursed through several years of experimental campaigns and associated maintenance and upgrade duties.

Insertable probes (B-dot, Mach, Langmuir) were used to characterize the plasma of the Rotating Wall Machine. This thesis detailed mostly B-dot measurements, which confirmed that the device plasma is exceedingly high β, and transitions from diamagnetic at

low I_p to paramagnetic at high I_p. A boundary layer effect was discovered at the device anode, inside of which MHD confinement is drastically lost leading to a likely radial outflow of particles from the column. At high I_p a helical equilibrium state was discovered and reconstructed using correlation techniques.

Insertable probes were also used to illustrate that the device's discretized flux ropes merge to form an axisymmetric profile within a short spatial distance of the guns. Measurements provided diffusion scale lengths and coefficients for comparison to theory, though further work is necessary to isolate the physical mechanism allowing non-ambipolar cross-field transport in the device.

The interaction of error fields with the rotating wall was shown to lead to asymmetries in wall rotation. Analytic theory was used to obtain a complete picture of these interactions and their asymmetries, illustrating that the total error field for a given wall rotation is complex and can often overcome the natural shielding of the wall. This proved vital to understand later measurements of the unstable plasma. Vertical field penetration was understood using normal mode analysis, yielding intuitive and quantitative understanding of why the vertical field penetration time decreases as wall rotation increases.

Understanding and subsequent reduction of the error field yielded the discovery of MHD mode-locking in the device. Analytic theory was employed to develop a torque balance model for this phenomenon including the effect of the error field, wall rotation and plasma ExB rotation. This model proved successful in qualitatively explaining the interaction of error fields and wall rotation with the rotating plasma, and predicted the observed mode-locking bifurcations. Asymmetry in wall rotation was also found, with only wall counter-rotation eliminating the mode-locking bifurcations.

Using locked and born-locked RWMs, the stabilizing effect of the rotating wall on the RWM was experimentally demonstrated. The rotating wall was found to decrease the locked mode growth rate and increase the stable operating window to higher I_p. It was

also found that the RWM could be prevented from locking, as the rotating wall shielded the error field necessary to lock the RWM. This effect could be asymmetric depending on the error field structure, with one direction of wall rotation locking the RWM earlier in time and the other direction inhibiting locking. The locked mode was also found to have a low-level residual rotation at 0 R_m, which Doppler shifted the resultant locked mode rotation at finite R_m. The extension of the RWM stability window was found to be symmetric in R_m within the precision of the measurement.

To conclude, the varied role of the rotating wall on the RWM was captured by considering the error field interactions, the mode-locking bifurcations, and the dynamics of the locked modes. This study provides a firm foundation for future studies in devices with flowing liquid metal walls, where much of the same phenomenology should occur. This study has also shown that the device is a model system for studying the interaction of MHD modes with error fields, resistive walls, and plasma flows. These results present a striking parallel to the development of RWM stability in the toroidal geometry, confirming that common underlying physical mechanisms are at play.

8.2 Implications for Future Experiments

This experiment has tested, for the first time, the effects of moving conductors on plasma stability. Should future devices be constructed with rotating solid or flowing liquid metal boundaries it is natural to ask what insights can be extrapolated from this work.

First and foremost, it has been shown that moving conductors modify the error field in non-intuitive ways. If a device has been constructed with an error field correction system designed for static wall operation, the requirements on control may be quite different from the system with moving conductors. Said differently, the error field eigenmodes of the static wall system are profoundly different from the eigenmodes of the moving wall system, and may overlap less well with the field from a set of correction coils. Furthermore, if the wall rotation speed is expected to vary throughout an experimental campaign, error field correction must be re-evaluated at each value of speed. For this experiment, error fields from misalignments could be canceled by currents in external (trim) coils. However, upon rotation of the wall this cancellation no longer occurred and the error field quickly rose. There is no reason to expect this behavior is not universal.

Beyond error fields, this work has shown that fast counter-rotation of a rotating boundary can effectively inhibit mode-locking bifurcations. This is a favorable result for future devices, as mode-locking is usually followed by a disruption and thus should be avoided. Furthermore, the stabilizing effect of a rotating boundary has been demonstrated in experiment. Thus, devices with flowing boundaries could be expected to operate closer to or beyond existing stability boundaries due to the stabilizing effect of the flow.

8.3 Future Work

While this thesis has elucidated many of the key effects of a moving boundary on the MHD stability of the linear plasma column, much room for future work exists. Roughly following the order of the thesis:

The Rotating Wall Machine is a flexible device which can robustly excite rotating and locked RWMs. Future upgrades could include a further lengthening of the plasma duration, such that a more complete steady state is reached on the time scale of RWM dynamics ($\approx 10\tau_w$). More importantly, the guns are known to produce cold and dense plasmas, which consequently have an exceedingly low Lundquist number. If a new plasma source were developed for the experiment (such as LaB_6), perhaps hotter and more collisionless plasmas would be generated. As it has been explained that the azimuthal flow is a direct consequence of the large resistivity in the device, this would also likely reduce the intrinsic ExB rotation present.

The device was also not designed with a serious campaign of error field reduction in mind. While in this study meticulous alignment of various conductors minimized the error field, a more concerted design-level effort could be undertaken. This would have the benefit of removing the 'intrinsic' error field as an unknown quantity. Likely some external error field would still be required, but at least it would be fully understood.

A fruitful area of further study involves a rigorous campaign of internal profile measurements (using probes) on plasmas which go through the locking bifurcations described in Chapter 6. Many of the approximations made in that analysis could be relaxed with dedicated measurements, and comparison with fully non-linear computational codes such as NIMROD, which has recently been extended to include resistive walls [93], may be possible. This may form a useful benchmark for the numerical codes as mode-locking is a fundamentally non-linear phenomena not before observed in such a simple configuration.

Also in the area of mode locking, an area of future study could involve the active con-

trol of the plasma ExB flow either through a fast switching power supply controlling $\tilde{B}_z$, internal bias probes, or through the biasing of the plasma gun assemblies. Experiments could then more deterministically approach the mode-locking bifurcation point and also transition through to the mode-unlocking bifurcation if desired. The hysteresis could then be measured and compared to the predictions of the simple mode-locking model or future non-linear computations.

A final avenue for future work on the experiment is the construction of a similarly scaled azimuthal manifold through which a liquid metal can flow. As the original motivation for the experiment was to compare solid conductors with liquid metals, in this sense the experiment is not yet complete. While the rotating wall cannot be strongly affected by the back-reaction of the MHD onto the flow, the same cannot be said of a liquid metal. Additionally, turbulence is likely to exist in the manifold, which could affect mode dynamics in unknown ways.

Appendices

Appendix A

Glass Wall Experiments

The effects of a hybrid insulating-conducting boundary condition on kink dynamics were explored in the device. A glass liner was placed inside the vacuum vessel, allowing radial electric fields to exist at the edge while eddy currents could still be maintained in the conducting walls. The kink mode was not able to lock to the wall in this configuration, precluding analysis of RWM stability. Interestingly, an $m = 2$ mode was found to be dominant within a narrow window of I_p.

It was shown in Chapter 6 that significant radial electric fields (E_r) were present throughout the device which gave rise to large ExB flows. However, E_r cannot exist at the conducting wall, and this was corroborated by measurement. In order to modify this constraint, a liner made of Simax® (similar to Pyrex®) was inserted within the vacuum vessel. The experimental geometry is shown in Fig. A.1. As the glass liner can allow finite E_r at the edge, it was thought that broader current profiles with reduced core ExB rotation could be achieved.

A.1 Lack of Kink Mode Wall-Locking

A first result of this campaign was that the kink mode was still found to rotate with kHz scale frequencies, well above the range where the rotating wall could affect the dynamics.

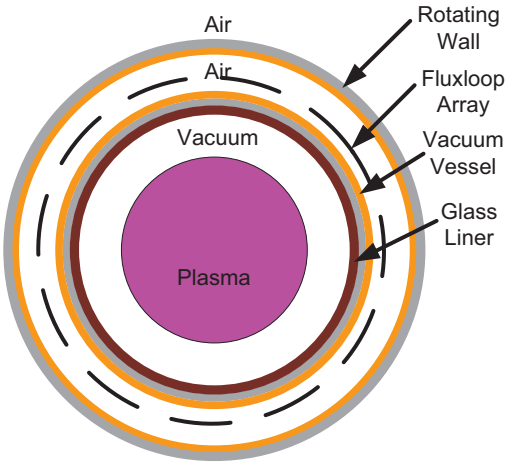

Figure A.1: End-on view of the experimental geometry with the glass liner.

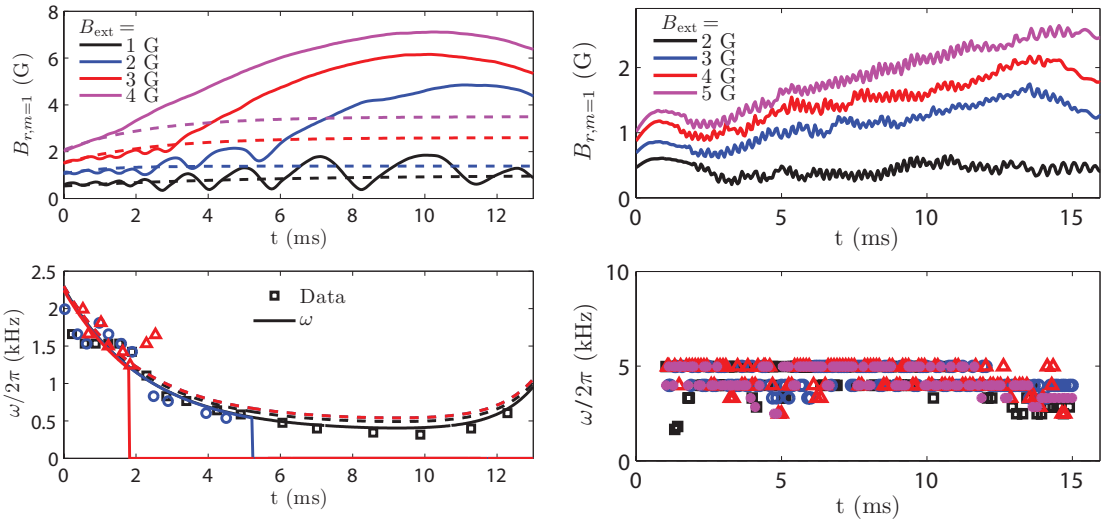

(a) Locking by B_{ext} without the glass liner

(b) With the glass liner, application of B_{ext} does not lock the mode.

Figure A.2: Comparison of the effect of B_{ext} in kink mode locking with and without the glass liner.

Furthermore, the technique of applying localized $m = 0$ fields ($\tilde{B}_z$), described in Chapter 6, was found to be ineffective in slowing down the rotation. Thus, it can be inferred that axisymmetric radial currents (and associated torques) are inhibited by the glass liner.

The application of a large error field (B_{ext}) was unable to lock the kink mode, as contrasted in Fig. A.2. This was likely a consequence of the inability of $\tilde{B}_z$ to slow the mode, as a slowly rotating kink (≈ 1 kHz) was a precondition for locking via B_{ext} to occur, as described in Chapter 6. Nonetheless, as the mode could not be locked experiments on RWM stabilization could not be carried out. The rotating wall did continue to interact with the error fields in a manner identical to what was described in Chapter 5.

A.2 Appearance of m = 2 Mode

An entirely unexpected consequence of the glass liner was the appearance of a dominantly $m = 2$ mode within a limited window in I_p. The contrast of the magnetic fluctuations with (Fig. A.3(a)) and without (Fig. A.3(b)) the glass wall is stark. With the liner, the dominant fluctuations were $m = 2$ unlike the kink modes ($m = 1$) seen with the purely conducting wall. Figure A.3(c) illustrates several discharges where both between $m = 1$ and $m = 2$ modes is seen. In terms of I_p, (and q), the window of excitation of the $m = 2$ mode is shown in Fig. A.3(d). This is in contrast to the kink mode explored throughout this thesis, in which the largest fluctuations are observed at the highest values of I_p.

Recent work by Khalzov [94] has theoretically predicted the existence of a stability window for higher m modes, which could potentially be destabilized at lower I_p than the $m = 1$. The stability is a strong function of the plasma flow, which is consistent with the hypothesis that the glass wall can modify the E_r (and thus ExB flow) profile. Further analysis of the glass wall modes is beyond the scope of this thesis.

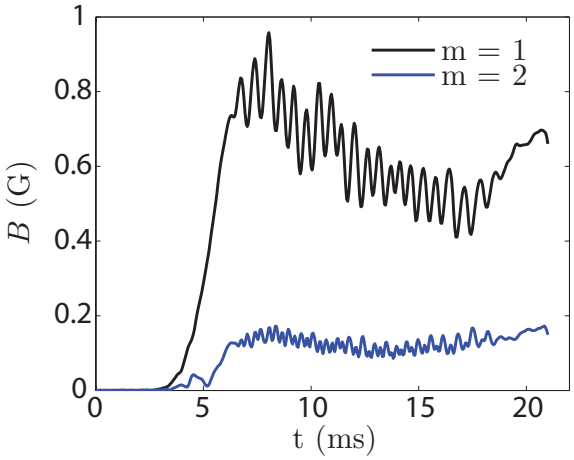

(a) Magnetic fluctuations without the glass liner, with a dominant kink mode.

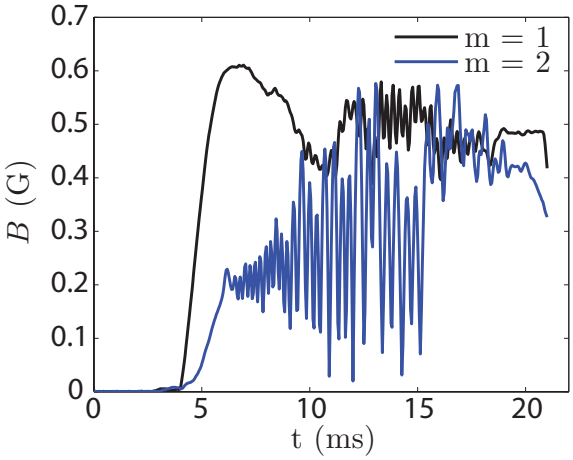

(b) Magnetic fluctuations with a glass liner, with a dominant $m = 2$ mode.

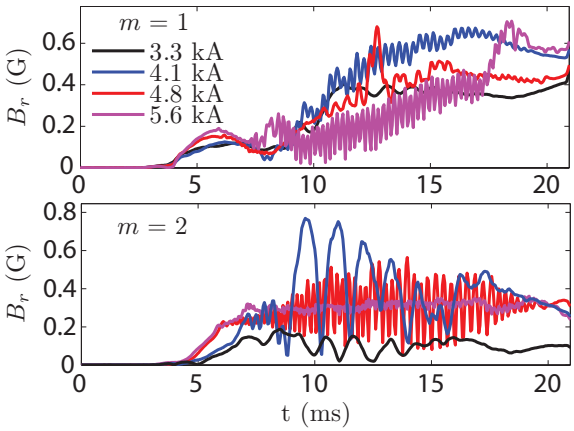

(c) Various glass-liner discharges indicating the appearance of the $m = 2$ mode within a narrow window in I_p.

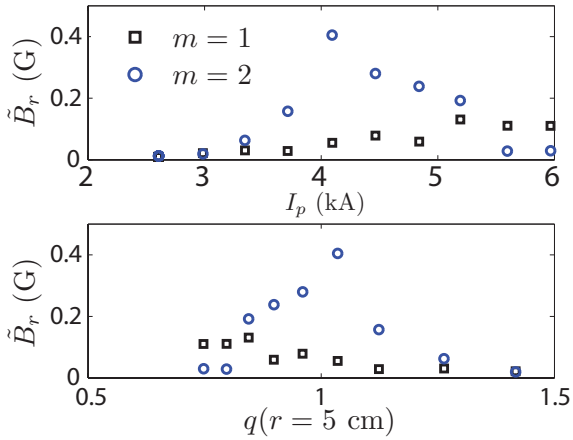

(d) Scaling of mode fluctuations with $I_p \propto q^{-1}$.

Figure A.3: Appearance of $m = 2$ mode with glass wall boundary conditions

Appendix B

Residual Magnetism in the Rotating Wall

Evidence is presented to illustrate that low-level magnetic fields (< 1 G) measured whenever the rotating wall spins in a magnetic field is due to low-level residual magnetism in the wall stainless steel. The technique to subtract this signal is presented and the impact on signal fidelity is described.

The high-speed rotating wall used throughout this thesis was made partly out of a 304 stainless steel (304SS), which was specified to be in fully annealed condition prior to machining. However, 304SS is susceptible to cold-work magnetization, and as such the finished product was left with a small amount of residually magnetic 'hot spots'. Magnetic surveys indicate that these hot spots were no greater than those of the device's other (static) 304SS components. However, as the wall rotates at high speed, the signals from the moving hot spots were readily detected by the sensitive flux loop array. While small, these signals initially posed difficulties as they prevented proper subtraction of integrator drift and subsequently introduced non-physical artifacts. In the rest of this Section the physical basis for the magnetic hot spot interpretation will be given, as well as the procedures taken to mitigate them.

B.1 Identification of Residual Magnetism

When the rotating wall spins in the presence of the axial guide field (B_z), signals of $\leq 1G$ are detected on all fluxloops of the B_r array, hereafter called B_{res}. A sample of B_{res} from a single coil of the B_r array is shown in Fig. B.1(a). B_{res} has an oscillatory behavior, and its period is exactly equal to that of the wall rotation period. Thus, B_{res} is 'locked' to the rotating wall. As the fluxloop array only measures time-varying fields, wall rotation is required to observe this signal. Looking at the entire B_r array as a whole (shown in Fig. B.1(b)) B_{res} is strongest at localized positions on the wall and no large-scale structure is observed. This is in contrast to what might be expected from motor-generator type behavior, where the dominant field would be large scale.

Scaling of B_{res} amplitude with guide field illustrates that B_{res} originates from residual magnetism in the steel wall. Figure B.1(c) illustrates that the structure of B_{res} is independent of field strength. However, even at $B_z = 0$, B_{res} is still visible and its structure is maintained. As no free currents are in the system with $B_z = 0$, this B_{res} must arise from magnetization currents. Furthermore, Fig. B.1(d) indicates that B_{res} does not scale linearly with B_z, another hallmark of magnetization. Thus, B_{res} is an unwanted and non-ideal component of the experiment, and efforts were taken to confidently subtract it from all subsequent analysis, as described in Section B.2.

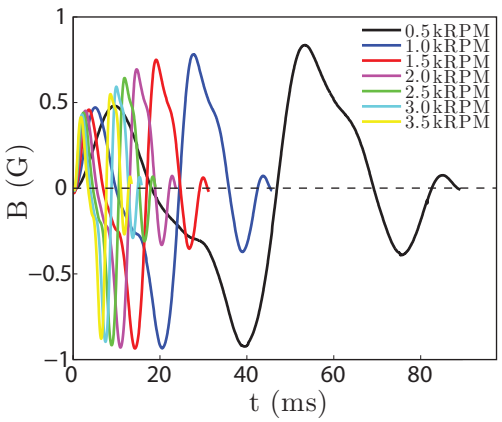

(a) Measurement of B_{res} from a single fluxloop.

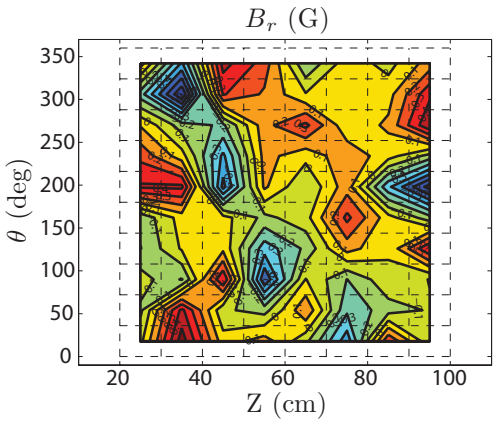

(b) Distribution of B_{res} throughout the fluxloop array, illustrating the random 'hot spots'.

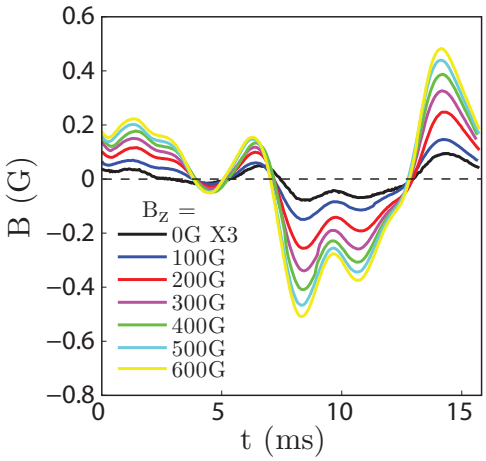

(c) B_{res} at various guide field strengths. Note that at $B_z = 0$, B_{res} is still visible and has the same structure as at large B_z.

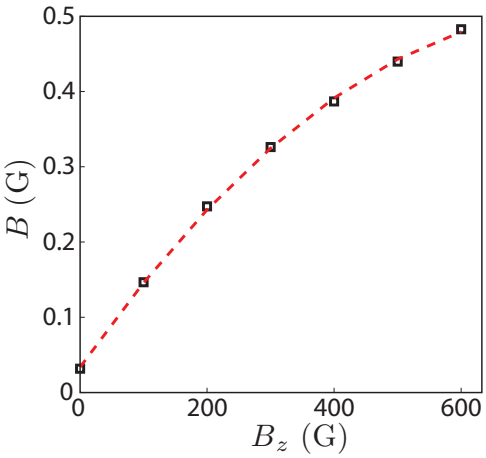

(d) Amplitude Scaling with B_z is non-linear, precluding the interpretation of B_{res} as motor-generator induced fields.

Figure B.1: Properties of residual magnetism signal, B_{res}

B.2 Subtraction from Plasma Data

As B_{res} is 'locked' to the wall, its subtraction requires knowledge of the wall phase throughout the discharge. This was measured on the experiment by directly digitizing the optical tachometer signal, which registered a pulse when a reflective sticker passed into its field of view. This pulse was also used as a trigger for the entire discharge, thus the phase of the wall during a discharge was known and controllable. With wall phase controlled, a baseline shot without plasma at a given speed was taken, which contained only B_{res}. This was then subtracted from all other plasma discharges at that wall speed. Baseline discharges every few hours indicated that B_{res} was constant over this timescale.

A conducting rod substituting for the plasma column (described in Chapter 5) was used to confirm the validity of this subtraction scheme. As the rod required no guide field to form a discharge, shots were taken without B_z and thus without B_{res}. Figure B.2(a) illustrates the results of this comparison. In this figure, the hypothesis is that:

$$\vec{B}_{\text{pure}} = \vec{B}_{\text{raw}} - \vec{B}_{\text{res}} \equiv \vec{B}_{\text{subtracted}} \tag{B.1}$$

The good agreement between B_{pure} and $B_{\text{subtracted}}$ indicates this is a good approximation. Figure B.2(b) shows the agreement of B_{pure} and $B_{\text{subtracted}}$ at a variety of R_m, using this same method.

Turning to real plasma data, Fig. B.2(c), the impact of the subtraction of B_{res} is found to be small. Firstly, the magnitude of B_{pure} is generally much smaller than the plasma signal in the presence of an instability. Furthermore, the phase-matched subtraction described above is effective in removing B_{res} from the plasma signal. Note B_{pure} is not available for plasma data as the discharge cannot be formed without the guide field. It should be noted that an implicit assumption is that the plasma does not respond significantly to B_{res}, thus violating the identity of Eq. B.1. This is not rigorously known,

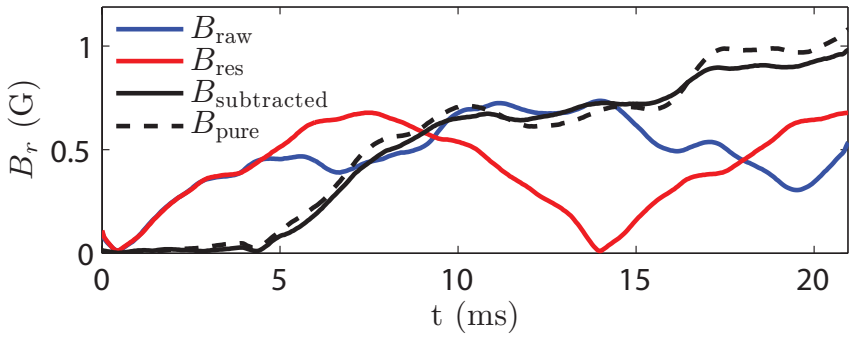

(a) Illustration of subtraction, steel rod, $R_m = 3.3$

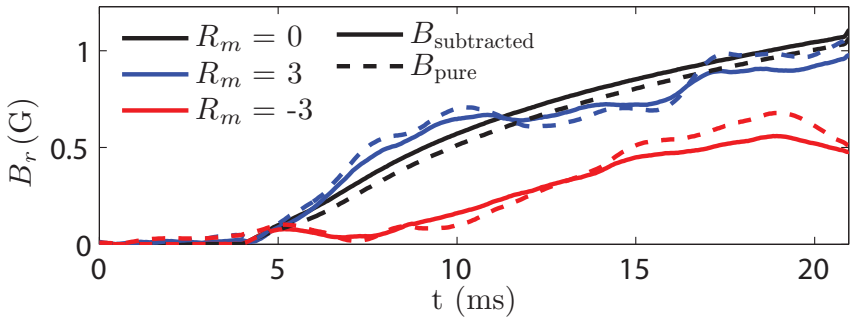

(b) Effectiveness of subtraction, steel rod, various R_m

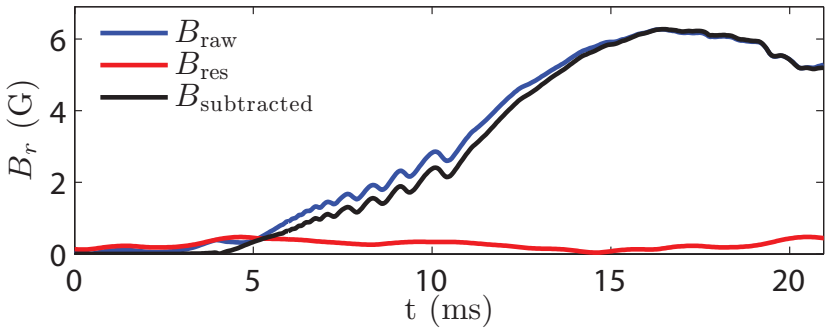

(c) Impact on real plasma data

Figure B.2: Subtraction of residual magnetism (B_{res}) from raw (B_{raw}) signals as measured by the fluxloop array. Data is from both the rigid rod and plasma as indicated. B_{pure} is from steel rod discharges with $B_z = 0$, thus no residual magnetism is present.

though the low amplitude of B_{res} lends some confidence that this is not an issue.

Similar residual magnetism issues were encountered at the Princeton Magneto-Rotational Instability (MRI) Experiment [95]. The solution there was to rebuild the experiment using as little stainless steel and as much plastic components as possible, especially on machined ports. This was deemed not a practical option on the rotating wall due to the large stresses on the wall. In conclusion, while it has been shown that magnetic 'hot spots' do not preclude analysis of the plasma in the device, it must be said that in hindsight a much more vigilant awareness of residual magnetism was warranted during device construction. Anneal often.

Appendix C

Thick Wall Error Field Calculations

For the entirety of this thesis calculations involving eddy currents within the walls of the device have been treated in a thin-wall formalism. This Appendix is included to illustrate the implications of relaxing this constraint, both for the steady-state and time-dependent analysis carried out in Chapter 5. First the induction equation is solved within the rotating and static walls, and matching problems are solved to determine the field structure and vertical field penetration time constant.

C.1 Magnetic Field Functional Form

Evolution of the magnetic field inside of a thick, rotating, conducting wall is given by the induction equation:

$$\frac{\partial \vec{B}}{\partial t} = \nabla \times \vec{V} \times \vec{B} + \frac{1}{\sigma \mu} \nabla^2 \vec{B} \tag{C.1}$$

Each term is treated in sequence. The long-cylinder approximation is maintained, such that B_z and derivatives in $\hat{z}$ are neglected. Letting $\vec{B} \propto \exp \gamma t$, the time derivative simply pulls out γ. γ is a complex quantity describing exponential growth, decay, or oscillations.

To calculate the advection Term, letting $\vec{V} = \Omega_w r\hat{\theta}$, for solid conductor rotation:

$$[\vec{V} \times \vec{B}]_{\hat{z}} = -V_\theta B_r \tag{C.2}$$

$$\left[\nabla \times \vec{V} \times \vec{B}\right]_{\hat{r}} = \frac{1}{r}\frac{\partial [\vec{V} \times \vec{B}]_{\hat{z}}}{\partial \theta} \tag{C.3}$$

$$= -\frac{1}{r}\frac{\partial (\Omega_w r B_r)}{\partial \theta} \tag{C.4}$$

$$= -\Omega_w \frac{\partial B_r}{\partial \theta} \tag{C.5}$$

This equation has to be transformed into an equation for only B_r. For the diffusion operator, an identity is used:

$$\nabla^2 \vec{B} = -\nabla \times (\nabla \times \vec{B}) + \nabla(\nabla \cdot \vec{B}) \tag{C.6}$$

$$= -\nabla \times (\nabla \times \vec{B}) \tag{C.7}$$

$$= -\left[\frac{1}{r^2}\frac{\partial}{\partial r}\left(r\frac{\partial B_\theta}{\partial \theta}\right) - \frac{1}{r^2}\frac{\partial^2 B_r}{\partial \theta^2}\right]\hat{r} + \frac{\partial}{\partial r}\left[\frac{1}{r}\frac{\partial}{\partial r}(rB_\theta) - \frac{1}{r}\frac{\partial B_r}{\partial \theta}\right]\hat{\theta} \tag{C.8}$$

Such that the radial component of the diffusion operator is given by:

$$\left[\frac{1}{\mu\sigma}\nabla^2 \vec{B}\right]_{\hat{r}} = -\frac{1}{\mu\sigma}\left[\frac{1}{r^2}\frac{\partial}{\partial r}\left(r\frac{\partial B_\theta}{\partial \theta}\right) - \frac{1}{r^2}\frac{\partial^2 B_r}{\partial \theta^2}\right] \tag{C.9}$$

The divergence equation states that $\frac{\partial}{\partial r}(rB_r) = -\frac{\partial B_\theta}{\partial \theta}$ which then allows B_θ to be replaced in Eq. C.9, yielding:

$$\left[\frac{1}{\mu\sigma}\nabla^2 \vec{B}\right]_{\hat{r}} = \frac{1}{r^2\mu\sigma}\left[r^2\frac{\partial^2 B_r}{\partial r^2} + 3r\frac{\partial B_r}{\partial r} + B_r + \frac{\partial^2 B_r}{\partial \theta^2}\right] \tag{C.10}$$

With all terms computed, the full vector induction equation (Eq. C.1) can now be ex-

pressed in terms of the scalar B_r:

$$0 = \gamma B_r + \Omega_w \frac{\partial B_r}{\partial \theta} - \frac{1}{r^2 \mu \sigma}\left[r^2 \frac{\partial^2 B_r}{\partial r^2} + 3r\frac{\partial B_r}{\partial r} + B_r + \frac{\partial^2 B_r}{\partial \theta^2}\right] \tag{C.11}$$

Using the $m = 1$ nature of the desired field solution, such that $B_r(r,\theta) \propto e^{-i\theta}$, to evaluate the $\hat{\theta}$ derivatives. Cancellation of terms occurs, yielding an ODE for B_r:

$$r^2 \frac{\partial^2 B_r}{\partial r^2} + 3r\frac{\partial B_r}{\partial r} + r^2 \mu\sigma(i\Omega_w - \gamma)B_r = 0 \tag{C.12}$$

A coefficient $\alpha^2 \equiv \mu\sigma(i\Omega_w - \gamma)$ is now defined. This is a Bessel equation in a transformed Bowman form [96]:

$$x^2 \frac{\partial^2 y}{\partial x^2} + (2p+1)x\frac{\partial y}{\partial x} + (\alpha^2 x^{2n} + \beta^2)y = 0 \tag{C.13}$$

where $y = B_r$, $x = r$, $p = 1$, $\beta = 0$, $n = 1$. Eq. C.13 has a solution of the form [96]:

$$f(x) = x^{-p}\left[A_1 J_{\frac{\sqrt{p^2-\beta^2}}{n}}\left(\frac{\alpha}{n}x^n\right) + A_1 Y_{\frac{\sqrt{p^2-\beta^2}}{n}}\left(\frac{\alpha}{n}x^n\right)\right] \tag{C.14}$$

With these substitutions, the solution for B_r can be found to be:

$$B_r(r,\theta) = \frac{1}{r}\left[A_1 J_1(\alpha r) + A_2 Y_1(\alpha r)\right] e^{-i\theta} \tag{C.15}$$

Using $\nabla \cdot \vec{B} = 0$, the B_θ solution is also readily obtained.

$$B_\theta(r,\theta) = -i\left[A_1\left(\alpha J_0(\alpha r) - \frac{1}{r}J_1(\alpha r)\right) + A_2\left(\alpha Y_0(\alpha r) - \frac{1}{r}Y_1(\alpha r)\right)\right] e^{-i\theta} \tag{C.16}$$

C.2 Thick Wall Vertical Field Penetration

If the shaft is hollow, then the full solution of Eqs. C.15-C.16 must be kept, giving field solutions of the form:

$$B_r(r,\theta) = \frac{1}{r}\left[A_1 J_1(\alpha r) + A_2 Y_1(\alpha r)\right] e^{-i\theta} \tag{C.17}$$

$$B_\theta(r,\theta) = -i\left[A_1\left(\alpha J_0(\alpha r) - \frac{1}{r}J_1(\alpha r)\right) + A_2\left(\alpha Y_0(\alpha r) - \frac{1}{r}Y_1(\alpha r)\right)\right] e^{-i\theta} \tag{C.18}$$

These field equations are then used in a matching problem to calculate vertical field penetration field structures with a rotating wall. In this case, two matching regions are present at $r = \{a, b\}$, the inner and outer radius. This gives 4 equations for 4 unknowns. Canceling the $e^{-i\theta}$ dependence yields:

$$\hat{r} : (B_0 - A_1 b^{-2}) = \frac{1}{b}\left[C_1 J_1(\alpha b) + C_2 Y_1(\alpha b)\right] \tag{C.19}$$

$$\hat{\theta} : (B_0 + A_1 b^{-2}) = \left[C_1\left(\alpha J_0(\alpha b) - \frac{1}{b}J_1(\alpha b)\right) + C_2\left(\alpha Y_0(\alpha b) - \frac{1}{b}Y_1(\alpha b)\right)\right] \tag{C.20}$$

$$\hat{r} : D_1 = \frac{1}{a}\left[C_1 J_1(\alpha a) + C_2 Y_1(\alpha a)\right] \tag{C.21}$$

$$\hat{\theta} : D_1 = \left[C_1\left(\alpha J_0(\alpha a) - \frac{1}{a}J_1(\alpha a)\right) + C_2\left(\alpha Y_0(\alpha a) - \frac{1}{a}Y_1(\alpha a)\right)\right] \tag{C.22}$$

This is written in matrix form with the coefficients $= [A_1, C_1, C_2, D_1]$.

$$\begin{bmatrix} \frac{1}{b^2} & \frac{1}{b}J_1(\alpha b) & \frac{1}{b}Y_1(\alpha b) & 0 \\ -\frac{1}{b^2} & \left(\alpha J_0(\alpha b) - \frac{1}{b}J_1(\alpha b)\right) & \left(\alpha Y_0(\alpha b) - \frac{1}{b}Y_1(\alpha b)\right) & 0 \\ 0 & \frac{1}{a}J_1(\alpha a) & \frac{1}{a}Y_1(\alpha a) & -1 \\ 0 & \left(\alpha J_0(\alpha a) - \frac{1}{a}J_1(\alpha a)\right) & \left(\alpha Y_0(\alpha a) - \frac{1}{a}Y_1(\alpha a)\right) & -1 \end{bmatrix} \begin{bmatrix} A_1 \\ C_1 \\ C_2 \\ D_1 \end{bmatrix} = \begin{bmatrix} B_0 \\ B_0 \\ 0 \\ 0 \end{bmatrix}$$

Inverting the matrix yields the required coefficients:

$$G = \alpha a J_0(\alpha b)Y_0(\alpha a) + 2Y_0(\alpha b)J_1(\alpha a) - \alpha a Y_0(\alpha b)J_0(\alpha a) - 2J_0(\alpha b)Y_1(\alpha a) \tag{C.23}$$

$$A_1 = \frac{B_0 b}{\alpha G}\left[\alpha^2 ab(J_{0b}Y_{0a} - Y_{0b}J_{0a}) + 2\alpha(a(Y_{1b}J_{0a} - J_{1b}Y_{0a})\right.$$
$$\left. + b(Y_{0b}J_{1a} - J_{0b}Y_{1a})) + 4(J_{1b}Y_{1a} - Y_{1b}J_{1a})\right] \tag{C.24}$$

$$C_1 = \frac{2B_0}{\alpha G}(\alpha a Y_0(\alpha a) - 2Y_1(\alpha a)) \tag{C.25}$$

$$C_2 = -\frac{2B_0}{\alpha G}(\alpha a J_0(\alpha a) - 2J_1(\alpha a)) \tag{C.26}$$

$$D_1 = \frac{2B_0}{G}(J_1(\alpha a)Y_0(\alpha a) - Y_1(\alpha a)J_0(\alpha a)) \tag{C.27}$$

The coefficients are then inserted into the field solution, given by the real component of:

$$B_{r,r>b}(r,\theta) = (B_0 - A_1 r^{-2})e^{-i\theta} \tag{C.28}$$

$$B_{\theta,r>b}(r,\theta) = -i(B_0 + A_1 r^{-2})e^{-i\theta} \tag{C.29}$$

$$B_{r,a<r<b}(r,\theta) = \frac{1}{r}\left[C_1 J_1(\alpha r) + C_2 Y_1(\alpha r)\right] e^{-i\theta} \tag{C.30}$$

$$B_{\theta,a<r<b}(r,\theta) = -i\left[C_1\left(\alpha J_0(\alpha r) - \frac{1}{r}J_1(\alpha r)\right) + C_2\left(\alpha Y_0(\alpha r) - \frac{1}{r}Y_1(\alpha r)\right)\right] e^{-i\theta} \tag{C.31}$$

$$B_{r,r<a}(r,\theta) = D_1 e^{-i\theta} \tag{C.32}$$

$$B_{\theta,r<a}(r,\theta) = -iD_1 e^{-i\theta} \tag{C.33}$$

Figure C.1 shows solution fieldlines to the field of Eqs. C.28-C.33 shows similar behavior to that of Fig. 5.3, though now with the behavior in the wall resolved. As with Fig. 5.3, flux exclusion and phase shifting occurs. However, the limit that $\delta\phi \mapsto \pm\pi$ at $R_m \mapsto \pm\infty$ is now relaxed. Thicker walls produce larger phase shifts.

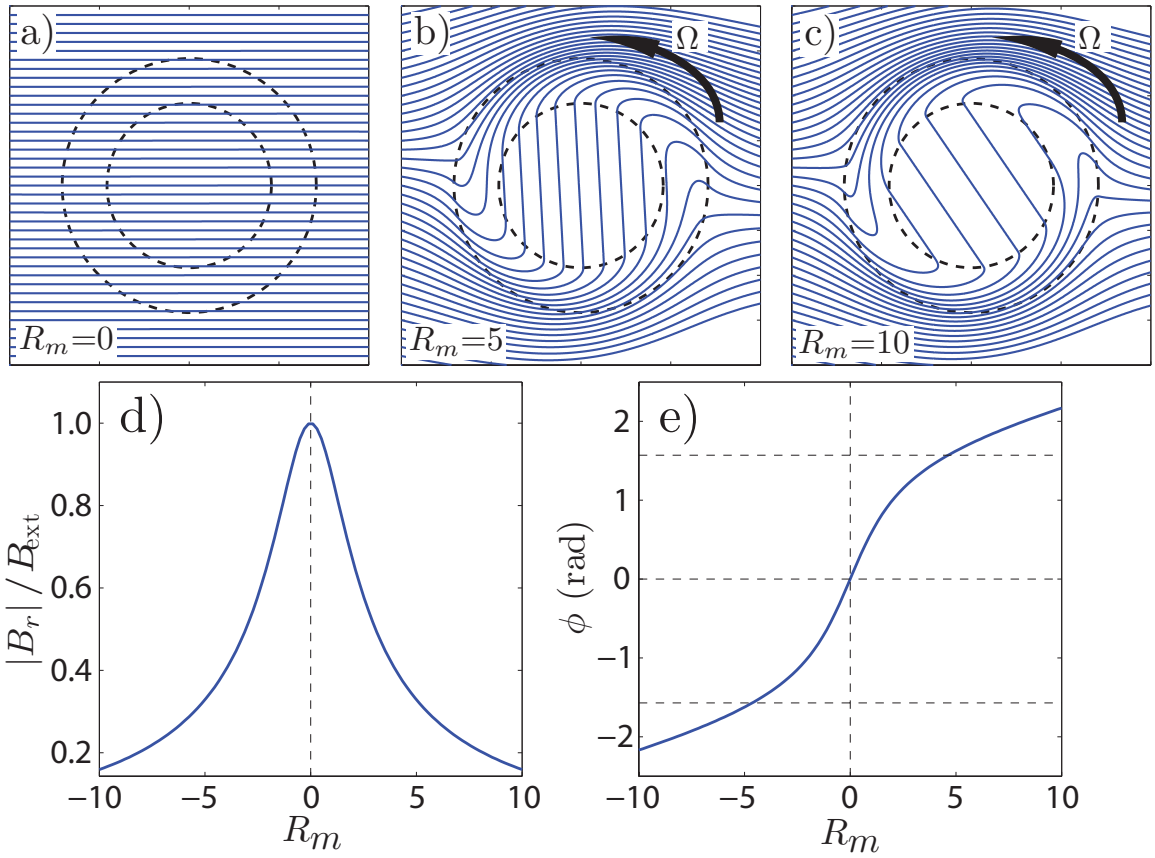

Figure C.1: (a)-(c) Fieldlines for hollow thick shell penetration at a variety of wall rotation speeds (R_m). (d)-(e) Flux exclusion and resultant phase shift for the thick wall.

C.3 Solid Shaft Field Penetration

The solution to the fields, given in Eqs. C.15-C.16, are modified if the shaft is solid. As $r = 0$ is included in the solution boundary, then coefficient A_2 must vanish. The solution is then:

$$B_r(r,\theta) = \frac{1}{r} A_1 J_1(\alpha r) e^{-i\theta} \tag{C.34}$$

$$B_\theta(r,\theta) = -iA_1 \left(\alpha J_0(\alpha r) - \frac{1}{r} J_1(\alpha r) \right) e^{-i\theta} \tag{C.35}$$

Only one boundary exists, at $r = a$, which matches the solid shaft solution C.35 and the infinite vacuum solution described in Section 5.2.1. The matching equations are:

$$\hat{r} : (B_0 - A_2 a^{-2}) = \frac{1}{a} A_1 J_1(\alpha a) \tag{C.36}$$

$$\hat{\theta} : (B_0 + A_2 a^{-2}) = A_1 \left(\alpha J_0(\alpha a) - \frac{1}{r} J_1(\alpha a) \right) \tag{C.37}$$

This system of equations is solved to give the required coefficients. Note this case has been treated in Perry [97].

$$A_1 = \frac{2B_0}{\alpha J_0(\alpha a)} \tag{C.38}$$

$$A_2 = a^2 B_0 \left(1 - \frac{2J_1(\alpha a)}{\alpha a J_0(\alpha a)} \right) \tag{C.39}$$

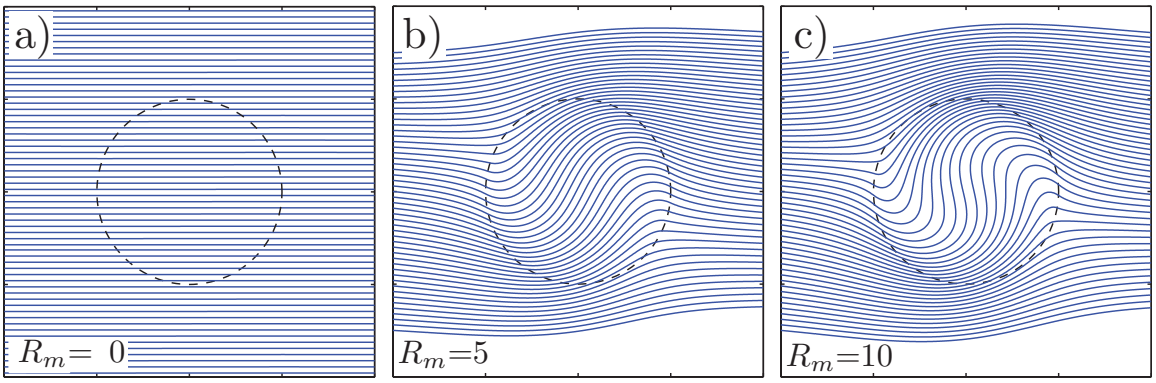

Figure C.2: Field solution for penetration through a solid rotating shaft at various rotation speeds (R_m)

The solution to the fields in this case is then the real component of:

$$B_{r,out}(r,\theta) = B_0\left[1 - \frac{a^2}{r^2}\left(1 - \frac{2J_1(\alpha a)}{\alpha a J_0(\alpha a)}\right)\right]e^{-i\theta} \tag{C.40}$$

$$B_{\theta,out}(r,\theta) = -iB_0\left[1 + \frac{a^2}{r^2}\left(1 - \frac{2J_1(\alpha a)}{\alpha a J_0(\alpha a)}\right)\right]e^{-i\theta} \tag{C.41}$$

$$B_{r,in}(r,\theta) = \frac{1}{r}\left(\frac{2B_0}{\alpha J_0(\alpha a)}\right)J_1(\alpha r)e^{-i\theta} \tag{C.42}$$

$$B_{\theta,in}(r,\theta) = -i\left(\frac{2B_0}{\alpha J_0(\alpha a)}\right)\left(\alpha J_0(\alpha r) - \frac{1}{r}J_1(\alpha r)\right)e^{-i\theta} \tag{C.43}$$

Populating these field solutions for a variety of wall rotation rates is shown in Fig. C.2. Note that the field is no longer constant in the interior, and flux exclusion and phase shift are now functions of the radial coordinate.

C.4 Thick Wall Penetration Time

To solve the thick wall vertical field penetration time, in analogy with the normal mode approach described in Section 5.4, a matching problem without forcing is formulated and non-trivial solutions found. The same functional forms of Section C.2 are used, though taking $\Omega_w = 0$ and as such $\alpha^2 \equiv i\mu_0\sigma(i\gamma)$. Again $r = a, b$ are the inner and outer radius respectively. The matching equations are:

$$B_{r,r>b}(r,\theta) = (-A_0 r^{-2})e^{-i\theta} \tag{C.44}$$

$$B_{\theta,r>b}(r,\theta) = -i(A_0 r^{-2})e^{-i\theta} \tag{C.45}$$

$$B_{r,a<r<b}(r,\theta) = \frac{1}{r}\left[A_1 J_1(\alpha r) + A_2 Y_1(\alpha r)\right] e^{-i\theta} \tag{C.46}$$

$$B_{\theta,a<r<b}(r,\theta) = -i\left[A_1\left(\alpha J_0(\alpha r) - \frac{1}{r}J_1(\alpha r)\right) + A_2\left(\alpha Y_0(\alpha r) - \frac{1}{r}Y_1(\alpha r)\right)\right] e^{-i\theta} \tag{C.47}$$

$$B_{r,r<a}(r,\theta) = A_3 e^{-i\theta} \tag{C.48}$$

$$B_{\theta,r<a}(r,\theta) = -iA_3 e^{-i\theta} \tag{C.49}$$

Which in matrix form is:

$$\begin{bmatrix} \frac{1}{b^2} & \frac{1}{b}J_1(\alpha b) & \frac{1}{b}Y_1(\alpha b) & 0 \\ -\frac{1}{b^2} & \left(\alpha J_0(\alpha b) - \frac{1}{b}J_1(\alpha b)\right) & \left(\alpha Y_0(\alpha b) - \frac{1}{b}Y_1(\alpha b)\right) & 0 \\ 0 & \frac{1}{a}J_1(\alpha a) & \frac{1}{a}Y_1(\alpha a) & -1 \\ 0 & \left(\alpha J_0(\alpha a) - \frac{1}{a}J_1(\alpha a)\right) & \left(\alpha Y_0(\alpha a) - \frac{1}{a}Y_1(\alpha a)\right) & -1 \end{bmatrix} \begin{bmatrix} A_0 \\ A_1 \\ A_2 \\ A_3 \end{bmatrix} = 0 \tag{C.50}$$

Taking the determinant to be equal to zero, a transcendental eigenvalue equation for α is found:

$$0 = \alpha^2\left[J_0(\alpha b)Y_0(\alpha a) - J_0(\alpha a)Y_0(\alpha b)\right] + \frac{2\alpha}{a}\left[J_1(\alpha a)Y_0(\alpha b) - J_0(\alpha b)Y_1(\alpha a)\right] \tag{C.51}$$

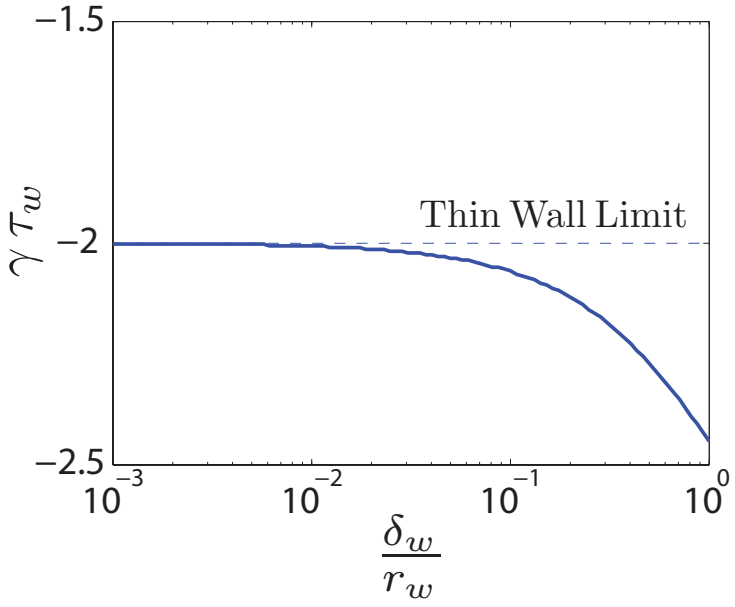

Figure C.3: Deviation from the thin-wall time-constant as wall thickness is increased

Using the fact that $b = a + \delta_w$, a Taylor expansion is performed. To first order, the thin wall result of $\tau = \sigma\mu_0 a\delta_w$ is recovered. Expanding Eq. C.51 to second order gives the first correction term,

$$0 = \left[\frac{2\alpha}{r_a} - \alpha^3\delta\right](J_{1a}Y_{0a} - Y_{1a}J_{0a}) + \frac{\alpha^3\delta}{2}(J_{1a}Y_{0a} - Y_{1a}J_{0a}) + \frac{\alpha^3\delta^2}{r_a}(J_{1a}Y_{2a} - Y_{1a}J_{2a}) + \frac{\alpha^4\delta^2}{2}(Y_{0a}J_{2a} - J_{0a}Y_{2a}) \tag{C.52}$$

The first term is the first order result, and the subsequent correction terms are from the second order expansion. This is solved numerically and is shown in Fig. C.3. The influence of finite wall thickness on the thin-wall time constant ($\gamma_0\tau_w = -2$) is found to vary slowly as non-dimensionalized thickness $\frac{\delta_w}{r_w}$ is increased.

Appendix D

Mode Locking with Active Feedback

Wall rotation was found to have a profound effect on the mode-locking bifurcations, as explored throughout Chapter 6. However, it is also known that a rotating wall is a physical realization of an ideal control system, albeit with a single value of complex gain [98]. It would thus be expected that an active feedback system would modify the mode-locking bifurcations of the plasma, and that different feedback schemes would yield different results. This idea will be studied in this Appendix using the formalism developed in Chapter 6.

D.1 Derivation of Torque

The geometry of the simplified configuration is presented in Fig D.1. As before, Laplace's equation is solved between the walls to form the field solutions:

$$I : B_r(r,\theta) = \Re\left[(A_0 - \tilde{b}r^{-2})e^{-i\theta}\right]$$
$$II : B_r(r,\theta) = \Re\left[(A_1 - A_2 r^{-2})e^{-i\theta}\right]$$
$$III : B_r(r,\theta) = \Re\left[(-A_3)r^{-2}e^{-i\theta}\right]$$

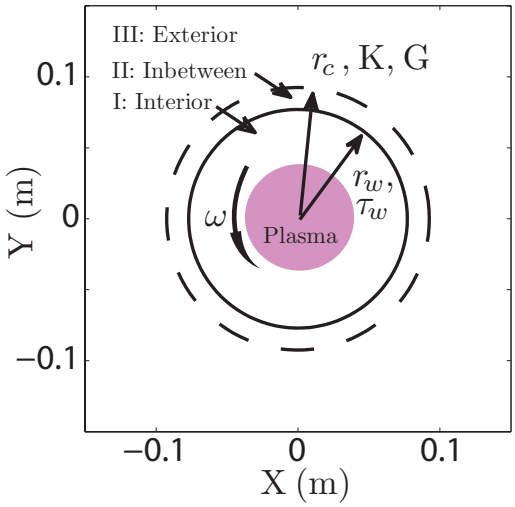

Figure D.1: Geometry used to calculate active feedback torques. The dotted line corresponds to the actuator location.

Where Eq. 6.5 can be used to find the B_θ component. At the static resistive wall at r_w, the matching conditions are:

$$B_r|_{r=r_w^-}^{r=r_w^+} = 0$$
$$B_\theta|_{r=r_w^-}^{r=r_w^+} = -\omega\tau B_r|_{r=r_w}$$

where τ is the wall time and ω is the mode rotation. At the control coil location, r_c, the matching conditions are:

$$B_r|_{r=r_c^-}^{r=r_c^+} = 0$$
$$B_\theta|_{r=r_c^-}^{r=r_c^+} = KB_\theta|_{r=r_w^-} + GB_r|_{r=r_w}$$

Where $K \equiv K_r + iK_i$ and $G \equiv G_r + iG_i$. Thus, only proportional gain is considered, and to simplify the analysis we assume the sensors are located at r_w. In this form, it will be found that the location of r_c is unimportant. Note the phase of $\{K, G\}$ relates to the spatial orientation of the feedback. It is clear that the feedback scheme corresponding

to the rotating is given by $G_r = -\Omega_w \tau$. Using these matching conditions, a matrix is generated to solve for the unknown field coefficients:

$$\begin{bmatrix} r_w^2 & -r_w^2 & 1 & 0 \\ -r_w^2 & (1+i\omega\tau)r_w^2 & (1-i\omega\tau) & 0 \\ 0 & r_c^2 & -1 & 1 \\ -(K+iG) & -1 & -r_c^{-2} & r_c^{-2} \end{bmatrix} \begin{bmatrix} A_0 \\ A_1 \\ A_2 \\ A_3 \end{bmatrix} = \begin{bmatrix} \tilde{b} \\ \tilde{b} \\ 0 \\ \tilde{b} r_w^{-2}(K-iG) \end{bmatrix}$$

This matrix can be inverted to obtain the required coefficients A_n. Equation 6.6 can then be used to calculate the torque in this configuration. It is given by:

$$\Gamma_{EM} = -A_{EM} \frac{K_i(1-G_i) - (1+K_r)(G_r - \omega\tau)}{(2+K_r-G_i)^2 + (K_i + G_r - \omega\tau)^2} \tag{D.1}$$

Where $A_{EM} \equiv \frac{4\tilde{b}^2 \pi L}{r_w^2 \mu_0}$ is a constant coefficient related to the mode amplitude and other constants. The full torque balance equation, corresponding to Eq. 6.3 takes the form:

$$0 = A_{\text{res}}(\Omega_0 - \omega) - A_{EM} \frac{K_i(1-G_i) - (1+K_r)(G_r - \omega\tau)}{(2+K_r-G_i)^2 + (K_i - \omega\tau + G_r)^2} \tag{D.2}$$

As Eq. D.2 has many input parameters $(K, G, \omega\tau)$, limits are explored. As before, solutions to Eq. D.2 correspond to equilibrium solutions, and points at which the discriminant of Eq. D.2 vanish are the bifurcations.

D.2 Feedback on Azimuthal Field

With $G \mapsto 0$, the only feedback is proportional to B_θ and thus corresponds to the most commonly used active control scheme. This scheme is preferred as there is less cross-talk between sensor and actuator in typical geometries [99]. In this scheme Eq. D.1 reduces

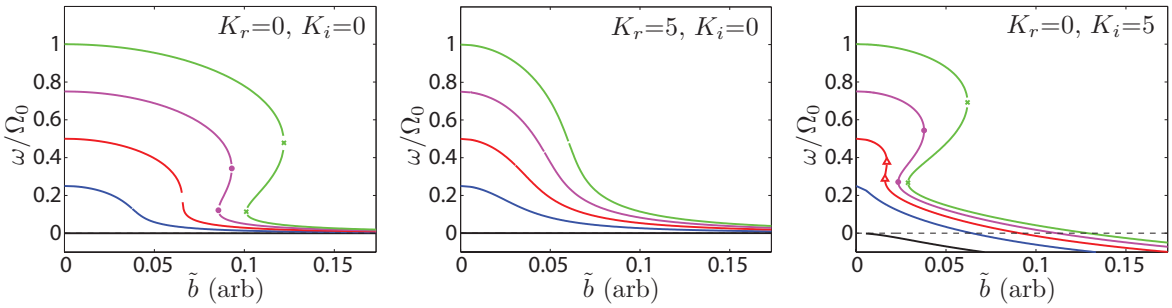

(a) Baseline, no feedback (b) K_r feedback (c) K_i feedback

Figure D.2: Solutions to Eq. D.2 as mode amplitude $\tilde{b}$ is increased, with $G = 0$, illustrating bifurcations.

to:

$$\Gamma_{EM} = -A_{EM} \frac{K_i + (1 + K_r)\omega\tau}{(2 + K_r)^2 + (K_i - \omega\tau)^2} \tag{D.3}$$

Note that this expression diverges at $K_r = -2$ and $K_i = \omega\tau$. These are unphysical and are removed by placing the sensors at $r \neq r_w$. Nonetheless, away from the divergence, the effect of this type of feedback is shown in Fig. D.2. Note that unlike prior plots, here the bifurcation diagrams are shown in the more traditional sense (ie, vs mode amplitude $\tilde{b}$). Thus, as an instability grows the plot is traversed from left to right, encountering a bifurcation.

Without feedback, Fig. D.2(a) shows the traditional picture. For large enough Ω_0, a bifurcation is reached at a critical mode amplitude. Note that no bifurcation is possible if Ω_0 is small. Figure D.2(b) shows effect of K_r feedback. The ability of the mode to lock to the wall is eliminated for large enough K_r. Thus, this feedback scheme is favorable from the point of view of avoiding mode-locking. Figure D.2(c) shows that K_i feedback is less effective at suppressing mode-locking, but instead tends to rotate large amplitude modes. This is consistent with the result that imaginary gain in general yields rotation of the mode under control.

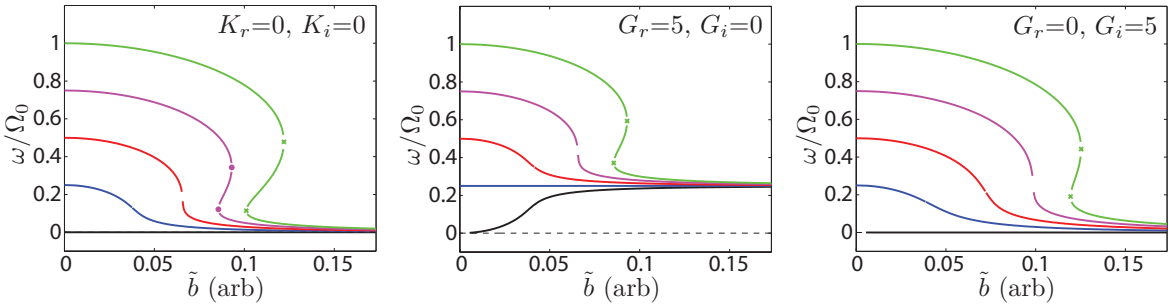

(a) Baseline, no feedback (b) G_r feedback (c) G_i feedback

Figure D.3: Solutions to Eq. D.2 as mode amplitude $\tilde{b}$ is increased, with $K = 0$, illustrating bifurcations.

D.3 Feedback on Radial Field

With gain only proportional to B_r, a less common scheme is explored. The limit of Eq. D.1 as $K \mapsto 0$, the torque is:

$$\Gamma_{EM} = -A_{EM} \frac{(\omega\tau - G_r)}{(2 - G_i)^2 + (G_r - \omega\tau)^2} \tag{D.4}$$

Fig. D.3 compares this scheme to the no-feedback case. In Fig. D.3(b) it can be seen that G_r feedback has effectively shifted the curves vertically, such that the new zero point is at approximately $\omega/\Omega_0 = 0.25$. As G_r feedback is the rotating wall limit, and only one wall is included in this model, this is expected. The G_r feedback has Doppler shifted the entire problem by G_r/τ. Figure D.3(c) shows that G_i feedback has tended to shift the curves to the right. Thus, this feedback scheme is favorable to avoid mode-locking.

Appendix E

List of Data Campaigns

A list of data campaigns undertaken as part of this thesis is presented. During a two year time-frame over 10,000 shots were taken with an average duty cycle of 3 minutes between discharges. Working on a small experiment yields the added challenge and experience of maintaining an experimental device and all associated subsystems throughout the campaigns. While engineering and maintenance work is not captured in this thesis, the sheer number of shots does illustrate the operational aspects of experimental work.

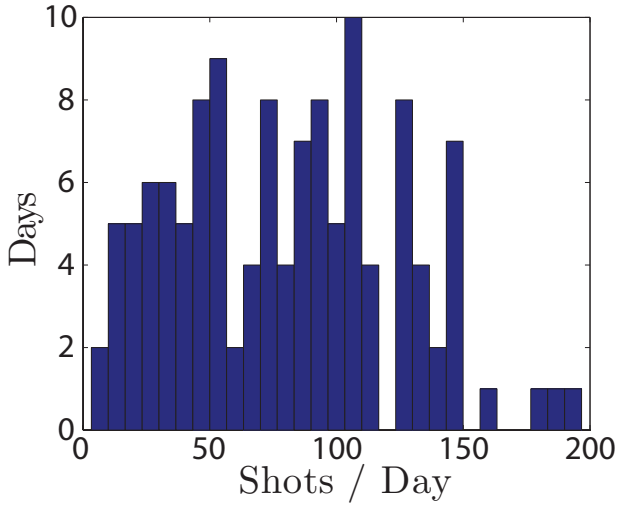

Distribution of shots per day over total data campaign

Tri-Bdot Probe Campaign (Summer 2010)

						Z (cm)			
Description	Amps/gun	Field	10	20	36	62	89	115	121
c7	0	500			X		X		
c7	300	500	X	X	X	X	X	X	X
c7	500	500	X	X	X	X	X	X	X
c7	750	500	X	X	X	X	X	X	
c7	1000	500				X			
m6	500	500	X	X	X	X	X	X	X
m6	580	500				X			
m6	750	300			X	X	X	X	
m6	750	500	X	X	X	X	X	X	
m6	750	750		X	X	X	X	X	
m6	1000	500			X	X	X	X	
m6, no g10 arc	750	500	X	X	X	X	X	X	
m6, no g10 arc	1000	500					X		
c7 all ramp	300-630	500			X	X	X		
m6 all ramp	300-630	500			X	X	X		
c7 g10 ramp	500-1000	500	X		X	X	X	X	
c7 g10 ramp	500-1000	750	X		X	X	X	X	
m6 float dot	300	500				X	X	X	X
m6 float dot	500	500					X	X	X
m6 float dot	750	500					X	X	X

Table E.1: Magnetic Probe Sweeps (in radius)

Rotating Wall Pre-Error Field Coil Campaign (Winter 2010-2011)

Gas	Gun	B_z (G) 400	500	600	700
H	m6	X	X	X	X
H	c7	X	X	X	X
He	m6	X	X	X	X
He	c7	X	X	X	X

Table E.2: I_p Scans - Unbalanced - Sept 2010.

Gas	Gun	Field	250A	500A	I_p 750A	1000A
H	c7	±500G			X	X
H	m6	±500G				X
He	c7	±500G	X	X	X	X
He	m6	±500G			X	

Table E.3: R_m Scans - Unbalanced - Oct 2010.

Gas	Gun	B_z	3	2	1	R_m 0	-1	-2	-3
H	m6	500G	X	X	X	X	X	X	X
He	c7	500G	X	X	X	X	X	X	X

Table E.4: I_p Scans - Unbalanced - Jan/Feb 2011.

Gas	Gun	B_z	3	1	R_m 0	-1	-3
H	c7	500G	X		X		X
H	c7	-500G			X		
H	m6	±500G			X		
He	c7	350G	X	X	X		X
He	c7	500G	X	X	X		X
He	c7	750G	X	X	X	X	X

Table E.5: I_p Scans - Balanced. Mar/April 2011.

Rotating Wall and Error Field Coil Campaign (Spring 2011)

V_{coil}	B_z	I_λ	5	3	1	R_m 0	-1	-3	-5
Y	-500 G	+	X	X	X	X	X	X	X
Y	-500 G	−	X			X		X	X
N	-500 G	+	X	X	X	X	X	X	X
N	-500 G	−	X	X	X	X	X	X	X
N	500 G	−	X	X	X	X	X	X	X
N	500 G	+	X	X	X	X	X	X	X

Table E.6: I_λ Scans: H, m6noArc, 1000a

I_p	5	3	1	R_m 0	-1	-3	-5
500A	X			X	X		X
625A	X	X	X	X	X	X	X
750A	X	X	X	X	X	X	X
875A	X	X	X	X	X	X	X
1000A	X	X	X	X	X	X	X

Table E.7: I_λ Scans: H, m6noArc, B_z=-500G, I_λ=+ve, with V_{coil}.

B_z	I_λ	5	3	1	R_m 0	-1	-3	-5
-500 G	400			X	X	X		
-500 G	600		X				X	
-500 G	800	X						X
-500 G	1200	X						X
-750 G	400				X			
-500 G	200				X			
-500 G	400				X			

Table E.8: I_p Scans: H, m6noArc, with V_{coil}.

Bibliography

[1] M. S. Chu and M. Okabayashi, *Plasma Physics and Controlled Fusion* **52**, 123001 (2010).

[2] M. Kruskal and M. Schwarzschild, *Proceedings of the Royal Society of London. Series A. Mathematical and Physical Sciences* **223**, 348 (1954).

[3] V. D. Shafranov, *At. Energ. (Sov. J. At. Energy)* **5**, 38 (1956).

[4] F. Troyon, R. Gruber, H. Saurenmann, S. Semenzato, and S. Succi, *Plasma Physics and Controlled Fusion* **26**, 209 (1984).

[5] E. J. Strait, *Physics of Plasmas* **1**, 1415 (1994).

[6] D. Pfirsch and H. Tasso, *Nuclear Fusion* **11**, 259 (1971).

[7] B. Alper, *Plasma Physics and Controlled Fusion* **31**, 205 (1989).

[8] C. G. Gimblett, *Nuclear Fusion* **26**, 617 (1986).

[9] C. G. Gimblett, *Plasma Physics and Controlled Fusion* **31**, 2183 (1989).

[10] A. Bondeson and D. J. Ward, *Physical Review Letters* **72**, 2709 (1994).

[11] C. M. Bishop, *Plasma Physics and Controlled Fusion* **31**, 1179 (1989).

[12] M. V. Umansky, R. Betti, and J. P. Freidberg, *Physics of Plasmas* **8**, 4427 (2001).

[13] C. C. Hegna, *Physics of Plasmas* **11**, 4230 (2004).

[14] J. P. Freidberg and R. Betti, *Physics of Plasmas* **8**, 383 (2001).

[15] R. Betti and J. P. Freidberg, *Physical Review Letters* **74**, 2949 (1995).

[16] R. Fitzpatrick and A. Aydemir, *Nuclear Fusion* **36**, 11 (1996).

[17] J. M. Finn, *Physics of Plasmas* **2**, 198 (1995).

[18] A. M. Garofalo, A. D. Turnbull, E. J. Strait, M. E. Austin, J. M. Bialek, M. S. Chu, E. D. Fredrickson, R. J. La Haye, G. A. Navratil, L. L. Lao, E. A. Lazarus, M. Okabayashi, B. W. Rice, S. A. Sabbagh, J. T. Scoville, T. S. Taylor, and M. L. Walker, *Physics of Plasmas* **6**, 1893 (1999).

[19] H. Reimerdes, A. M. Garofalo, G. L. Jackson, M. Okabayashi, E. J. Strait, M. S. Chu, Y. In, R. J. La Haye, M. J. Lanctot, Y. Q. Liu, G. A. Navratil, W. M. Solomon, H. Takahashi, and R. J. Groebner, *Physical Review Letters* **98**, 055001 (2007).

[20] R. Fitzpatrick, *Physics of Plasmas* **9**, 3459 (2002).

[21] M. F. F. Nave and J. A. Wesson, *Nuclear Fusion* **2575** (1990).

[22] R. Fitzpatrick, *Nuclear Fusion* **33**, 1049 (1993).

[23] T. H. Jensen, A. W. Leonard, and A. W. Hyatt, *Physics of Fluids B: Plasma Physics* **5**, 1239 (1993).

[24] J. M. Finn and C. R. Sovinec, *Physics of Plasmas* **5**, 461 (1998).

[25] C. G. Gimblett and R. S. Peckover, *Proceedings of the Royal Society of London. Series A. Mathematical and Physical Sciences* **368**, 75 (1979).

[26] A. M. Garofalo, G. L. Jackson, R. J. La Haye, M. Okabayashi, H. Reimerdes, E. J. Strait, J. R. Ferron, R. J. Groebner, Y. In, M. J. Lanctot, G. Matsunaga, G. A. Navratil, W. M. Solomon, H. Takahashi, M. Takechi, and A. D. Turnbull, *Nuclear Fusion* **47**, 1121 (2007).

[27] A. H. Boozer, *Physical Review Letters* **86**, 5059 (2001).

[28] J. W. Berkery, S. A. Sabbagh, R. Betti, B. Hu, R. E. Bell, S. P. Gerhardt, J. Manickam, and K. Tritz, *Physical Review Letters* **104**, 035003 (2010).

[29] B. Hu and R. Betti, *Physical Review Letters* **93**, 1 (2004).

[30] H. Reimerdes, J. W. Berkery, M. J. Lanctot, a. M. Garofalo, J. Hanson, Y. In, M. Okabayashi, S. A. Sabbagh, and E. J. Strait, *Physical Review Letters* **106**, 1 (2011).

[31] E. Olofsson, Mode Control of RFP, in *MHD Control Workshop*, Princeton, NJ, 2009.

[32] S. A. Sabbagh, J. W. Berkery, R. E. Bell, J. M. Bialek, S. P. Gerhardt, J. E. Menard, R. Betti, D. A. Gates, B. Hu, O. N. Katsuro-Hopkins, B. P. LeBlanc, F. M. Levinton, J. Manickam, K. Tritz, and H. Yuh, *Nuclear Fusion* **50**, 025020 (2010).

[33] M. Okabayashi, G. Matsunaga, J. S. DeGrassie, W. W. Heidbrink, Y. In, Y. Q. Liu, H. Reimerdes, W. M. Solomon, E. J. Strait, M. Takechi, N. Asakura, R. V. Budny, G. L. Jackson, J. M. Hanson, R. J. La Haye, M. J. Lanctot, J. Manickam, K. Shinohara, and Y. B. Zhu, *Physics of Plasmas* **18**, 056112 (2011).

[34] W. F. Bergerson, C. B. Forest, G. Fiksel, D. A. Hannum, R. D. Kendrick, J. S. Sarff, and S. Stambler, *Physical Review Letters* **96**, 015004 (2006).

[35] M. I. Brookhart, C. Paz-Soldan, D. A. Hannum, A. J. Clinch, C. R. Sovinec, C. B. Forest, and R. D. Kendrick, *Bull. Am. Phy. Soc.* **51**, 9004P (2010).

[36] W. F. Bergerson, D. A. Hannum, C. C. Hegna, R. D. Kendrick, J. S. Sarff, and C. B. Forest, *Physical Review Letters* **101**, 235005 (2008).

[37] V. D. Pustovitov, *Physics of Plasmas* **16**, 052503 (2009).

[38] D. A. Hannum, *Characterizing the Plasma of the Rotating Wall Machine*, PhD thesis, Madison, WI, 2010.

[39] G. Fiksel, A. F. Almagri, D. Craig, M. Iida, S. C. Prager, and J. S. Sarff, *Plasma Sources Science and Technology* **5**, 78 (1996).

[40] D. J. D. Hartog, D. Craig, G. Fiksel, and J. S. Sarff, *Plasma Sources Science and Technology* **6**, 492 (1997).

[41] I. H. Hutchinson, *Principles of Plasma Diagnostics*, Cambridge University Press, Cambridge, 2005.

[42] L. Spitzer, *Physics of Fully Ionized Gases*, Interscience, New York, NY, 1962.

[43] L. A. Dorf, T. P. Intrator, X. Sun, J. Hendryx, G. A. Wurden, I. Furno, and G. Lapenta, *Physics of Plasmas* **17**, 102101 (2010).

[44] X. Sun, T. P. Intrator, L. A. Dorf, I. Furno, and G. Lapenta, *Physical Review Letters* **100**, 205004 (2008).

[45] I. Furno, T. P. Intrator, G. Lapenta, L. A. Dorf, S. Abbate, and D. D. Ryutov, *Physics of Plasmas* **14**, 022103 (2007).

[46] D. D. Ryutov, I. Furno, T. P. Intrator, S. Abbate, and T. Madziwa-Nussinov, *Physics of Plasmas* **13**, 032105 (2006).

[47] R. Lorenzini, E. Martines, P. Piovesan, D. Terranova, P. Zanca, M. Zuin, A. Alfier, D. Bonfiglio, F. Bonomo, A. Canton, S. Cappello, L. Carraro, R. Cavazzana, D. F. Escande, A. Fassina, P. Franz, M. Gobbin, P. Innocente, L. Marrelli, R. Pasqualotto, M. E. Puiatti, M. Spolaore, M. Valisa, N. Vianello, and P. Martin, *Nature Physics* **5**, 570 (2009).

[48] W. F. Bergerson, F. Auriemma, B. E. Chapman, W. X. Ding, P. Zanca, D. L. Brower, P. Innocente, L. Lin, R. Lorenzini, E. Martines, B. Momo, J. S. Sarff, and D. Terranova, *Physical Review Letters* **107**, 1 (2011).

[49] A. Weller, A. D. Cheetham, A. W. Edwards, R. D. Gill, A. Gondhalekar, R. S. Granetz, J. A. Snipes, and J. A. Wesson, *Physical Review Letters* **59**, 2303 (1987).

[50] J. E. Menard, R. E. Bell, E. D. Fredrickson, D. A. Gates, S. M. Kaye, B. P. LeBlanc, R. Maingi, S. S. Medley, W. Park, S. A. Sabbagh, A. C. Sontag, D. Stutman, K. Tritz, W. Zhu, and T. N. R. Team, *Nuclear Fusion* **45**, 539 (2005).

[51] I. T. Chapman, M.-D. Hua, S. D. Pinches, R. J. Akers, A. R. Field, J. P. Graves, R. J. Hastie, C. A. Michael, and the MAST Team, *Nuclear Fusion* **50**, 045007 (2010).

[52] S. Yoshikawa, *Physical Review Letters* **27**, 1772 (1971).

[53] W. A. Cooper, J. P. Graves, A. Pochelon, O. Sauter, and L. Villard, *Physical Review Letters* **105**, 035003 (2010).

[54] P. M. Bellan, *Fundamentals of Plasma Physics*, Cambridge University Press, Cambridge, 1 edition, 2006.

[55] R. J. Bickerton, *Proceedings of the Physical Society* **72**, 618 (1958).

[56] J. B. Taylor, *Physical Review Letters* **33**, 1139 (1974).

[57] J. B. Taylor, *Reviews of Modern Physics* **58**, 741 (1986).

[58] M. Kruskal and J. L. Tuck, *Proceedings of the Royal Society of London. Series A. Mathematical and Physical Sciences* **245**, 222 (1958).

[59] I. Furno, T. P. Intrator, D. D. Ryutov, S. Abbate, T. Madziwa-Nussinov, A. Light, L. A. Dorf, and G. Lapenta, *Physical Review Letters* **97**, 015002 (2006).

[60] I. Furno, T. P. Intrator, E. Torbert, C. Carey, M. D. Cash, J. K. Campbell, W. J. Fienup, C. A. Werley, G. A. Wurden, and G. Fiksel, *Review of Scientific Instruments* **74**, 2324 (2003).

[61] F. Arcudi, G. L. Delzanno, and J. M. Finn, *Physics of Plasmas* **17**, 062106 (2010).

[62] D. D. Ryutov, R. H. Cohen, and L. D. Pearlstein, *Physics of Plasmas* **11**, 4740 (2004).

[63] M. G. Linton, *Physics of Plasmas* **13**, 058301 (2006).

[64] W. Gekelman, J. E. Maggs, and H. Pfister, *Plasma Science, IEEE Transactions on* **20**, 614 (1992).

[65] I. Furno, T. P. Intrator, E. Hemsing, S. C. Hsu, S. Abbate, P. Ricci, and G. Lapenta, *Physics of Plasmas* **12**, 055702 (2005).

[66] X. Sun, T. P. Intrator, L. A. Dorf, J. Sears, I. Furno, and G. Lapenta, *Physical Review Letters* **105**, 255001 (2010).

[67] E. G. Zweibel and M. Yamada, *Annual Review of Astronomy and Astrophysics* (2009).

[68] J. E. Maggs, T. A. Carter, and R. J. Taylor, *Physics of Plasmas* **14**, 052507 (2007).

[69] W. B. Kunkel, *Physics of Fluids* **27**, 2369 (1984).

[70] B. V. Somov, The Generalized Ohms Law in Plasma, volume 341 of *Astrophysics and Space Science Library*, pp. 193–204, Springer New York, 2007.

[71] Y. In, I. Bogatu, A. M. Garofalo, G. Jackson, J. Kim, R. La Haye, M. Lanctot, L. Marrelli, P. Martin, M. Okabayashi, H. Reimerdes, M. Schaffer, and E. J. Strait, *Nuclear Fusion* **50**, 042001 (2010).

[72] M. L. Dudley and R. W. James, *Proceedings of the Royal Society of London. Series A. Mathematical and Physical Sciences* **425**, 407 (1989).

[73] E. J. Strait, T. S. Taylor, A. D. Turnbull, J. R. Ferron, L. L. Lao, B. W. Rice, O. Sauter, S. J. Thompson, and D. Wrblewski, *Physical Review Letters* **74**, 2483 (1995).

[74] I. H. Hutchinson, *Plasma Physics and Controlled Fusion* **43**, 145 (2001).

[75] N. C. Logan, E. J. Strait, and H. Reimerdes, *Plasma Physics and Controlled Fusion* **52**, 045013 (2010).

[76] D. A. Gates and T. C. Hender, *Nuclear Fusion* **36**, 273 (1996).

[77] G. L. Delzanno, E. G. Evstatiev, and J. M. Finn, *Physics of Plasmas* **14**, 072902 (2007).

[78] V. D. Pustovitov, *Nuclear Fusion* **51**, 013006 (2011).

[79] Z. Yan, M. Xu, P. H. Diamond, C. Holland, S. H. Mller, G. R. Tynan, J. H. Yu, and S. H. Muller, *Physical Review Letters* **104**, 10 (2010).

[80] V. D. Pustovitov, *Nuclear Fusion* **49**, 045003 (2009).

[81] V. D. Pustovitov, *Plasma Physics Reports* **27**, 195 (2001).

[82] V. D. Pustovitov, *Nuclear Fusion* **47**, 1583 (2007).

[83] C. G. Gimblett and R. J. Hastie, *Physics of Plasmas* **11**, 1019 (2004).

[84] E. J. Strait, a. M. Garofalo, and M. Okabayashi, *Physics of Plasmas* **12**, 084701 (2005).

[85] C. G. Gimblett and R. J. Hastie, *Physics of Plasmas* **12**, 084702 (2005).

[86] G. L. Delzanno, E. G. Evstatiev, and J. M. Finn, *Physics of Plasmas* **14**, 092901 (2007).

[87] V. A. Svidzinski, V. V. Mirnov, and H. Li, *Physics of Plasmas* **15**, 092106 (2008).

[88] C. Paz-Soldan, W. F. Bergerson, M. I. Brookhart, D. A. Hannum, R. D. Kendrick, G. Fiksel, and C. B. Forest, *Review of Scientific Instruments* **81**, 123503 (2010).

[89] C. Paz-Soldan, M. I. Brookhart, A. J. Clinch, D. A. Hannum, and C. B. Forest, *Physics of Plasmas* **18**, 052114 (2011).

[90] C. Paz-Soldan, M. I. Brookhart, A. T. Eckhart, D. A. Hannum, C. C. Hegna, J. S. Sarff, and C. B. Forest, *Physical Review Letters* **107**, 245001 (2011).

[91] C. Paz-Soldan, M. I. Brookhart, C. C. Hegna, and C. B. Forest, *Physics of Plasmas* **19**, 056104 (2012).

[92] C. Paz-Soldan, M. I. Brookhart, C. C. Hegna, and C. B. Forest, *submitted to Physics of Plasmas* (2012).

[93] A. L. Montgomery, C. C. Hegna, C. R. Sovinec, A. J. Cole, and S. E. Kruger, Error-Field and Resistive Wall Coupling in NIMROD, in *Bull. Am. Phy. Soc.*, p. 9134P, 2010.

[94] I. V. Khalzov, B. P. Brown, N. Katz, and C. B. Forest, *Physics of Plasmas* **2** (2012).

[95] E. Schartman, H. Ji, and M. J. Burin, *Review of Scientific Instruments* **80**, 024501 (2009).

[96] M. Abramowitz and I. A. Stegun, *Handbook of Mathematical Functions: with Formulas, Graphs, and Mathematical Tables*, Dover Publications, Dover, 1965.

[97] M. Perry, *Low Frequency Electromagnetic Design*, Electrical Engineering and Electronics, Taylor and Francis, Boca Raton, FL, 1 edition, 1985.

[98] R. Fitzpatrick and T. H. Jensen, *Physics of Plasmas* **3**, 2641 (1996).

[99] V. D. Pustovitov, *Plasma Physics and Controlled Fusion* **44**, 295 (2002).